Searches for supersymmetry in the fully hadronic channel and jet calibration with the ATLAS detector at the LHC

Baptiste Abeloos

NNT : 2017SACLS200

Thèse de doctorat de l'université Paris-Saclay préparée à l' Université Paris-Sud

Ecole doctorale n°576
PHENIICS
Spécialité : Physique des particules

par

M. Baptiste Abeloos

Recherche de particules supersymétriques dans le canal hadronique et calibration des jets avec le détecteur ATLAS du LHC

Thèse présentée et soutenue au LAL, le 20 juillet 2017.

Composition du Jury :

M.	Achille Stocchi	Professeur des Universités (LAL)	Président du jury
M.	Filip Moortgat	Directeur de recherche (CERN)	Rapporteur
M.	Pascal Pralavorio	Directeur de recherche (CPPM)	Rapporteur
M.	Christophe Clément	Professeur des Universités (Stockholm)	Examinateur
Mme.	Caroline Collard	Chargée de recherche (Strasbourg)	Examinatrice
M.	Nikola Makovec	Chargé de recherche (LAL)	Directeur de thèse

Laboratoire de l'Accélérateur Linéaire LAL 17-049

"*Il n'existe rien de constant sinon le changement.*"

Siddhartha Gautama

École Doctorale PHENIICS Doctoral School

Titre : Recherche de particules supersymétriques dans le canal hadronique et calibration des jets avec le détecteur ATLAS du LHC

Résumé : Le Modèle Standard de la physique des particules est un modèle décrivant très bien les particules élémentaires et leurs interactions mais plusieurs raisons motivent les physiciens à rechercher de la physique au-delà de ce modèle. La supersymétrie correspond à une des extensions les plus prometteuses. La thèse est axée sur deux sujets, et repose sur les données acquises en 2015 et 2016 avec le détecteur ATLAS du LHC (CERN): La première partie est un travail de performance permettant d'améliorer la mesure de l'énergie des jets de particules. Ces objets sont générés par l'hadronisation des quarks et des gluons par interaction nucléaire forte et sont difficiles à reconstruire. Ma contribution correspond à la dernière étape et repose entièrement sur les données. La méthode se base sur les mesures effectuées sur les photons qui servent d'objets de référence. Mon travail a consisté à mettre en place la méthode, estimer les corrections en énergie et évaluer les incertitudes. Les corrections obtenues sont de l'ordre de 2-3% en fonction de l'énergie des jets. L'incertitude sur l'échelle en énergie des jets est estimée à environ 1% pour les trois types de jets étudiés. Les résultats sont actuellement utilisés par la collaboration ATLAS. Cette méthode permet également de mesurer la résolution en énergie des jets du détecteur. Une résolution de l'ordre de 17%-22% est obtenue à 40 GeV en fonction du type de jet étudié, et 4% à 1 TeV, avec une incertitude de l'ordre de 10%. La deuxième partie de la thèse porte sur la recherche d'un signal de supersymétrie. Le signal recherché correspond à la production d'une paire de squarks ou de gluinos et comprend des jets et de l'énergie transverse manquante dans l'état final. Mon travail porte principalement sur l'optimisation des critères de sélections en se basant sur plusieurs modèle simplifiés de supersymétrie. Neuf nouvelles régions de signal ont été introduites dans l'analyse. Les limites tracées au cours du Run 1 sur la masse des squarks et gluinos ont ainsi été augmentées pour atteindre une valeur maximal respective de l'ordre de 1.6 TeV et 2 TeV sur les modèles étudiés.

Title : Search for supersymmetry in the fully hadronic channel and jet calibration with the ATLAS detector at the LHC

Abstract : The Standard Model of particle physics is a very precise model describing the elementary particles and their interactions. However, some issues lead physicists to search for physics beyond the Standard Model. Supersymmetry is an extension of the Standard Model providing solutions to the current issues. In this thesis, results are obtained using the data collected in 2015 and 2016 with the ATLAS detector at the LHC (CERN). The thesis is based in two parts: The first part is a performance analysis improving the energy measurement of high energy objects called "jets". They are generated by the hadronization of quarks and gluons in the detector via the strong nuclear interaction. My contribution is the last step of the the reconstruction and calibration chain and is fully based on data. The method uses the very precise measurement of the photon energy, and provides corrections to the jet energy scale. My contribution consists in set-up the method, estimate the corrections, measure the jet energy scale and evaluate the uncertainties. Corrections are at the order of 2-3% as a function of the jet energy scale. The uncertainty of the jet energy scale is estimated to be at the order of 1% for the three jet types. Results are now used by the ATLAS Collaboration. This method is also used to estimate the jet energy resolution. A resolution at the order of 17%-22% at 40 GeV depending on the jet type, and 4% at 1 TeV is obtained with an uncertainty at the order of 10%. The second part of the thesis corresponds to the search for supersymmetry. The signal corresponds to a pair of supersymmetric particles called squarks and gluinos and corresponds to jets and missing transverse energy in the final state. My contribution mainly corresponds to the optimisation of the selections using several simplified models of supersymmetry. Nine signal regions have been introduced in the analysis. Limits on the mass of squarks and gluinos computed during the Run 1 have been greatly improved to reach a maximal value respectively at the order of 1.6 TeV and 2 TeV.

Contents

Introduction

The Higgs boson discovered by ATLAS and CMS during the Run 1 of the Large Hadron Collider (LHC) is the last particle predicted by the Standard Model of particle physics. The Standard Model is now a well established and precise model. Nevertheless, some issues remain in particle physics such as the hierarchy problem, the absence of dark matter candidate, the matter-antimatter asymmetry, the observation of neutrino oscillation, and the absence of gravitation in the model. Therefore, searches for physics beyond the Standard Model is the priority of the LHC. Supersymmetry is one of the most promising theory of new physics. The theory predicts the existence of new particles that can solve some current issues of the Standard Model. In particular supersymmetry can bring solution to the hierarchy problem, can provide a dark-matter candidate, and can unify the coupling constant of the gauge groups. Searches in the Run 2 of the LHC benefited from the increase of the center-of-mass energy of the proton-proton collisions from $\sqrt{s}$ = 8 TeV to $\sqrt{s}$ = 13 TeV, leading to an increase of the cross-section production of the supersymmetric particles, and to a better sensitivity on the models. Squarks and gluinos are the supersymmetric particles associated to the quarks and gluons, and can be produced at the LHC with strong interaction. They can be probed with a signature defined by more than two jets and transverse missing energy in the final states (fully hadronic channel). Therefore, a good measurement of the jet energy scale is crucial for the search of supersymmetry, and for many other analysis searching for new physics. This thesis is divided in six chapters:

The first chapter gives the theoretical context of the search. It briefly presents the Standard Model of particle physics and its different issues. The supersymmetry is introduced, with a focus on the Minimal Supersymmetric Standard Model (MSSM) and the searches for squarks and gluinos with the ATLAS detector in the fully hadronic channel. The second chapter firstly describes the experimental devices used at CERN to accelerate the proton bunches at almost the speed of light. The data from the proton-proton collisions is collected with the ATLAS detector which is described in the second part. The last part describes the methods used to reconstruct the physics objects from the collected data. The third chapter defines the jets and describes all the steps to reconstruct and calibrate the jets from the data. A large contribution of this thesis is part of the last step of the calibration, corresponding to the in-situ calibration. The fourth chapter is dedicated to the in-situ calibration using the gamma+jet direct balance method. In this method, the photon is used as a reference object for the calibration. The method was developed and applied to jets with a transverse momentum between $\sim$ 40 GeV and $\sim$ 1 TeV, using the 2015 and 2016 data. This chapter describes the method, the selections applied to the data, the corrections derived from the method, and the evaluation of the systematics. The fifth chapter describes the measurement of the jet energy resolution of the detector, using the gamma+jet direct balance method. This chapter describes the method to extract the jet energy resolution, the results and the evaluation of the systematics. The last chapter is fully dedicated to the search for squarks and gluinos in the fully hadronic channel (also known as the 0-lepton channel). This chapter includes the description of the strategy of the analysis, the description of the signal and background, the selections applied to the data, the definition and optimisation of the signal regions, the methods used for the background estimation, the evaluation of the systematics, the results and the limits obtained on the models.

Chapter 1

Supersymmetry

"Education is the most powerful weapon which you can use to change the world. "

Nelson Mandela

Contents

1.1 The Standard Model of particle physics

During the 20th century, theories and discoveries of physicists have resulted in the development of one model describing the elementary particles and their interactions: the Standard Model of particle physics. This model has proven to be extremely successful in describing experimental data over many decades. The Higgs boson is the last elementary particle discovered. It was predicted by the Standard Model [1–4] in the '60 and discovered by the CERN in 2012 [5] [6]. The Standard Model describes three of the four fundamental forces of nature: electromagnetism, weak and the strong interactions. The behaviour of particles is described by the unification of quantum mechanics and special relativity in a theory called quantum field theory [7]. The Standard Model is based on the $SU(3)_C \times SU(2)_L \times U(1)_Y$ gauge symmetry [8], including the symmetry group of strong interaction $SU(3)_C$, and the gauge group of electroweak interaction $SU(2)_L \times U(1)_Y$. The gauge symmetry of the electromagnetic interaction $U(1)_{em}$ appears in the SM as a subgroup of $SU(2)_L \times U(1)_Y$. In this sense, the electroweak interaction can be seen as the unification of electromagnetism and weak interaction via a mechanism called the Brout-Englert-Higgs mechanism (BEH) [9–14].

1.1.1 Matter particles

Matter particles can be classified in the two families called quarks and leptons, belonging to the broader group of spin-1/2 fermions. Quarks and leptons consists of a group of six particles related in pair (doublet). The two lightest and more stables particles belong to the first generation, and the heaviest and short-lived particles belong to the second and third generations. The matter in the universe is made from particles of the first generation, while heaviest particles decay in the next more stable generations. The particles of the Standard Model are represented in Figure 1.1. The first generation of the quarks is composed of quark up and down, the second of charmed and strange quarks, and the third of bottom (or beauty) and top quarks. Quarks interact by strong nuclear force, and come in three different colours. They only mix together to form colourless objects. The six leptons are similarly arranged in three generations: the electron and electronic neutrino (first generation), the muon and muonic neutrino, and the tau and tauic neutrino. The electron, muon and tau have the same electric charge but an increasing mass while neutrinos are electrically neutral and have a very small mass. An anti-particle is associated with each fermion, with the same mass and statistic rules, but opposite electric charge. Anti-particles are not represented in Figure 1.1.

1.1.2 Forces and carrier particles

The three forces described by the Standard Model result from an exchanged of force-carrier particles. These particles are spin-1 bosons, and are also known as vector bosons. These bosons exchanged can be seen as discrete amounts of energy transfers. Each fundamental force has its own corresponding boson. The electromagnetic force is carried by photons, the weak interaction is carried by Z and $W^{\pm}$ bosons, and the strong interaction is carried by gluons. The vector bosons are represented in figure 1.1. The elementary particle that should be responsible for the gravitation is called the graviton, and have not been observed yet. The inclusion of the gravitation in the Standard Model has proved to be a huge challenge. The microscopic world ruled by quantum mechanics and the macroscopic world ruled by general relativity are difficult to fit in a single framework. Luckily, at elementary particle scale, the effects of gravity are negligible. The last particle of the Standard Model is the Higgs boson. The existence of such a spin-0 particle has been predicted in the '60 with the Brout-Englert-Higgs (BEH) mechanism.

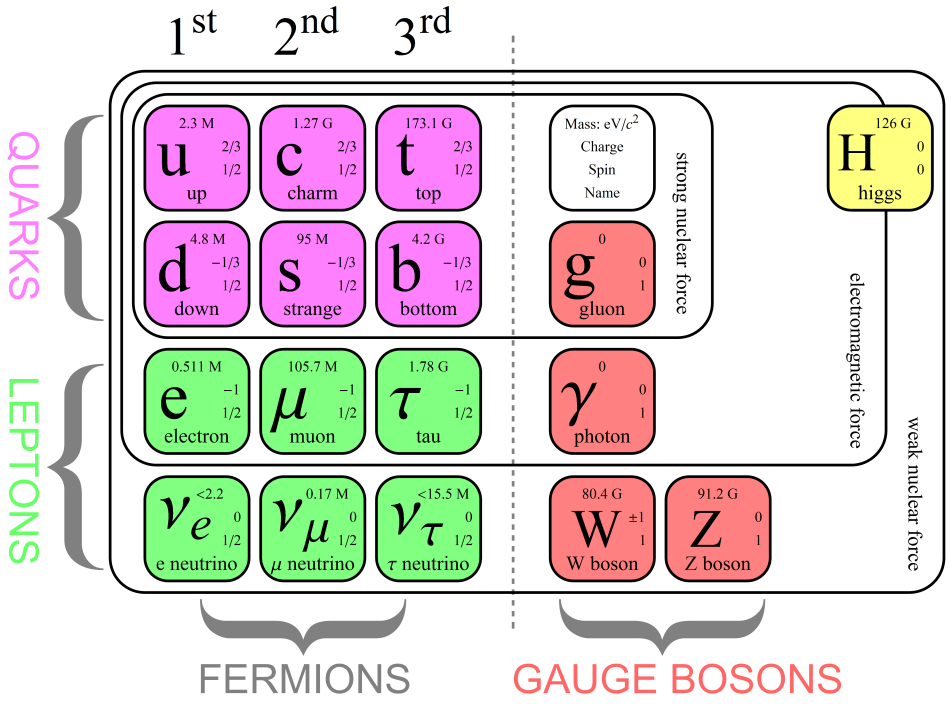

Figure 1.1: The Standard Model of particle physics, with quarks (purple), leptons (green), gauge bosons (red), and Higgs boson (yellow). The first, second, and third columns show the three generations of fermions, the fourth, fifth columns show the vector bosons, and the sixth columns shows the Higgs boson. The gluon is the vector boson of strong nuclear force, the photon is the vector boson of electromagnetism, and the Z and $W^{\pm}$ are the vector bosons of weak interaction. The Higgs boson is linked to the electroweak symmetry breaking. The mass, charge, spin and name of each particle is given in the Figure [15].

1.1.3 The BEH mechanism

An unbroken gauge symmetry $SU(3)_C \times SU(2)_L \times U(1)_Y$ would imply that gauge bosons are all massless, while a non-zero mass of W and Z bosons have been measured. The problem is fixed by introducing a single $SU(2)_L$ doublet scalar field Φ, causing the spontaneous breaking of $SU(2)_L \times U(1)_Y$ gauge symmetry via the Higgs mechanism.

$$\Phi = \begin{pmatrix} \Phi^+ \\ \Phi^0 \end{pmatrix}, \tag{1.1}$$

Where Φ^+ and Φ^0 correspond to a charged and a neutral complex scalar field. The new term in the Lagrangian involving Φ is then given by:

$$\mathcal{L}_{Higgs} = |\mathcal{D}_\mu \Phi|^2 - V(\Phi), \tag{1.2}$$

Where the first term contains the kinetic and gauge-interaction terms, and the second term is the potential energy function. The gauge invariant potential V is given by:

$$V(\Phi) = -\mu^2 \Phi^\dagger \Phi + \lambda (\Phi^\dagger \Phi)^2, \tag{1.3}$$

Where μ and λ are free parameters. The Higgs term in the Lagrangian can then be expressed as:

$$\mathcal{L}_{Higgs} = |\mathcal{D}_\mu \Phi|^2 + \mu^2 \Phi^\dagger \Phi - \lambda (\Phi^\dagger \Phi)^2, \tag{1.4}$$

- If $\lambda < 0$, then V is unbounded and there is no stable vacuum state.
- If -μ^2 and λ are both positives, the potential energy function has a minimum at $\Phi = 0$. In this case the symmetry is unbroken in the vacuum (Figure 1.2 on the left).
- If -μ^2 is negative and λ is positive, the minimum is not 0 and the vacuum or minimum energy state is not invariant under $SU(2)_L \times U(1)_Y$ transformation: the gauge symmetry is spontaneously broken in the vacuum (Figure 1.2 on the right).

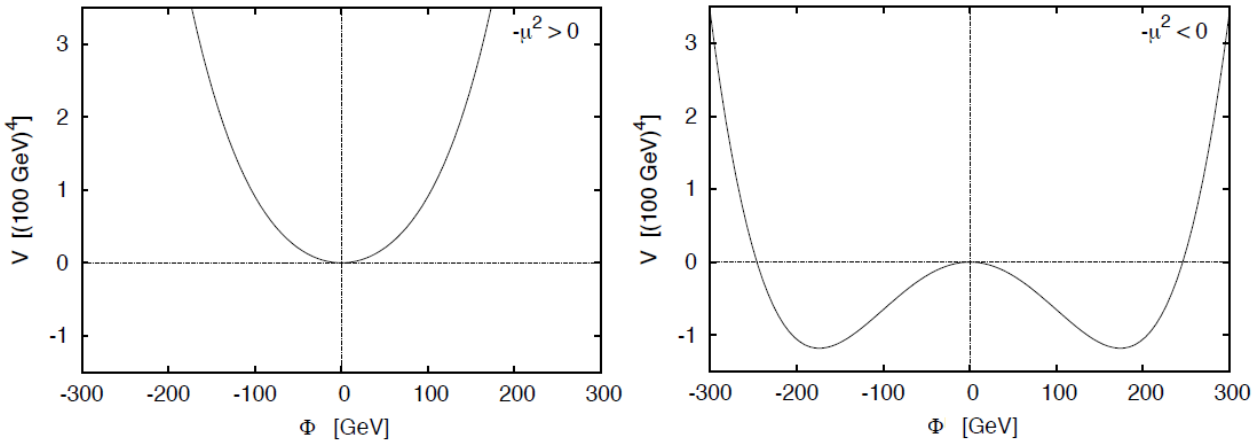

Figure 1.2: Shape of the Higgs potential for negative (a) and positive μ^2 (b) [16].

The vacuum expectation value (VEV) is invariant by $SU(2)_L$ transformation, if Φ is excited it can be written as:

$$\Phi = \frac{1}{\sqrt{2}} \begin{pmatrix} 0 \\ v + h \end{pmatrix}, \tag{1.5}$$

We can then examine the gauge-kinetic term acting on Φ:

$$\mathcal{D}_\mu = \partial_\mu - i\frac{g'}{2}B_\mu - i\frac{g}{2}W_\mu^a \sigma^a, \tag{1.6}$$

Where g and g' are respectively the coupling constants of $SU(2)_L$ and $U(1)_Y$ interactions, W_μ^a, a = 1,2,3 correspond to the three gauge fields of the group SU(2), B_μ to the gauge field of U(1), and σ^a to the Pauli matrices. Then it follows:

$$\mathcal{D}_\mu \Phi = \frac{1}{2} \begin{pmatrix} -\frac{i}{2}g(W_\mu^1 - iW_\mu^2)(v + h) \\ \partial_\mu h + \frac{i}{2}g'(W_\mu^3 - g'B_\mu)(v + h) \end{pmatrix}. \tag{1.7}$$

by introducing the combinations corresponding to the charged W bosons,

$$W_\mu^\pm = (W_\mu^1 \mp iW_\mu^2)/\sqrt{2}, \tag{1.8}$$

One can define the mass term of the W as:

$$M_W = \frac{gv}{2}, \tag{1.9}$$

Since M_W have been directly measured as $M_W = 80.370 \pm 0.019$ [17], and g can be computed from the Fermi constant $\frac{G_F}{(\hbar c)^3} = \frac{\sqrt{2}}{8}\frac{\sqrt{g^2}}{m_W^2} = 1.1663787(6) \times 10^{-5} GeV^{-2}$ [18], one can determine that $v \simeq 246$ GeV. The field A_μ does not couple to the Higgs field, and thus does not acquire a mass through the Higgs mechanism. This state is then identified as the photon.

$$A_\mu = sin\theta_W W_\mu^3 + cos\theta_W B_\mu, \tag{1.10}$$

The field Z_μ couples to the Higgs fields and thus receives a mass from the Higgs field and is identified to the Z boson:

$$Z_\mu = cos\theta_W W_\mu^3 + sin\theta_W B_\mu, \tag{1.11}$$

with:

$$\cos\theta_W = \frac{m_W}{m_Z} = \frac{g'}{\sqrt{g^2 + g'^2}}, \tag{1.12}$$

$$\sin\theta_W = \frac{g}{\sqrt{g^2 + g'^2}}, \tag{1.13}$$

The mass of the Z boson is then defined as:

$$m_Z = \frac{v}{2}\sqrt{g^2 + g'^2}, \tag{1.14}$$

The Higgs couples to himself and his mass is defined as:

$$m_h^2 = 2\mu^2 = 2\lambda v, \tag{1.15}$$

The Higgs boson was discovered at CERN in 2012 by ATLAS [5] and CMS [6] experiment. Its discovery in 2012 is one of the biggest success of the Standard Model. Including the Higgs mechanism, the Standard Model has 19 free parameters that can not be predicted by the theory and have to be measured experimentally: 6 for the quarks mass, 3 for the leptons mass, 4 for the CKM matrix, 1 for θ_{QCD}, 3 for the coupling constant of the group $U(1)_Y$, $SU(2)_L$, $SU(3)_C$ and two concerning the Higgs mechanism with the Higgs mass and the VEV. The Higgs mass have been measured by ATLAS and CMS as: m_H = 125.09 $\pm$ 0.21 (stat) $\pm$ 0.11 (sys) GeV [19]. Despite of the very high precision of the Standard Model predictions in particle physics, some reasons lead physicist to search for physics beyond the Standard Model [20].

1.2 Motivations for physics beyond the Standard Model

1.2.1 Matter anti-matter asymmetry

The Big Bang theory assumes that matter and anti-matter should have been produced in almost equal amounts in the initial conditions [21]. But today, the universe is almost entirely composed of matter. This problem is known as the matter anti-matter asymmetry. The mechanism that could explain this asymmetry is not explained yet.

1.2.2 Neutrino masses and neutrino oscillations

Many recent experiments have shown that neutrinos do oscillate [22, 23] and have a non zero mass. The origin of this mass is still unknown, and the mechanism of neutrino oscillations is not explained yet. The experimental discovery of neutrino oscillation, and thus neutrino mass by Super-Kamiokande Observatory and the Sudbury Neutrino Observatories was recognized with the 2015 Nobel prize for physics.

1.2.3 Cosmological observations

Differences between cosmological observations and theoretical predictions of the general relativity, lead physicist to postulate the existence in the universe of a new matter called *dark matter*. The existence of such a matter would explain the differences between predictions and observations. The contribution of dark matter in the universe is estimated to about 26.8% of the total energy of the universe, and the matter described by the Standard Model would contributes to 4.9%. The remaining 68.3% should be an unknown form of energy, due to a constant energy density filling space homogeneously, and that would explain the observations on the acceleration of the expansion of the universe. This phenomena is known as *dark Energy*. The Standard Model provides no candidate for dark matter and this is a motivation for the search for physics beyond the Standard Model.

1.2.4 Gravitation

The Standard Model includes electromagnetism, weak and strong interactions, but the gravitation is not included in the Standard Model. A strong motivation leads physicists to search for a model unifying all the interactions as discussed in section 1.1.2. The inclusion of the gravitation in the Standard Model is one of the greatest challenges of particle physics.

1.2.5 The hierarchy problem

The hierarchy problem concerns the quadratic corrections applied to the Higgs mass. In the renormalization procedure, parameters in the Lagrangian are not physical parameters. Then, the Higgs mass m_0 in the Lagrangian is not physical. The physical mass of the Higgs depends on the renormalized value, and on a typical energy scale defined as Λ_{UV} corresponding to the scale limit of the theory and where it is necessary to include new physics. Figure 1.3 (a) shows the radiative correction applied to m_H^2 from a loop containing a Dirac fermion f with mass m_f. If the Higgs field couples to the fermion with a term -$\lambda H \bar{f} f$, then the associated correction to the Higgs mass is defined by:

$$m_H^2 = m_0^2 - \frac{|\lambda_f|}{8\pi^2}\Lambda_{UV}^2 + ..., \tag{1.16}$$

With, Λ_{UV}^2, the ultraviolet momentum cut-off used to regulate the loop integral. It should be interpreted as the high energy scale at which new physics modifies the behaviour of the theory. The problem is that if new physics is at the order of the Planck scale M_p or at the Grand Unification

scale, the quantum corrections applied to m_H^2 would be about 30 orders of magnitude larger than the experimental value measured at the LHC $(m_H = 125)^2$ GeV.

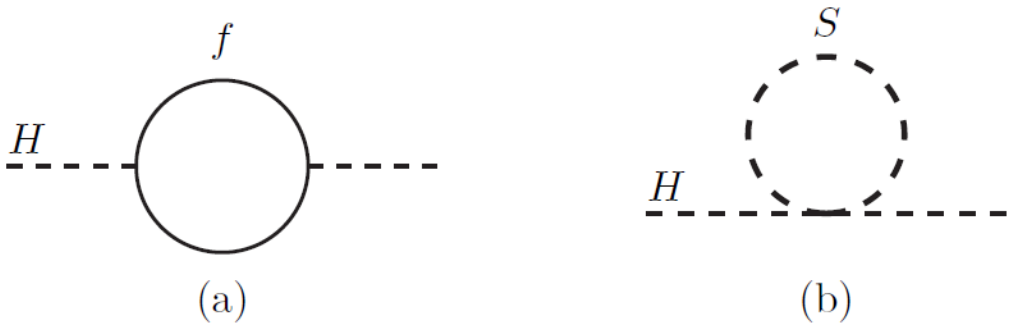

Figure 1.3: One-loop radiative corrections to the Higgs mass, due to a Dirac fermion (a) and a scalar boson (b) [24].

1.3 Supersymmetry

Supersymmetry [24] (SUSY) is an extension of the Standard Model providing solutions to some issues of the Standard Model. The theory postulates the existence of a new symmetry in nature between bosons and fermions. It assumes the existence of a new particle for each particle of the Standard Model with a spin differing by 1/2. For each fermion, a boson is associated and vice versa. This new particle is called a *superpartner*. The existence of such a superpartner would modify the radiative corrections to the Higgs mass and would solve the problem of hierarchy (section 1.3.1). The pair of fermion/boson are unified in one object called a supermultiplet. In a same multiplet, the boson is the superpartner of the fermion and vice versa. A supersymmetric transformation turns a bosonic state into a fermionic state and vice versa:

$$Q\,|Boson\rangle = |Fermion\rangle\,, \qquad Q\,|Fermion\rangle = |Boson\rangle\,, \tag{1.17}$$

Where Q is the generator of such transformation. Q and $Q^\dagger$ are fermionic operators and must satisfy an algebra of anti-commutation relations:

$$\{Q, Q^\dagger\} = P^\mu, \tag{1.18}$$

$$\{Q, Q\} = \{Q^\dagger, Q^\dagger\} = 0, \tag{1.19}$$

$$[P^\mu, Q] = [P^\mu, Q^\dagger] = 0, \tag{1.20}$$

Where P^μ is the four-momentum generator of spacetime translations. The single-particle states of a supersymmetric theory fall into irreducible representations of the supersymmetry algebra, called supermultiplets. Each supermultiplet contains both fermionic and bosonic states, which are commonly known as superpartners of each other.

1.3.1 Motivations

The existence of new particles modify the radiative correction to the Higgs mass. Since fermions and bosons contribute with an opposite sign to the Higgs mass, the radiative corrections cancel if for each fermion/boson, a boson/fermion is associated with the same mass and electric charge. Figure 1.3 illustrates the first order corrections of a fermion-loop and scalar particle. Many supersymmetric models provide a good candidate for dark matter with a stable and electrically neutral particle interacting only by weak interaction.

The renormalization equations can be used to compute the running coupling constant at higher scale value. Figure 1.4 shows the extrapolation of the coupling constants of electromagnetism ($U(1)_Y$ gauge symmetry), weak interaction ($SU(2)_L$ gauge symmetry) and strong interaction ($SU(3)_C$ gauge symmetry). On the left part, the coupling constant are computed with the particles of the Standard Model and can not be unified in one point. On the right part, the coupling constant are computed including the particles of the Minimal Supersymmetric Standard Model. In this case, the three coupling constants can be unified at higher energy scale in what is called *Grand Unification Theory*. The unification of the coupling constant is a motivation for physics beyond the Standard Model.

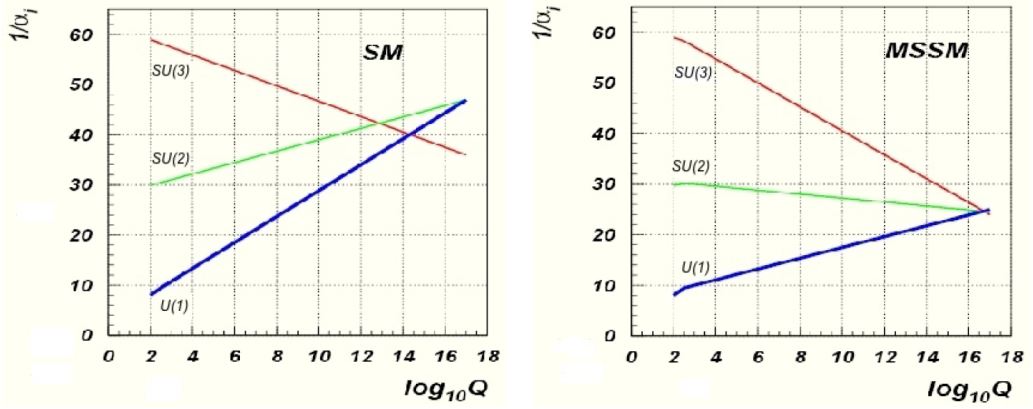

Figure 1.4: Evolution of the coupling constant as a function of the energy scale (log scale). On the left, the coupling constants of the Standard Model do not converge. On the right, coupling constants of the Minimal Supersymmetric Standard Model can be unified at the Grand Unification scale [25].

1.3.2 SUSY symmetry breaking

The unification of fermions and bosons in supermultiplet would imply that the number of fermions and bosons is equal. For instance, the superpartner of the electron is a spin-0 boson with the same mass as the electron, but such a particle have never been observed. Then the theory of supersymmetry must be a broken symmetry such as the mass of the particle and superpartner are different. The symmetry breaking would explain the fact that superpartner have not be discovered yet. The mechanism of broken symmetry have been applied successfully to the electroweak theory of the Standard Model of particle physics. There are many spontaneous symmetry breaking models for SUSY, but none are approved unanimously. An alternative would be to add explicit terms in the Lagrangian that would break the symmetry. The symmetry breaking must keep some properties of the model unchanged such as radiative corrections to the Higgs mass, to solve the hierarchy problem. Thus, no quadratic divergences have to be added. The Lagrangian can be expressed as:

$$\mathcal{L} = \mathcal{L}_{Susy} + \mathcal{L}_{Soft}, \tag{1.21}$$

Where $\mathcal{L}_{Soft}$ contains all the broken terms such as masses and coupling constants. The term $\mathcal{L}_{Susy}$ includes the invariant part of the supersymmetry. The symmetry breaking is then an explicit symmetry breaking instead of a spontaneous symmetry breaking as for the Higgs sector.

1.3.3 The MSSM

The Minimal Supersymmetric Standard Model (MSSM) [26] is the extension of the Standard Model predicting the minimal number of new particle states realizing the supersymmetry. The MSSM allows the unification of gauge coupling constants and provides a candidate for Dark Matter. The MSSM imposes the R-parity conservation to explain the stability of the proton. If supersymmetry is realized in nature, it must be a broken symmetry. The symmetry breaking in the MSSM is introduced with an explicit soft symmetry terms in the Lagrangian, and the exact mechanism of symmetry breaking leads to various MSSM models. The MSSM includes 124 parameters with 19 parameters from the Standard Model.

1.3.3.1 Particles of the MSSM

In a supersymmetric extension of the Standard Model, each of the known fundamental particle is associated with a superpartner differing by spin-$\frac{1}{2}$. The name of the scalar superpartners of the Standard Model fermions are called sfermions, and include squarks and sleptons. They are represented with a tilde used to characterize the supersymmetric partner. The bosonic superpartners of the fermions are called by adding "ino", and are represented in Figure 1.5. The left part shows the particles of the Standard Model, while superpartners are shown in the right part. The fermionic superpartners of the gauge vector bosons of the Standard Model are called gauginos [27–29]. The strong interaction is carried by gluons whose superpartners are the gluinos. The electroweak interaction is carried by the spin-1 gauge bosons $W^{\pm}$, W^0 and B^0 whose superpartners are spin-$\frac{1}{2}$ winos $\tilde{W}^{\pm}$, $\tilde{W}^0$ and binos $\tilde{B}^0$.

Supersymmetry includes two Higgs doublets instead of one in the Standard Model. Thus, the number of degrees of freedom increases from 4 to 8. After the electroweak symmetry breaking, five degrees of freedom remain. This leads to five physical Higgs states including two neutral CP-even (h^0, H^0), one neutral (A^0), and two charged Higgs bosons (H^+, H^-). We call Higgsinos the four fermionic superpartners of the Higgs boson ($\tilde{H}_u^0$, $\tilde{H}_d^0$, $\tilde{H}_u^+$, $\tilde{H}_d^-$). In the Standard Model, after the electroweak symmetry breaking, eigenstates W^0 and B^0 combine to form the mass eigenstates Z^0 and γ. In the same way in supersymmetry, $\tilde{W}^0$, $\tilde{B}^0$, $\tilde{H}_u^0$, $\tilde{H}_d^0$ are combined to form 4 new mass eigenstates: the neutralinos ($\tilde{\chi}_{i=1,..,4}^0$), and $\tilde{W}^{\pm}$, $\tilde{H}_u^+$, $\tilde{H}_d^-$ are combined to form 4 new mass eigenstates: the charginos ($\tilde{\chi}_{i=1,2}^{\pm}$). Table 1.1 is a summary of the mass eigenstates after the symmetry breaking. The gravitino is included in the Table and would correspond to the fermionic superpartner of the graviton.

1.3.3.2 R-parity

Within the Standard Model, the requirement of gauge invariance automatically guarantees baryon (B) and lepton (L) number conservation. In supersymmetry, these quantum numbers can be violated. For instance, if baryon number and lepton number are both violated, the proton would decay and would not be a stable particle. Proton lifetime have been measured to be larger than 10^{30} years. The proton can therefore be considered as a stable particle. This problem can be solved assuming the existence of a new quantum number, the R-parity that would be conserved under supersymmetric interactions. The conservation of this quantum number should be interpreted as the conservation of a matter parity. R-parity is defined as:

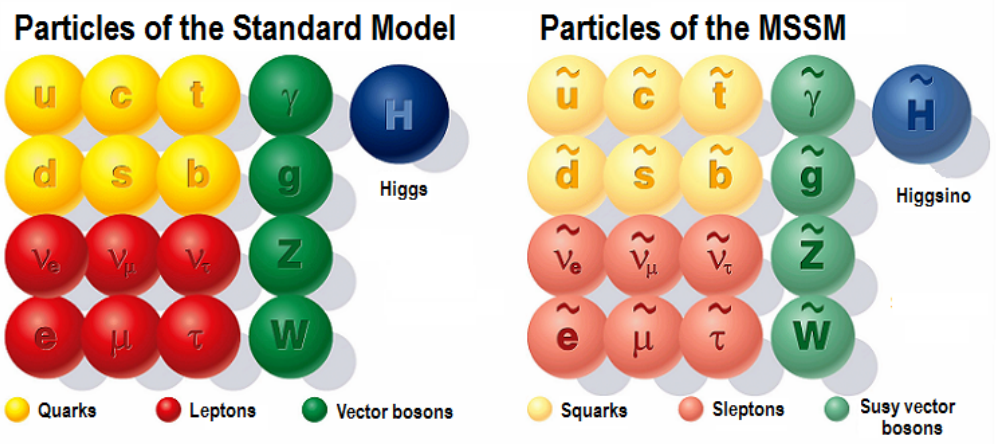

Figure 1.5: Particle of the Standard Model (left) and the associated particles of the MSSM (right). In yellow, the quarks (left) and scalar quarks (right), in red, the leptons (left) and scalar lepton (right), in green, the gauge bosons (left) and gauginos (right), in blue, the Higgs boson (left) and the Higgsino (right).

Names	spin	R-parity	gauge eigenstates	mass eigenstates
Higgs bosons	0	$+1$	$H_u^0 \quad H_d^0 \quad H_u^+ \quad H_d^-$	$h^0 \quad H^0 \quad A^0 \quad H^\pm$
squarks	0	-1	$\tilde{u}_L \quad \tilde{u}_R \quad \tilde{d}_L \quad \tilde{d}_R$	same
			$\tilde{s}_L \quad \tilde{s}_R \quad \tilde{c}_L \quad \tilde{c}_R$	same
			$\tilde{t}_L \quad \tilde{t}_R \quad \tilde{b}_L \quad \tilde{b}_R$	$\tilde{t}_1 \quad \tilde{t}_2 \quad \tilde{b}_1 \quad \tilde{b}_2$
sleptons	0	-1	$\tilde{e}_L \quad \tilde{e}_R \quad \tilde{\nu}_e$	same
			$\tilde{\mu}_L \quad \tilde{\mu}_R \quad \tilde{\nu}_\mu$	same
			$\tilde{\tau}_L \quad \tilde{\tau}_R \quad \tilde{\nu}_\tau$	$\tilde{\tau}_1 \quad \tilde{\tau}_2 \quad \tilde{\nu}_\tau$
neutralinos	1/2	-1	$\tilde{B}^0 \quad \tilde{W}^0 \quad \tilde{H}_u^0 \quad \tilde{H}_d^0$	$\tilde{\chi}_1^0 \quad \tilde{\chi}_2^0 \quad \tilde{\chi}_3^0 \quad \tilde{\chi}_4^0$
charginos	1/2	-1	$\tilde{W}^\pm \quad \tilde{H}_u^+ \quad \tilde{H}_d^-$	$\tilde{\chi}_1^\pm \quad \tilde{\chi}_2^\pm$
gluino	1/2	-1	$\tilde{g}$	same
gravitino	3/2	-1	$\tilde{G}$	same

Table 1.1: Particles of the MSSM [24].

$$R = (-1)^{3(B-L)+2s}, \tag{1.22}$$

where s is the spin of the particle, B is the baryonic number equal to $\frac{1}{3}$ for quarks and -$\frac{1}{3}$ for anti-quarks and is L the leptonic number, equal to 1 for leptons and -1 for anti-leptons. The proton decay in the case of R-parity violation is illustrated in Figure 1.6. The initial state is composed of the 3 quarks (uud) of the proton, with a R = 1. The quarks u and d interact to produce an anti-squark $\tilde{s}$, the R-parity of intermediate state is $R_p = -1$. The final state is composed of the positron, the antiquark u and the quark u, with R = +1.

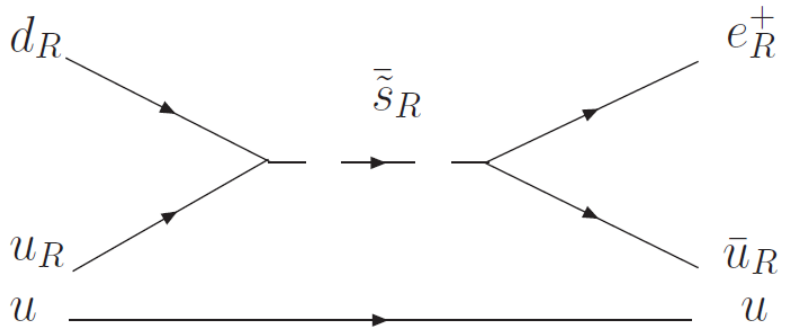

Figure 1.6: Diagramm of the proton decay, assuming the violation of R-parity. On the left part, the proton composed of the 3 quarks u,u,d have R-parity $R_p = +1$. The quarks u and d interact to produce anti-squark s, the intermediate state have R-parity $R_p = -1$. The anti-squark s decays to produce a positron and an anti-quark u. The R-parity in the final state is then $R_p = +1$ [24].

Another consequence of R-parity conservation is that supersymmetric particles are produced in pair. The lightest supersymmetric particle (LSP) can not decay and is therefore a stable particle. The LSP is a good candidate for dark matter. By definition, R-parity is assumed to be conserved in the MSSM. The violation of R-parity [16] is also studied and corresponds to an extension of the MSSM.

1.3.4 Supersymmetric models

Since no superpartners have been observed in nature, SUSY if realized must be a broken symmetry. Various mechanisms for the SUSY symmetry breaking have been proposed [30] such as the gravity-mediated SUSY breaking (SUGRA) or gauge mediated SUSY breaking (GMSB). In these models, only a small part of the parameter space of the MSSM is considered. Another approach to constrain SUSY is to use the simplified models. Simplified models are based on effective Lagrangian, corresponding to one specific production and a fixed decay chain.

1.3.4.1 pMSSM

Since the parameter space of the MSSM is too large to be scanned and compared with the data, the pMSSM [31–35] includes a series of assumptions to reduce the number of parameters from 124 to 19 real parameters. No specific theoretical assumption associated to a SUSY breaking mechanism is introduced. Assumptions include: R-parity conservation, no CP violation, no flavor-changing neutral current, the two first generations of squarks and leptons with the same quantum numbers are mass-degenerate. The 19 parameters include 10 squarks and sleptons masses, 3 gaugino masses associated with the three groups $U(1)_Y$, $SU(2)_L$, and $SU(3)_C$, higgsino mass parameter (μ), the ratio of the VEV of the two Higgs fields ($\tan\beta$), the Higgs boson mass m_A, and the trilinear coupling for

the third generations (A_b, A_t, A_τ). The LSP can be the lightest neutralino or another particle such as the gravitino. There is no theoretical upper bound on the parameters characterising the masses, but an additional limit of 4 TeV is applied on the sparticle masses.

1.3.4.2 mSUGRA/CMSSM

In the minimal SUperGRAvity model (mSUGRA/CMSSM), the SUSY breaking mechanism is mediated by gravity. The model is described by five parameters including a universal scalar mass m_0, a universal gaugino mass ($m_{1/2}$), a universal trilinear scalar coupling (A_0), all defined at the Grand Unification scale ($\tan\beta$), and the sign of the higgsino mass parameter (μ). In the mSUGRA/CMSSM model, the value of three parameters could be: $\tan\beta$ = 30, A_0 = -2m_0, and $\mu > 0$ such that the lightest scalar Higgs boson is approximately 125 GeV in a large fraction of the (m_0,$m_{1/2}$) parameter space.

1.3.4.3 mGMSB

In gauge-mediated SUSY breaking models (GMSB) [36–40], the LSP is assumed to the gravitino. The gravitino has a very small mass which can be neglected, and a small coupling to other particles. The mGMSB is described by 6 parameters. Due to the small coupling with the LSP, the decays of SUSY particles are dominated by the decay into NLSP. The NLSP decays subsequently to the LSP. Therefore, the nature of the NLSP is determinant for the experimental signature.

1.3.4.4 Simplified models

Simplified models [41, 42] are another approach to constrain new physics using an effective Lagrangian. They involve only few particles and decay modes and are described by a small number of parameters such as particles masses, production cross-sections, and branching ratios. The sensitivity of the searches for new physics can be presented as a function of these parameters and in particular as a function of the new particle masses. The branching ratio for simplified models is often fixed at 100% to reduce the number of parameters. Some exemples are described in section 1.3.6.

1.3.5 Production of squarks and gluinos at the LHC

The dominant production modes of squarks and gluinos via QCD interaction [43–46] are shown in equations (1.23 - 1.26). I remind that supersymmetric particles must be produced in pair due to the conservation of R-parity.

$$gg \rightarrow \tilde{g}\tilde{g}, \tilde{q}_i\tilde{q}_j, \tag{1.23}$$
$$gq \rightarrow \tilde{g}\tilde{q}_i, \tag{1.24}$$
$$q\bar{q} \rightarrow \tilde{g}\tilde{g}, \tilde{q}_i\tilde{q}_j, \tag{1.25}$$
$$qq \rightarrow \tilde{q}_i\tilde{q}_j, \tag{1.26}$$

The production modes for gluon-gluon and quark-gluon fusions are detailed in Figure 1.7. The production modes for quarks-antiquark interaction and quark-quark scattering are detailed in Figure 1.8. The production cross-section depends on the center of mass energy of the collision. The increase of the center of mass energy at the LHC from 8 TeV to 13 TeV for the Run 2 allows a good improvement in the cross-section production of squarks and gluinos. The cross-section for $\sqrt{s}$ = 8 TeV and $\sqrt{s}$ = 13-14 TeV are shown in Figure 1.9. For instance, the cross-section production for $\tilde{g}\tilde{g}$ with $m_{\tilde{g}}$ = 1200 GeV is given by $\sigma_{\tilde{g}\tilde{g}} \simeq 4.5 fb$ at $\sqrt{s}$ = 8 TeV, and $\sigma_{\tilde{g}\tilde{g}} \simeq 80 fb$ at $\sqrt{s}$ = 13-14 TeV. For $\tilde{q}\tilde{q}$ production with $m_{\tilde{q}}$ = 1000 GeV, the cross-section is increased from $\sim$ 20 fb to $\sim$210 fb.

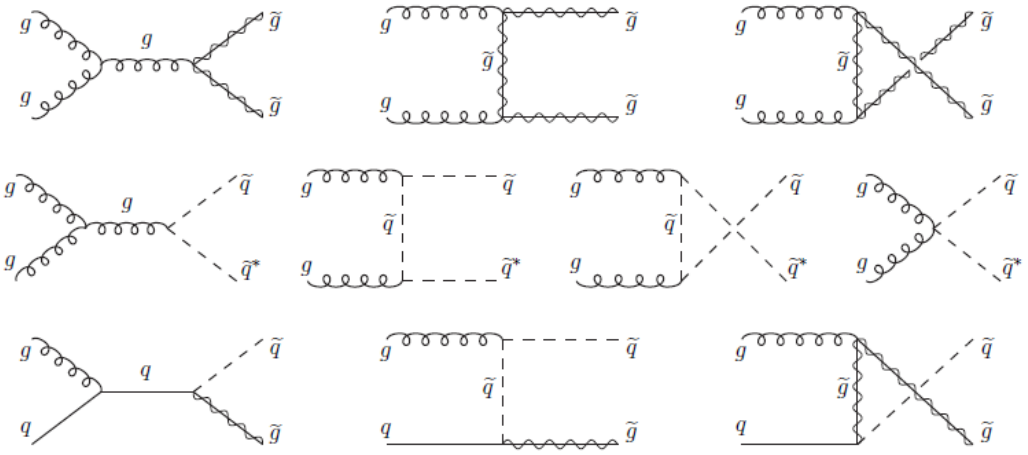

Figure 1.7: Feynman diagrams for gluinos and squarks production at hadron collider from gluon-gluon and gluon-quark fusion [24].

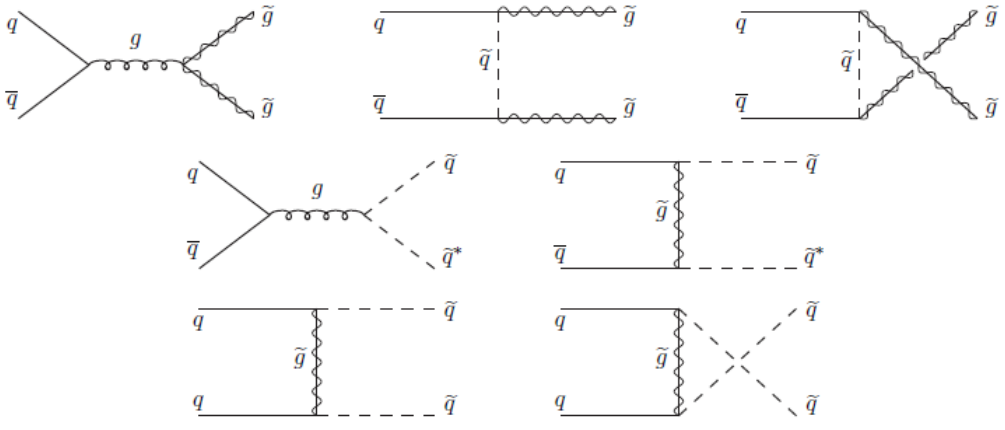

Figure 1.8: Feynman diagrams for gluinos and squarks production at hadron collider from strong quark-antiquark annihilation and quark-quark scattering [24].

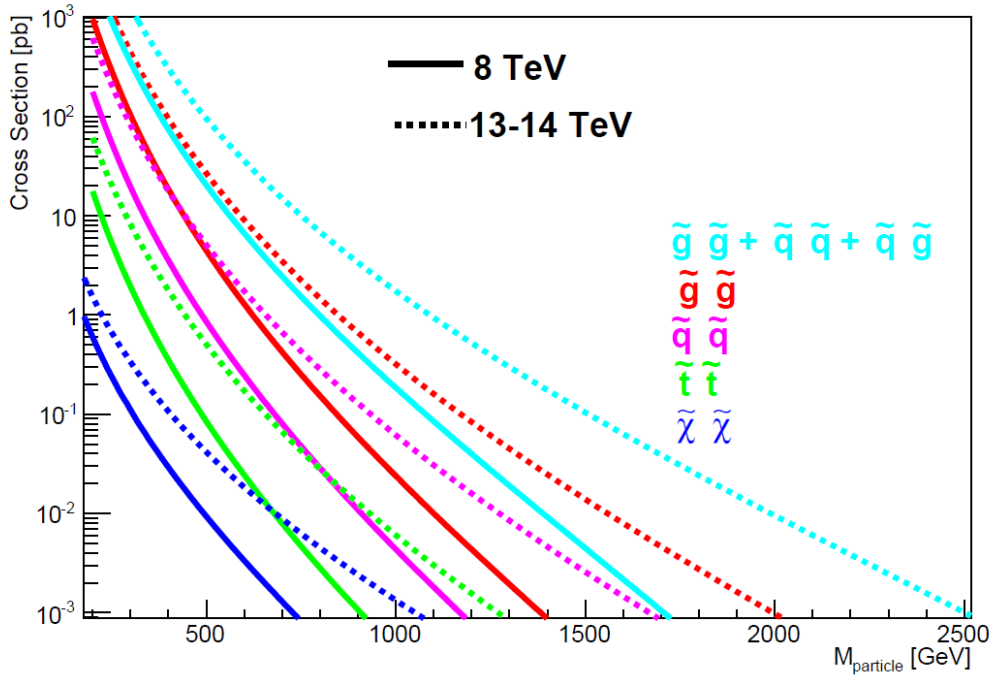

Figure 1.9: Production cross-sections of SUSY particle at the LHC at $\sqrt{s} = 8$ (continuous lines) TeV and 13-14 TeV (dotted lines) [47].

1.3.6 Squarks and gluinos in the fully hadronic channel

Various channels are studied in ATLAS for the searches for squark and gluino depending on the final states. The fully hadronic channel is characterized by jets and transverse missing energy E_T^{miss} in the detector. The transverse missing energy is due to the emission of the LSP $\tilde{\chi}_1^0$ in the final state. This final state allows to probes various models such as the pMSSM, the mSUGRA/CMSSM and several simplified models. During my Ph.D, the searches for squarks and gluinos in the context of simplified models of the MSSM have been performed (chapter 6).

If the decay $\tilde{q} \to q\tilde{g}$ is kinematically allowed, it will be the squark dominant decay due to the QCD coupling. Squarks can also decay by weak interaction into neutralino and chargino (if kinematically allowed) following decays (1.27), and (1.28) for left-handed squarks.

$$\tilde{q} \to q\tilde{\chi}_i^0, \tag{1.27}$$
$$\tilde{q} \to q'\tilde{\chi}_i^{\pm}, \tag{1.28}$$

If the reaction $\tilde{g} \to q\tilde{q}$ is allowed, it will be the dominant decay of gluino due to QCD coupling. In the case where squark have a mass significantly higher than the gluino, the gluino can decay via weak interaction following the reaction (1.29) or (1.30) via an off-shell squark.

$$\tilde{g} \to qq\tilde{\chi}_i^0, \tag{1.29}$$
$$\tilde{g} \to qq'\tilde{\chi}_i^{\pm}, \tag{1.30}$$

The decay topologies of the simplified models for squark-squark and gluino-gluino are respectively shown in Figures 1.10 and 1.11. Simplified models include direct decays of squark (Figure 1.10 (a)) and gluino (Figure 1.11 (a)) into jets+$\tilde{\chi}_1^0$, or one-step decays via an intermediate particle. One-step decay of $\tilde{q}\tilde{q}/\tilde{g}\tilde{g}$ via the lightest chargino are shown respectively in Figures Figure 1.10 (b) and 1.11 (b). One-step decay of $\tilde{g}\tilde{g}$ via the second lightest neutralino is shown in Figure 1.11 (d). In Figures 1.10 (c) and 1.11 (c), the intermediate particles are the chargino and the second lightest neutralino. The free parameters for these models are $m_{\tilde{q}}$, $m_{\tilde{g}}$, $m_{\tilde{\chi}_1^0}$ (and $m_{\tilde{\chi}_1^\pm}/m_{\tilde{\chi}_2^0}$ for the one-step grids).

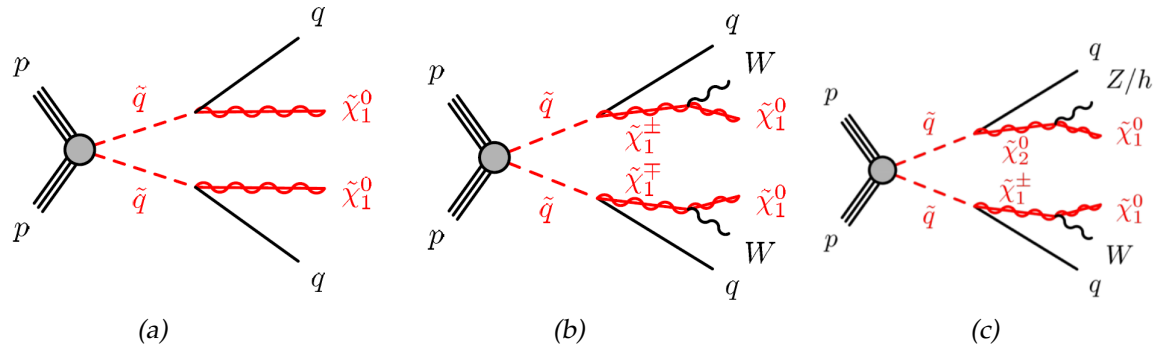

Figure 1.10: Decay topology of the MSSM squarks pair production with direct and one-step decays [48].

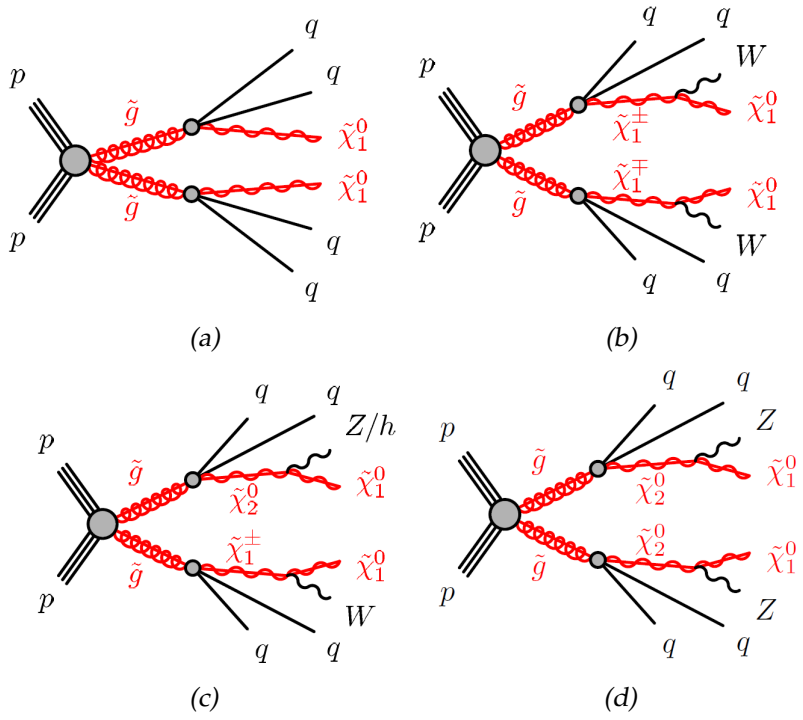

Figure 1.11: Decay topology of the MSSM gluino pair production with direct and one-step decays [48].

1.3.7 ATLAS results from the LHC Run 1

Several studies have been performed in the Run 1 for the searches for squarks and gluinos. The summary with the ATLAS results can be found in the reference [30], and the details for the specific channel with jets and missing transverse momentum can be found in [49]. In the last chapter of this thesis, limits obtained with 13 TeV data are compared to the Run 1 results.

Limits obtained with gluino pair production (a),light-flavoured squarks and gluinos (b), and light-flavoured squarks pair production (c) are shown in Figure 1.12. In each of these simplified models, only direct decay of squarks and gluinos into jets + transverse missing energy are considered, with a branching ratio of 100%. The other particles except the LSP are decoupled. In Figure (a) and (c), the cross-section is evaluated assuming decoupled light-flavoured squarks and gluinos with masses set to 4.5 TeV. In Figure (b), the masses of light-flavoured squarks are set to 0.96 times the mass of the gluino. The maximum exclusion limit on $m_{\tilde{g}}$ is obtained at 1425 GeV (a) and 1580 GeV (b) with $m_{\tilde{\chi}_1^0}$ = 0 GeV. In Figure (c) limits are shown for scenarios with eight degenerate light-flavour squarks, or with only one non-degenerate light-flavour squarks. The maximum exclusion limit on $m_{\tilde{q}}$ is obtained at ∼900 GeV with $m_{\tilde{\chi}_1^0}$ = 0 GeV. Exclusion limits obtained on simplified models considering gluinos pair production (top) and squarks pair production (bottom) decaying into jets + transverse missing energy via an intermediate chargino are shown in Figure 1.13. The mass of the chargino is fixed to $m_{\tilde{\chi}_1^0}$ = 60 GeV in Figures (a) and (c), and defined as $m_{\tilde{\chi}^\pm} = (m_{\tilde{g}} + m_{\tilde{\chi}_1^0})/2$ in Figure (b) and (d).

1.4 Conclusion

This chapter presents the theoretical and experimental context of the thesis. The first section briefly presents the Standard the Standard Model of particle physics. The model is very predictive, but several issues presented in the second section lead physicists to search for physics beyond the Standard Model. Supersymmetry can bring solutions to the current issues of particle physics, and predicts the existence of new particles that can be produced at the LHC. The last section presents the supersymmetry and the MSSM. The upgrade of the LHC from Run 1 to Run 2, and the increase of the center of mass energy allows the improvement of the production cross-section of supersymmetric particles. I contributed to the searches for squarks and gluinos with the ATLAS detector, in the channel with no lepton in the final state.

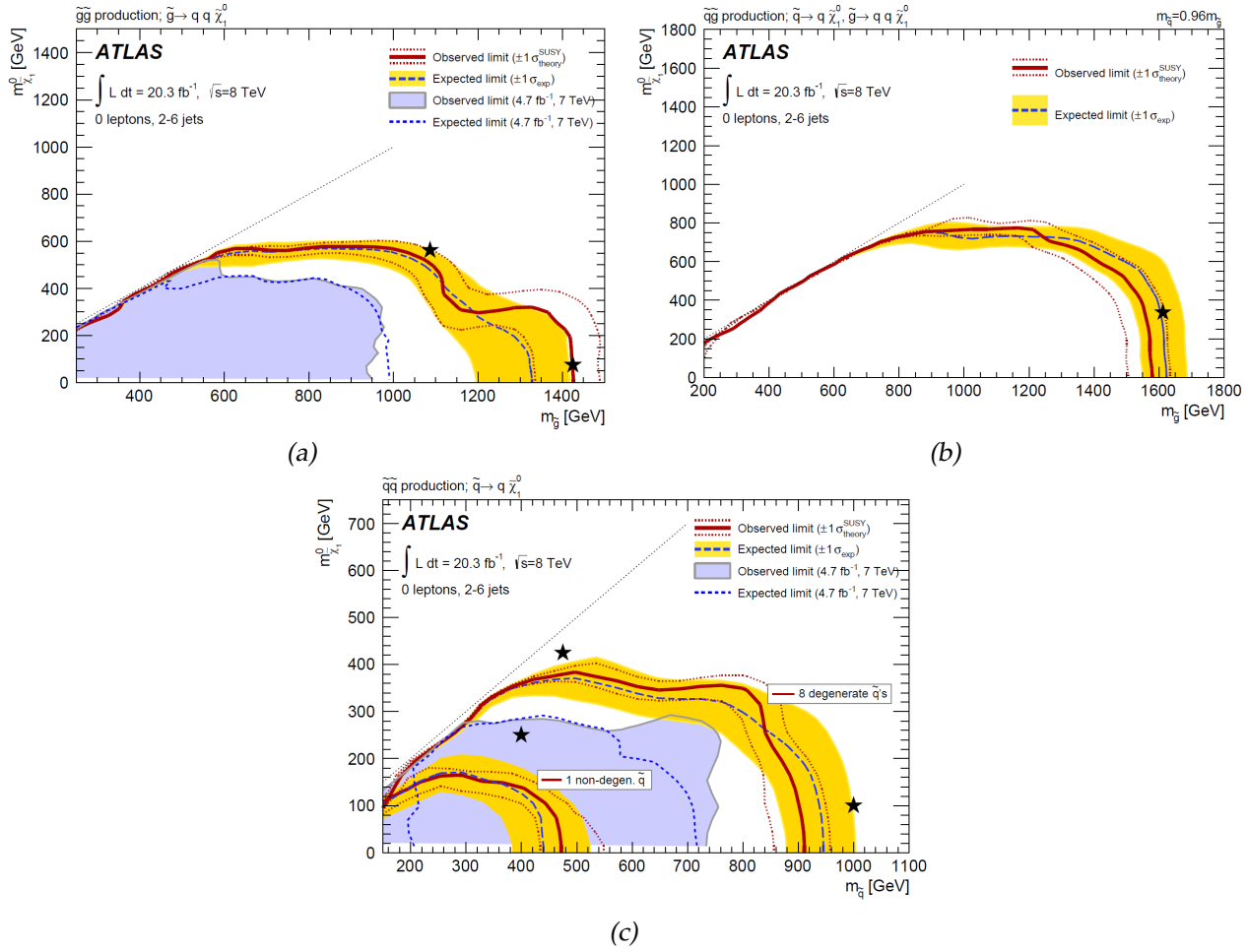

Figure 1.12: Exclusion limits for direct production of gluino pairs with decoupled squarks (a), light-flavour squarks and gluinos (b), and light-flavour squark pairs with decoupled gluinos, using Run 1 data [49]. Gluinos (light flavour squarks) are required to decay to two quarks (one quark) and a neutralino $\tilde{\chi}_1^0$. In Figure (c), limits are shown for scenario with eight degenerated light-flavoured squarks ($\tilde{q}_L$ + $\tilde{q}_R$), or only one non-degenerate light-flavour squark produced. The blue dashed lines show the expected limits at 95% CL, with light (yellow) bands indicating the 1 σ excursions due to the experimental and background-only theory uncertainties. Observed limits are indicated by medium (maroon) curves, where the solid contour represents the nominal limit, and the dotted lines are obtained by varying the signal cross-section by the renormalisation, factorisation scale and PDF uncertainties. Results with 4.7 fb^{-1} are represented by the shaded (light blue) areas and light blue dotted lines. The black stars indicate benchmark models [49].

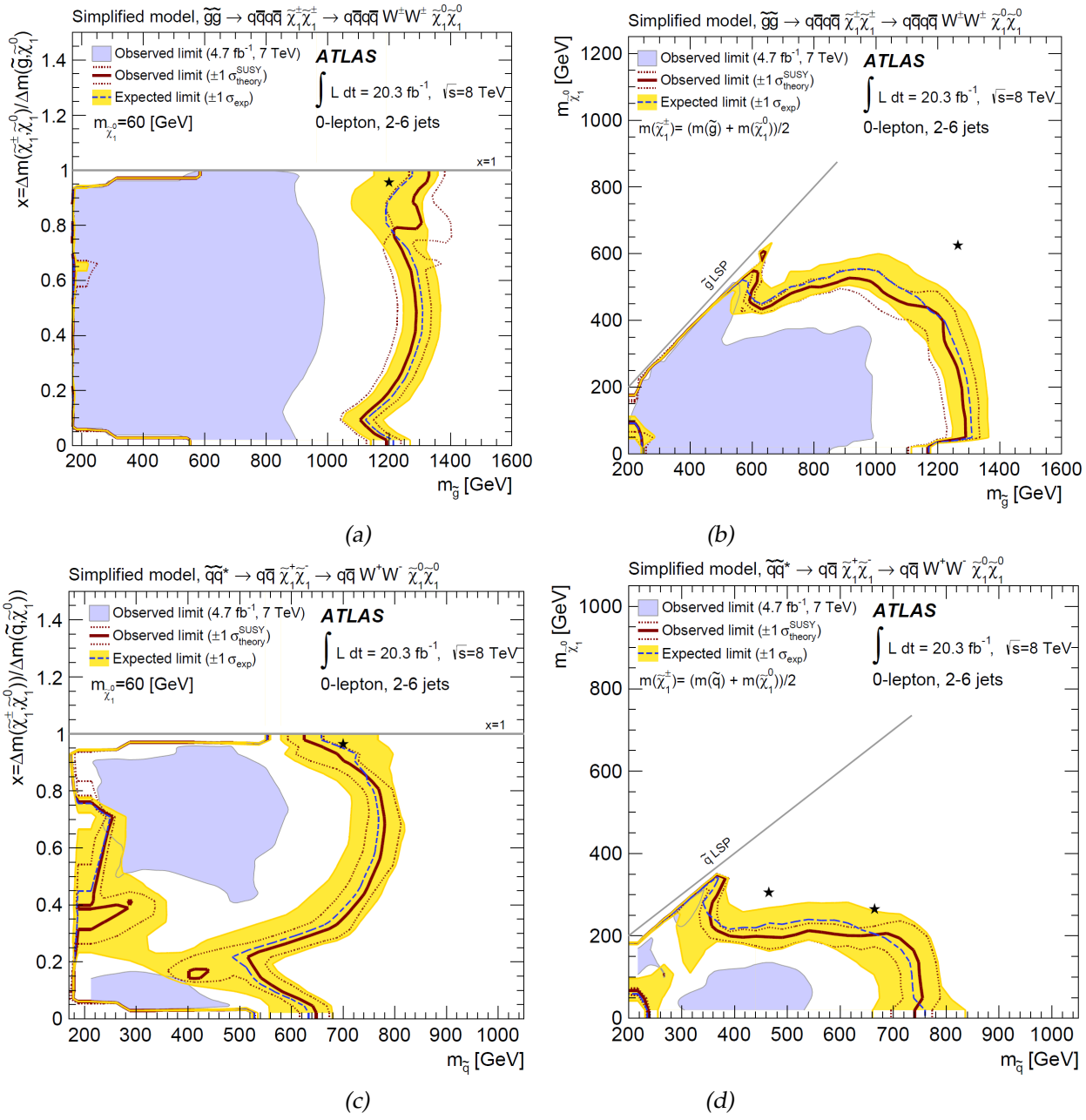

Figure 1.13: Exclusion limits for pair-produced gluinos each decaying via an intermediate $\tilde{\chi}^{\pm}$ to two quarks, a W boson, and a $\tilde{\chi}_1^0$ (top) or pair-produced light squarks each decaying via an intermediate $\tilde{\chi}^{\pm}$ to a quark,a W boson and a $\tilde{\chi}_1^0$ (bottom). The left-hand Figures show results for models with fixed $m_{\tilde{\chi}_1^0}$ = 60 GeV and varying values of x = $(m_{\tilde{\chi}^{\pm}}$ - $m_{\tilde{\chi}_1^0})/(m_y$ - $m_{\tilde{\chi}_1^0})$, where y = $\tilde{g}$ (y = $\tilde{q}$ for the top (bottom) Figure [49]. The right-hand plots show results for models with a fixed value of x = 1/2 and varying values of $m_{\tilde{\chi}_1^0}$. Exclusion limits are obtained by using the signal region with the best expected sensitivity at each point. The blue dashed lines show the expected limits at 95% CL, with the light (yellow) bands indicating the 1σ excursions due to experimental and background-only theory uncertainties. Observed limits are indicated by medium dark (maroon) curves, where the solid contour represents the nominal limit, and the dotted lines are obtained by varying the signal cross-section by the renormalisation and factorisation scale and PDF uncertainties. Results with 4.7 fb^{-1} are represented by the shaded (light blue) areas and light blue dotted lines. The black stars indicate benchmark models [49].

Chapter 2

The ATLAS experiment

"It is harder to crack a prejudice than an atom. "

Albert Einstein

Contents

The ATLAS collaboration includes around 3000 scientists from about 180 institutions around the world, and representing 38 countries. This chapter is an introduction to the ATLAS experiment. The first section presents the Large Hadron Collider and the experimental devices used to accelerate protons to almost the speed of light. The second section describes the ATLAS detector used to collect the data from the collision. The third section describes how physics objects are reconstructed from the ATLAS detector.

2.1 The Large Hadron Collider

The Large Hadron Collider (LHC) [50] is the largest and most powerful particle accelerator in the world. It's a circular collider of 26.7 km circumference designed for proton-proton collisions with a nominal centre-of-mass energy of $\sqrt{s}$ = 14 TeV. Collisions such as lead-lead or proton-lead can also be performed. In the following, only proton-proton collisions are discussed. In the LHC, two high energy beams are accelerated in two separate pipes, at ultra-high vacuum. They are accelerated and guided around the accelerator ring by a strong magnetic field maintained by superconducting electromagnets. Thousands of magnets are used to direct the beam around the accelerator. These include 1232 dipole magnets of 15 m length to accelerate the beam, and 392 quadrupole magnets of 5-7 m long to focus the beam. Magnets are capable of maintaining a maximum field of 8.33 T at a temperature of 1.9 K. Before the collision, another type of magnets are used to "squeeze" the particles to increase the chances of collisions. Much of the accelerator is connected to a distribution system of liquid helium, which cools the magnets and other devices. The designed luminosity of the LHC is $\sim 10^{34}\text{cm}^2\text{s}^{-1}$ with a frequency of 25 ns per beam crossing. The LHC is built at the CERN laboratory in Geneva, 100 metres below the surface, on the previous site of the Large Electron Positron (LEP) collider. The construction started in 1998 and the first collisions took place in 2009.

2.1.1 Proton beam acceleration

The LHC is the last accelerator of the CERN's accelerator complex (Figure 2.1). The proton beam is previously and progressively accelerated by a succession of machines. Protons are produced with ionised hydrogen gas using an electric field, and accelerated to 50 MeV with the accelerator LINAC 2. The beam is injected into the Proton Synchrotron Booster (PSB) to an energy of 1.4 GeV. Then, protons are accelerated to 25 GeV by the Proton Synchrotron (PS), and to 450 GeV by the Super Protron Synchrotron (SPS). Within the PS, the beam is shaped into 25 ns spaced bunches, while 50 ns bunch spacing was maintained during the Run 1, and 75 ns in 2010. Seventy-two bunches are provided in the SPS every 3.6 s, forming a bunch-train. The beam is finally transferred in the two beam pipes of the LHC, each beam pipe accelerating the protons in an opposite directions. Collisions are produced in different points of the LHC, each point corresponding to a different detectors: ALICE [51], ATLAS [52], CMS [53], LHCb [54], TOTEM [55] and LHCf [56]. ATLAS and CMS are general purpose experiments, designed to search for the Higgs boson and new physics research. The LHCb experiment is designed to study rare physical processes in the B meson decay and the matter-antimatter asymmetry. ALICE experiment is designed to study the quark-gluon plasma during heavy-ions collisions, especially with lead nuclei. TOTEM is designed to study the elastic scattering, and the proton-proton cross-section, and LHCf is dedicated to the production of neutral particles to help understanding the origin of the ultra-high-energy cosmic rays. The typical life time of the beam is $\sim$ 14h. The beam is affected [57] by the proton-proton collisions, by collisions with residual gas in the beam pipe, and by electron clouds created by the pipe.

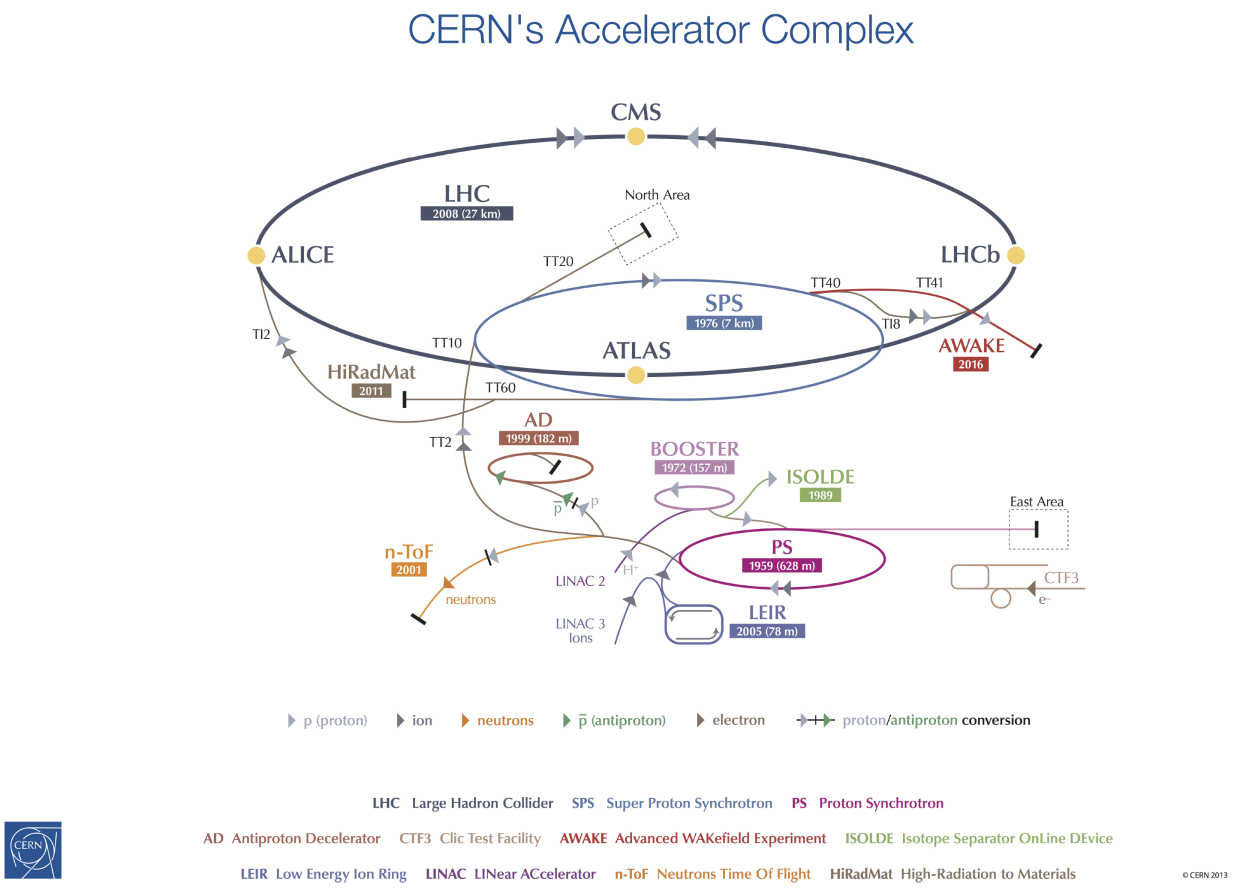

Figure 2.1: CERN's accelerator complex [58]

2.1.2 Description and performance

2.1.2.1 Luminosity

The number of interactions N per second depends on the instantaneous luminosity $\mathcal{L}$ of the accelerator, and on the production cross-section σ of the specific physical process. N is defined as:

$$N = \mathcal{L} \times \sigma. \tag{2.1}$$

For a Gaussian beam distribution, the integrated luminosity can be expressed as:

$$\mathcal{L} = \frac{N_b^2 n_b^2 f_{rev} \gamma}{4\pi\epsilon\beta^*} F, \tag{2.2}$$

Where N_b is the number of particles per bunch, n_b is the number of bunches per beam, f_{rev} is the revolution frequency of the machine ($\sim$ 40 MHz), γ is the Lorentz factor of the beam, ϵ is the normalized transverse emittance, and β^* is the beta function at the interaction point. The factor F depends on the crossing angle between the two beams. Improvements in the machine allow the increase of the number of protons per bunches, and the number of bunches per beam. This resulted in an increase of the instantaneous luminosity peak value in ATLAS from $\mathcal{L}$ = 2.07 $\times$ 10^{32} cm^{-2}s^{-1} in 2010 [59–62] to $\mathcal{L}$ = 7.73 $\times$ 10^{33} cm^{-2}s^{-1} in 2012 [63,64], and to 1.38 = $\times$ 10^{34}cm^{-2}s^{-1} in 2016 [65]. The peak luminosity delivered to ATLAS in 2016 as a function of time is shown in Figure 2.2. From Run 1 to Run 2, the instantaneous luminosity has been increased to improve physics measurement and searches for new physics. The integrated luminosity (L) corresponds to the instantaneous luminosity integrated over time: L = $\int \mathcal{L}$dt. The LHC delivered luminosity for various data-taking is shown in Figure 2.3. In 2012, an integrated luminosity of around 23 fb^{-1} was delivered at $\sqrt{s}$ = 8 TeV, and $\sim$38 fb^{-1} in 2016 at $\sqrt{s}$ = 13 TeV. In practice, all the delivered luminosity by the LHC is not recorded by the experiments. Figure 2.4 shows the difference between delivered and recorded luminosity with the ATLAS detector. In 2015 (a) and 2016 (b), respectively $\sim$93% and $\sim$95% of the delivered luminosity is recorded. The blue area corresponds to data used in the analyse, including additional criteria on the reconstructed physics objects.

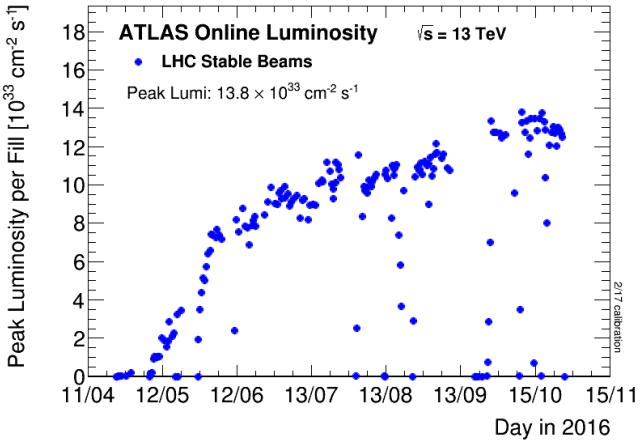

Figure 2.2: The peak instantaneous luminosity delivered to ATLAS during stable beams for pp collisions at 13 TeV centre-of-mass energy is shown for each LHC fill as a function of time in 2016.

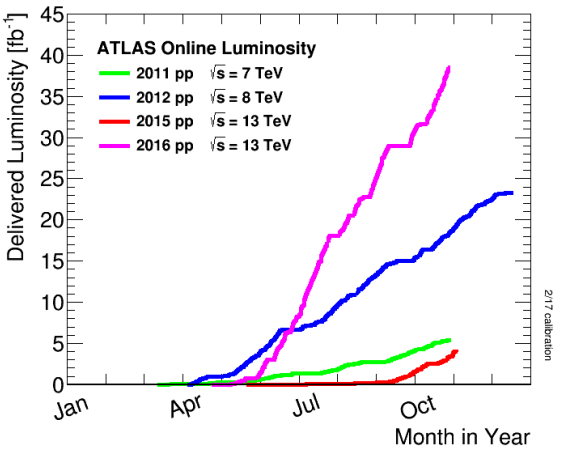

Figure 2.3: The integrated luminosity versus day delivered to ATLAS during stable beams and for high energy pp collisions.

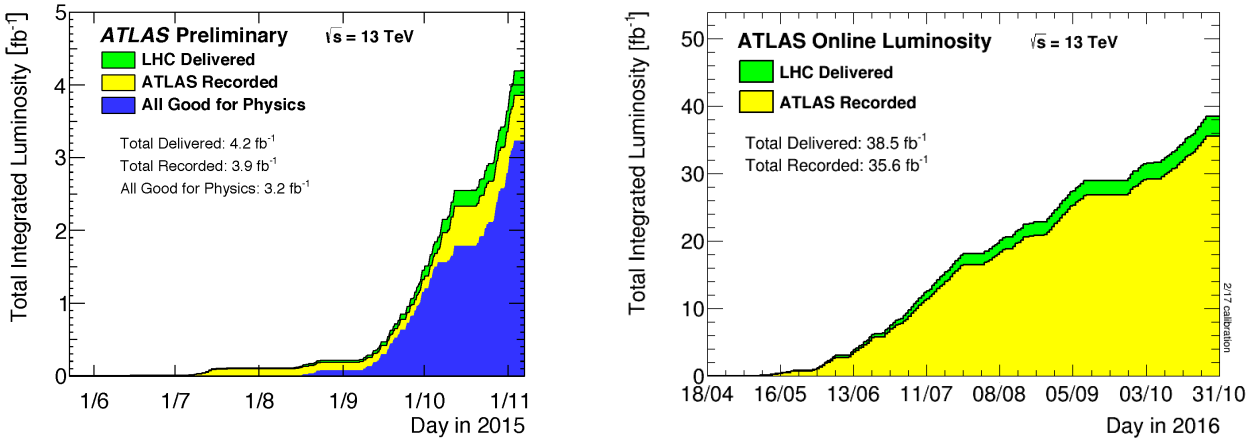

(a) *(b)*

Figure 2.4: The integrated luminosity of stable beams versus time delivered to (green) and recorded by ATLAS (yellow) during stable beams for pp collisions at 13 TeV centre-of-mass energy in 2015 (a) and 2016 (b). The recorded luminosity reflects the DAQ inefficiency. The blue area (a) corresponds to the All Good Data Quality, which is selected with additional criteria on the reconstructed physics objects.

2.1.2.2 Pile-up

The performance of the detector can be affected by the high number of interactions in the same bunch crossing. The average number of interactions per beam crossing $\langle\mu\rangle$ increased from 9.1 in 2010, to 20.7 in 2012, and to 24.9 in 2016. Pile-up corresponds to additional information recorded by the detector during the hard-scattered interaction of interest. The out-of-time pile-up is due to interactions from neighbouring bunch crossings, while in-time pile-up results from additional interactions in the same bunch crossing. Pile-up have an impact on the reconstructed objects in the detector such as tracks or vertex reconstruction [66]. The number of proton-proton interactions per bunch follows a Poisson distribution with mean value μ. During a fill, μ decreases with the fill intensity and increasing emittance. In data, μ is calculated using the following formula:

$$\mu = \frac{L \times \sigma_{inel}}{n_b f_{rev}}, \tag{2.3}$$

Where σ_{inel} is the total inelastic cross-section ($\sim$ 70mb), n_b the number of colliding bunches, and f_{rev} the LHC revolution frequency. The delivered luminosity with 2015 and 2016 data as a function of the mean number of interactions per crossing is shown in Figure 2.5. The mean number of interactions per crossing corresponds to the mean of the Poisson distribution of the number of interactions per crossing calculated for each bunch. In 2015, $\langle\mu\rangle = 13.7$, while in 2016 $\langle\mu\rangle = 24.9$.

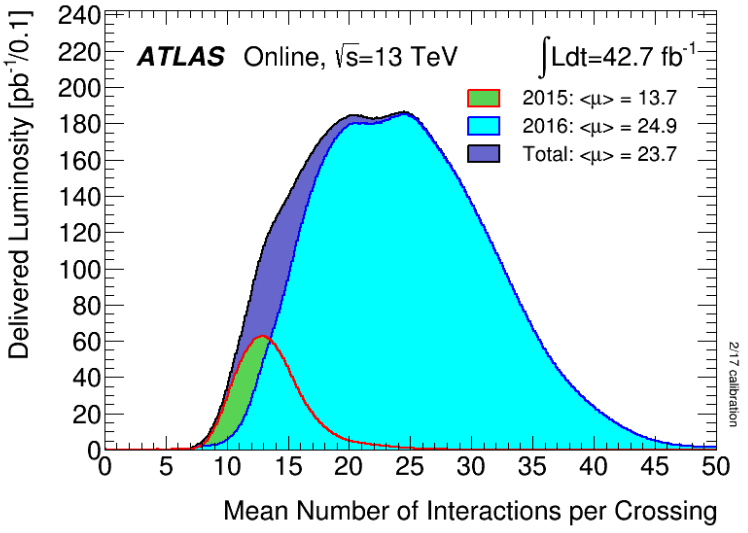

Figure 2.5: The luminosity-weighted distribution of the mean number of interactions per crossing for the 2015 (a) and 2016 (b) pp collision data at 13 TeV centre-of-mass energy.

2.1.3 LHC schedule

The first collisions took place in 2009, with a center of mass energy of 0.9 TeV. Energy of the collision has been increased to 2.36 TeV in the rest of the year. In 2010, event collisions reached an energy of 7 TeV in the center of mass. 2011 is the first year of intensive data taking. In 2012, data is collected with an energy of 8 TeV, and the discovery of the Higgs boson is announced in July 2012. From 2013 to 2015, the LHC is shutdown to prepare the increase of a centre of mass energy to 13 TeV and 14 TeV [67–71]. In 2016, the peak luminosity increased from L = $\sim$ 1.38$\times$ 10^{34} cm^{-2}s^{-1} to $\sim$ 1.7$\times$ 10^{34} cm^{-2}s^{-1}. The Run 3 (2021 to 2023) will also benefit from an increase of the luminosity to 2.0$\times 10^{34} cm^{-2} s^{-1}$ after a shutdown of two years [72]. From 2023 to 2026, improvements in the

detector will be done for the upgrade to High Luminosity-LHC (HL-LHC) [73,74] in order to increase the luminosity by a factor of 10 in 2035. This is illustrated in Figure 2.6.

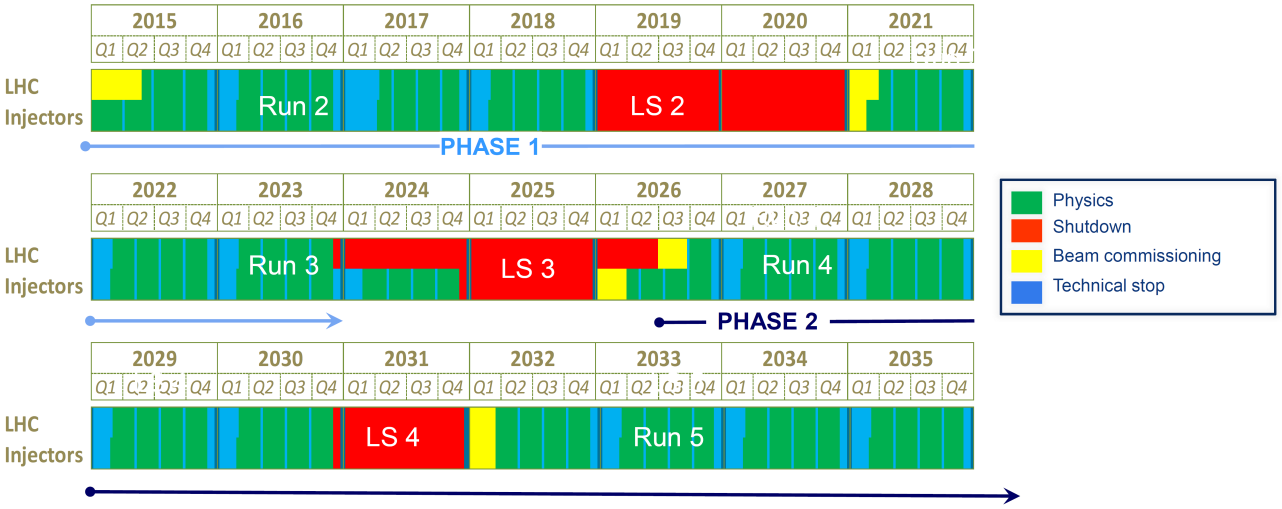

Figure 2.6: The outline LHC schedule out to 2035.

2.2 The ATLAS detector

2.2.1 Overview

The ATLAS detector [75,76] (A Toroidal LHC ApparatuS) is general-purpose detector of the LHC, built for the search of the Higgs boson and new physics (Figure 2.7). ATLAS is designed as a cylindrical detector and corresponds to the largest experimental setup in particle physics with 46 m of length, 25 m of diameter, and 7000 tones of weight. The ATLAS detector is composed of four sub-detectors: the inner tracking detector, the electromagnetic calorimeter, the hadronic calorimeter, and the muon spectrometer.

2.2.2 Nomenclature

The beam direction defines the z-axis, and the x-y plane is transverse to the beam direction. The positive x-axis is defined as pointing from the collision point to the center of the LHC ring. The y-axis is pointing upward. The cylindrical coordinates (r,ϕ) are used in the transverse plane, with the pseudo-rapidity (η). The distance r is defined as the distance from the beam axis, ϕ as the polar angle, and η as the pseudo-rapidity: $\eta = -\ln(\tan\theta/2)$. The transverse momentum p_T, the transverse energy E_T, and the missing transverse energy $E_T^{miss} = |\vec{p_T^{miss}}|$ are defined in the x-y plane. The distance ΔR is defined in the η-ϕ plane as $\Delta R = \sqrt{(\Delta\eta)^2 + (\Delta\phi)^2}$.

2.2.3 The inner detector

The inner detector [77] is the closest sub-detector of ATLAS to the beam interaction. It is designed to reconstruct the charged particle tracks [78] from the collisions, and the primary and secondary vertices. It consists of three different components: the Pixel Detector, the Semi Conductor Tracker (SCT), and the Transition Radiation Tracker (TRT) (Figure 2.8). These sub-detectors cover a sensitive radial distance from the interaction point of 33-122.5 mm, 299-514 mm, and 554-1082 mm. The inner

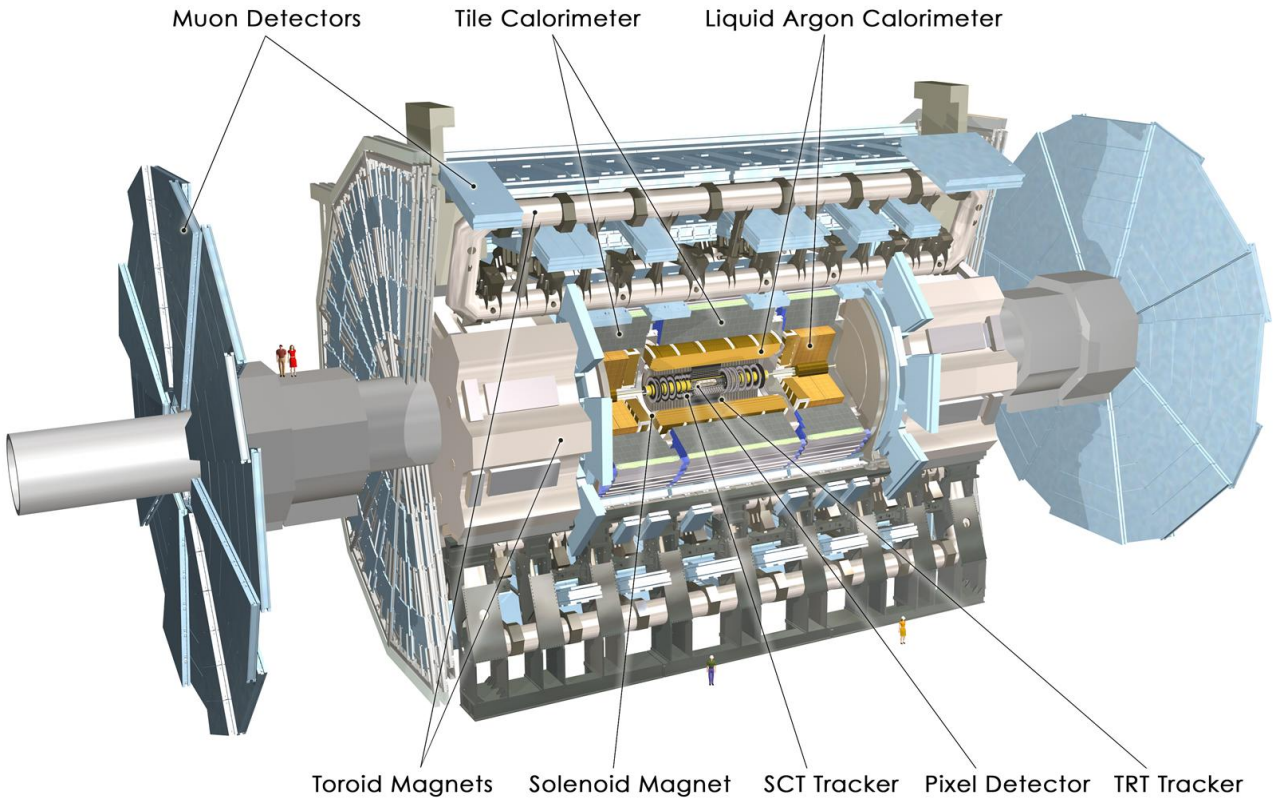

Figure 2.7: The ATLAS detector.

detector is immersed in a 2T magnetic field produced by solenoid magnets in order to bend the trajectories of the charged particles. It has a full coverage in ϕ and covers the pseudo-rapidity range of $|\eta| < 2.5$.

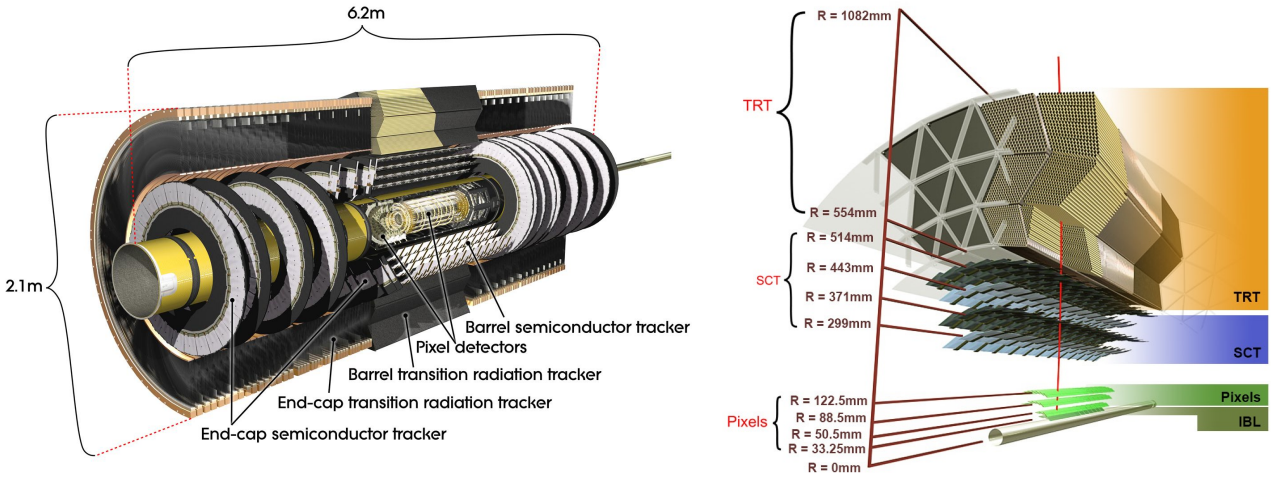

(a) *(b)*

Figure 2.8: The ATLAS inner detector.

2.2.3.1 The Pixel Detector

The pixel detector [79, 80] is designed for precise tracking measurement of charge particles with 40 MHz bunch crossing identification, and for vertices reconstruction. The secondary vertex reconstruction is very important for the identification of particles such as b-jets. The pixel detector provides a coverage of $|\eta| < 2.5$. It consists of three cylindrical barrel layers in the central region $|\eta| < 1.37$, and three disks on both sides for the forward measurement (Figure 2.9). The three barel layers are at a radius of 50.5 mm, 88.5 mm, and 122.5 mm from the beam pipe. Each layer is composed of hundreds of modules consisting of 8 double pixel sensors directly coupled to the 16 readout. Pixels are defined as 50 μm $\times$ 400 μ m rectangular shaped oriented along the beam axis, with a thickness of 250 μm. Between the Run 1 and the Run 2, a new pixel detector layer: the Insertable B-Layer (IBL) [81, 82] is added very closed to the beam pipe. It provides a good vertex reconstruction and b-jet identification despite the increasing pile-up and radiation in the detector.

2.2.3.2 The Semi Conductor Tracker

The Semi Conductor Tracker (SCT) is located after the pixel detector, between 299 mm and 554 mm from the beam pipe. It is composed of silicon strip sensors of 6.36×6.40 cm^2 arranged in eight layers (Figure 2.8). In total, 4088 module of two inclined sensors are used, corresponding to a surface of 63 m^2 with approximately 6.3 millions readout channels. The SCT contributes to the measurement of the momentum, the impact parameter, and the vertex position. The end cap is composed of 18 discs with silicon strips, extending radially the coverage of the SCT.

2.2.3.3 The Transition Radiation Tracker

The Transition Radiation Tracker (TRT) [83, 84] is the final system of the inner detector. It is located between 554 mm and 1082 mm from the beam pipe. Its goal is to provide a continuous tracking at high distance from the interaction point. Tracking is carried out by $\sim$ 370 000 drift tubes (straws) of 4 mm diameter, made of Kapton acting like a cathode, and is kept at high voltage of negative polarity.

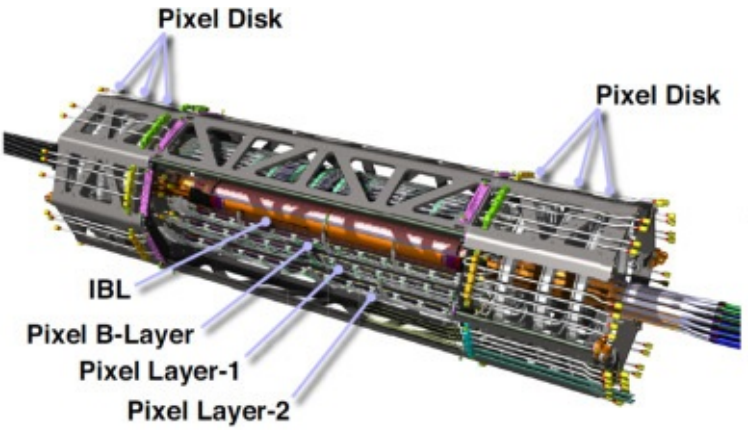

Figure 2.9: The pixel detector.

Each tube is filled with a mixture gas based on Xenon (70%) for good X-ray absorptions, CO_2 (27%) and 0_2 (3%) to increase the electron drift velocity and for photon-quenching. Tracks are reconstructed from the electrons collected with the ionisation of the gas by the charged particle. They are drifted to the central wire at both ends of each tube, and provide timing information. The TRT is used to discriminate electrons from heavier charged particles such as $\pi^{\pm}$. It is composed of the barrel, and two end-caps. The barrel provides a coverage of $|\eta| < 0.7$ and is composed of ∼50 000 straws, while the region $0.7 < |\eta| < 2.5$ is covered by the end-caps.

2.2.4 The ATLAS calorimeters

The ATLAS calorimeter is designed to provide an accurate measurement of the energy and position of electrons and photons, and the energy and directions of jets. The very high centre-of-mass energy and luminosity require good performance over a large energy range. A fast detector response and a high granularity is needed to minimize the pile-up, both in time and space. The ATLAS calorimeter (Figure 2.10) is composed of the electromagnetic calorimeter and the hadronic calorimeter. It covers a pseudo-rapidity up to $|\eta| < 4.9$ with a symmetric measurement in ϕ. The EM calorimeter is based on the liquid argon technology while the hadronic calorimeter also uses scintillator tile technology. The size of the calorimeter is defined to fully contain and absorb most of the electromagnetic and hadronic showers. It corresponds to the biggest part of the detector with a total mass of $\sim$ 4000 tons.

2.2.4.1 The electromagnetic calorimeter

The electromagnetic calorimeter [52] is an accordion-type calorimeter based on liquid argon (LAr) as active material, and lead as passive material (absorber). Electrons mostly interact with the calorimeter via ionization and bremsstrahlung (dominant at high energy), while the photon energy is mostly deposited in the calorimeter via photoelectric effect, Compton scattering, and conversion into e^+e^- (dominant at high energy). The liquid argon is particularly resistant to the radiations, stable and provides a good linearity from the input energy. Electrons emitted in the active material are quickly drifted with a uniform high voltage and collected in the readout electrodes (Figure 2.11 (a)).

The ATLAS calorimeter is divided into a Barrel, and two end-caps (Figure 2.10). The barrel covers the region $|\eta| < 1.475$ and is made of two identical half barrels of 3.2 m, with an internal radius of 1.4 m. Each end-cap is divided in two wheels covering respectively the regions $1.375 < |\eta| < 2.5$, and 2.5

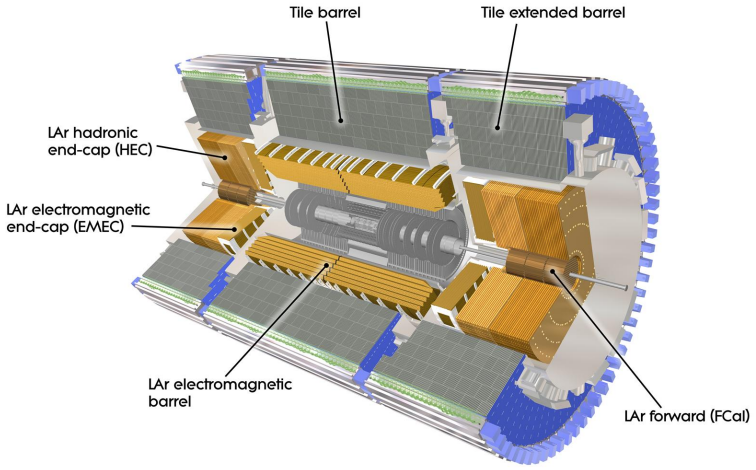

Figure 2.10: The ATLAS calorimeter.

$< |\eta| < 3.2$. The signal is collected with three longitudinal sampling: the front layer, the middle layer, and the back layer (Figure 2.12). Most of the energy is collected by the two first layers. The layers have an active thickness of $6X_0$, $16X_0$, and $3X_0$ in the $\eta = 0$ region (Figure 2.11 (b)), and a respective granularity in the $\Delta\eta \times \Delta\phi$ plane of 0.03×0.1, 0.025×0.025, and 0.05×0.025. In the region $|\eta| < 1.8$, a presampler is added before the front layer and is used to correct the energy losses in the upstream material. The active depth of the presampler is 11 mm of liquid argon in the Barrel and 4 mm in the end-cap, which corresponds to $0.08X_0$ and $0.03X_0$ and to a granularity $\Delta\eta \times \Delta\phi = 0.025\times0.1$. The active depth of the module is $\sim$26 X_0, meaning that most of the electromagnetic shower are absorbed by the calorimeter. Signal collected in the readout is sent to the front-end-board (FEB), amplified, optimized, and digitalized. Then the signal is sent to the level-1 trigger for a possible record. The energy resolution is usually parametrized with the following formula:

$$\frac{\sigma_E}{E} = \frac{a}{E} \oplus \frac{b}{\sqrt{E}} \oplus c, \tag{2.4}$$

where 'a' is the noise term describing the energy fluctuations deposited in the calorimeter. It depends on the electronic noise and the pile-up, and it is expected to be dominant at low energy. The term 'b' is the stochastic term. It depends on the choice of the absorber, the active material, and the thickness of the sampling layers. The last term is the constant term. It is expected to be dominant at high energy and depends on the depth of detector, the non-uniformities, the cracks...

2.2.4.2 The hadronic calorimeter

The hadronic calorimeter (Figure 2.10) includes the Tile calorimeter, the Hadronic end-cap (HEC), and the Forward Calorimeter (FCAL). The Tile calorimeter is divided into a Barrel ($|\eta| < 1.0$), and two extended Barrels ($0.8 < |\eta| < 1.7$). It uses iron as absorber and scintillating tiles as active medium. Three longitudinal layers are used for the measurements corresponding approximately to a thickness of $1.4X_0$, $4.0X_0$ and $1.8X_0$ at $\eta = 0$, to a granularity of 0.1×0.1 for the two first layers, and 0.2×0.1 for the third layer. Energy losses due to the longitudinal leakages have been estimated to less than 2.5% at 300 GeV. Due to higher radiations at large pseudo-rapidity, the LAr technology is also used in the HEC and FCAL. The HEC provides an hadronic coverage of ($1.5 < |\eta| < 3.2$), with a thickness of $\sim$ 12 X_0. The FCAL provides a coverage of $3.1 < \eta < 4.9$ with a granularity in the $\Delta\eta \times \Delta\phi$ plane of 0.2×0.2. Electromagnetic and hadronic calorimeters are non-compensating. It means that the detector

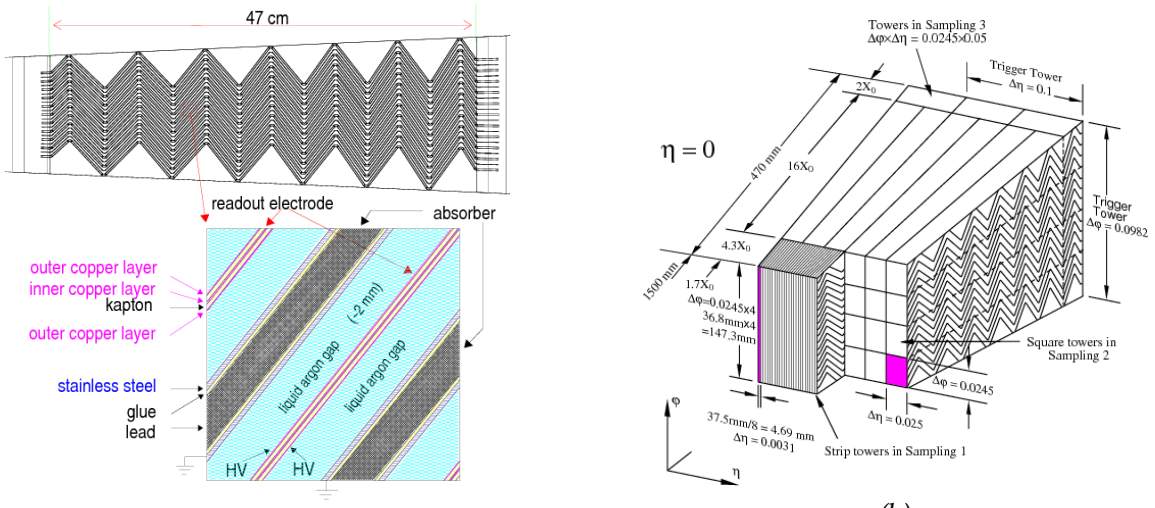

(a) *(b)*

Figure 2.11: The ATLAS accordion-type liquid argon calorimeter (a). The structure of the barrel accordion calorimeter, the presampler is in front of the accordion (b).

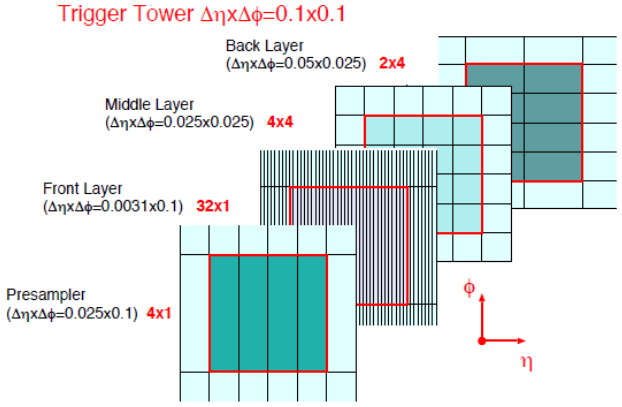

Figure 2.12: The ATLAS calorimeter sampling.

response is different for electromagnetic and hadronic particles. By default, the detector is calibrated for electromagnetic particles.

2.2.5 The muon spectrometer

The muon spectrometer [75] (Figure 2.13) is based on the magnetic deflection of muon tracks. The magnetic field is provided by large barrel toroid in the range $|\eta| < 1.0$, by two smaller end-cap magnets in the range $1.4 < |\eta| < 2.7$, and by a combination of barrel and end-cap fields in the region $1.0 < |\eta| < 1.4$. This configuration provides a field that is mostly orthogonal to the muon trajectories. In the region $|\eta| < 2.0$, measurements are done solely by monitoring drift tubes (MDT). Each module is composed of three layers of drift tubes made of aluminium. A total of 400 000 tubes are composing the MDT. Tubes are filled with non-inflammable mixture of 93% Ar, and 7% of CO_2, corresponding to a total volume of 800 m^3. Electrons are collected in the wires at the center of each tube. In the end-cap region, measurements are done by the Cathode Strip Chambers (CSC), which provides a better granularity. The CSCs are multiwire chambers filled with a non-inflammable mixture of 30% Ar, 50% CO_2, and 20% CF_4. Cathodes are segmented into strips, perpendicular to the wires (anodes). This allows for two independent measurement of the muon. One collecting electrons in the wires after the ionization for accurate measurements, and the other, parallel to the wires providing the transverse coordinate. In the region $|\eta| < 1.05$, trigger is done by Resistive Plate Chambers (RPCs). The RPC consists of a gaseous detector formed by two parallel plates separated by 2 mm and containing the gas. The primary ionisation electrons are multiplied into avalanche by a high and uniform electric field. Beyond $|\eta| = 1.05$, the trigger is done by the thin Gap Chambers (TGCs) which corresponds to multiwire proportional chambers located in the end-cap. They are based on the same principle as the CSC.

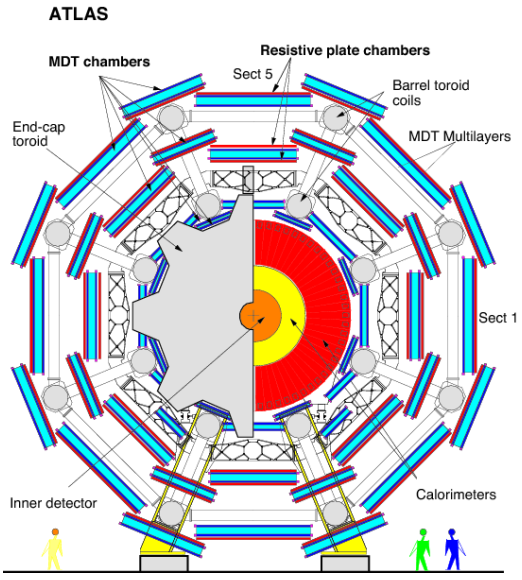

Figure 2.13: The ATLAS muon spectrometer.

2.2.6 The trigger system

The trigger system [85, 86] is the component of the detector deciding whether or not to keep a given collision. It is based on hardware and software and it reduces the event rate from 40 MHz to $\sim$ 1 kHz. It is composed of the level-1 trigger based on hardware, and a High Level Trigger (HLT)

based on software. The level-1 trigger corresponds to a first selection using reduced granularity from calorimeter and muon detector to determine Regions Of Interest (ROIs). The ROIs are defined to search for electrons, photons, taus, jets and missing transverse energy E_T^{miss}. The ROIs are sent to the HLT with a rate of 2.5μs where a most sophisticated selection based on the offline object reconstruction is applied. The rate after the level-1 trigger is approximately 100 kHz. The HLT system is based on algorithms using the full granularity of the detector as input. Rate is reduced from $\sim$ 100 kHz to approximately 1kHz, with a processing time of 200 ms.

The Run 2 upgrade includes a system for pile-up suppression in the level-1 calorimeter trigger: the Multi-Chip Modules (nMCM) increasing the performance on the E_T^{miss} trigger (Figure 2.14). The new muon trigger now requires coincidence with hit from the innermost muon chambers, reducing the rate of this trigger with small signal losses. The Fast Tracker (FTK) is a fast hardware-based tracking system located after the level-1 trigger, providing a full track reconstruction to the HLT. Improvements is also done in the HLT. The level-2 trigger and event-filter are now merged in the HLT for the Run 2, reducing code and algorithm duplication.

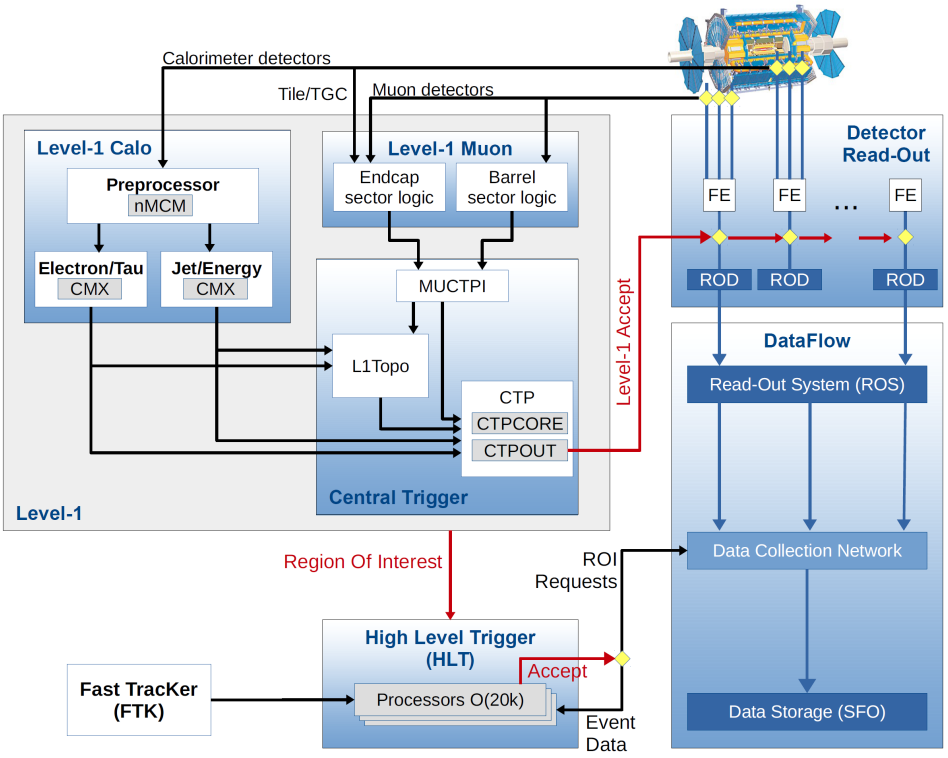

Figure 2.14: The ATLAS trigger system and data acquisition in Run 2.

2.3 Objects reconstruction

2.3.1 Tracks

Tracks are reconstructed from the pixel and SCT detectors (Inner Detector) [66, 87]. The first step of the track reconstruction [88] is the reconstruction of clusters based on a dedicated algorithm. This algorithm is based on the deposited energy in the pixel SCT, and TRT detectors. The clusterization begins with the deposition of enough energy deposition in one pixel, and usually include multiple adjacent pixels. After the clusterization, primary-tracks are reconstructed with an iterative track-finding

algorithm using information of the SCT. A pattern-recognition is used, allowing various combinatorial track candidates. This step is followed by an ambiguity-solver that assigns an individually track score to each candidate. The track score is based on simple measures of the track quality, such as the χ^2 of the track fit, and missing hit in the detector after the fit (hole). The algorithm suppresses the large number of tracks with incorrect assigned clusters. Shared clusters and clusters used in multiple tracks candidates are limited. Clusters can be shared by a maximum of two tracks. A cluster is removed from a track candidate if it decreases the number of shared clusters. The track is then scored again and returns to the order list of remaining candidates. The flow of track candidates through the ambiguity-solver is summarized in Figure 2.15. The requirements for tracks candidates are the following:

- p_T > 400 MeV,
- $|\eta|$ < 2.5,
- minimum 7 of pixels and SCT hits (12 are expected),
- maximum of either one shared pixel cluster or two shared SCT clusters on the same layer,
- no more than two holes in the combined pixel SCT detector,
- no more than one hole in the pixel detector,
- $|d_0^{BL}|$ < 2.0 mm,
- $|z_0^{BL} \sin\theta|$ < 3.0 mm,

where d_0^{BL} is the transverse impact parameter calculated with respect to the measured beam-line position, and z_0^{BL} is the longitudinal difference along the beam line between the point where d_0^{BL} is measured and the primary vertex, θ is the polar angle of the track. The following selections are added for the tight selection of tracks:

- minimum of 9 SCT hits if $|\eta| \leq 1.65$,
- minimum of 11 SCT hits if $|\eta|$ > 1.65,
- either one IBL or next-to-innermost-pixel-layer hit,
- no pixel hole,

The performance of track reconstruction in jets can be estimated using a sample of dijets MC events. The reconstruction efficiency of charged-primary-particle as a function of the angular distance of the particle to the jet axis is shown in Figure 2.16. The efficiency is calculated for different p_T ranges. All charged particles studied are required to be created before the IBL. The efficiency is minimum at the center of the jet where track density is maximum, and increases at higher ΔR where density decreases. The track reconstruction efficiency decreases with jet p_T due to an increasing tracks density matched to the jet axis as shown in Figure 2.17 in the regions $|\eta|$ < 1.2 and $|\eta|$ > 1.2.

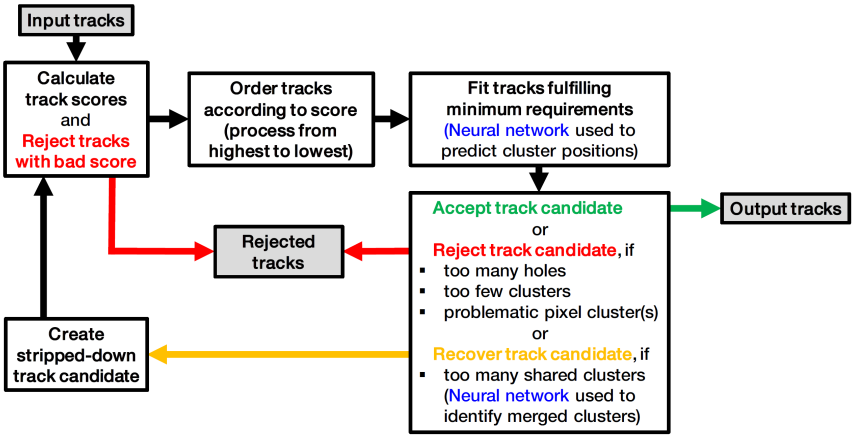

Figure 2.15: Sketch of the flow of tracks through the ambiguity solver.

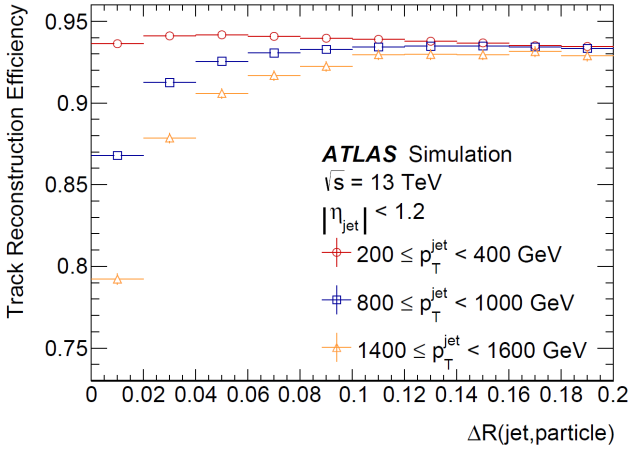

Figure 2.16: The efficiency to reconstruct charged primary particles in jets with $|\eta| < 1.2$ as a function of the angular distance of the particle from the jet axis for various jet p_T for simulated dijet MC events.

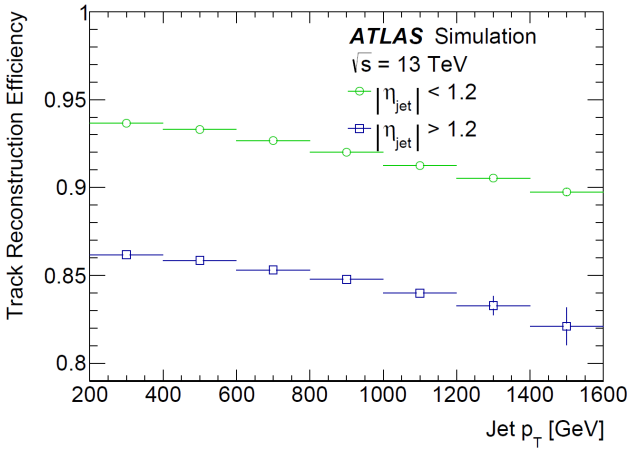

Figure 2.17: The track reconstruction efficiency is compared for charged primary particles in jets with $|\eta|$<1.2 ($|\eta|$>1.2) for the entire jet-p_T range as a function of the jet p_T for simulated dijet MC events.

2.3.2 Primary vertex

The primary vertex corresponds to the hard scattering point. It is reconstructed from tracks with an iterative vertex finding algorithm [89, 90]. The z-position of reconstructed tracks is used as vertex seed. An iterative fit using the goodness of χ^2 is applied to test the compatibility of tracks with the vertex. Tracks displayed by more than 7σ are removed from the list, and used to seed new vertices. The iterative procedure is repeated until no additional vertices can be found. Vertices are required to contain at least two tracks. The increasing number of fake tracks in high pile-up environment increases the probability to reconstruct a fake vertex. Primary vertices are difficult to reconstruct due to the high number of vertices in the collisions. The number of reconstructed vertices as a function of the average number of interactions per bunch crossing is shown in Figure 2.18.

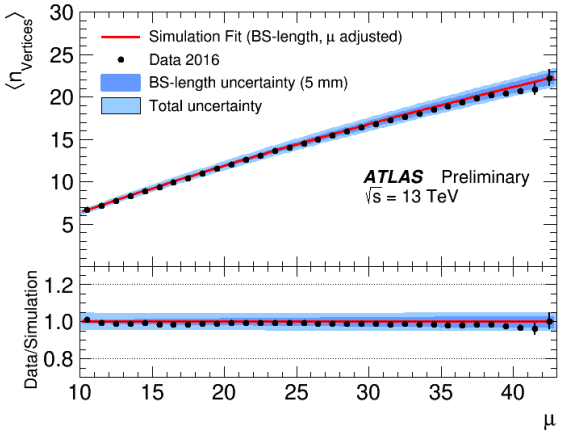

Figure 2.18: Distribution of the average number of reconstructed vertices as a function of μ. The curve represents the result of a fit to the simulation, while dots correspond to the 2016 data [91].

2.3.3 Electrons and photons

2.3.3.1 Reconstruction

Electrons and photons are very precisely measured by the ATLAS calorimeter and have played a critical role for the Higgs discovery. They are reconstructed from energy deposits in the electromagnetic calorimeter, and from tracks in the ID. The energy deposits in the calorimeter cells are merged into clusters with a clustering algorithm [92] described in section 3.2.1. The cluster building efficiency is estimated as 99% with the Monte Carlo simulation at E_T = 15 GeV, and as 99.9% at E_T = 45 GeV.

A reconstruction algorithm is then applied using clusters in input, and a final algorithm decides if the resulting particle candidate is an electron or a photon. The algorithm applied selections based on the shower shape to the EM clusters. At least one track must be matched to a cluster to form an electron. If multiple tracks are matched, they are sorted as a function of the hits number in the ID, the ΔR of the extrapolation, the p_T, and the track with the best score is used for the matching. The photon reconstruction is very similar to the electron reconstruction but different shower shape selections are applied. The photon shower is narrower and tend to be deeper in the calorimeter. Selected clusters with no associated track in the ID are reconstructed as photons. Converted photons correspond to photons decaying into a pair of electron-positron. They are classified as single-track if only one track is reconstructed, and double track if the two tracks are consistent with coming from a massless particle. Unconverted photons are hard to distinguish from the π^0 ($\pi^0 \to \gamma\gamma$). The two

photons are mainly detected and separated with the front layer of the calorimeter, which has a thinner granularity.

2.3.3.2 Identification

Two identifications criteria are commonly used: loose and tight. The first one gives the highest efficiency to select photons but also the largest background background contamination. The second one, applied in this thesis, improves the purity of the sample. The variables used for each identification are detailed in the Figure 2.19. The loose identification only looks at the energy deposits in the hadronic calorimeter and at the shape of the shower measured by the middle layer of the electromagnetic calorimeter. The same cuts are used for converted and unconverted photons and gives an identification photon efficiency (estimated with MC) higher than 99% for $E_T^\gamma > 40$ GeV. The tight identification criteria adds selections on the shape of the shower as it is seen in the strips layer. This layer is more powerful to reject background from jets in which light hadrons such as π^0 and η decaying to two collimated photons. The tight identification increases the purity, but decreases the efficiency to 85% for photons with $E_T > 40$ GeV.

The efficiency of the ID algorithm for electrons is shown in Figure 2.20. The efficiency for electron candidates with E_T = 25 GeV is in the range from 78% to 92% and increases with E_T (left). At the same energy, the background rejection efficiency (right) is in the range from 0.3 to 0.8% and decreases with E_T. The electron identification performance may be influence by the parasitic collisions taking place in the same beam crossing or consecutive bunch crossing.

The efficiency of the tight identification estimated with three in-situ methods described in [94], and based on the data collected in 2015 is shown in Figure 2.21. The photon identification efficiency increases from 52-64% (47-61%) for unconverted (converted) photons at E_T 10 GeV to 88-92% (96-98%) for $E_T > 100$ GeV.

2.3.3.3 Calibration

Various corrections are applied to data on reconstructed photons and electrons [95, 96]. The first data corrections are based on Monte Carlo. They allow an equal response in the longitudinal layers of the ECAL between data and simulation, correct the geometrical effects, and the effects due to non-nominal high-voltage. Then, corrections of the energy deposited in front of the calorimeter are applied. The energy losses are estimated to be between a few percent and 20% for a 100 GeV electron depending on $|\eta|$. Energy losses outside of the cluster are corrected ($\sim$5%), and the variation of the energy response as a function of the impact point on the calorimeter is corrected. Finally, a residual correction based on data is applied to correct the non-uniformity of the detector response as a function of η. The residual corrections are parametrized as:

$$E_i^{data} = E_i^{MC}(1 + \alpha_i), \tag{2.5}$$

where E_i^{data} and E_i^{MC} correspond to the energy of electron in data and MC, and α_i parametrize the data/MC deviation in a given pseudo-rapidity region using calibrated electron. The α_i parameters as a function of η using the 2015 and 2016 data are shown in Figure 2.22. They are estimated to be in the range of 2%. The uncertainty on the electron/photon energy scale includes the uncertainty on the calibration of the presampler, on the two first layers intercalibration, on the gain used in the readout chain, on the description of the material before the calorimeter, on the in-situ calibration, on the baseline shifts, and on pile-up and temperature.

2.3.4 Muons

Muons are reconstructed using information provided by the ID, the calorimeters, and the Muon spectrometer (MS). Four types are defined depending on which subdetector is used for the muon

Category	Description	Name	Loose	Tight
Acceptance	$\|\eta\| < 2.37$, $1.37 < \|\eta\| < 1.52$ excluded	–	✓	✓
Hadronic leakage	Ratio of E_{T} in the first sampling of the hadronic calorimeter to E_{T} of the EM cluster (used over the range $\|\eta\| < 0.8$ and $\|\eta\| > 1.37$)	R_{had_1}	✓	✓
	Ratio of E_{T} in all the hadronic calorimeter to E_{T} of the EM cluster (used over the range $0.8 < \|\eta\| < 1.37$)	R_{had}	✓	✓
EM Middle layer	Ratio in η of cell energies in 3×7 versus 7×7 cells	R_{η}	✓	✓
	Lateral width of the shower	w_{η_2}	✓	✓
	Ratio in ϕ of cell energies in 3×3 and 3×7 cells	R_{ϕ}		✓
EM Strip layer	Shower width for three strips around strip with maximum energy deposit	$w_{s\,3}$		✓
	Total lateral shower width	$w_{s\,\mathrm{tot}}$		✓
	Energy outside core of three central strips but within seven strips divided by energy within the three central strips	F_{side}		✓
	Difference between the energy associated with the second maximum in the strip layer, and the energy reconstructed in the strip with the minimal value found between the first and second maxima	ΔE		✓
	Ratio of the energy difference associated with the largest and second largest energy deposits over the sum of these energies	E_{ratio}		✓

Figure 2.19: Description of the shower shape variables used for the loose and tight photon identification criteria.

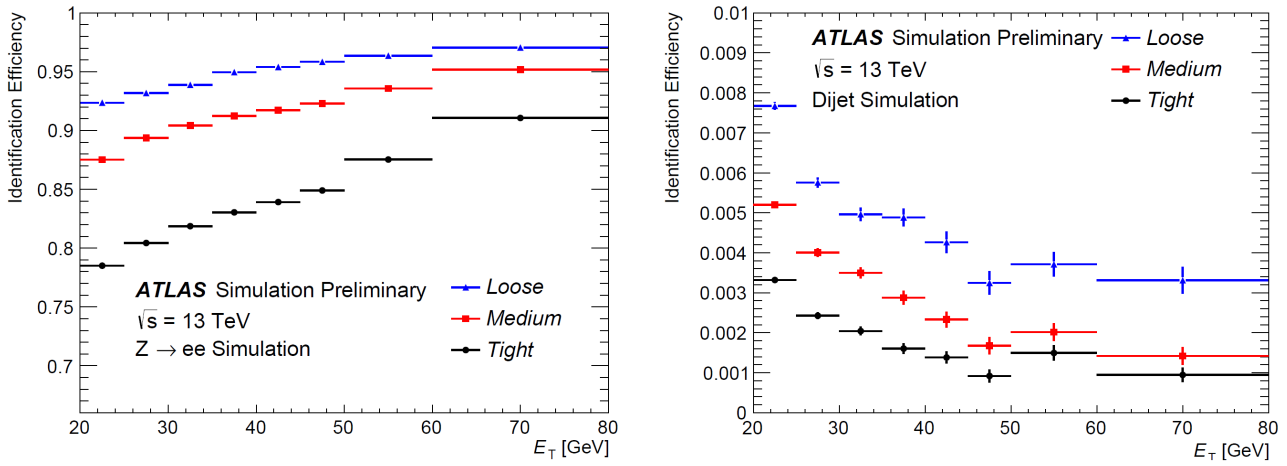

Figure 2.20: Efficiency to identify electrons from Z→ ee decays (left) and the efficiency to identify hadrons as electrons (background rejection, right) estimated using simulated dijet samples. The efficiency are obtained using Monte Carlo simulations, and are measured with respect to reconstructed electrons. The candidates are matched to true electrons for Z → ee events. For background rejection studies the electron matched to true electron candidates are not included in the analysis. Note that the last bin used for the optimisation of the ID is 45-50 GeV, which is why the signal efficiency increases slightly more in the 50 GeV bin than in others, and the background efficiency increases in this bin as well [93].

reconstruction [98]:

Combined (CB) muons: Tracks are reconstructed independently in the ID and MS. A combined track is performed with a global fit using hits from both the ID and MS. Muons are mainly reconstructed from MS tracks, and extrapolated to the ID tracks. The combined reconstruction with extrapolation from ID tracks to MS tracks can also be used as a complementary approach.

Segment-tagged (ST) muons: ST muons correspond to low p_T muons or muons emitted in a reduced MS acceptance region, with only one hit in the MS. In this cases, muons are reconstructed if the extrapolation from the ID tracks is associated with at least one track segment in the MDT or CST.

Calorimeter-tagged (CT) muons: This reconstruction type allows for the reconstruction of muons emitted in the central region, and with $15 < p_T < 100$ GeV. The muon is reconstructed if a track in the ID can be matched to an energy deposit in the calorimeter compatible with a minimum-ionizing particle.

Standalone (SA) muons: Muons are reconstructed from the MS only. This type is used to extend the acceptance for muon reconstruction in the region $2.5 < |\eta| < 2.7$, which is not covered by the ID.

The choice of the reconstruction muon type is made before producing the collection of muons used in the physics analysis. The preference is given to CM muons, then ST muons, and then to CT muons. The overlap with SA muons is solved by analyzing the track hits and selecting tracks with the better fit.

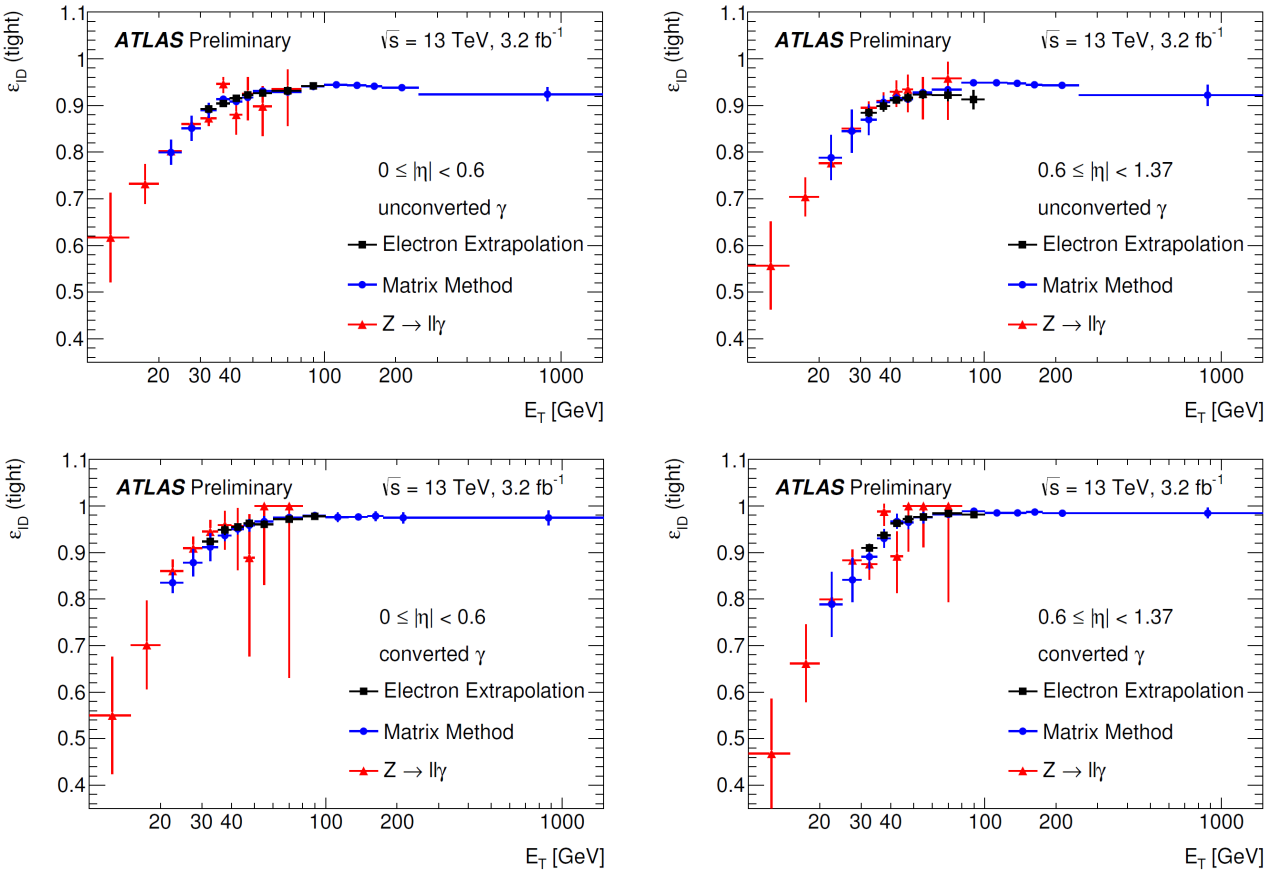

Figure 2.21: Comparison of the data-driven measurements of the identification efficiency for unconverted (up) and unconverted (down) photons as a function of E_T in the region 10 GeV < E_T < 1500 GeV, for two pseudo-rapidity intervals. The uncertainty bars represent the sum in quadrature of the statistical and systematics uncertainties estimated in each method [94].

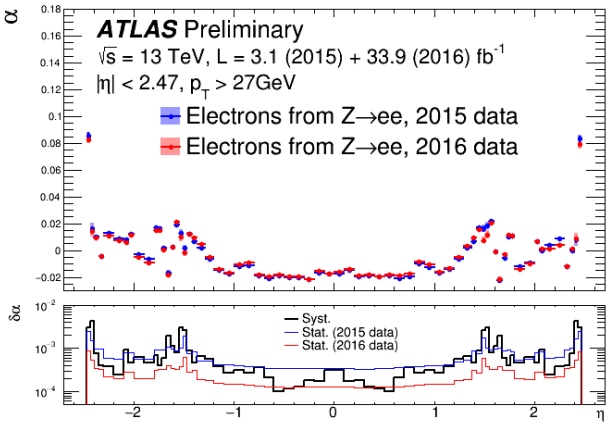

Figure 2.22: Energy scale correction factor α from Z→ee events as a function of η, applied to match data to the MC. Electrons or positrons are required to satisfy p_T > 27 GeV and $|\eta|$ < 2.47. The total systematic uncertainty on this quantity is represented as the red and blue bands on the top plot and as the thick black line on the bottom plot. In the bottom inset, the thin blue (resp. red) line represents the 2015 (resp. 2016) statistical uncertainty. The differences (within ± 0.2%) between the 2015 and 2016 data energy scale correction factors are mostly related to small changes in detector conditions (LAr temperature) as well as to the higher luminosity of the 2016 data compared to 2015 [97].

2.3.5 Jets

Jets are produced by collimated objects emitted from the hadronization and fragmentation of quarks and gluons. They are reconstructed from the energy clusters in the calorimeter using a jet-finding algorithm called anti-k_T [99]. This algorithm provides cone-shaped jets, defined by the cone parameter R. The cone radius is defined by default as R = 0.4. Three jet schemes are used in the thesis, corresponding to three different inputs [100] in the jet reconstruction. Jets at EM scale are reconstructed from clusters calibrated at the EM scale (ATLAS default calibration). Jets at LC scale (local cluster calibration) are reconstructed from clusters with a different correction whether they are produced from an electromagnetic or hadronic particle. Jets with particle flow (EMPFlow) are reconstructed by combining tracks information from the inner detector and clusters information from the calorimeters. More details on the jet reconstruction are provided in chapter 3.

2.3.6 Missing transverse energy

The missing transverse momentum (E_T^{miss}) is defined as the momentum imbalance in the transverse plane where momentum conservation is expected [101, 102]. The E_T^{miss} may be the signature of undetected particles such as the neutrino, but also the signature of physics beyond the Standard Model with neutralino in case of supersymmetry, extra dimension... The E_T^{miss} reconstruction is therefore essential for various searches for new physics. The E_T^{miss} is calculated as:

$$(E_T^{miss})_{x,(y)} = (E_T^{miss})^{e}_{x,(y)} + (E_T^{miss})^{\gamma}_{x,(y)} + (E_T^{miss})^{\tau}_{x,(y)} + (E_T^{miss})^{jets}_{x,(y)} + (E_T^{miss})^{\mu}_{x,(y)} + (E_T^{miss})^{soft}_{x,(y)}, \quad (2.6)$$

where each object is reconstructed by the negative vectorial sum of the transverse momenta of the respective calibrated objects. Soft term is reconstructed from detector signal objects associated to a track, but not associated with any reconstructed object after the selections.

Reconstruction and performance is estimated in events with small E_T^{miss} such as Z→ee/$\mu\mu$. Distributions of simulations and 2015 data is illustrated in Figure 2.23 for events with Z→ee (left) and

Z→$\mu\mu$ (right).

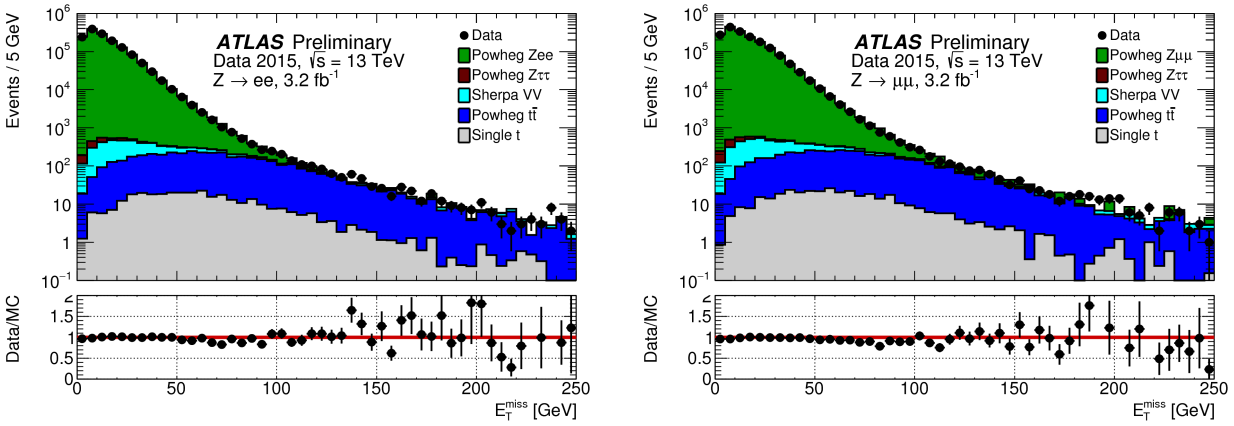

Figure 2.23: ETmiss distribution for a final state of Z decay to a pair of electrons (left), and to a pair of muons (right). The expectation from MC simulation is superimposed after each MC sample is weighted with its corresponding cross-section. Jets are selected requiring pT > 20 GeV. For central jets with pT < 50 GeV, the Jet Vertex Tagger (CONF-2014-018) value is required to be greater than 0.64 [103].

2.4 Conclusion

This section presents the Large Hadron Collider and the ATLAS detector. The center-of-mass energy of the proton-proton collisions and the accelerator luminosity are key parameters for the searches for new physics. The Run 2 of the LHC benefits from the increase of center-of-mass energy from 8 TeV to 13 TeV and from a higher luminosity compared to the Run 1. A new component (IBL) has been added in the tracker system. The last section is dedicated to the object reconstruction in ATLAS and to the performance of the detector.

Chapter 3

Reconstruction and jet calibration

"Anger and intolerance are the enemies of correct understanding."

Mahatma Gandhi

Contents

3.1 Introduction

Jets are the experimental signatures of quarks and gluons produced in high-energy physics. They are key elements in many physics analyses at the LHC. Due to the QCD interaction, partons decay hadronically before interacting with the detector. Therefore, they can not be directly detected. A jet is a collection of collimated objects generated by the hadronisation of partons. Jets are reconstructed by a jet algorithm using the energy deposits in the detector. The measurement is affected by detector effects such as the non-compensation of the calorimeter, the energy losses due to dead material, the energy leakages outside the calorimeter, the signal losses in the calorimeter clustering and the jet reconstruction [104]. In this chapter, the steps from the reconstructed jets to the fully calibrated jets [105–108] will be described. The first step is the reconstruction of the jets from the input objects, also known as jet finding. In ATLAS, jets are reconstructed by default from calorimeter topological clusters (topo-clusters) [92]. The definition of topo-cluster and the descriptions of the main inputs [100] are detailed in the section 3.2. The algorithm used for the jet reconstruction is called anti-k_t [99, 109] and is described in the section 3.3. Jets can be reconstructed from data or from Monte Carlo simulations. The geometry of the detector is treated using Geant4 [110, 111]. We call ' Truth jets ', the jets reconstructed from simulated stable particles, excluding muons and neutrinos. Once jets are reconstructed, various corrections based on simulation or data are applied to the jets as described in Figure 3.1. The first correction applied to the reconstructed jet is the origin correction. The correction recalculates the four-momentum of jets to point to the hard-scatter primary vertex [112], rather than the center of the detector (section 3.4). The energy is kept constant by the correction. Pile-up corrections [113] are described in the section 3.5 and are divided in two steps. The first step is an area-based p_T density subtraction [114] applied for each event, the second is a residual correction based on MC. The absolute MC-based calibration is described in section 3.6. This correction use truth jets information and corrects the energy and pseudo-rapidity bias. The GSC (Global Sequential Correction) is a set of corrections that reduces in particular the JES dependence on the initial parton (section 3.7) [104, 115]. The last step of the jet reconstruction and calibration chain is a residual correction applied to data, on the jet p_T. The corrections are derived using in-situ methods, which are described in section 3.8.

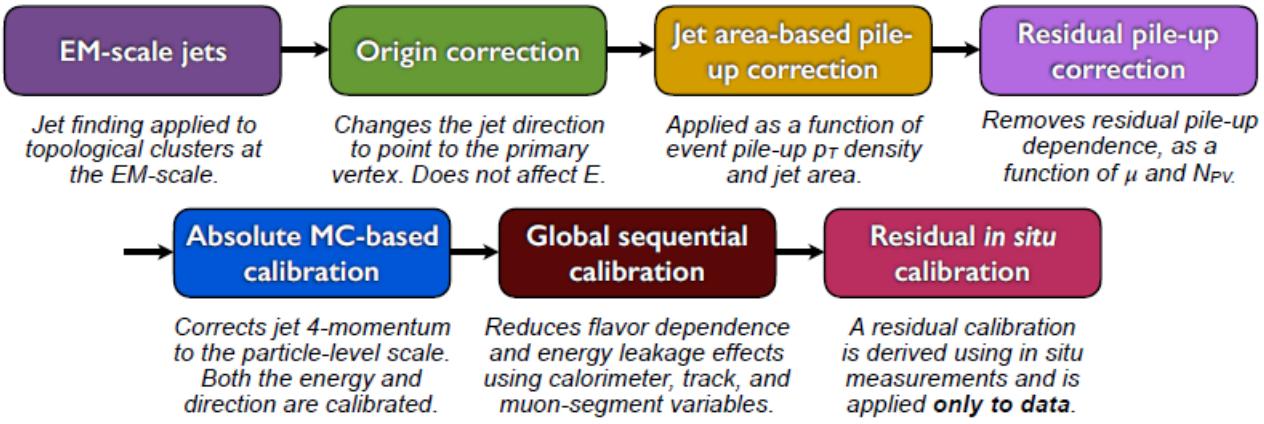

Figure 3.1: Calibration steps for EM-scale jets from the constituent scale to the final in-situ calibration.

3.2 Inputs to jets reconstruction

3.2.1 Topo-clusters

A cluster is a collection of adjacent calorimeter cells merged together with a specific 3D clustering algorithm [92]. The cluster is initiated by an energy deposit above 4 σ, where σ correspond to the standard deviation of the electronic noise and pile-up. The longitudinal and lateral adjacent cells with energy deposit above 2 σ are iteratively added to the cluster. The cluster is closed by including the neighbouring cells with a positive energy to limit the leakages of energy. This algorithm allows finding the small energy depositions, and limiting the noise contributions. Most of the clusters are not isolated and another algorithm is used to separate the clusters between each local maxima depositions. In the following part, the two main cluster calibrations used in ATLAS: the electromagnetic scale (EM scale), and the hadronic scale based on the local cluster weighting method will be presented. In addition, a third kind of input are used in ATLAS combining tracking and calorimeter information, called Particle Flow objects (PFlow).

3.2.2 Electromagnetic cluster calibration

The electromagnetic cluster calibration is the default calibration in ATLAS, defined during the conception of the detector. The response of the calorimeter correctly reproduces the energy deposited by electromagnetic particles. This response has been set up by sending a beam of electrons in the calorimeter and validated in the hadronic calorimeter with a muon beam and cosmics muons. The jets reconstructed with this calibration are called jets at "EM scale". This scale is corrected using the invariant mass of the Z boson decaying into two electrons. The jets in ATLAS calibrated at EM scale with the algorithm anti-k$_t$ for R = 0.4 (section 3.3) are called Antik_t4EMTopo.

3.2.3 Local cluster calibration

Since the ATLAS calorimeter is non-compensating, the response of the detector for hadronic and electromagnetic particles is different (lower for hadronic particles). The main motivation for the local cluster calibration (LC) [116] is to provide a specific calibration for hadronic and electromagnetic clusters. This allows increasing the linearity of the response, as well as the resolution of jets built from a mix of hadronic and electromagnetic signal. It also improves the resolution of full event observables such as E_T^{miss} which combine signal from the whole calorimeter system and require balanced electromagnetic and hadronic responses. Another motivation for the LC calibration is to correct the energy losses due to the topo-cluster threshold, in particular at the neighbourhood of the cluster. An additional motivation is to correct the energy losses in the inactive material. The method can be described as follows:

- The nature of the cluster is estimated with a probability p for hadronic particles and (1-p) for electromagnetic particles. The probability p depends on the properties of the particle such as the energy of the cluster, the pseudo-rapidity, the depth in the calorimeter and the average energy density of cells.
- A correction is applied for each cluster with specific hadronic correction $C_{HAD} \times p$ and electronic correction $C_{EM} \times (1-p)$. Since the cluster calibration is at EM scale by default, $C_{EM} = 1$. The response for hadronic particles is smaller than for EM particles, therefore $C_{HAD} > C_{EM}$. The factors C_{HAD} and C_{EM} depend on the cell signal itself, thus yielding to a different correction for each cell:

$$C = C_{HAD}.p + C_{EM}.(1-p). \tag{3.1}$$

- Energy losses out of the cluster are corrected. This correction depends on variables such as the pseudo-rapidity of the cluster, the depth in the calorimeter and the neighbouring energy measurement. Specific corrections are applied for electromagnetic and hadronic clusters. The formula (3.1) is used with $C_{EM} \neq 1$.

- Additional energy correction is applied to correct losses in dead material (e.g between electromagnetic and hadronic calorimeter).

The ATLAS jet calibrated at local scale with the anti-k_t algorithm for R = 0.4 are called Antik_t4LCTopo.

3.2.4 Jets with particle flow

The particle flow introduces an alternative approach in which measurements from both tracker and calorimeter are combined [117]. The principle of this method is to include tracks informations from the inner detector [118] instead of calorimeter deposits when the performance is better. This improves the accuracy of the charged hadrons measurement and retains the measurements of neutral particle energies. To get an idea of the impact of the charged and neutral particles in a jet, the CMS collaboration has estimated the fractions of the jet energy contribution from charged particles, photons and neutral hadrons as 65%, 25% and 10% respectively [119]. The main advantages of integrating tracking for the jets are the following:

- At low energy, the momentum resolution of the tracker for charged particles is significantly better than the energy resolution of the calorimeter.

- The angular resolution of a single charged particle reconstructed using the tracking detector is much better than using the calorimeter.

- The low p_T charged particles originating from a parton hadronisation will be deviated out of the jet cone due to the magnetic field in the inner detector. By including the tracks association to the primary vertex, these particles will be taken into account in the jet reconstruction algorithm even if they are deviated out of the jet cone.

- Since tracks are associated with a vertex during the reconstruction, the effects of additional particles due to multiple in-time pile-up interactions can be limited by rejecting signals from pile-up vertices during jet reconstruction.

The capabilities of the tracker in reconstructing the charged particles [120] [121] are complemented by the calorimeter's ability to reconstruct both charged and neutral particles. In the forward regions and outside the acceptance of the tracker, only the topo-clusters are used as input to the particle flow algorithm. Thus, a combination of the two system is preferred for an optimal event reconstruction.

However, the particle flow introduces a complication. For any tracks used in the jet reconstruction, it is necessary to correctly identify its signal in the calorimeter to avoid the double-counting in the energy measurement. In the particle flow algorithm, a boolean decision is taken to whether use the tracker or the calorimeter. If the tracker is used, the corresponding calorimeter energy must by substracted. The performance of the algorithm depends on the ability to accurately substract all of the single particle's energy without removing energy deposited by other particles. Up to now in ATLAS, the clusters used as inputs are calibrated at electromagnetic scale. Further development is needed to combine the LC clusters with the particle flow.

The ATLAS jet calibrated at particle flow level with the anti-k_t algorithm for R = 0.4 are called Antik_t4EMPFlow.

3.3 Algorithm anti-k_t

The anti-k_T algorithm is the default jet clustering algorithm used in the ATLAS experiment. It's an inclusive jet finding algorithm belonging to a class of sequential recombination jet algorithms. In ATLAS, topo-clusters are the objects by default used for this algorithm. The distance d_{ij} between the objects i and j is defined as follows:

$$d_{ij} = max(p_{T,i}^{2p}, p_{T,j}^{2p}) \frac{\Delta R_{ij}^2}{R^2}, \tag{3.2}$$

Where $p_{T,i}$ is the transverse momentum of the object i, $\Delta R_{ij} = \sqrt{(\eta_i - \eta_j)^2 + (\phi_i - \phi_j)^2}$ is the distance between the objects i and j in the $\eta - \phi$ plan, and R is the size of the jet cone. The value of p defines the type of algorithm:

- p = -1 is the anti-k_T algorithm,
- p = 0 corresponds to the Cambridge/Aachen algorithm,
- p = 1 is the k_T algorithm.

The maximal distance d_{iB} for the combination is defined as the distance between the object i and the beam:

$$d_{iB} = p_{T,i}^{2p}. \tag{3.3}$$

The algorithm proceeds by identifying the smallest distance d = min(d_{ij} , d_{iB}). If d = d_{ij}, the algorithm recombines the objects i and j in one object i. If $d = d_{iB}$, the algorithm removes i from the list and defines it as a jet. The distances are recalculated and the process is repeated until the end of the list. The algorithm allows progressively increasing the jet size around a core until the size of the jet (R) is reached. The anti-k_t algorithm is collinear and infrared-safe. Figure 3.2 compares four jet clustering algorithms used at parton-level for R = 1. This algorithm behaves like an idealised cone algorithm defined by a size R. In the following, jets are reconstructed with anti-k_T algorithm, using R = 0.4. A p_T threshold of 7 GeV is required in the jet reconstruction.

3.4 Origin correction

After the jet clustering algorithm, the jets are by default pointing to the center of the calorimeter. The origin correction changes this direction to point to the primary vertex. The correction modifies the four momentum of the jet as illustrated in Figure 3.3, but the energy is kept unchanged. The origin correction highly improves the resolution of the jets in η. Figure 3.4a shows the improvement of the jet resolution with the origin correction using Run1 data [123]. The resolution in ϕ is not changed by the origin correction as shown in Figure 3.4b.

3.5 Pile-up correction

With 25 ns of bunch spacing instead of 50 ns during the Run 1, the detector was exposed to more in-time and out-of-time pile-up. The same procedure as in 2012 is performed, using an updated MC simulations matching the Run 2 detector and beam conditions. The pile-up correction proceeds in two steps: first, an area-based substraction [124] is applied in data and MC simulation, second, a residual correction is derived from the MC.

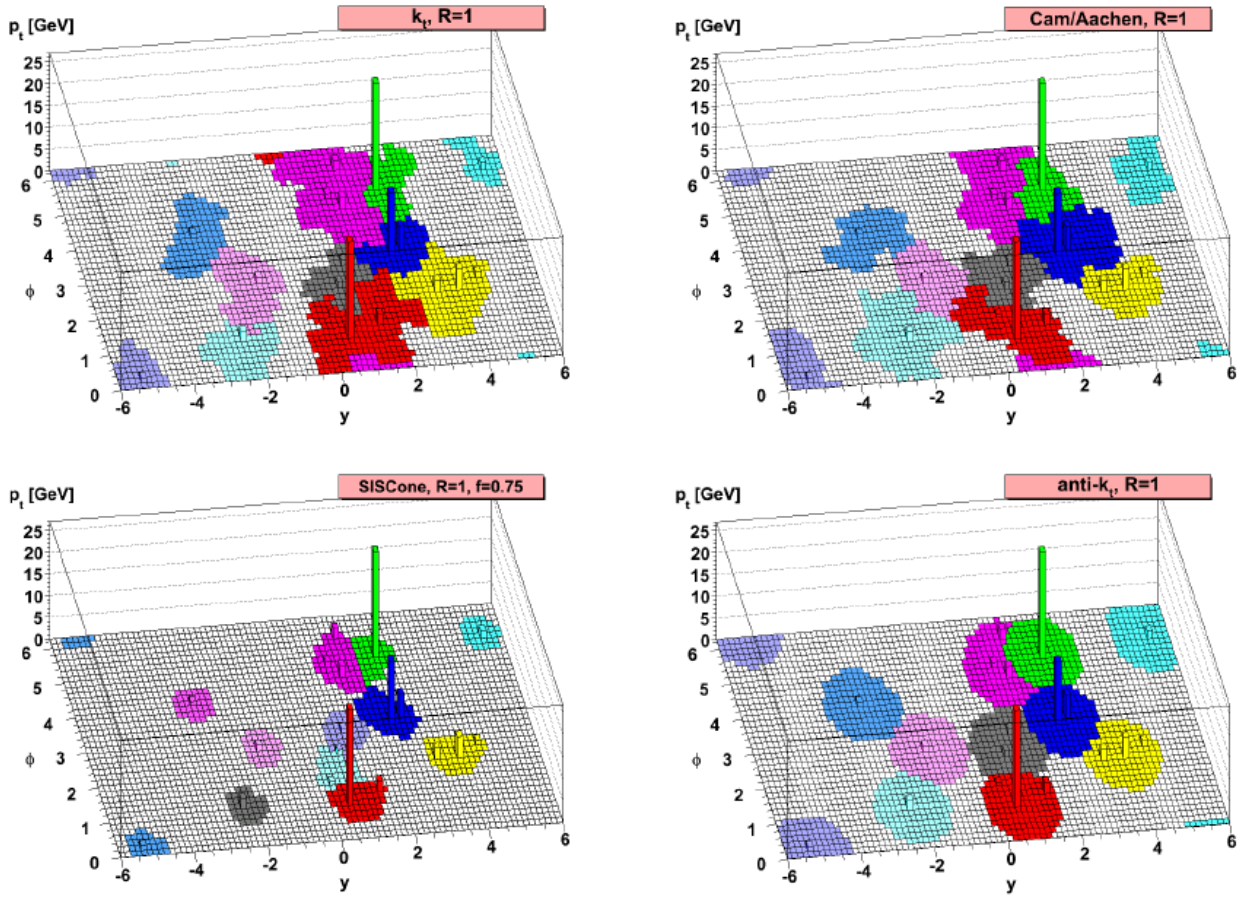

Figure 3.2: A sample of parton-level event generated with Herwig [122], clustered with four different jets algorithms (R=1), illustrating the "active" catchment areas of the resulting hard jets [99].

The area-based subtraction procedure is used to remove the per-event pile-up contribution using the median p_T density (ρ) of the jet in the $\eta \times \phi$ plan. The energy density of each jet is taken as $p_T \times A$, where A is the area of the jet. The pile-up event density for jets at 13 TeV is roughly the same as the one seen at 8 TeV. This is because the increases in the center of mass energy and in-time/out-of-time pile up are compensated by an increase of the noise threshold. It is observed that after this correction, some dependencies of the jet p_T on the pile-up remain.

An additional correction is then applied as a function on the number of primary vertices (N_{PV}) and the average number of interaction per bunch crossing μ. The residual correction can correct both in-time and out-of-time pile-up. The dependencies of the jet p_T on N_{PV} and $< \mu >$ can be seen in Figure 3.5a and 3.5b. The pile-up subtracted p_T^{corr} after area based and residual correction is therefore given by:

$$p_T^{corr} = p_T^{const} - \rho \times A - \alpha \times (N_{PV} - 1) - \beta \times \mu, \tag{3.4}$$

where p_T^{const} refers to the constituent scale before any pile-up corrections are applied.

3.6 Absolute MC-based calibration

The absolute MC-based calibration corrects the energy and η biases from detector effects in the measurement. Reconstructed jets are geometrically matched to the truth jets within $\Delta R = 0.3$. An

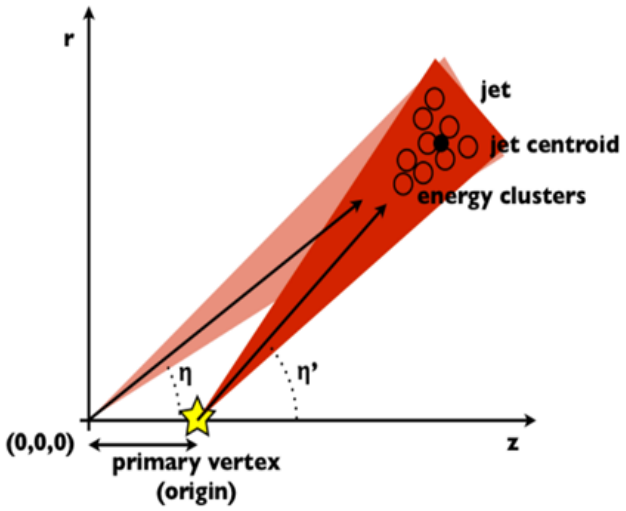

Figure 3.3: Origin correction changes the jet direction, from the center of the detector by default to the reconstructed primary vertex. The four-vector is modified but the energy are kept unchanged.

isolated calorimeter jet is required to have no other jet of p_T > 7 GeV within ΔR = 1.0, and only one truth jets of p_T^{truth} > 7 GeV within ΔR = 0.6. Jet response is defined as the mean of a Gaussian fit applied on the distribution of E^{reco}/E^{truth}, in bins of E^{truth} and η_{det}. Response and η biases as a function of η_{det} are respectively shown in Figures 3.6 (a) and 3.6 (b).

3.7 GSC

The Global Sequential Correction (GSC) is a set of additional corrections reducing the JES dependences from the initial parton [125]. The five steps correct the jet energy dependences on (in order):

- The energy deposited in the first layer of the Tile calorimeter,
- The energy deposited in the third layer of the electromagnetic calorimeter,
- The number of tracks associated with the jet,
- The p_T-weighted width of the tracks associated with the jet,
- The number of muon segments associated with the jet.

The first four schemes allow the improvement of the jet energy resolution and the jet energy scale. The last correction reduces the tails in the response distribution caused by the high p_T jets that are not fully contained in the calorimeter. The average jet p_T response in MC simulation as a function of the five GSC variables is shown in Figure 3.7.

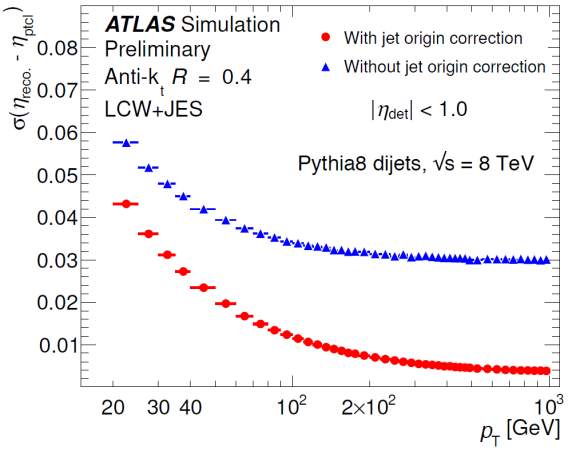

(a) η resolution

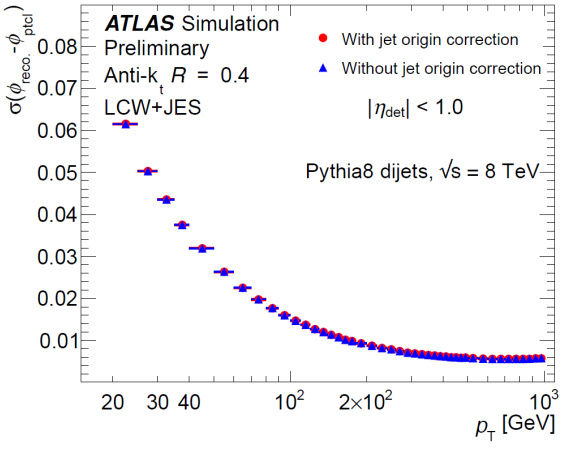

(b) ϕ resolution

Figure 3.4: Effects of the origin correction on jets η resolution (a) and jets ϕ resolution (b) for LC jets with R = 0.4 [123]

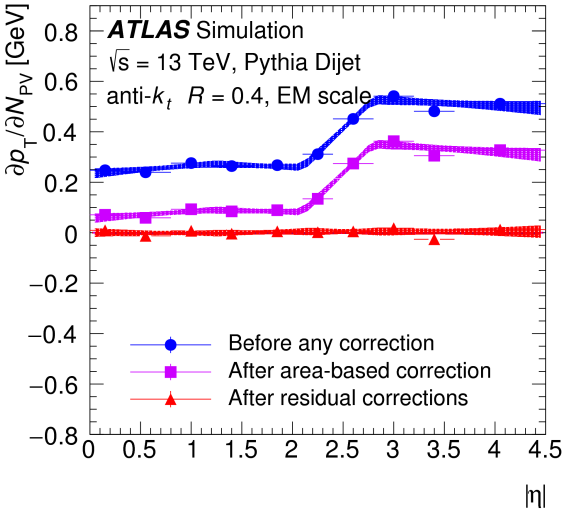

(a) In-time pile-up dependence

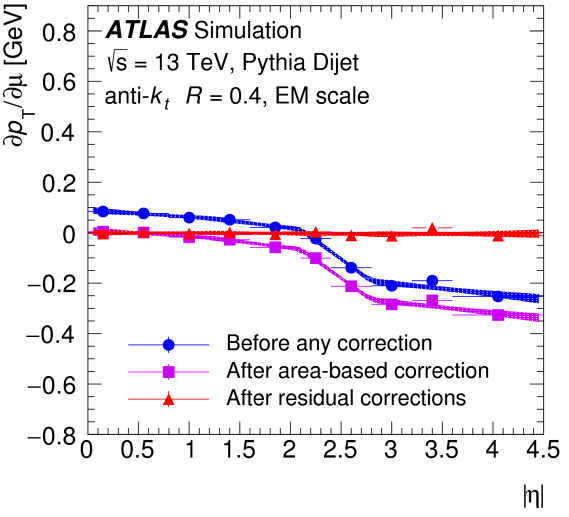

(b) Out-of-time pile-up dependence

Figure 3.5: Dependence of EM jet p_T on in-time pile-up with N_{pv} averaged over <μ> (a) and out-of-time pile-up, with <μ> averaged over N_{pv} (b) as a function of $|\eta|$. The dependence is shown before pileup correction (circle), after area subtraction (square) and after the fitted residual correction (triangle) [105].

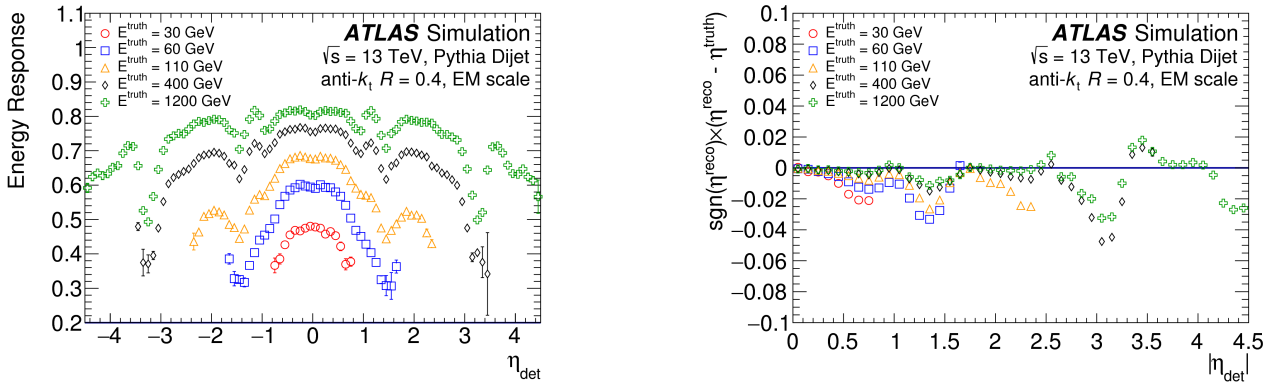

(a) (b)

Figure 3.6: Energy response of EM scale jets with anti-k_t R = 0.4 as a function of η_{det} (a) and difference between η_{truth} and η_{reco} as a function of η_{det}(b) after the origin and pile-up corrections [105].

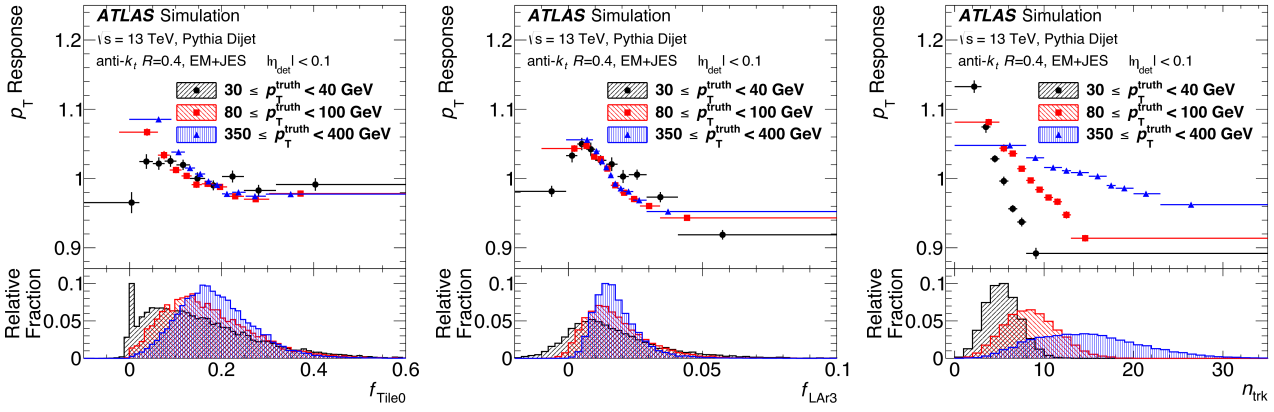

(a) 1st Tile Calorimeter Layer (b) 3rd LAr Calorimeter Layer (c) Number of tracks

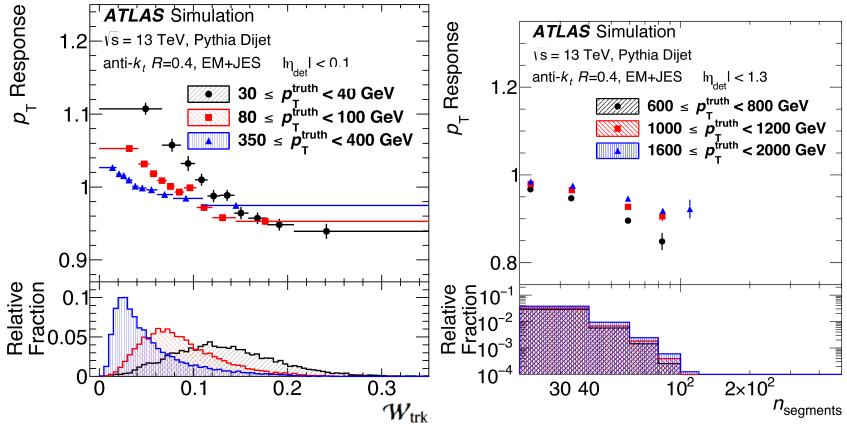

(d) Track width (e) Number of muon segments

Figure 3.7: The average jet p_T response in MC simulation as a function of the GSC variables for various ranges of p_T^{true}. The fractional energy in the first Tile Calorimeter layer (a), in the third LAr calorimeter layer (b), the number of tracks (c), the track width (d) and the number of segments per jet (e) are shown. Jets are calibrated with EM+JES scale without GSC corrections [105].

3.8 In-situ calibration

The in-situ calibration is the final step of the jets calibration. This step provides a residual correction on the jet p_T after the GSC corrections by comparing the data to the Monte Carlo simulations. This correction is applied to the data. The data-to-MC differences could arise from mis-modeling of pile-up activity, underlying events [126] [127], model dependence of physics of jets formation, approximations on QED/QCD interactions and hadronisations, and limitations in the description of the detector material. The first step of the in-situ calibration consists of a relative p_T calibration with respect to η using the dijet method. This step is called η-intercalibration and is described section 3.8.1. The second step is an absolute p_T calibration, applied for central jets using calibrated Z/γ+jet events [96]. This section is described in section 3.8.2. The final part is the multijet method (section 3.8.3) which calibrates jets with very high p_T, that can not be calibrated with the Z/γ methods.

3.8.1 Inter-calibration in η and dijet method

The η-intercalibration corrects the jet dependencies on the pseudo-rapidity using dijet events. It provides a relative correction for jets in data from residuals effects remaining after the previous calibrations. At leading order the two jets are expected to be balanced in p_T, and the jet in the central region ($|\eta| < 0.8$) is used as a reference.

3.8.1.1 The central reference region

The eta-intercalibration provides a residual correction for jets in the forward region of the detector. The central region of the detector is used as a reference because of better performance in this region of calorimeter. The transverse momentum balance is quantified by the asymmetry A, defined as:

$$A = \frac{p_T^{probe} - p_T^{ref}}{p_T^{ave}}, \tag{3.5}$$

where p_T^{probe} is the transverse momentum of the forward jet, p_T^{ref} is the transverse momentum of the jet in the central region and p_T^{ave} is the average transverse momentum of the two jets, $p_T^{ave} = \frac{p_T^{prob}+p_T^{ref}}{2}$. The asymmetry is then used to measure the η inter-calibration factor c of the probe jet defined by:

$$\frac{1}{c} = \frac{p_T^{probe}}{p_T^{ref}} = \frac{2 + \langle A \rangle}{2 - \langle A \rangle}, \tag{3.6}$$

where $\langle A \rangle$ is the average value of the asymmetry in a bin of p_T^{ave} and η_{det}. The analysis is performed in bins of η_{det} and p_T^{avg} where η_{det} is defined as the pseudo-rapidity of the jet with respect to the detector position.

3.8.1.2 The matrix method

A disadvantage of the central reference region method is that all the events are required to have a jet in the central reference region. This can be a significant loss of event statistics, especially in the forward region. In order to use the full statistics, one can extend the default method by replacing the "probe" and "reference" jets by "right" and "left" jets defined by $\eta^{left} < \eta^{right}$. Equations (3.5) and (3.6) become:

$$A = \frac{p_T^{right} - p_T^{left}}{p_T^{ave}}, \tag{3.7}$$

$$R = \frac{p_T^{left}}{p_T^{right}} = \frac{c^{right}}{c^{left}} = \frac{2 + \langle A \rangle}{2 - \langle A \rangle}, \tag{3.8}$$

Where R denotes the ratio of the response, c^{left} and c^{right} are the η inter-calibration factors for left and right jets. In this approach, the average response ratio $\langle R_{ijk} \rangle$ is evaluated in each bin of η^{left}, η^{right}, and p_T^{avg}, corresponding respectively to bins i-j-k. The correction factor c_{ik} are computed for each η-bin i, and for a fixed p_T^{avg}-bin k, and are obtained by minimizing the following matrix of linear equations:

$$S(c_{1k}, ..., c_{Nk}) = \sum_{j=1}^{N} \sum_{i=1}^{j-1} \left(\frac{1}{\Delta \langle R_{ijk} \rangle} (c_{ij} \langle R_{ijk} \rangle - c_{ij}) \right)^2 + X(c_{1k}, ..., c_{Nk}), \tag{3.9}$$

Where N is the number of η-bins, $\Delta \langle R_{ijk} \rangle$ is the statistical uncertainty of $\langle R \rangle$ and $X(c_{ik}, ..)$ is used to quadratically suppress the deviations from the unity of the average correction. The minimization of equation (3.9) is applied separately for each p_T-bin k, and the resulting calibration factor c_i are scaled such that the average calibration factor in the reference region $|\eta_{det}| < 0.8$ equal to unity.

3.8.1.3 Derivation of a residual correction

The residual correction is derived from data/MC ratio $C_i = \frac{c_i^{data}}{c_i^{MC}}$ of the measured η inter-calibration factors. This correction is applied to data only. Powheg+Pythia8 [128, 129] is used as the reference Monte Carlo. Figures 3.8 (a) and 3.8 (b) show the relative jet response calibrated at EM scale as a function of $\eta^{detector}$, using 2015 data, Sherpa [130] and Powheg+Pythia8 in the specific range $25 < p_T^{avg} < 40$ and $115 < p_T^{avg} < 145$. Figures 3.8 (c) and 3.8 (d) show this response with respect to the jet p_T for a range of $1.2 < \eta_{det} < 1.5$ and $2.6 < \eta_{det} < 2.8$. The response in data for all p_T ranges is larger than in both MC samples, and in the 2012 data. This is due to the reduction in the number of samples used for the pulse reconstruction in the LAr calorimeter from five to four. This change is sensitive to the differences in the pulse shape between data and MC. This effect is corrected by the η-intercalibration.

3.8.2 Z/γ+jet method

Two different processes are used to compute the absolute in-situ corrections: γ+jet and Z+jet. The two processes are similar but are used for different jet p_T ranges. They are combined with the multijet method (section 3.8.3) to provide the final calibration. The principle of the Z/γ+jet method is to compare the jet p_T with the p_T of a reference particle (Z/γ) measured with high precision. At leading order, due to transverse momentum conservation, the parton and the reference object have the same p_T. The very precise measurement of the Z/γ p_T is used as a reference for the jet p_T calibration. A set of criteria is applied to select events with Z/γ balancing to leading jet. Figure 3.9 shows a typical event used for the calibration. Topological selections are applied on the angle between the jet and the reference object, and to limit the impact of the sub-leading jet p_T. At low p_T, Z+jet [131, 132] is more precise since the Z decays into two leptons $Z \to e^+e^-/\mu\mu$. The detection of two leptons allows a very efficient background rejection. The γ+jet is used for higher p_T range. Two methods for each Z or γ+jet processes can be performed: Direct Balance and MPF methods.

3.8.2.1 The Direct Balance method

The Direct Balance method compares the jet p_T with the Z/γ p_T. To limit contributions from the radiations, the Direct Balance method uses the Z/γ p_T projection to the jet axis:

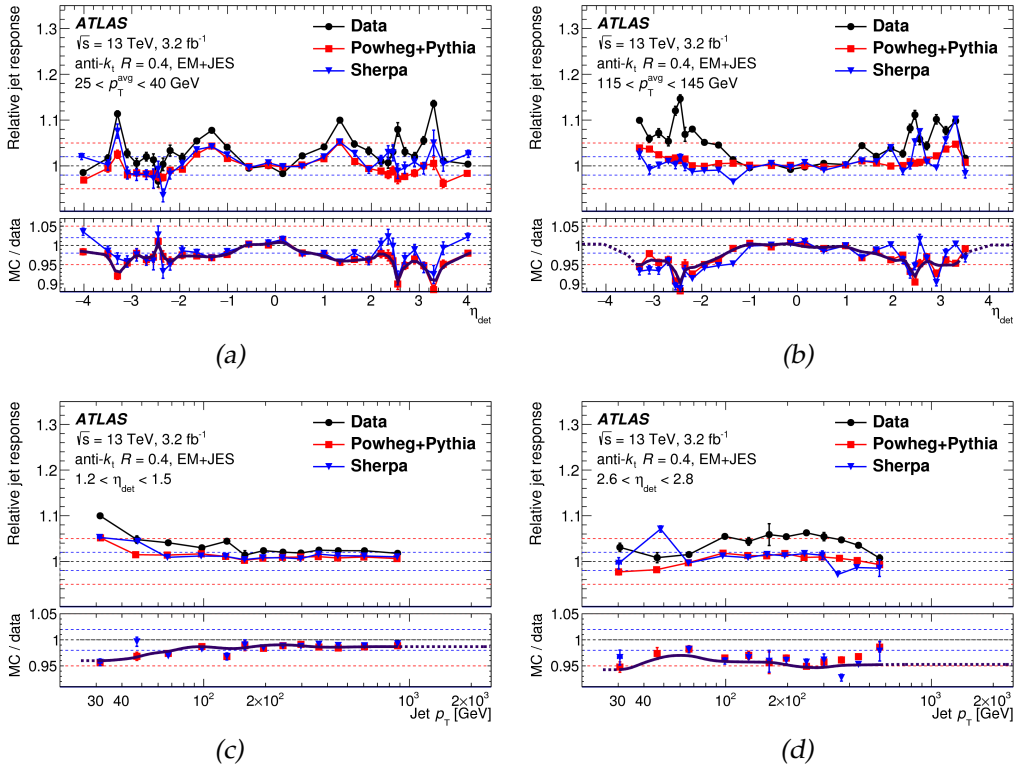

Figure 3.8: Relative response of EM+JES jets as a function of η at low p_T(a), and high p_T (b), and as a function of jet p_T within the ranges $1.2 < \eta_{det} < 1.5$ (a), and $2.6 < \eta_{det} < 2.8$ (d). The bottom panels show the MC-to-data ratios and sthe overlayed curve reflects the smoothed in-situ correction. Results are obtained with the matrix method. The binning is optimized for data and Powheg+Pythia [105].

$$p_T^{ref} = p_T^{Z/\gamma} \times |\cos \Delta\phi(jet, Z/\gamma)|, \tag{3.10}$$

With $\Delta\phi(jet, Z/\gamma)$ the azimuthal angle between the leading jet and the boson. The p_T^{ref} is used to compute the balance in different p_T ranges:

$$B = \frac{p_T^{leadingjet}}{p_T^{ref}}. \tag{3.11}$$

Since out-of-cone energy losses are not included in the jet energy, B is lower than one. The distribution is fitted with a Gaussian function, and the mean $\langle B^{data} \rangle$ of the fit is used. The balance is computed for data and MC and the ratio $\mathcal{R}$ is used as the in-situ correction:

$$\mathcal{R} = \frac{\langle B^{MC} \rangle}{\langle B^{data} \rangle}. \tag{3.12}$$

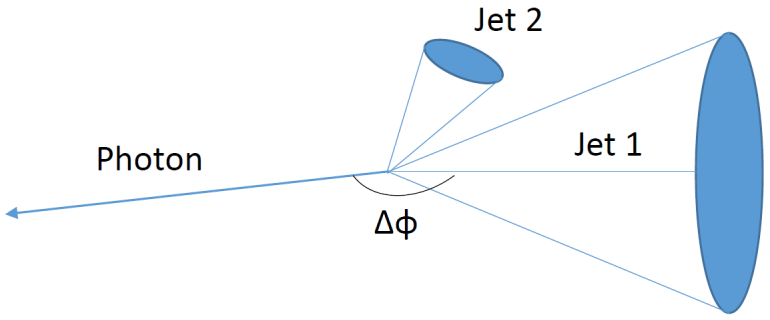

Figure 3.9: Typical γ+jet event selected for the in-situ calibration. The $\Delta\Phi$ should be close to π and the impact of the sub-leading jet p_T should be limited by the topological selections.

3.8.2.2 MPF method

The Missing Projection Fraction (MPF) method is an alternative method to the Direct Balance method. This technique allows taking into account the radiations out of the jet cone. At leading order:

$$\overrightarrow{p_T}^{\gamma} + \overrightarrow{p_T}^{parton} = \overrightarrow{0}, \text{ at parton level,} \tag{3.13}$$

$$\overrightarrow{p_T}^{\gamma} + \overrightarrow{p_T}^{recoil} = \overrightarrow{0}, \text{ at particle level.} \tag{3.14}$$

The ISR or FSR are excluded using the event selection criteria. After interaction with the calorimeter, this equation can be written as:

$$R_{EM}.\overrightarrow{p_T}^{\gamma} + R_{MPF}.\overrightarrow{p_T}^{recoil} = -\overrightarrow{E_T}^{miss}, \tag{3.15}$$

Where R_{EM} is the response of the detector to the Z/γ particle that interacts electromagnetically and R_{MPF} is the detector response to the jets. ${E_T}^{miss}$ is the missing transverse momentum of the event. Since the detector is calibrated at electromagnetic scale, $R_{EM} \sim 1$ and

$$R_{EM}.\overrightarrow{p_T}^{\gamma} + R_{MPF}.\overrightarrow{p_T}^{recoil} = -\overrightarrow{E_T}^{miss} = \overrightarrow{p_T}^{\gamma} - R_{MPF}.\overrightarrow{p_T}^{\gamma}, \tag{3.16}$$

$$E_T^{\gamma} - R_{MPF}.E_T^{\gamma} = -\overrightarrow{n}_{\gamma}.\overrightarrow{E_T}^{miss}, \tag{3.17}$$

This lead to MPF equation:

$$R_{MPF} = 1 + \frac{\overrightarrow{n}_{\gamma}.\overrightarrow{E_T}^{miss}}{E_T^{\gamma}}, \tag{3.18}$$

The MPF is measured in data and MC, and the ratio MC-to-data is used as a correction:

$$\mathcal{R} = \frac{\langle R_{MPF}^{data} \rangle}{\langle R_{MPF}^{MC} \rangle}. \tag{3.19}$$

The MPF and Direct Balance method have different sensitivities to additional soft parton radiation as well as to pile-up interaction. The multijetmethod balance high p_T jet again several lower p_T jets fully calibrated with the previous method.

3.8.3 Multijet method

This is the last step of the in-situ calibration. The multijet balance allows the extension of the calibration to higher jet p_T. The Z/γ+jet methods are indeed statistically limited at high p_T. In the multijet balance technique, event with single isolated high p_T jet recoiling against a system of jets of lower p_T are selected. The recoil system is fully calibrated with the previous in-situ technics. This allows the calibration of higher jet p_T. The multijet balance is defined as:

$$R_{MJB} = \frac{p_T^{leadjet}}{p_T^{recoil}}. \tag{3.20}$$

The mean value of MJB is measured in both data and MC in bins of p_T^{recoil}. Since the leading jet is not calibrated by the previous methods, its energy is underestimated and the response is lower than one. The double ratio defined as:

$$\mathcal{R} = \frac{\langle R_{MJB}^{data} \rangle}{\langle R_{MJB}^{MC} \rangle}. \tag{3.21}$$

is used to eliminate the biases of the underlying event and estimate the deviations of the leading jet response in data with respect to the MC. Figure 3.10 shows the MJB and double ratio for jets using the EM+JES(in-situ) calibration approach. With 3.2fb^{-1}, jets can be calibrated from p_T = 300 GeV to 2 TeV.

3.9 Combination of the in-situ methods

The in-situ methods are combined to provide the final jet calibration and uncertainties. Each method is assigned a p_T dependence weight through a χ^2 minimization depending on the response ratio and the uncertainty. Two different calibrations have been applied for 2015 and 2016 data. Figure 3.11 (a) shows the weights used for the combination with 2015 data as a function of jet p_T. The Z+jet MPF method is used for the lowest jet p_T for a range between 20 GeV to 500 GeV. The γ+jet DB method is used from 36 GeV to 950 GeV while the multijet method from 300 GeV to 2 TeV. The calibration is dominated at low p_T jets by the Z+jet corrections until 65 GeV. This method is indeed more precise due to the decay of Z into $e^+e^-/\mu^+\mu^-$. From 65 GeV to approximatively 600 GeV, the γ+jet method is dominant. This is due to higher statistics for this method on this range and to the precise measurement of the photon p_T. From 600 GeV, the γ+jet statistical uncertainty increases significantly and the multijet method becomes dominant.

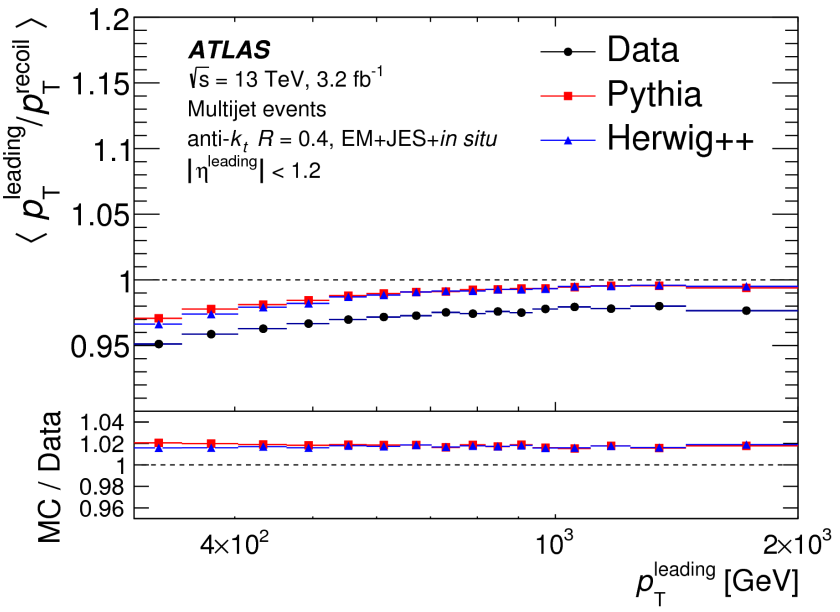

Figure 3.10: Average p_T response of the leading EM+JES jet, calibrated with the η-intercalibration, against the recoil system in multijet events as a function of $p_T^{leading}$. The Z/γ+jet calibrations have been applied only to sub-leading jets in the recoil system. The response is given for data and two distinct Monte Carlo generators. The Monte Carlo-to-data ratio is shown in the bottom of the Figure and reflects the derived in-situ correction [105].

Figure 3.11 (b) shows the $\sqrt{\chi^2/N_{dof}}$ distribution used the combination fit. Low values of $\sqrt{\chi^2/N_{dof}}$ indicate a good agreement between the in-situ methods. Below 36 GeV and above 950 GeV, the exclusive methods used for the calibration are respectively the Z+jet and multijet methods.

The final combination of Z+jet, γ+jet and multijet methods is shown in Figure 6.49 as a function of jet p_T for 2015 data (a) and 2016 data (b). The weights used for the 2015 calibration have been described in Figure 3.11. The higher statistics in 2016 data allowed the improvement of the calibration range and the decrease of statistical and total uncertainties of the in-situ methods. The Z+jet 2015 uncertainties are dominated by statistical errors. This method in 2016 have largely benefited from a higher statistics. An important point of the analyse is that the Monte Carlo generators used for Z+jet and γ+jet are differents. A future improvement in the in-situ calibrations would be to use the same Monte Carlo generators for the two methods, to have consistency in the combination and uncertainties estimations. The multijet uncertainties are dominated by uncertainties on Z/γ+jet calibrations since Z/γ+jet calibration are used to calibrate sub-leading jets for the multijet method.

The final 2015 and 2016 in-situ calibrations are shown in Figure 3.13. The 2015 calibration is illustrated with dark line, yellow band for statistical uncertainty and brown band for total uncertainty. The 2016 in-situ jet calibration is shown in dark line with blue band for statistical uncertainty green band for total uncertainty. Due to higher statistics in 2016 compared to 2015 with respectively 27 fb^{-1} and 3.2 fb^{-1}, the 2016 calibration range has been slightly improved at low and high jets p_T. The p_T correction is generally higher with 2016 except at low p_T. Investigation is still on-going to understand this effect. The good stability between 2015 and 2016 of the electron energy derived in Z events seems to exclude that this effect is due to a change of the LAr energy scale.

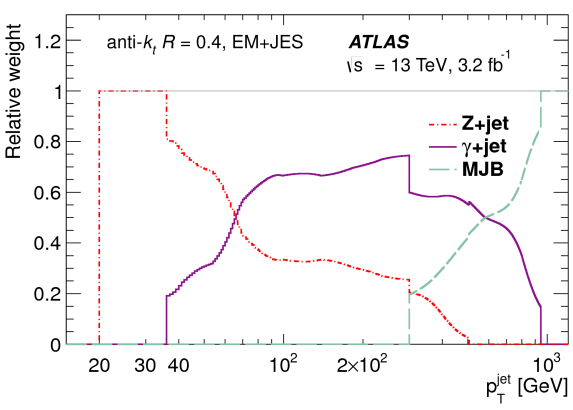

(a)

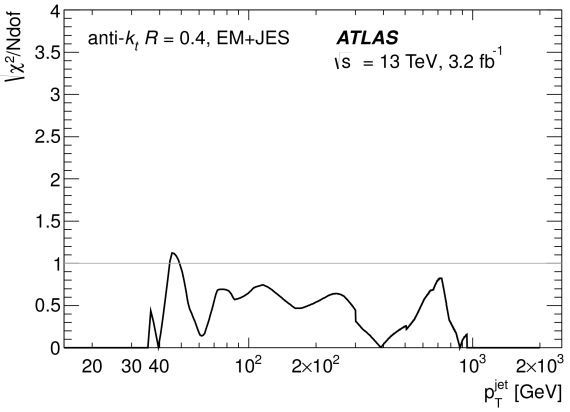

(b)

Figure 3.11: Relative weight assigned to Z+jet, γ+jet and multijet balance methods for the in-situ combination as a function of jet p_T (a). The weight are derived through a χ^2 minimization, accounting for statistical and systematic uncertainties. Figure (b) shows the $\sqrt{\chi^2/N_{dof}}$ distributions as a function of jet p_T from combination fit of the data-to-MC response ratio from the three in-situ methods. Z+jet events are used from 20 GeV to 500 GeV, γ+jet between 36 GeV and 950 GeV and multijet events from 300 GeV to 2 TeV. The low values of $\sqrt{\chi^2/N_{dof}}$ distribution indicate good agreement between the three in-situ techniques. The horizontal dotted line is drawn at unity to help guide the eye [105].

3.10 Systematic uncertainties

This section is related to the uncertainties of the jet calibration. Figure 3.14 shows the respective combined uncertainties for 2015 data jet calibration with respect to jet p_T (a) and η for p_T^{jet} = 80 GeV (b). The final jets uncertainties are represented in grey area. This uncertainty includes uncertainties on in-situ methods, flavor compositions and flavor responses, pile-up, and punch-through. The final jet uncertainty with respect to p_T (a) is dominated by in-situ uncertainties. At 20 GeV, the jet uncertainty is estimated to 4.5% and decreases with p_T to reach 1% at 150 GeV. From 100 GeV to 1 TeV, the uncertainty is reasonably flat. From 1 TeV to 2 TeV, the uncertainty increases due to multijet uncertainties. Above 2 TeV, uncertainties are computed with single particle response [134] and increase from 2% to 2.8%. Uncertainties as a function of η are reasonably constants for $|\eta| < 2.2$ (b) and reach a maximum of 2.5 % for the most forward jets. The pics between $2.2 < |\eta| < 2.6$ are due to non-closure uncertainty in the η-intercalibration.

Uncertainties on the 2016 calibration is shown in Figure 3.15 with respect to p_T (a) and to η (b) for p_T = 80 GeV. At 20 GeV, the total uncertainty is the same in 2015 and 2016 at the level of ∼4.5%. Uncertainties on the in-situ methods have been improved with more statistics, but pile-up effects are dominant below 160 GeV in 2016. The uncertainty decreases to 1% at 90 GeV and the minimum is reached at 200 GeV with 0.6 %. At higher p_T, the uncertainty slightly increases to 1.2% with multijet method. Above 2 TeV, the uncertainty sharply increases with single jet response.

The final calibration includes 80 systematic uncertainties terms propagated from each individual calibration. The majority (67) of these uncertainties are due to Z+jet, γ+jet and multijet insitu methods. All the systematic uncertainties are summarized in Table 3.1. The punch-through uncertainty corresponds to the uncertainty related to the energy deposited in the muon chamber by high p_T jets. The AFII non-closure uncertainty corresponds to the uncertainty on the modelling of fast simulation samples, which are used for example in the absolute MC-based calibration.

The list includes uncertainties on the Z+jet, γ+jet, multijet methods, η intercalibration, pile-up, jet

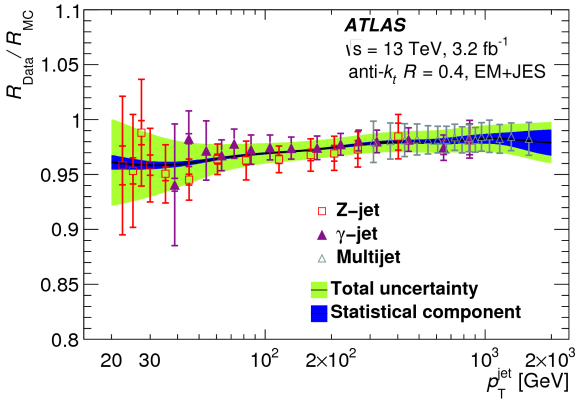

(a)

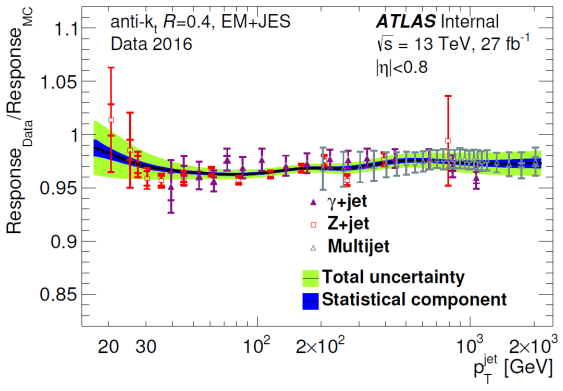

(b)

Figure 3.12: Ratio of EM+JES jet response in data to nominal Monte Carlo generator, as a function of jet p_T for γ+jet, Z+jet and multijet in-situ calibration. The final derived correction (black line), its statistical uncertainty (blue) and the total uncertainty band (green) are also shown. Figure (a) shows the in-situ calibrations using 2015 data (3.2 fb^{-1}) while Figure (b) shows the calibration with 2016 data (27.0 fb^{-1}) [133].

flavor and punch-through.

3.11 Conclusion

This chapter describes the various steps involved in the jet reconstruction and calibration. Many corrections are applied to obtain the fully calibrated jets. The first corrections are based on Monte Carlo simulations while the final corrections are based on data with in-situ methods. The in-situ methods are combined and provide the official corrections for 2015 [135] and 2016 [133] data. The combined uncertainty is computed and is included in all physics analysis using jets. The next chapter describes the γ+jet analysis developed for the Run2 during my Ph.D.

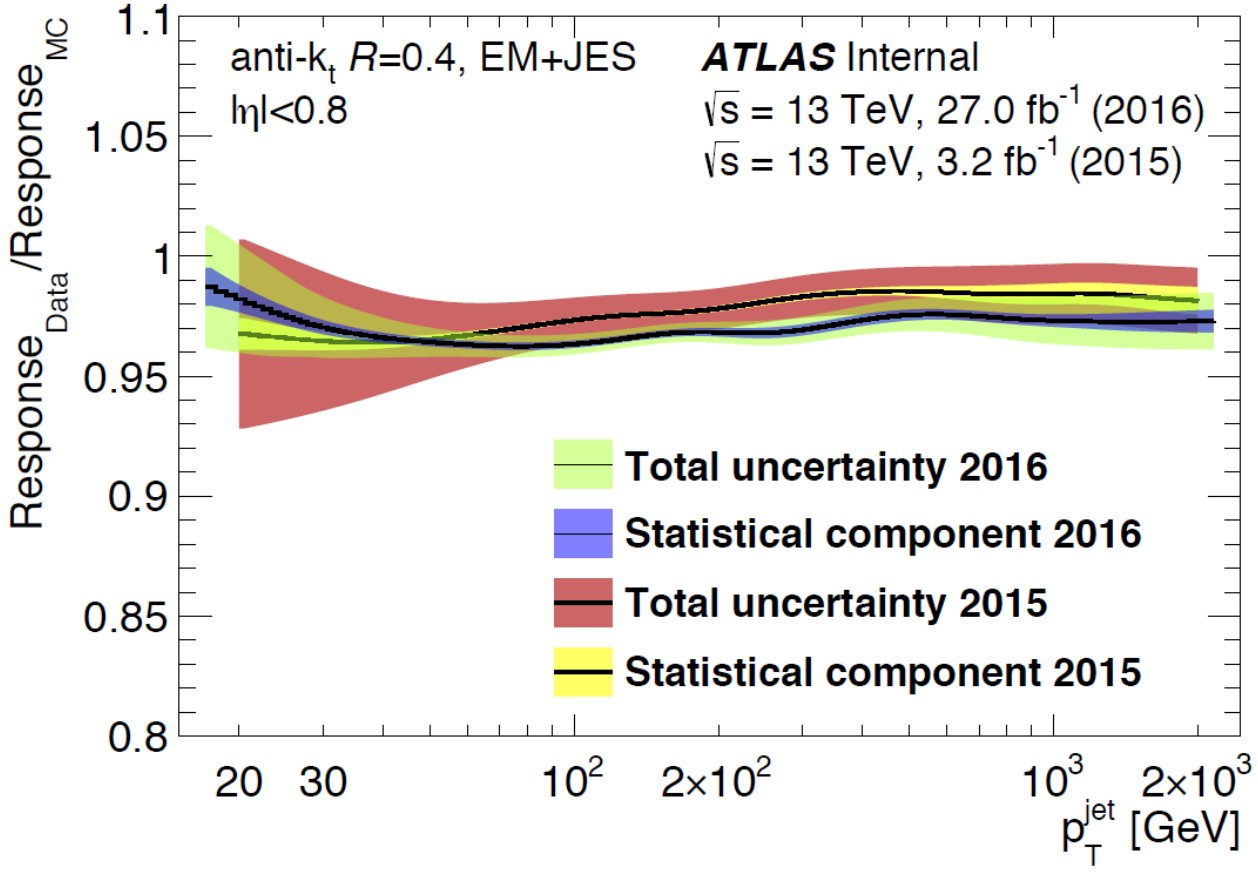

Figure 3.13: Combined jet response ratio of data to Monte Carlo simulation as a function of jet p_T for data from 2015 (brown band) and 2016 (light green band), performed by Z+jet, γ+jet and multijet analysis. Results are shown for anti-k_t with R = 0.4 calibrated with EM+JES scheme. The results of the in-situ combinations are shown in dark line. The outer band shows the total uncertainty from the combination while the inner band only shows the purely statistical component. The final calibration applies the 2015 central value for 2015 runs and the 2016 central value2016 runs [105].

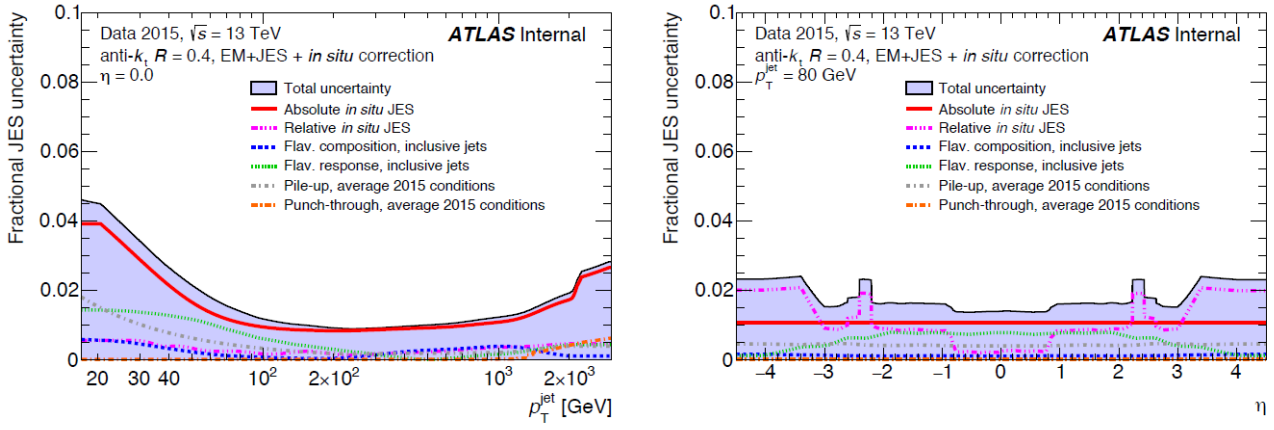

(a) (b)

Figure 3.14: Combined uncertainty in the JES of fully calibrated jets with 2015 data (3.2fb^{-1}) as a function of jet p_T at $\eta = 0$ (a) and η at $p_T = 80$ GeV (b). Systematics uncertainty components include pile-up, punch-through and uncertainties propagated from the Z/γ+jet and MJB (absolute in-situ JES) and η-intercalibration (relative in-situ JES). The flavor composition and response uncertainties assume a quark and gluon composition simulated by Pythia dijet Monte Carlo [105].

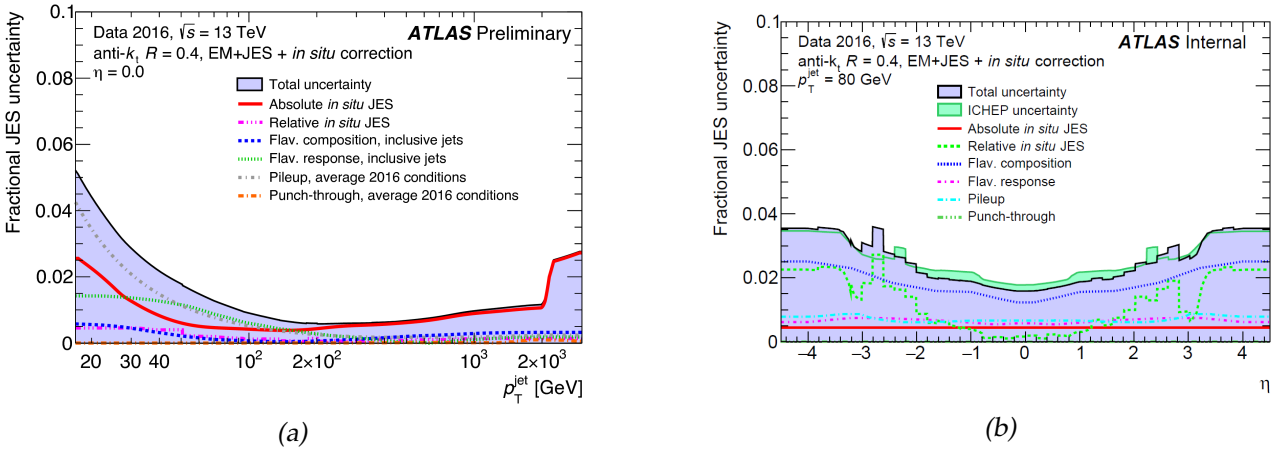

(a) *(b)*

Figure 3.15: Combined uncertainty in the JES of fully calibrated jets with 2016 data (27.0 fb^{-1}) as a function of jet p_T at $\eta = 0$ (a) and η at $p_T = 80$ GeV (b). Systematics uncertainty components include pile-up, punch-through and uncertainties propagated from the Z/γ+jet and MJB (absolute in-situ JES) and η-intercalibration (relative in-situ JES). The flavor composition and response uncertainties assume a quark and gluon composition simulated by Pythia dijet Monte Carlo.

Name	Description
Z–jet	
Electron scale	Uncertainty in the electron energy scale
Electron resolution	Uncertainty in the electron energy resolution
Muon scale	Uncertainty in the muon momentum scale
Muon resolution (ID)	Uncertainty in muon momentum resolution in the ID
Muon resolution (MS)	Uncertainty in muon momentum resolution in the MS
MC generator	Difference between MC generators
JVT	Jet vertex tagger uncertainty
$\Delta\phi$	Variation of $\Delta\phi$ between the jet and Z boson
2nd jet veto	Radiation suppression through second-jet veto
Out-of-cone	Contribution of particles outside the jet cone
Statistical	Statistical uncertainty over 13 regions of jet p_{T}
γ–jet	
Photon scale	Uncertainty in the photon energy scale
Photon resolution	Uncertainty in the photon energy resolution
MC generator	Difference between MC generators
JVT	Jet vertex tagger uncertainty
$\Delta\phi$	Variation of $\Delta\phi$ between the jet and γ
2nd jet veto	Radiation suppression through second-jet veto
Out-of-cone	Contribution of particles outside the jet cone
Photon purity	Purity of sample in γ–jet balance
Statistical	Statistical uncertainty over 15 regions of jet p_{T}
Multijet balance	
α^{MJB} selection	Angle between leading jet and recoil system
β^{MJB} selection	Angle between leading jet and closest subleading jet
MC generator	Difference between MC generators
$p_{\mathrm{T}}^{\mathrm{asymmetry}}$ selection	Second jet's p_{T} contribution to the recoil system
Jet p_{T} threshold	Jet p_{T} threshold
Statistical components	Statistical uncertainty over 16 regions of $p_{\mathrm{T}}^{\mathrm{leading}}$
η-intercalibration	
Physics mismodeling	Envelope of the MC, pile-up, and event topology variations
Non-closure	Non-closure of the method in the $2.0 < \lvert\eta_{\mathrm{det}}\rvert < 2.6$ region
Statistical component	Statistical uncertainty
Pile-up	
μ offset	Uncertainty of the μ modeling in MC simulation
N_{PV} offset	Uncertainty of the N_{PV} modeling in MC simulation
ρ topology	Uncertainty of the per-event p_{T} density modeling in MC simulation
p_{T} dependence	Uncertainty in the residual p_{T} dependence
Jet flavor	
Flavor composition	Uncertainty in the jet composition between quarks and gluons
Flavor response	Uncertainty in the jet response of gluon-initiated jets
b-jet	Uncertainty in the jet response of b-quark-initiated jets
Punch-through	Uncertainty in GSC punch-through correction
AFII non-closure	Difference in the absolute JES calibration using AFII
Single-particle response	High-p_{T} jet uncertainty from single-particle and test-beam measurements

Table 3.1: Summary of the systematic uncertainties on the JES. The uncertainties include those from Z+jet, γ+jet, multijet, η-intercalibration, pile-up, jet flavor, punch-through, AFII non-closure and single hadon response. These uncertainties are combined for the final JES uncertainty [105].

Chapter 4

Jet calibration with the in-situ γ+jet Direct Balance technique

"The only man who never makes a mistake is the man who never does anything. "

Theodore Roosevelt

Contents

4.1 Method

The γ+jet Direct Balance method [123] [136] is used to correct the jet p_T from data (section 3.8.2). The correction is applied after the η-intercalibration (section 3.8.1) and is one of the last steps of the jet reconstruction and calibration (Figure 3.1). The method uses the independent measurement of the photon p_T as a reference for jet p_T. Ideally, with a perfect detector measurement and assuming the jet cone includes all the particles recoiling against the photon, the jet and the photon have the same p_T. However, this measurement is affected by:

- the uncertainties on the p_T measurement of the jet and the photon,
- additional parton radiations (sub-leading jets),
- contributions from underlying events and pile-up.

To reduce the contributions from additional parton radiations, the variable p_T^{ref} is used and is defined as:

$$p_T^{ref} = p_T^{Z/\gamma} \times |\cos \Delta\phi(jet, Z/\gamma)|, \tag{4.1}$$

with $\Delta\phi(jet, Z/\gamma)$, the azimuthal angle between jet and Z/γ. The variable p_T^{ref} allows to ignore the fraction of the boson p_T perpendicular to the jet axis. The balance is defined by:

$$\mathcal{B} = \frac{p_T^{leadingjet}}{p_T^{ref}}. \tag{4.2}$$

The balance is proportional to the jet response of the detector and it is lower than one since all the particles from the initial parton hadronisation are not included in the jet cone. The balance is studied in bins of p_T^{ref}. In each bin, the balance distribution is fitted with a Gaussian function, and the mean is used for the balance. Only jets with p_T > 7 GeV are kept after the reconstruction stage where only the primary vertex correction is applied. Therefore, after the absolute MC-based calibration, there is no jets lower than 15 GeV. The jet energy response was illustrated in Figure 3.6 (a) for jets above 30 GeV. The width of the distribution is used to compute the jet energy resolution as described in the chapter 5.

4.2 Event selection

4.2.1 Trigger selection

Due to the huge amount of information originating from collisions (∼30 MHz), only a fraction can be recorded and stored(∼1 kHz). Specific triggers have been added to select events as a function of the leading photon p_T. For low p_T photons, events are kept randomly with a specific rate depending on the trigger (prescaled triggers). Above a certain p_T^{γ}, all events are recorded (un-prescaled trigger). The p_T threshold has been fixed to 120 GeV for 2015, and 140 GeV for 2016 data. The list of triggers used in 2015 and 2016 is shown in Table 4.1. The second column shows the associated bins in p_T^{ref}. To reach 100% trigger efficiency, the lower p_T bin associated to each trigger is fixed 5 GeV above the trigger p_T. Since the γ+jet calibration starts at 40 GeV, the two first triggers are not used. The first bin starts at 40 GeV, and is triggered by HLT_g35_loose_L1EM15. From 140 GeV (120 GeV with 2015 data), the bins have been defined to get enough events in each bin.

Table 4.1: List of triggers used in 2015 and 2016 and corresponding bins in p_T^{ref}.

Trigger	Binning
HLT_g20_loose_L1EM12	25 GeV < p_T^{ref} < 30 GeV
HLT_g25_loose_L1EM15	30 GeV < p_T^{ref} < 35 GeV
HLT_g35_loose_L1EM15	40 GeV < p_T^{ref} < 45 GeV
HLT_g40_loose_L1EM15	45 GeV < p_T^{ref} < 50 GeV
HLT_g45_loose_L1EM15	50 GeV < p_T^{ref} < 55 GeV
HLT_g50_loose_L1EM15	55 GeV < p_T^{ref} < 65 GeV
HLT_g60_loose	65 GeV < p_T^{ref} < 75 GeV
HLT_g70_loose	75 GeV < p_T^{ref} < 85 GeV
HLT_g80_loose	85 GeV < p_T^{ref} < 105 GeV
HLT_g100_loose	105 GeV < p_T^{ref} < 125 GeV
HLT_g120_loose	125 GeV < p_T^{ref} < 160 GeV
HLT_g140_loose (2016 only)	125 GeV < p_T^{ref} < 160 GeV
//	160 GeV < p_T^{ref} < 210 GeV
//	210 GeV < p_T^{ref} < 260 GeV
//	260 GeV < p_T^{ref} < 310 GeV
//	310 GeV < p_T^{ref} < 400 GeV
//	400 GeV < p_T^{ref} < 600 GeV
//	600 GeV < p_T^{ref} < 800 GeV
//	800 GeV < p_T^{ref} < 1000 GeV
//	1000 GeV < p_T^{ref} < 1500 GeV (2016 only)

Table 4.2: Photon selections in the γ+jet Direct Balance method.

	Photon selections:
1	Tight photon identification
2	$p_T^\gamma > 25$ GeV
3	$\|\eta^\gamma\| < 1.37$
4	Isolation selections

4.2.2 Photon selection

A tight photon identification criteria is applied to reject jets mis-reconstructed as photons. A selection on the photon transverse momentum of 25 GeV is applied. This selection is imposed by the trigger with the lower p_T threshold. Events with photons emitted in the barrel regions of the calorimeter are selected ($|\eta| < 1.37$). A selection is applied on isolation to reject background such as π^0. The π^0 usually decay into two photons that are very close and can be reconstructed as one photon. The isolation selection is applied to the clusters track energy density, and depends whether photons convert or not into e^-/e^+ in the inner detector (converted photons). The selections to reject events with converted leading photons are the following:

- if one or two tracks are reconstructed, $\frac{E_T^{cluster}}{p_T^{tracks}} > 2$,
- else $\frac{E_T^{cluster}}{p_T^{tracks}} < 0.5$ or $\frac{E_T^{cluster}}{p_T^{tracks}} > 1.5$.

A calorimetric isolation discriminator E_T^{cone} is computed from the reconstructed transverse energy around the photon candidate, where the pile-up and the photon energy are excluded. In addition, a tracking-based discriminator p_T^{cone} based on tracks energy is used. The two quantities are computed inside a cone around the photon that needs to be optimized. The recommended isolation working point "FixedCutTight" has been applied, and the following cones size R = 0.2 and R = 0.4 are used to compute E_T^{cone} and p_T^{cone}. The selection is defined as $E_T^{cone40} < 0.022 \times p_T^\gamma + 2.45$, and $\frac{p_T^{cone20}}{p_T^\gamma} < 0.05$. Photon selections criteria are summarized in Table 4.2.

4.2.3 Jet selection

A jet cleaning [137] is applied to reject jets not associated with real energy deposit in the calorimeter. The jets are selected in the central region of the calorimeter: $|\eta^{jet}| < 0.8$. A leading jet p_T^{jet} threshold of 20 GeV is applied. The suppression of pile-up jets is applied using a variable called the jet-vertex-tagger (JVT) [138]. This variable is reconstructed from the tracks p_T associated with the jet and originating from the hard scatter vertex, and from the pile-up information. A value of JVT = -0.1 is assigned to jets with no associated tracks. A selection of JVT > 0.59 is applied for $p_T^{jet} < 60$ GeV and $|\eta| < 2.4$ to limit pile-up effects. Jet selections criteria are summarized in Table 4.3.

4.2.4 Topological selection

Two selections are applied. First, a selection on the sub-leading jet p_T to limit the impact of the QCD radiations on the event topology. The value of the cut is a compromise between limiting bias, and limiting statistical uncertainty. The nominal cut has been fixed to 15 GeV for low p_T jets and

Table 4.3: Jet selections in the γ+jet Direct Balance method.

	Jet selections:
1	Jet cleaning
2	$\mid \eta^{jet1} \mid < 0.8$
3	$p_T^{jet} > 20$ GeV
4	JVT > 0.59 if $p_T^{jet} < 60$ GeV and $\mid \eta \mid < 2.4$

$0.1 \times p_T^{\gamma}$ for higher p_T jets. The selection has been defined as $p_T^{jet2} <$ max(15 GeV, $0.1 \times p_T^{ref}$). The second topological selection is applied on the angle $\Delta\phi$ between the leading jet direction and the photon direction to select events with photon and leading-jet back-to-back. This angle should be close to π, but as for selection on sub-leading jet p_T, the value of the cut is a compromise between limiting bias, and limiting statistical uncertainty. The selection has been fixed to $\Delta\phi > 2.8$.

4.3 Fit procedure and distributions

The balance is estimated for each bin with iterative Gaussian fits applied on selected events. The function is initially fitted on range [μ-2σ, μ+2σ], where μ corresponds to the mean of the balance distribution, and σ corresponds to the Root Mean Square of the balance distribution. The fit is performed with 15 iterations. Each iteration updates the mean and RMS using the mean and width of the Gaussian distribution. The p_T threshold at reconstruction level affects the tail of the balance distribution. This threshold affects differently data and MC and specific ranges have been defined below 55 GeV to improve the fits. For the simulation, the ranges [μ - 0.7 σ, μ + 1.3 σ] and [μ - 0.6 σ, μ + 1.3 σ] have been chosen for the bins 40 < p_T^{ref} < 45 and 45 < p_T^{ref} < 55. For the data, the range [μ - 0.7 σ, μ + 1.4 σ] and [μ - 0.6 σ, μ + 1.3 σ] have been chosen for the same bins. The balance distributions are shown in Figures 4.1 and 4.2 using 2016 data and Pythia8 [129], for four different p_T bins. Below 55 GeV, the left side of the distributions is biased, and a rebinning has been performed to improve the fit. Above 55 GeV, the range of the fit has been fixed to [μ - 2σ, μ + 2σ] for each bin. The distributions in the other bins are shown in appendix .1.

4.4 X-axis mapping

The x-axis mapping procedure is a method to scale x-axis from p_T^{ref} to p_T^{jet}. Since triggers depend on p_T^{γ}, the distributions have been performed as a function of p_T^{ref} instead of p_T^{jet}. However, the final calibration must be computed as a function of p_T^{jet}. Thus, after the estimation of the corrections in each p_T^{ref} bin, p_T^{ref} is projected over p_T^{jet} in each bin, and the mean of the projection is taken as the mapped value. The x-axis mapping has been applied for both 2015 and 2016 data. The values after the mapping are those used in Figure 6.49.

Each lower value of the p_T^{ref} bins has been scaled with the factor $p_T^{jet}/p_T^{bin-center}$. This choice fixed the minimum value of the calibration range. The maximum of the calibration could not be fixed with this method due to low statistics in the overflow. Then, the last upper bin has been scaled with the same scale factor to fix the maximum. The 2015 and 2016 γ+jet calibrations have been defined respectively on the p_T^{jet} ranges of [36 GeV, 950 GeV] and [37 GeV, 1280 GeV].

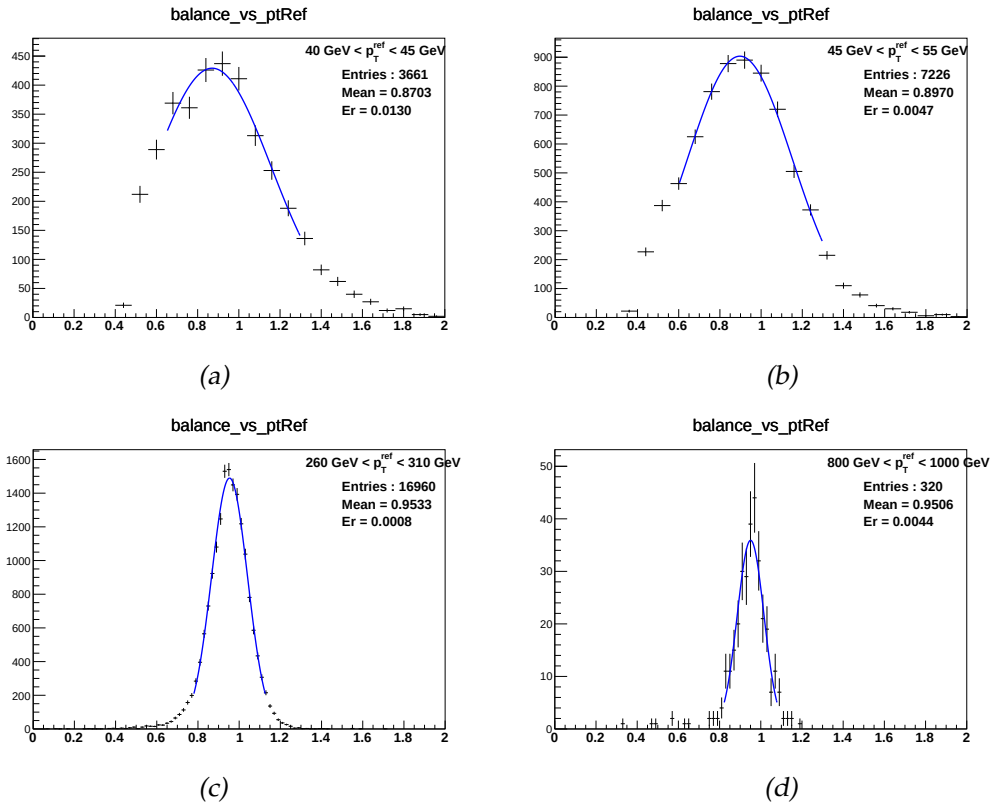

Figure 4.1: Distributions of p_T^{jet}/p_T^{ref} in different bins in p_T for EM jets calibrated up to the η-intercalibration, and using the 2016 data at $\sqrt{s}$ = 13 TeV. Jets are selected in the central region of the calorimeter: $|\eta| < 0.8$. Below 55 GeV, the Gaussian fit (blue line) has been performed using specific ranges due to bias in the left part of the distribution. Above 55 GeV, the fit range has been fixed to mean $\pm$ 2 σ for all bins.

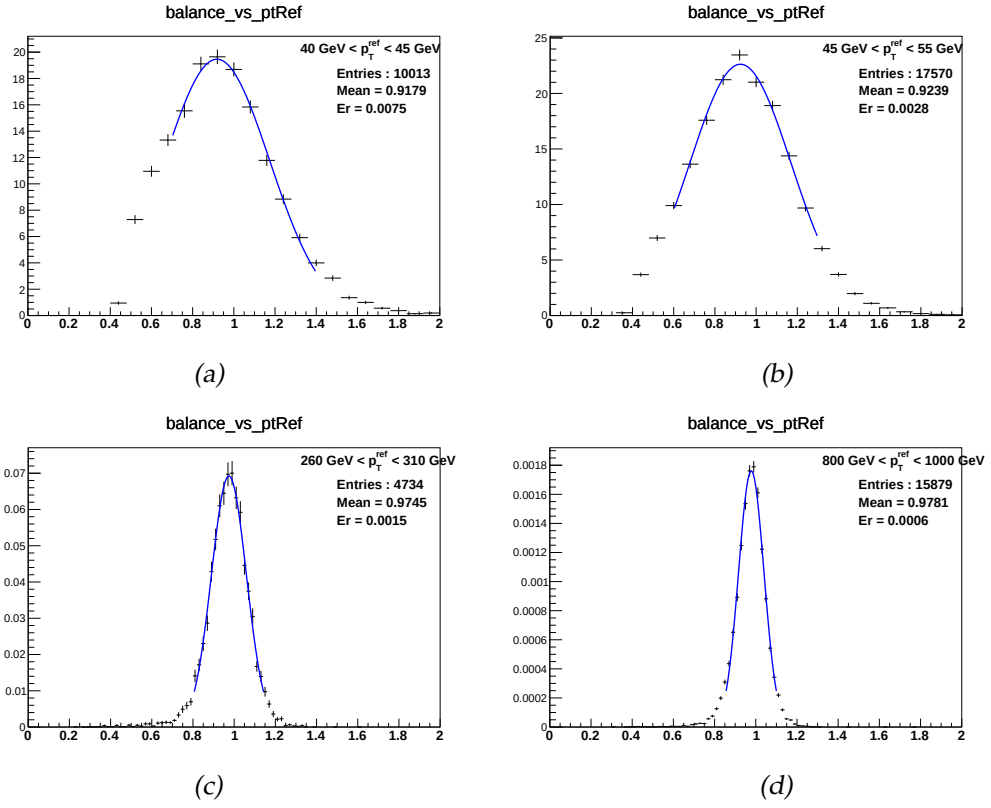

Figure 4.2: Distributions of p_T^{jet}/p_T^{ref} in different bins in p_T for EM jets calibrated up to η-intercalibration using Pythia8. Jets are selected in the central region of the calorimeter: $|\eta| < 0.8$. Below 55 GeV, the Gaussian fit (blue line) has been performed using specific ranges due to bias in the left part of the distribution. Above 55 GeV, the fit range has been fixed to mean $\pm$ 2 σ for all bin.

4.5 Central values of the γ+jet method

4.5.1 Balance vs p_T

The balance mean is estimated in each p_T^{ref} bin from 40 GeV to 1.5 TeV for data and MC. The nominal Monte Carlo used for the calibration is Pythia8 while Sherpa2.2 [130] [139] is used to compute the uncertainties on the generator. Figure 4.3 shows the balance as a function of p_T^{ref} for EM jets calibrated up to η-intercalibration, using 2015 data on the left and 2016 data on the right. These values are those used for the 2015 and 2016 in-situ combination in Figure 6.49. The upper part shows the balance as a function of p_T^{jet} for Pythia8 and Sherpa. Since the out-of-cone energy is not corrected, the balance value is lower than one for both data and MC. The data response is underestimated by the nominal generator Pythia8 in all bins, except the last one in 2015, which suffers from low statistics in data. The bottom part of the plot shows the Monte Carlo to data ratio. With 2015 data, a shift of 3% is seen between data and Pythia8 below 100 GeV (6% for the first bin), and the shift is at the level of 2% above 100 GeV. With 2016 data, the shift between data and Pythia8 is at the level of ∼5% below 100 GeV, and 3% above 100 GeV. The balance as a function of p_T^{jet} with EM jets, and using the 2015 data can be found in the 2015 JES paper [140].

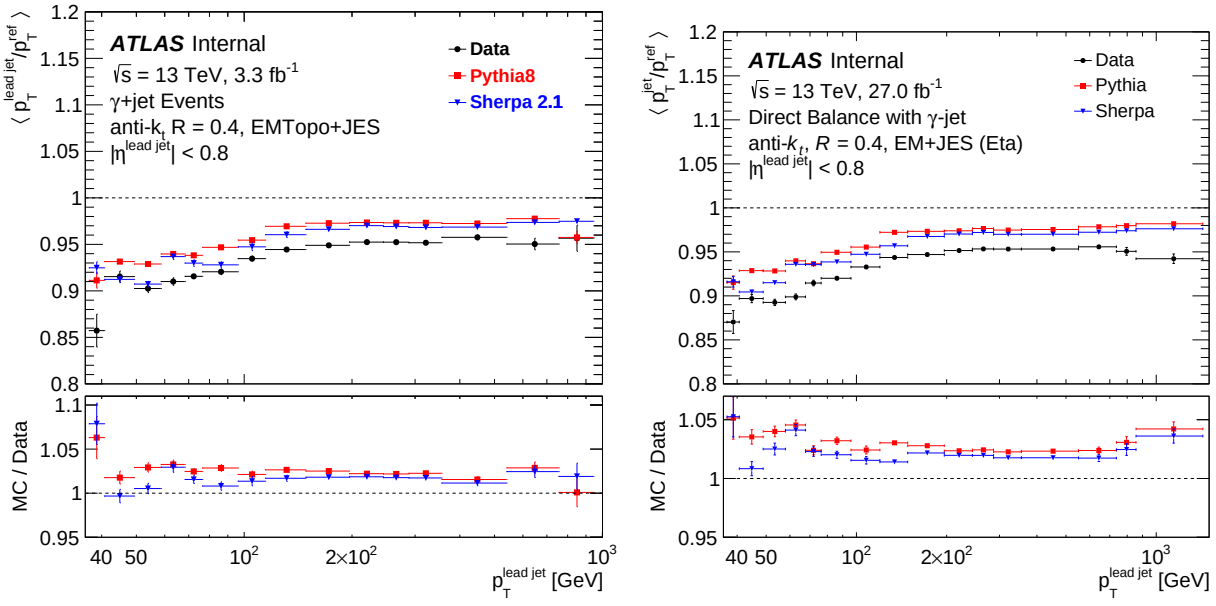

Figure 4.3: Ratio $\left\langle p_T^{jet}/p_T^{ref} \right\rangle$ for EM+JES jets calibrated up to η-intercalibration, using the γ+jet Direct Balance technique, as a function of p_T^{jet} for both data and MC. On the left, the balance is shown using the 2015 data, while on the right 2016 data is used. Pythia8 is represented by red squares, Sherpa by blue triangles while data is represented by the circles. Jets are selected in the central region of the hadronic calorimeter $|\eta^{jet}| < 0.8$. Error bars indicate the statistical uncertainties.

The balance as a function of p_T^{jet} for LC jets is shown in Figure 4.4 with 2015 data on the left, and 2016 data on the right. The results are very similar to those of EM jets. With 2015 data, the agreement between data and Pythia8 is within 3% below 100 GeV (6% for the first bin), and 2% above 100 GeV. With 2016 data, the agreement is at the level of ∼5% below 100 GeV, and 3% above 100 GeV.

The balance as a function of p_T^{jet} using 2016 data with EMPFlow [117] jets is shown is Figure 4.5. Similar results are obtained. The agreement between data and Pythia8 is at the level of 4% below 70

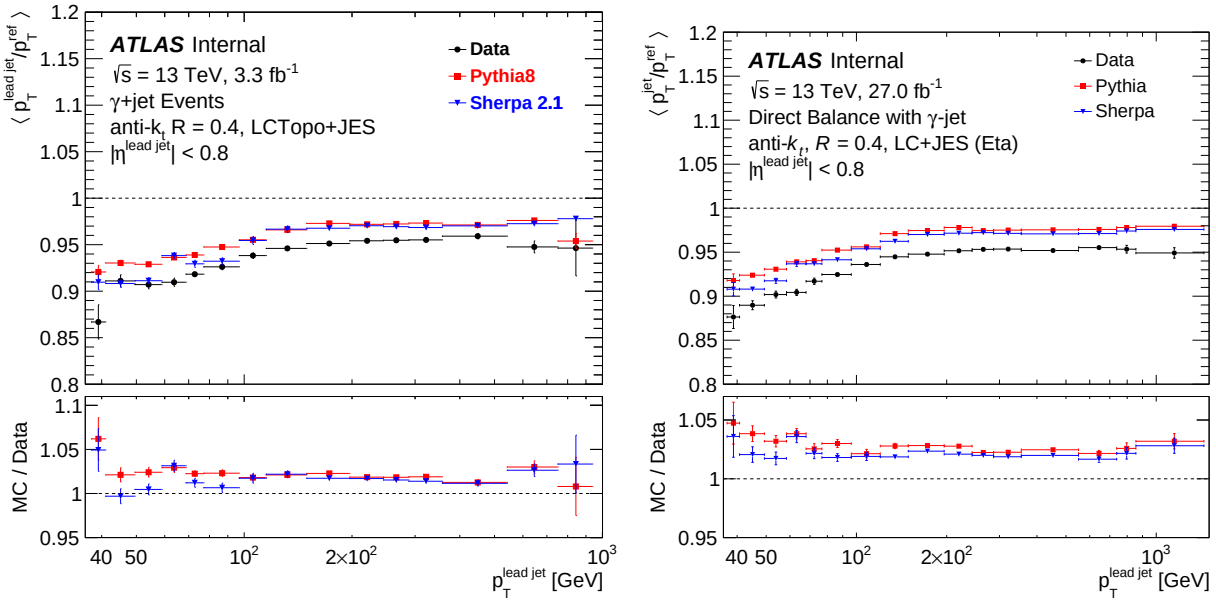

Figure 4.4: Ratio $\left\langle p_T^{jet}/p_T^{ref} \right\rangle$ for LC+JES jets calibrated up to η-intercalibration, using the γ+jet Direct Balance technique, as a function of p_T^{jet} for both data and MC. On the left, the balance is shown using the 2015 data, while on the right 2016 data is used. Pythia8 is represented by red squares, Sherpa by blue triangles while data is represented by the circles. Jets are selected in the central region of the hadronic calorimeter $|\eta^{leadjet}| < 0.8$. Error bars indicate the statistical uncertainties.

GeV, and 3% above 70 GeV.

The comparison between 2015 and 2016 balances is shown in Figure 4.6 for EM jets (left), and LC jets (right). An agreement of ∼1% between 2015 and 2016 data is observed. This difference can be explained by changes in Tile calorimeter between 2015 and 2016. The comparison of the ratio Pythia8 over 2016 data, between EM, LC and EMPFlow jets as a function of p_T^{jet} is shown in Figure 4.7. A very good agreement, at the level of ∼1-2% is seen between EM, LC and EMPFlow jets.

The in-situ corrections have been derived separately with 2015 and 2016 data for EM (Figure 4.3), LC (Figure 4.4), and EMPFlow (Figure 4.5) jets. A difference at the level of ∼1% is seen with the balance between 2015 and 2016 data for EM and LC jets (figure 4.6). Below 100 GeV, the correction is at the level of ∼3-5% (6% for the first bin with EM and LC jets). Above 100 GeV, the MC-to-data agreement is at the level of ∼2-3%. The larger amount of data collected in 2016 allowed the increase of the calibration range with γ+jet DB method. A very good agreement is seen between the ratio MC-to-data for EM, LC and EMPFlow jets (4.7). The corrections estimated with the method are combined with Z+jet and multijet method for the final calibration. The combination of the methods is shown for EM jets in Figures 6.49, and 3.13.

4.5.2 Balance vs η

The balance as a function of η is shown in Figure 4.8 for EM (left) and LC (right) jets calibrated up to the η-intercalibration. The central values are computed with 2015 and 2016 data, and with Pythia8 and Sherpa2.2. The bottom part shows the MC-to-data ratio with Pythia8 and Sherpa2.2, and the ratio between 2015 and 2016 data (pink). The results with EMPFlow using 2016 data is shown in Figure

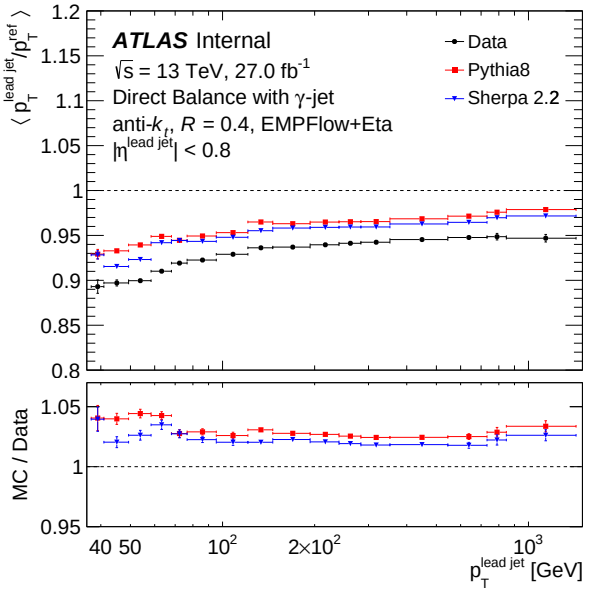

Figure 4.5: Ratio $\left\langle p_T^{jet}/p_T^{ref} \right\rangle$ for EMPFlow+JES jets calibrated up to η-intercalibration, using the γ+jet Direct Balance technique, as a function of p_T^{jet} for 2016 data and MC. Pythia8 is represented by red squares, Sherpa by blue triangles while data is represented by the circles. Jets are selected in the central region of the hadronic calorimeter $|\eta^{leadjet}| < 0.8$. Error bars indicate the statistical uncertainties.

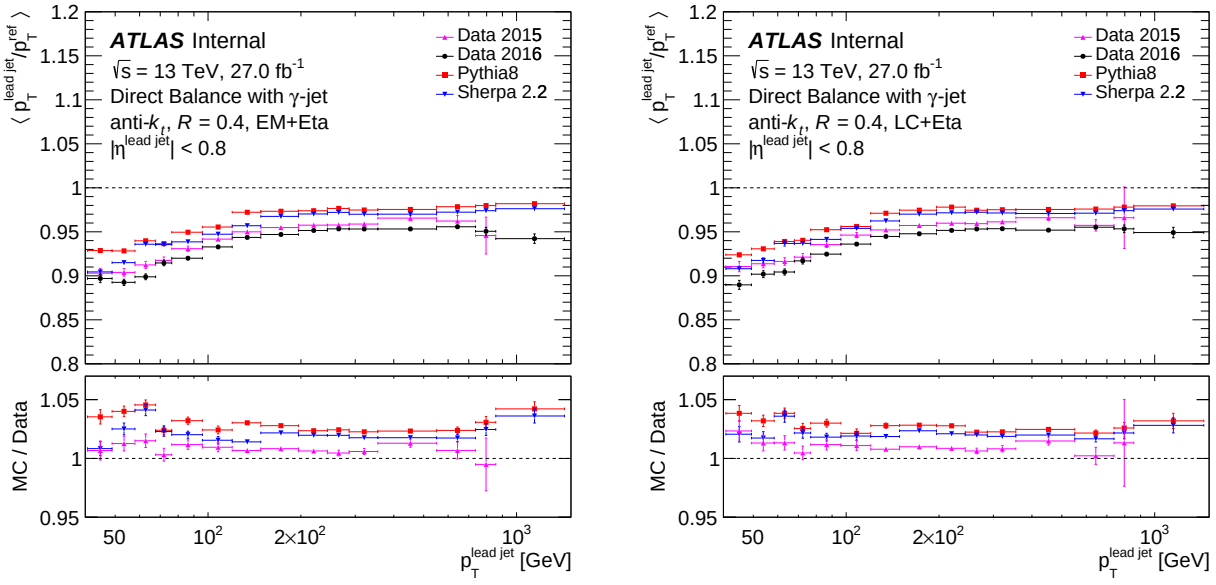

Figure 4.6: The ratio $\left\langle p_T^{jet}/p_T^{ref} \right\rangle$ as a function of p_T^{jet} for EM+JES jets (left) and LC+JES jets (right) calibrated up to the η-intercalibration, using the γ+jet Direct Balance technique. The central values of the balance are computed with 2015 data (up triangles in pink), 2016 data (black circles), nominal Monte Carlo generator Pythia8 (red squares), and the generator Sherpa2.2 (down triangles in blue). The bottom parts of the plots show the MC-to-data ratio with Pythia8 (red squares) and Sherpa2.2 (blue down triangles). The pink up triangles show the ratios of 2015 data over 2016 data. Error bars indicate the statistical uncertainties.

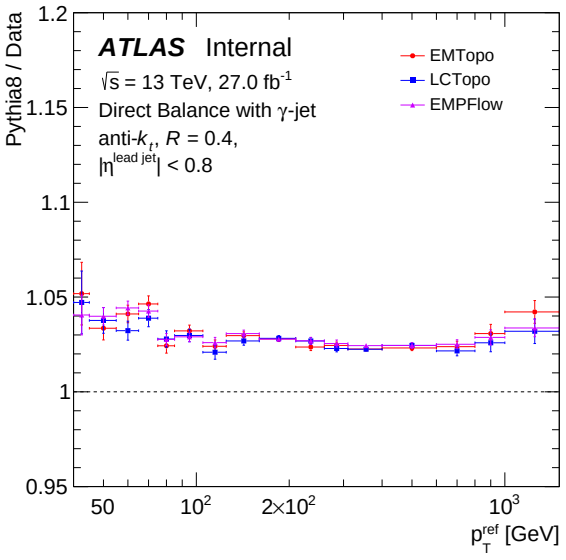

Figure 4.7: Comparison of the in-situ corrections with 2016 data for EM, LC and EMPFlow jets as a function of p_T^{ref} using the γ+jet Direct Balance technique. The corrections are derived from the ratio of the balance $\left\langle p_T^{jet}/p_T^{ref} \right\rangle$ between Pythia8 and data. EM jets are represented with red circles, LC jets with blue squares, and EMPFlow jets with purple triangles. Error bars indicate the statistical uncertainties.

4.9. The comparison between EM, LC and EMPFlow is shown in Figure 4.12 (left). The MC-to-data ratio is flat at the level of 1%, and corresponds to a cross-check for the η-intercalibration.

4.5.3 Balance vs ϕ

Figure 4.10 shows the balance as a function of ϕ with 2015 and 2016 data for EM jets (left) and LC jets (right). The ratio of the balance between 2015 and 2016 data is shown in pink on the bottom of the plots. A difference at the level of 1% in the jet response is observed between 2015 and 2016 data for both EM and LC jets. The results with EMPFlow jets using 2016 data is presented in Figure 4.11. An agreement at the level of 3-4% is seen between data and Pythia8. The comparison between EM, LC, and EMPFlow jets with 2016 data as shown in Figure 4.12 (right). A very good agreement at the level of 1% is seen.

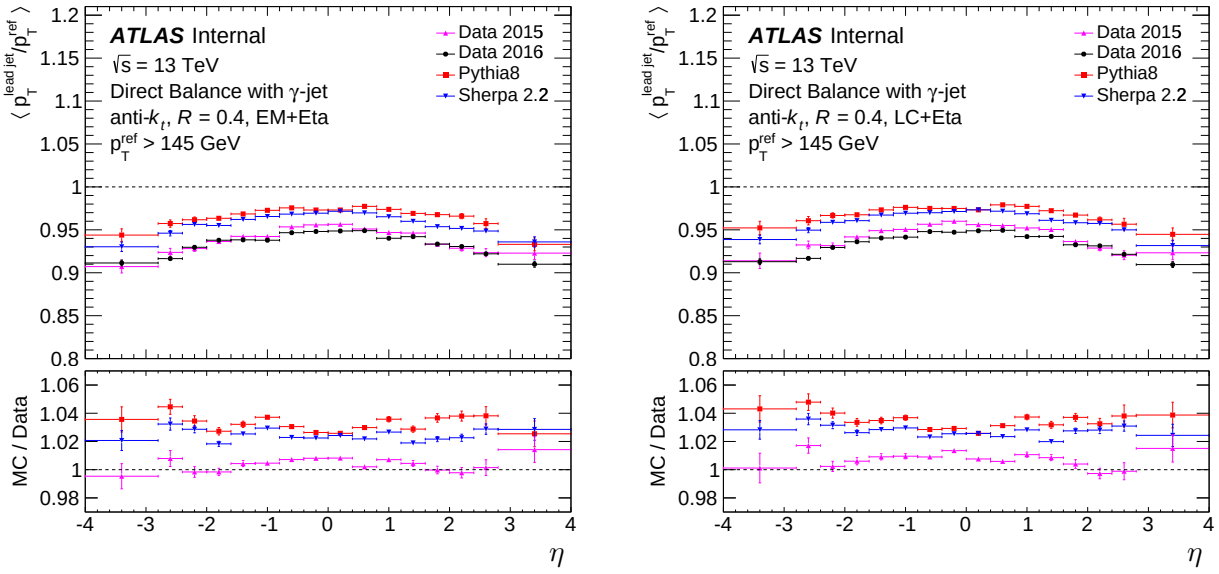

Figure 4.8: The ratio $\left\langle p_T^{jet}/p_T^{ref} \right\rangle$ for EM+JES (left) and LC+JES (right) jets calibrated up to the η-intercalibration, using the γ+jet Direct Balance technique, as a function of η. The balances are computed with 2015 data (up triangles in pink), 2016 data (black circles), nominal Monte Carlo generator Pythia8 (red squares), and Sherpa2.2 (down triangles in blue). The bottom part shows the MC-to-data ratio with Pythia8 (red squares) and Sherpa2.2 (blue down triangles). The pink up triangles show the ratios between 2015 and 2016 data. Error bars indicate the statistical uncertainties.

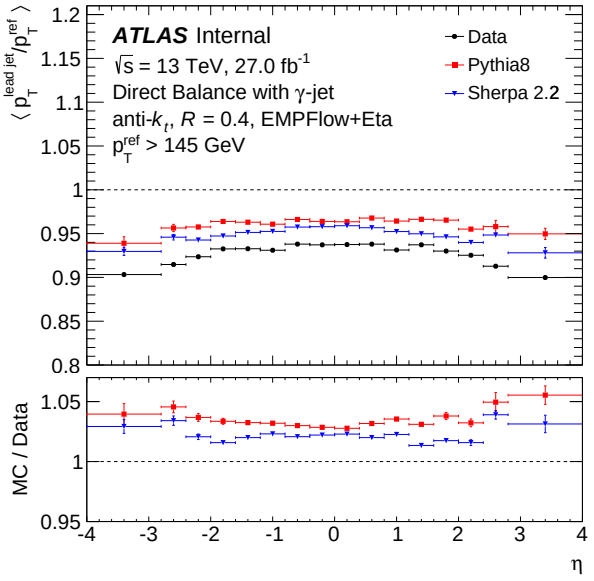

Figure 4.9: The ratio $\left\langle p_T^{jet}/p_T^{ref} \right\rangle$ for EMPFlow+JES calibrated up to the η-intercalibration, using the γ+jet Direct Balance technique, as a function of η. The balances are computed with 2016 data (black circles), nominal Monte Carlo generator Pythia8 (red squares), and Sherpa2.2 (down triangles in blue). Events are selected with $p_T > 145$ GeV. The bottom parts of the plots show the Monte Carlo to data ratio with Pythia8 (red squares) and Sherpa2.2 (blue down triangles). Error bars indicate the statistical uncertainties.

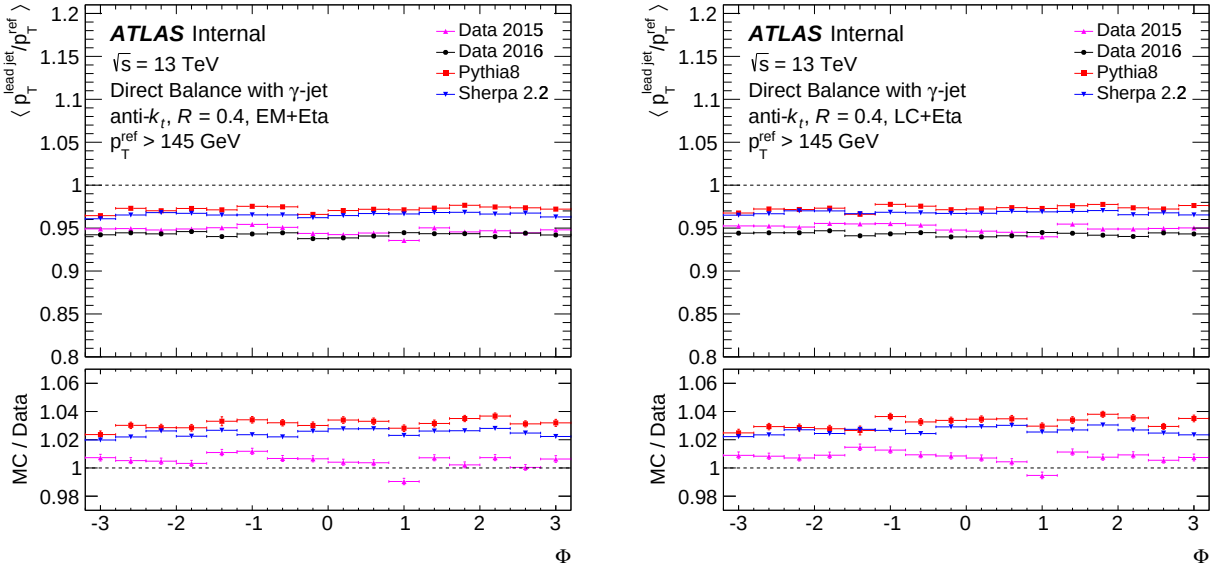

Figure 4.10: The ratio $\left\langle p_T^{jet}/p_T^{ref} \right\rangle$ for EM+JES (left) and LC+JES (right) jets calibrated up to the η-intercalibration, using the γ+jet Direct Balance technique, as a function of ϕ. The balances are computed with 2015 data (up triangles in pink), 2016 data (black circles), nominal Monte Carlo generator Pythia8 (red squares), and Sherpa2.2 (down triangles in blue). The bottom part shows the MC-to-data ratio with Pythia8 (red squares) and Sherpa2.2 (blue down triangles). The pink up triangles show the ratios between 2015 and 2016 data. Error bars indicate the statistical uncertainties.

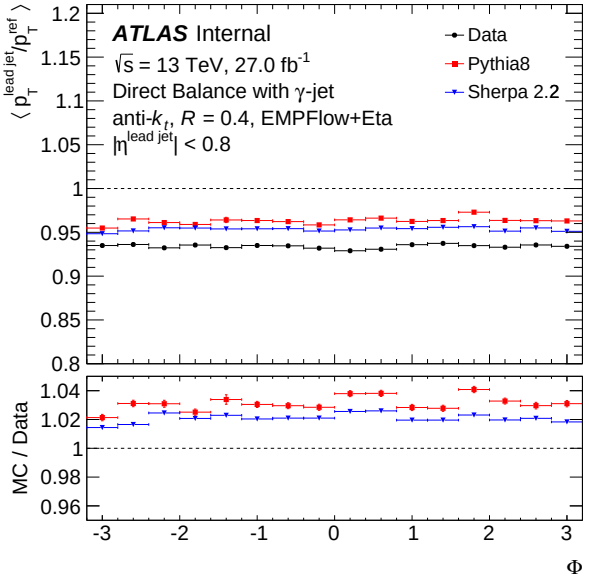

Figure 4.11: The ratio $\left\langle p_T^{jet}/p_T^{ref} \right\rangle$ for EMPFlow+JES calibrated up to the η-intercalibration, using the γ+jet Direct Balance technique, as a function of ϕ. The balances are computed with 2016 data (black circles), nominal Monte Carlo generator Pythia8 (red squares), and Sherpa2.2 (down triangles in blue). Events are selected with p_T > 145 GeV. The bottom parts of the plots show the Monte Carlo to data ratio with Pythia8 (red squares) and Sherpa2.2 (blue down triangles). Error bars indicate the statistical uncertainties.

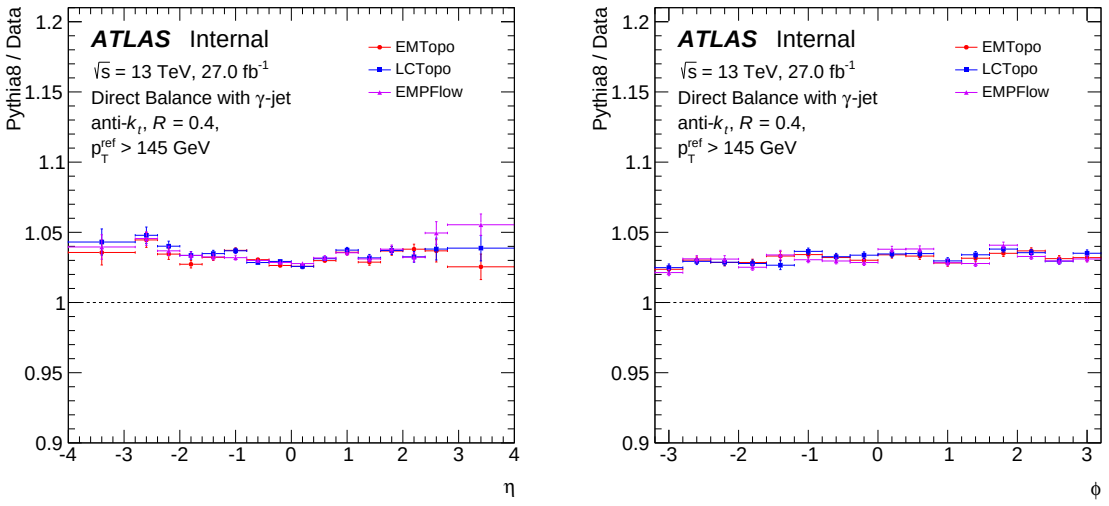

Figure 4.12: Comparison of the in-situ corrections with 2016 data for EM, LC and EMPFlow jets as a function of η (left) and ϕ (right) using the γ+jet Direct Balance technique. The corrections are derived from the ratio of the balance $\left\langle p_T^{jet}/p_T^{ref} \right\rangle$ between Pythia8 and data. EM jets are represented with red circles, LC jets with blue squares, and EMPFlow jets with purple triangles. Error bars indicate the statistical uncertainties.

4.6 Systematic uncertainties

4.6.1 Modelling uncertainty

The nominal event generator used for the γ+jet Direct Balance method is Pythia8. The uncertainty on the generator is estimated by comparing Pythia8 with Sherpa. The data to Monte Carlo ratio is computed for both Monte Carlo and the relative difference between the ratios is used as the Monte Carlo uncertainty. This is one of the dominant uncertainties of the γ+jet in-situ calibration.

4.6.2 Photon energy and resolution

The uncertainties on the photon energy scale (PES) and the photon energy resolution (PER) are provided by the EGamma performance group. These errors are propagated to the data to Monte Carlo ratio. The relative differences with the nominal data to Monte Carlo ratio are used as PES and PER uncertainties. The uncertainties on PES are dominant for jets with very high p_T.

4.6.3 Sub-leading jet p_T

The choice of the sub-leading jet p_T selection is a compromise between topology and statistics. The nominal cut has been fixed to 15 GeV for low p_T jets and $0.1 \times p_T^{\gamma}$ for higher p_T jets. The uncertainty on this selection is estimated by changing the values of the selections to 10 GeV and $0.05 \times p_T^{\gamma}$ for tighter selection and 20 GeV and $0.15 \times p_T^{\gamma}$ for looser selection (Table 4.4). The balance computed with loose and tight selections is propagated to the data to Monte Carlo ratio. The absolute difference with the nominal selection is computed for loose ans tight selections.

Table 4.4: Selections applied to estimate the uncertainty on sub-leading jet p_T.

Sub-leading jet p_T cut:	
Low value	max(10 GeV, 0.05 $\times p_T^{ref}$)
Nominal value	max(15 GeV, 0.1 $\times p_T^{ref}$)
High value	max(20 GeV, 0.15 $\times p_T^{ref}$)

Table 4.5: Selections applied to estimate the uncertainty on $\Delta\phi$.

$\Delta\phi$ cut:	
Low value	2.7
Nominal value	2.8
High value	2.9

4.6.4 $\Delta\phi$ angle

The uncertainty on the topological angle $\Delta\phi$ between the leading jet and the photon is computed with the same method as for the sub-leading jet p_T. The value of the $\Delta\phi$ cut must be close to π to select events with γ and jet in the same and opposite direction, but with a statistical constraint. The nominal selection has been fixed to 2.8. The uncertainty on $\Delta\phi$ is computed with loose and tight selections fixed respectively at 2.7 and 2.9 (Table 4.5).

The balance computed with loose and tight selections is propagated to the data to Monte Carlo ratio. The absolute difference with the nominal selection is computed for loose and tight selections. The uncertainty on $\Delta\phi$ in the analysis is negligible after all other selections have been applied. This result is not surprising since $\Delta\phi$ is strongly correlated to the selection of sub-leading jet p_T.

4.6.5 JVT

The uncertainty on JVT is derived from variations applied on the JVT cut. The nominal, loose and tight selections follow the official JetEtMiss recommendations, and are summarized in Table 4.6 for EM and LC jets.

The balance computed with loose and tight selections is propagated to the data to Monte Carlo ratio. The absolute difference with the nominal ratio is computed for loose and tight selections. The uncertainty on JVT is found to be negligible after all other selections have been applied.

4.6.6 Purity of the γ+jet sample

The uncertainty on the photon identification of the γ+jet sample is estimated with the ABCD method [141]. This section describes the ABCD method and the process to estimate the purity uncertainty with the γ+jet Direct Balance method.

Table 4.6: Selections applied to estimate the JVT uncertainty.

JVT cut:	
Low value	0.11
Nominal value	0.59
High value	0.91

4.6.6.1 The ABCD method

Two weakly correlated variables are selected: photon isolation and tight photon identification criteria. Using these two variables, four regions A,B,C,D are defined. Figure 4.13 illustrates these four regions. The event pre-selection is defined by the selection of the γ+jet analysis except the isolation, and tight identification criteria is replaced by loose identification criteria. Photons that failed the tight identification criteria are characterized as Loose Not Tight (LNT). Region A corresponds to the signal region with isolated photons, that passed the tight identification selection. Region B corresponds to events that failed the isolation selection and passed the tight identification criteria. The region C corresponds to events that passed the isolation selection and failed the tight identification criteria while the region D includes non isolated photons that failed the tight identification criteria.

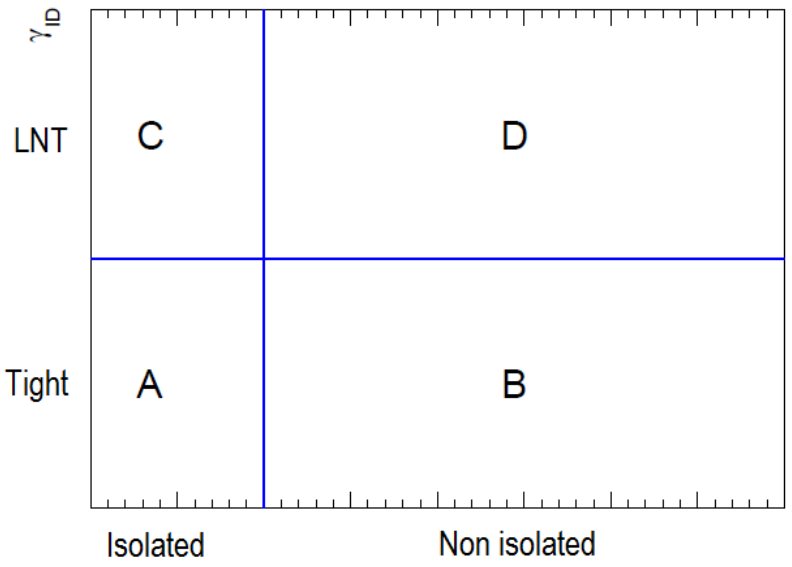

Figure 4.13: The four regions ABCD defined by isolation selection (x-axis) and tight identification criteria (y-axis). The events pre-selection includes all γ+jet selections except isolation, and tight identification criteria is replaced by loose identification criteria. Region A is defined by isolated and identified photons, region B by non-isolated and identified photons, region C by isolated and non-identified photons while region D is defined by non-isolated and non-identified photons. An isolation gap separates the regions A,C from regions B,D.

The assumptions of the method are the following:

- the signal contamination in the region B, C and D is small,
- the isolation profile of the background is the same in the LNT region as in the tight region.

From these assumptions:

$$\frac{N_A^{bkg}}{N_C^{bkg}} = \frac{N_B^{bkg}}{N_D^{bkg}}. \tag{4.3}$$

Thus, neglecting the signal leakages in the regions B, C and D, the number of signal events is defined at leading order as:

$$N_A^{sig} = N_A - N_A^{bkg} = N_A - N_B \times \frac{N_C}{N_D}. \tag{4.4}$$

The purity of the sample can obtained as follows:

$$\mathcal{P}_{\gamma+jets} = N_A^{sig}/N_A = 1 - \frac{N_B N_C}{N_A N_D}. \tag{4.5}$$

A first correction can be applied to treat signal leakages in the regions B,C and D. Let c_B, c_C and c_D be these corrections, such as $c_k = \frac{N_k^{sig}}{N_A^{sig}}$ and is estimated with pure Monte Carlo simulations. Then,

$$N_A^{sig} = N_A - (N_B - c_B N_A^{sig}) \times \frac{N_C - c_c N_A^{sig}}{N_D - c_D N_A^{sig}}. \tag{4.6}$$

N_A^{sig} is computed by iteration.

A second correction can be applied to treat correlations between variables used for the tight identification criteria and isolation. The specific variables for tight identification criteria are the following: $f_1, \Delta E, w_{s,tot}(wtots1), F_{side}(fracs1), w_{s,3}(weta1), E_{ratio}$. The shower shape variables, defining the loose and tight identification criteria are described in Figure 2.19. Table 4.7 illustrates the correlation factors between identification variables used for the tight working point (x-axis) and isolation variables (y-axis). The variables used for the tight identification criteria are correlated to isolation variables. In particular topoetcone40 is correlated to Eratio, fracs1 and wotot1 to respectively 16%, 13% and 17%.

Table 4.7: Correlations between isolation variables and shower shape variables used for tight identification criteria, using 2015 data, with γ+jet selections except isolation, and with loose identification selection instead of tight identification selection. The variables weta1 and fracs1 are also known as $w_{s,3}$ and F_{side}.

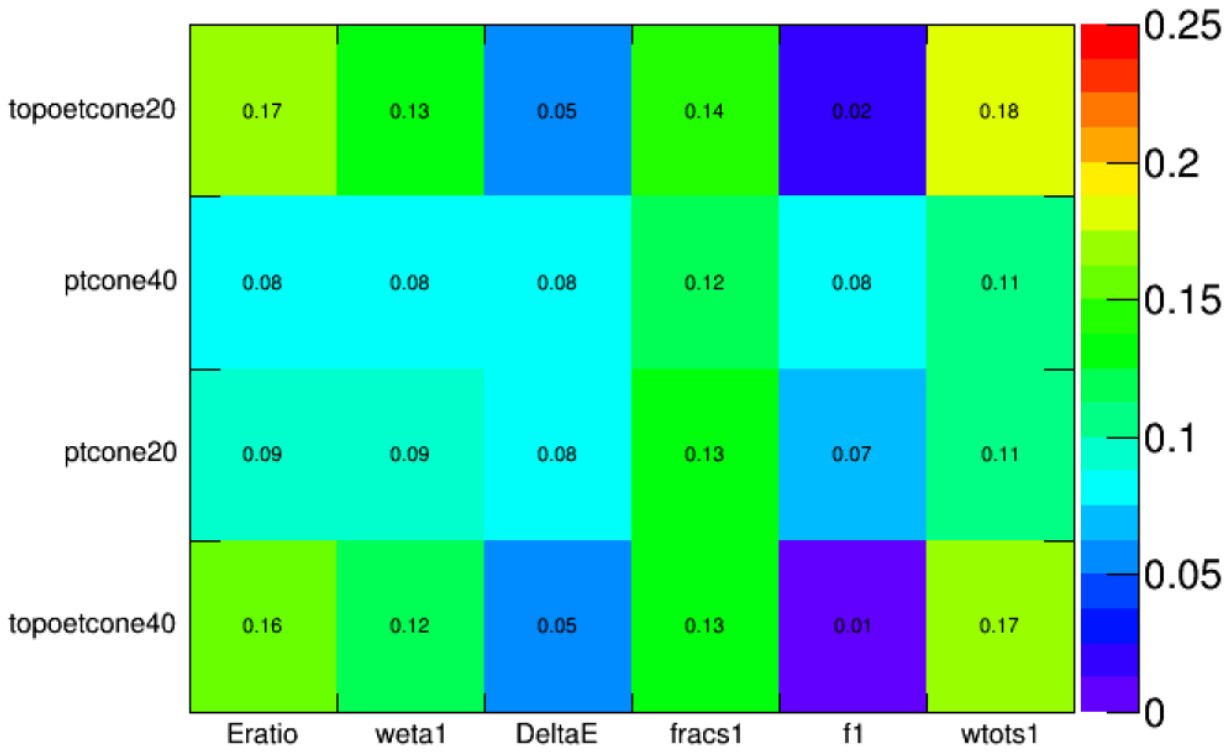

To limit the correlations between isolations variables and tight identification selections, one can choose to apply the most correlated identification selections to all events in the pre-selection, with

the statistical constraint to get enough events to correctly apply the ABCD method. Then, instead of loose identification selections, three $Loose'$ selections with additional cuts have been tested with 2015 data for various official isolation selections:

- $Loose'1$: $w_{s,tot}, F_{side}, w_{s,3}, E_{ratio}$,
- $Loose'2$: $w_{s,tot}, w_{s,3}, E_{ratio}$,
- $Loose'3$: $w_{s,tot}$.

Depending on the purity for each $Loose'$ selection, $Loose'2$ has been chosen to provide high purity with large statistics after the selections. The update of this analysis using 2016 data have not been done yet. The correlation factor R is defined as:

$$R = \frac{N_A^{MC} N_D^{MC}}{N_B^{MC} N_C^{MC}}. \tag{4.7}$$

With enough statistics and if the x-axis and y-axis variables are perfectly independent, R should be close to one. R is used to correct the number of events in the signal region from the correlations in the variables. The number of signal events can be expressed as follows:

$$N_A^{sig} = N_A - R \times (N_B - c_B N_A^{sig}) \times \frac{N_C - c_c N_A^{sig}}{N_D - c_D N_A^{sig}}. \tag{4.8}$$

4.6.6.2 Estimation of the purity uncertainty

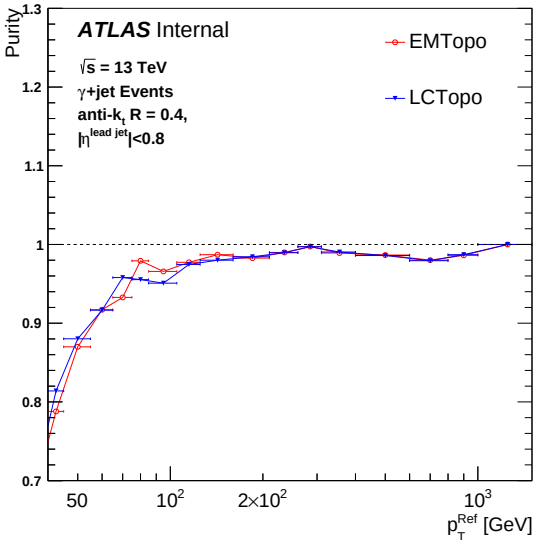

Figure 4.14: Purity of the γ+jet sample for EM+JES jets (blue) and LC+JES jets (red) after all selections have been applied. The estimation has been performed with 2016 data using the ABCD method.

The uncertainty on the JES due to the multijet background is given by:

$$\Delta_{Purity} = (1 - \mathcal{P}) \frac{\mathcal{B}^{LNT} - \mathcal{B}^{Tight}}{\mathcal{B}^{Tight}}. \tag{4.9}$$

The purity $\mathcal{P}$ is estimated with the ABCD method, $\mathcal{B}^{Tight}$ is the balance estimated with the nominal selections, and $\mathcal{B}^{LNT}$ is computed by changing the selections on the photon identification. The estimation of the purity $\mathcal{P}$ with 2016 data as a function of p_T^{ref} using the ABCD method is shown in Figure 4.14. The method has been applied to EM and LC jets. Very similar results are obtained with EM and LC jets. The purity of the sample is estimated to be at ∼80% at 40 GeV and progressively increases as a function of p_T^{ref}. The purity reaches a level of 98-99% above 100 GeV. The purity uncertainty is the limiting factor for the γ+jet DB method at low p_T. Above 60 GeV, the uncertainty on the purity become negligible.

4.6.7 Out-of-cone

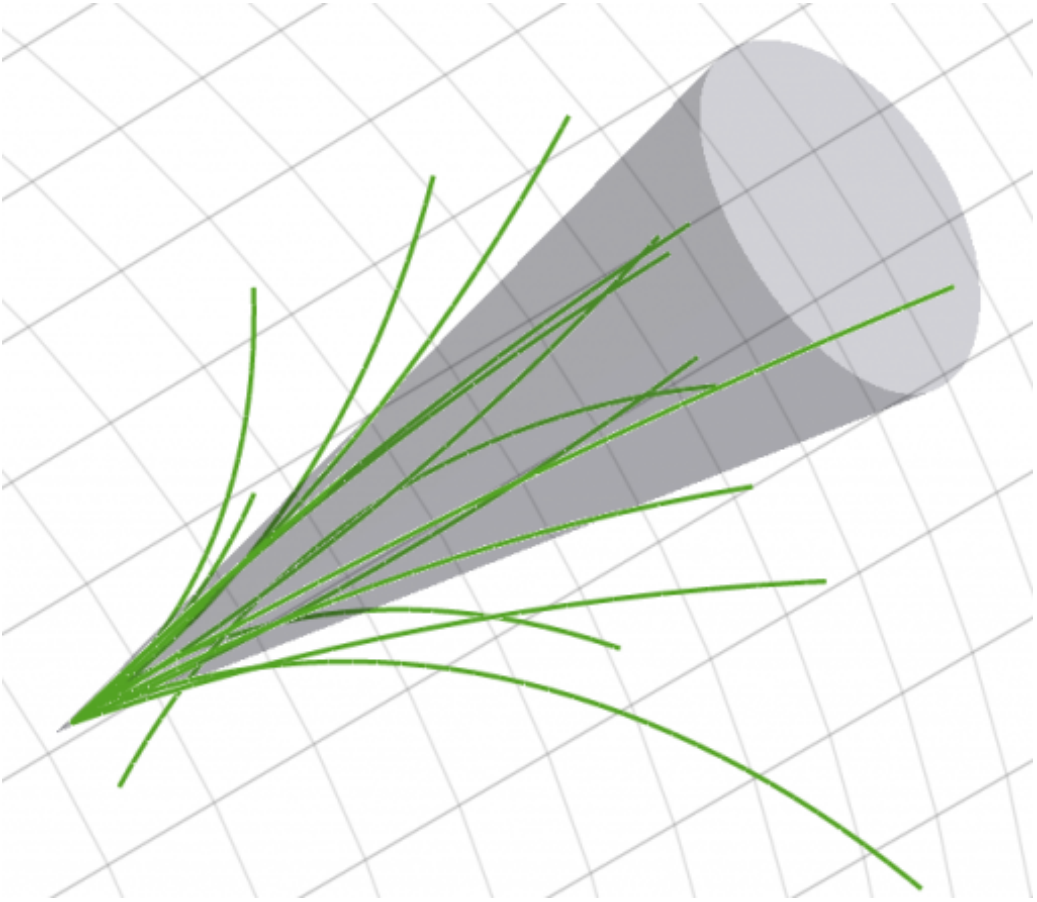

Figure 4.15: Illustration of the out-of-cone effects. Jet energy reconstruction doesn't include out-of-cone radiations. Energy losses are estimated by the simulations.

In the jet reconstruction, a choice is made on the radius used for the anti-k_t algorithm. The jet radius is R = 0.4 by default. If R is too small, a large energy fraction out of the jet cone is not included in the reconstruction, but if R is too large the pile-up effects increase (Figure 4.15). Since the energy out of

the jet cone is not included, the jet energy doesn't reconstruct the initial parton energy. This has no impact on the in-situ calibration if the out-of-cone effect is correctly estimated by the simulation since the calibration is given by the data to Monte Carlo ratio. The impact of the out-of-cone radiations are estimated with charged particle tracks associated to the primary vertex. For each track, the angular distance ΔR with the jet is computed:

$$\Delta R(track, jet) = \sqrt{(\eta_{track} - \eta_{jet})^2 + (\phi_{track} - \phi_{jet})^2}. \tag{4.10}$$

The impact of underlying events (UE) and out-of-cone energy deposits (OC) are estimated from the distribution of tracks energy density as a function of the distance r to the jet axis. The energy density distribution is fitted with the following function:

$$f(r) = \frac{a}{r^b + c} + C, \tag{4.11}$$

Where a, b, and c are free parameters. The parameter C is interpreted as the energy density contribution from underlying events. The underlying events contributions $p_T^{UE,IC}$ (IC) in the jet cone energy is computed as follows:

$$p_T^{UE,IC} = \int_0^R C.2\pi \mathrm{d}r = C\pi R^2, \tag{4.12}$$

Where R defines the radius of the jet cone. The out-of-cone radiation, excluding underlying events contribution is computed as follows:

$$p_T^{ALL-UE,OC} = \int_R^2 \frac{a}{r^b + c} 2\pi r \mathrm{d}r. \tag{4.13}$$

The energy integrated on the jet cone, including the underlying events contribution is estimated as:

$$p_T^{ALL,IC} = \int_0^R (\frac{a}{r^b + c} + C).2\pi r \mathrm{d}r. \tag{4.14}$$

The out-of-cone uncertainty is estimated from the k-terms (k_{OOC}), defined as:

$$k_{OOC} = \frac{p_T^{ALL,IC}}{p_T^{ALL,IC} - p_T^{UE,IC} + p_T^{ALL-UE,OC}}. \tag{4.15}$$

The energy of the initial parton can be estimated with the following relation:

$$p_T^{part} = k_{OOC} \times p_T^{jet}. \tag{4.16}$$

Figure 4.16 is an illustration of the estimation of the out-of-cone effects from the fit. The k-terms are computed in each p_T bin. The underlying contribution is estimated from the fit while IC and OC are estimated by subtracting UE in the histogram. Figure 4.17 shows the the out-of-cone fit using 2016 data (a) and (b) in different p_T bins. Fits using Pythia8 are shown in (c) and (d). The other distributions with EM jets are shown in appendix .2.

Figure 4.18 shows the estimation of the underlying events contribution using 2016 data for EM (a), LC (b) as a function of p_T^{ref}. The results with EMPFlow jets are shown in Figure 4.19. The bottom of the figures show the data-to-MC ratio. For EM, LC, and EMPFlow jets. A shift of ∼10% is seen between data and MC. This effect is not understood yet. Figure 4.20 shows the estimation of the K-terms, as a function of p_T^{ref} using 2016 data for EM (a), and LC (b) jets. Results with EMPFlow are shown in Figure 4.21. An agreement at the level of 1% is seen in average for EM, LC, and EMPFlow jets, with a 2% difference in the first and last bin.

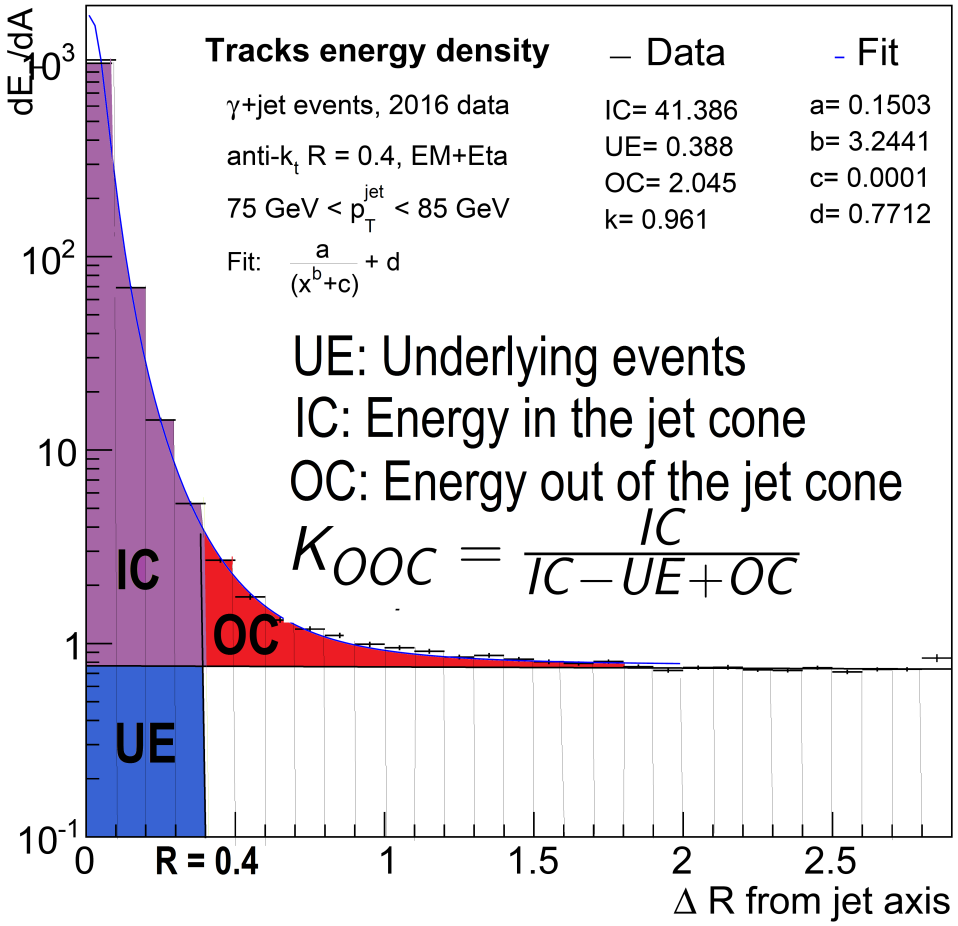

Figure 4.16: Illustration of the out-of-cone effects and k-terms estimation. The tracks energy density of charged particles is drawn as a function of the distance $\Delta R$from the jet axis. The energy in the jet cone includes underlying events contribution (UE) and energy from parton hadronisation (IC). The energy out of the jet cone (OC) is estimated by subtracting underlying events contribution. The k-terms are computed from IC, UE and OC, and are used for the estimation of out-of-cone uncertainty.

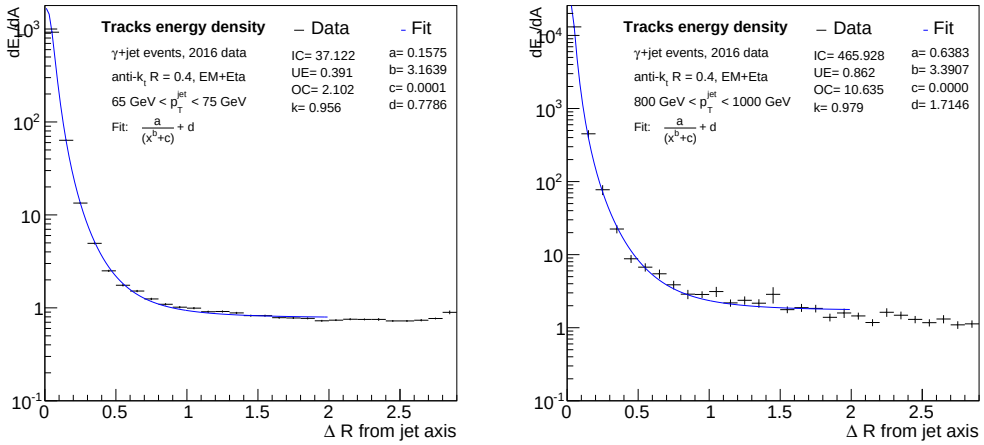

Figure 4.17: Energy density of tracks matched to the primary vertex of EM jets, after γ+jet selections, in different p_T ranges using 2016 data (top) and Pythia8 (bottom). The tracks energy density is fitted with the function $f = a/(x^b + c) + d$ in blue for data and red for Pythia8. The K-terms are computed from UE, IC and OC. Underlying events contribution is estimated from the fit, while OC and IC are estimated from the histogram by subtracting the underlying events contribution.

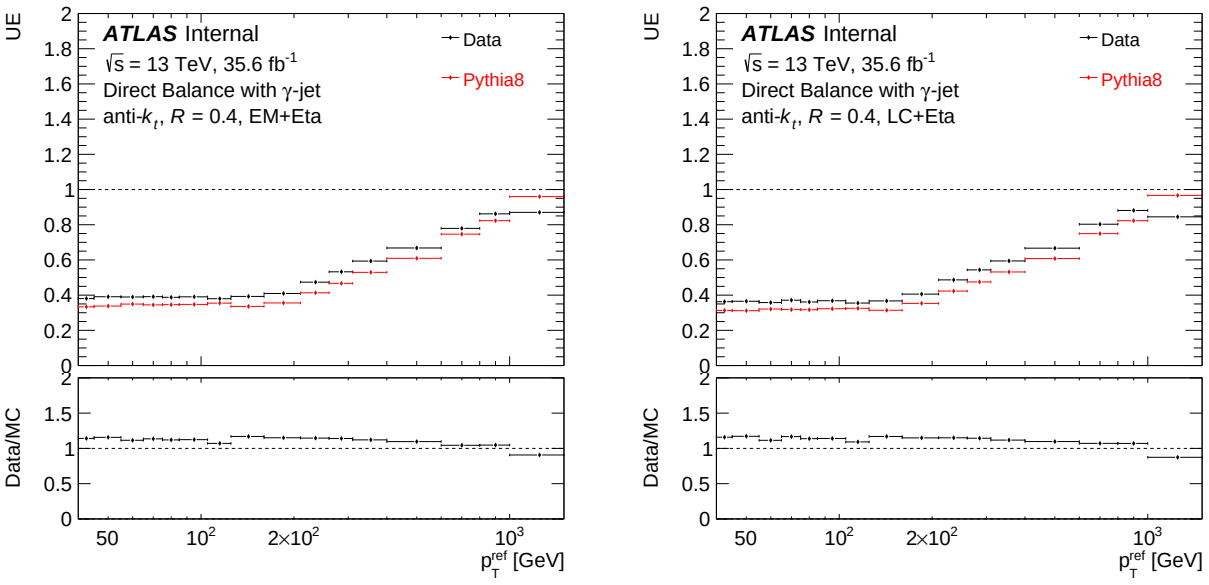

Figure 4.18: Estimation of the underlying events contribution as a function of p_T^{ref} for 2016 data (black) and Pythia8 (red), with EM (a) and LC (b) jets calibrated up to η-intercalibration. The underlying events contribution is estimated from the fit on tracks energy density, using tracks associated to the primary vertex after γ+jet selections.

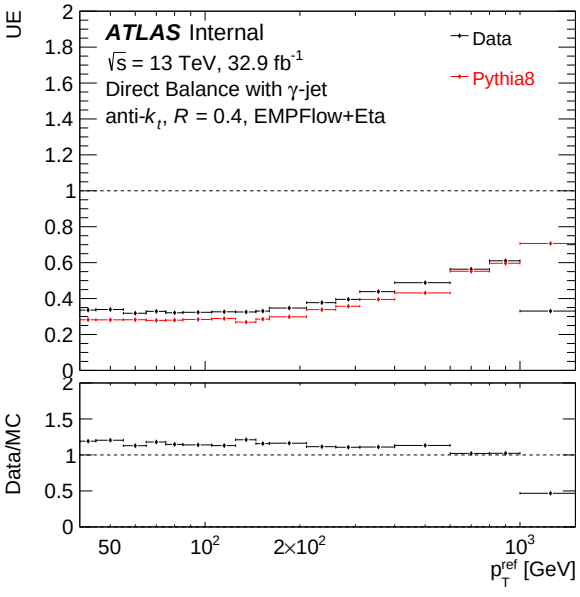

Figure 4.19: Estimation of the underlying events contribution as a function of p_T^{ref} for 2016 data (black) and Pythia8 (red), with EMPFlow jets calibrated up to η-intercalibration. The underlying events contribution is estimated from the fit on tracks energy density, using tracks associated to the primary vertex after γ+jet selections.

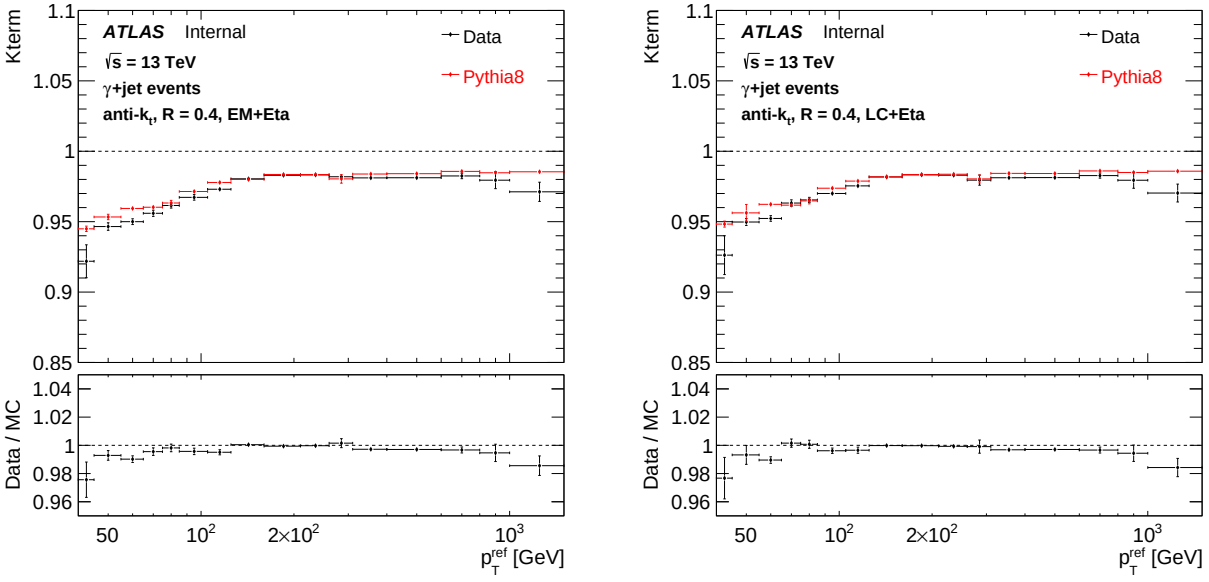

Figure 4.20: Estimation of K-term as a function of p_T^{ref} for 2016 data (black) and Pythia8 (red), with EM (a) and LC (b) jets calibrated up to η-intercalibration. The K-terms are estimated from tracks energy density, using tracks associated to the primary vertex after γ+jet selection. An agreement of approximately 1% is seen between data and Pythia8, with larger discrepancies and statistical uncertainty on the first and last bin.

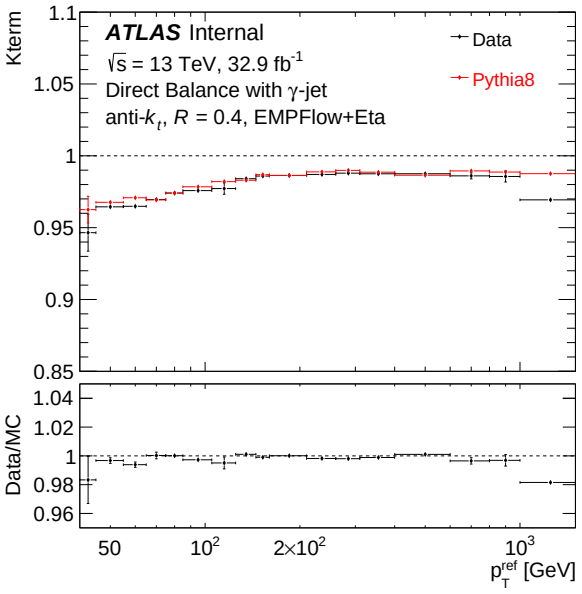

Figure 4.21: Estimation of K-terms as a function of p_T^{ref} for 2016 data (black) and Pythia8 (red), with EMPFlow jets calibrated up to η-intercalibration. K-terms are estimated from tracks energy density, using tracks associated to the primary vertex after γ+jet selection. An agreement of approximately 1% is seen between data and Pythia8, with larger discrepancies and statistical uncertainty on the first and last bin.

The uncertainty associated to the out-of-cone effect is estimated as:

$$\Delta_{ooc} = \frac{k_{data} - k_{Pythia8}}{k_{data}}. \tag{4.17}$$

The out-of-cone uncertainty is symmetric, and is one of the dominant systematic uncertainties at low p_T.

4.7 Bootstrap and statistical uncertainties

The Bootstrap method [142] is a method used to determine the systematic uncertainties on the JES. The motivation of this method is to limit the statistical fluctuations on the evaluation of the systematic uncertainties. The principle of the method is the following. For each distribution used to compute the systematic uncertainties, a set of N replicas is generated. Each replica is produced from the nominal distribution, by fluctuating every event with a Poisson distribution. The weights used for the fluctuations are produced uniquely by the bootstrap tool before the selections. They are produced event by event, and can be generated using the run and event number. Therefore, for one event the fluctuations are applied coherently for each distributions, and for different events the fluctuations are independent. The Poisson parameter has been fixed to μ = 1 so that the average over Bootstrap replicas for a given event yields one event. The number of replicas is a free parameter. This method has been applied for all the systematics of the γ+jet DB method, except for the statistical uncertainty (section 4.7).

The statistical uncertainty on Jet Energy Scale is estimated from the fit. The error on the mean value from the fit is used as statistical uncertainty.

4.8 Final uncertainties with γ+jet method

The uncertainties on the Jet Energy Scale estimated with γ+jet DB method are presented in Figure 4.22 and Figure 4.23, respectively for EM and LC jets calibrated up to the η-intercalibration. Down and up uncertainties are presented. The uncertainties are combined with uncertainties from the other in-situ methods to provide the final JES uncertainty. The total uncertainty is represented in grey area and corresponds to the quadratic sum of each contribution. The sum includes contributions from Photon Energy Resolution (PER), Monte Carlo simulation (MC), Photon Energy Scale (PES), Sub-leading jet p_T (Veto), Jet Vertex Tagging (JVT), $\Delta\phi$ cut between the photon and the leading jet (dPhi), Statistical uncertainty (Stat), Purity and out-of-cone (OOC). The statistical uncertainty, purity, out-of-cone and Monte Carlo simulations are symmetric. Other uncertainties have been computed separately for both up and down variations. The estimation of the JES uncertainties has been computed with the Bootstrap method using 30 replicas for each variation. A rebinning algorithm has been used to merge bins with non-significant variations.

In Figure 4.22, the uncertainties are computed for EM jets calibrated up to η inter-calibration. The total uncertainty is estimated to be at 2.5% at 40 GeV and is dominated by the uncertainty on the purity of the sample, the statistical uncertainty and the out-of-cone effects. It decreases to 1% at 55 GeV. From 55 GeV to 250 GeV, the uncertainty is dominated by the MC modelling. The minimum is reached at 250 GeV (0.8%). Above 250 GeV, the uncertainty slightly increases and is dominated by the MC modelling and the uncertainty on the Photon Energy Scale. Above 1280 GeV the method is limited by statistics. Uncertainties on the Photon Energy Resolution, sub-leading jet p_T, JVT and $\Delta\phi$ are negligible.

The uncertainties with LC jets are shown in Figure 4.23. Below 55 GeV, the total uncertainty is at the level of 1.5-2%, and is dominated by the uncertainty on purity of the sample, the statistical uncertainty and the out-of-cone effects. The difference with EM jet uncertainty is mostly due to the purity estimation, which is sensitive to statistical fluctuations at low p_T. Above 55 GeV, the uncertainty decreases to be $\sim$0.8%. The major difference with EM jets is on the error of modelling uncertainty. This error is estimated to 0.8% for EM jets and is the dominant uncertainty between 55 GeV and 200 GeV while it is less than 0.5% for LC jets. The modelling uncertainty is estimated with Pythia8 (nominal) and Sherpa2.2 for γ+jet, while Sherpa2.2 and Powheg+Pythia8 are used for Z+jet.

The uncertainties using EMPFlow jets are shown in Figure 4.24. Below 55 GeV, the total uncertainty is at the level of 1.5-2%, and is dominated by the purity. Above 55 GeV, the uncertainty decreases to $\sim$0.8-1% and is dominated by modelling and Photon Energy Scale uncertainties. Above $\sim$900 GeV, the uncertainty is dominated by statistical uncertainty.

4.9 Calibrated jets

This section presents the balance using jets fully calibrated with the corrections provided by the combination of all the in-situ methods (Figure 6.49 and Figure 3.13). Figure 4.25 shows the balance with 2015 data, as a function of p_T, for EM jets (a) and LC jets (b) fully calibrated with the in-situ method. For EM jets, a 1% agreement within error bars is seen between data and Pythia8. The 1% error is mostly due to the differences between γ+jet calibration and the other in-situ methods used of the combination. The differences slightly increases at low and high p_T where Z+jet and multijet method dominate. Similar results are seen with LC jets, with $\sim$1-2% differences below 100 GeV, and 1% above ($\sim$2% on the last bin). The Figure 4.25 (a) can be found in the Figures list of the 2015 JES paper [105].

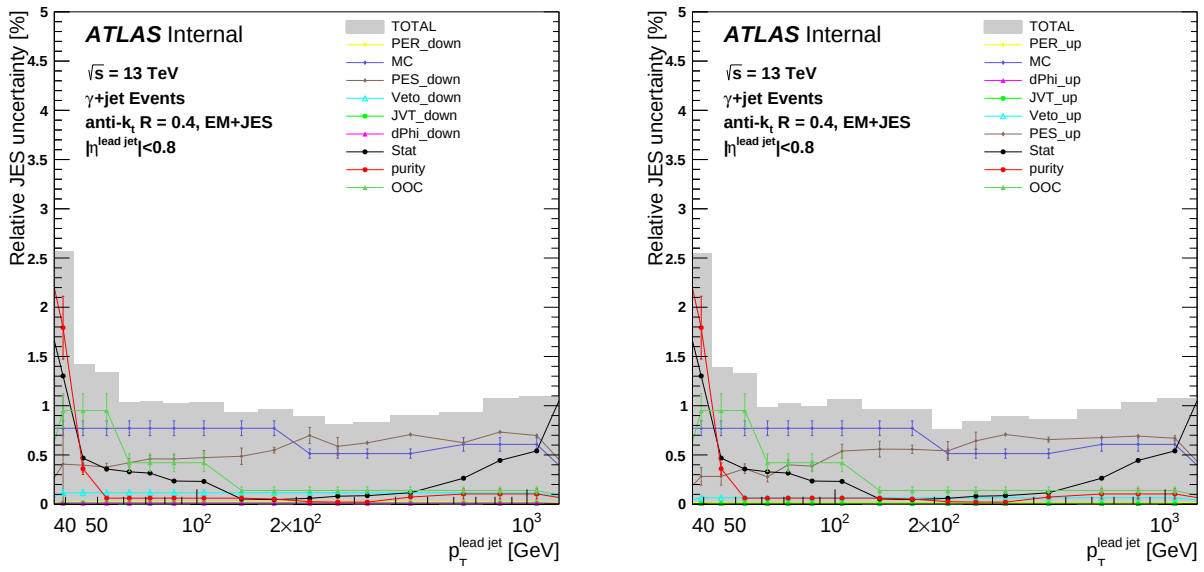

Figure 4.22: Systematic uncertainties on EM jets calibrated up to η-intercalibration with γ+jet Direct Balance method. Systematics down (left) and up (right) are estimated using 2016 data. The total uncertainty (grey area) is computed with quadratic sum of all components, and includes uncertainties on Photon Energy Resolution (PER), Monte Carlo simulation (MC), Photon Energy Scale (PES), Subleading jet p_T (Veto), Jet Vertex Tagging (JVT), $\Delta\phi$ cut between the photon and the leading jet (dPhi), Statistical uncertainty (Stat), Purity and out-of-cone (OOC).

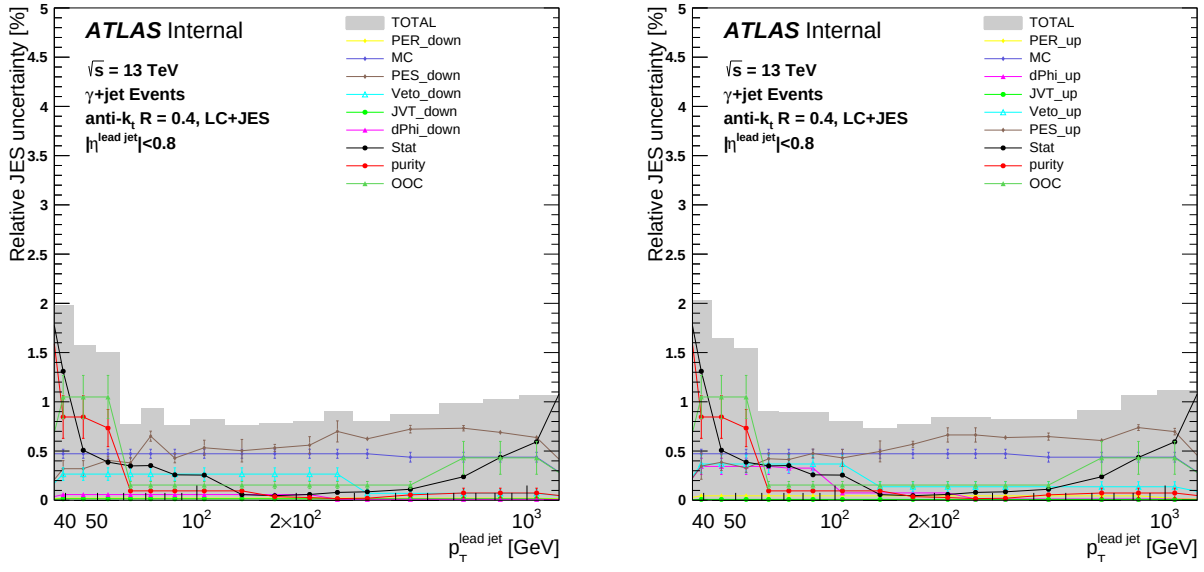

Figure 4.23: Systematic uncertainties on LC jets calibrated up to η-intercalibration with γ+jet Direct Balance method. Systematics down (left) and up (right) are estimated using 2016 data. The total uncertainty (grey area) is computed with quadratic sum of all components, and includes uncertainties on Photon Energy Resolution (PER), Monte Carlo simulation (MC), Photon Energy Scale (PES), Subleading jet p_T (Veto), Jet Vertex Tagging (JVT), $\Delta\phi$ cut between the photon and the leading jet (dPhi), Statistical uncertainty (Stat), Purity and out-of-cone (OOC).

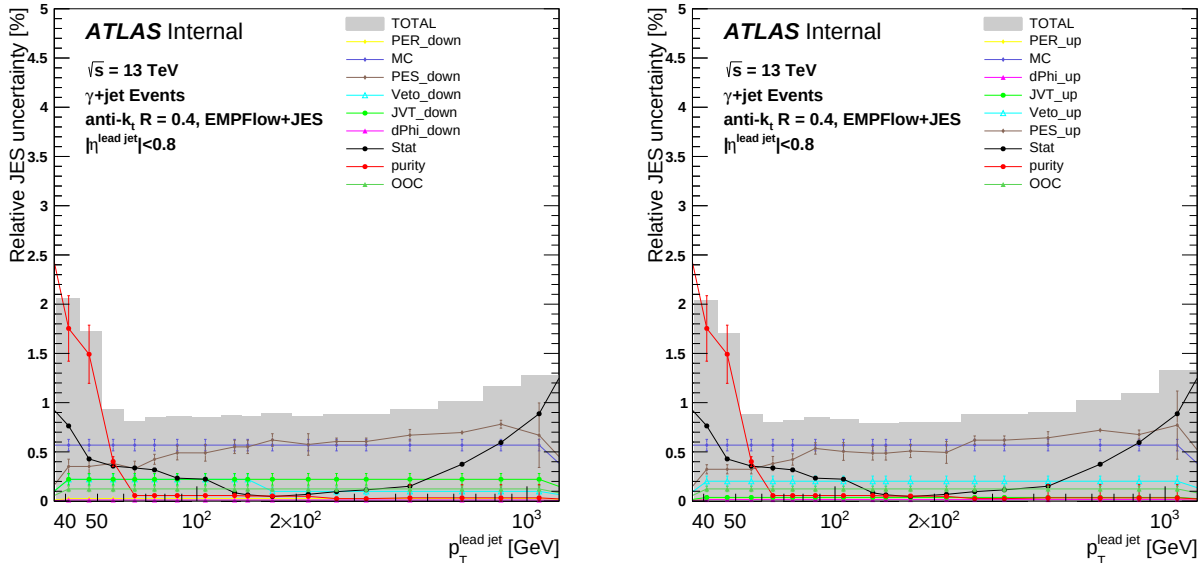

Figure 4.24: Systematic uncertainties on EMPFlow jets calibrated up to η-intercalibration with γ+jet Direct Balance method. Systematics down (left) and up (right) are estimated using 2016 data. The total uncertainty (grey area) is computed with quadratic sum of all components, and includes uncertainties on Photon Energy Resolution (PER), Monte Carlo simulation (MC), Photon Energy Scale (PES), Sub-leading jet p_T (Veto), Jet Vertex Tagging (JVT), $\Delta\phi$ cut between the photon and the leading jet (dPhi), Statistical uncertainty (Stat), Purity and out-of-cone (OOC).

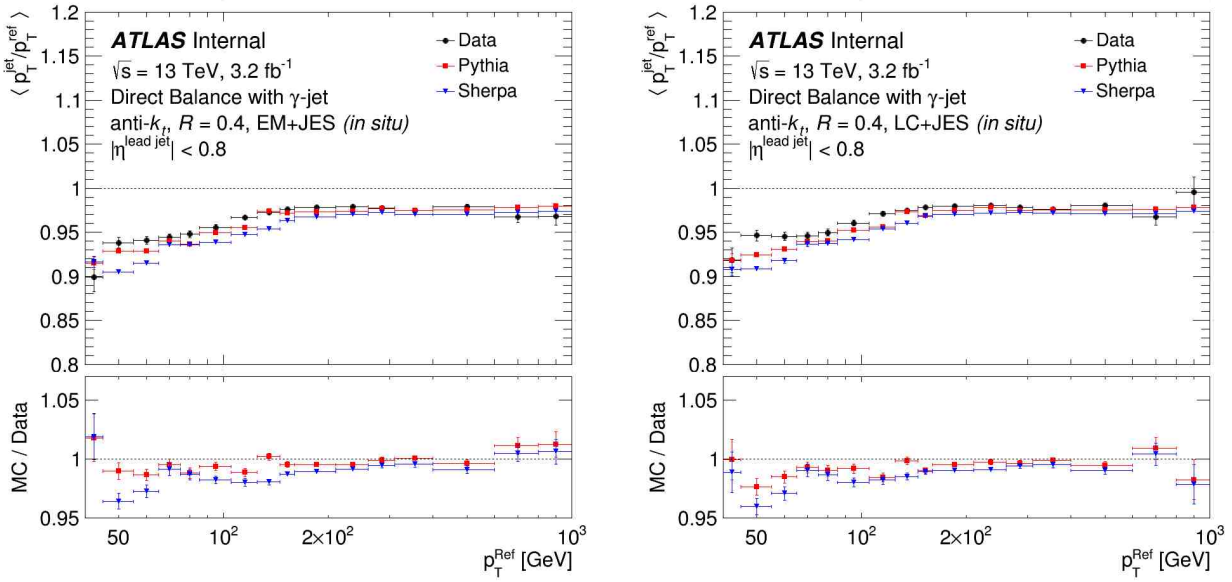

(a) *(b)*

Figure 4.25: Ratio $\left\langle p_T^{jet}/p_T^{ref} \right\rangle$ for jets fully calibrated at EM+JES scheme (a) and LC+JES scheme (b), with 2015 data using the γ+jet Direct Balance technique, as a function of p_T^{ref} for both data and MC simulation. Jets are selected in the central region of the hadronic calorimeter $|\eta^{leadjet}| < 0.8$. Error bars indicate the statistical uncertainties.

The balance plot with 2016 fully calibrated jets is shown in Figure 4.26 with EM+JES (a) and LC+JES (b). The data-to-MC agreement is at the level of ∼1% for both EM and LC jets. On higher p_T bins, we can see the decrease of γ+jet weights, progressively replaced by the multijet method.

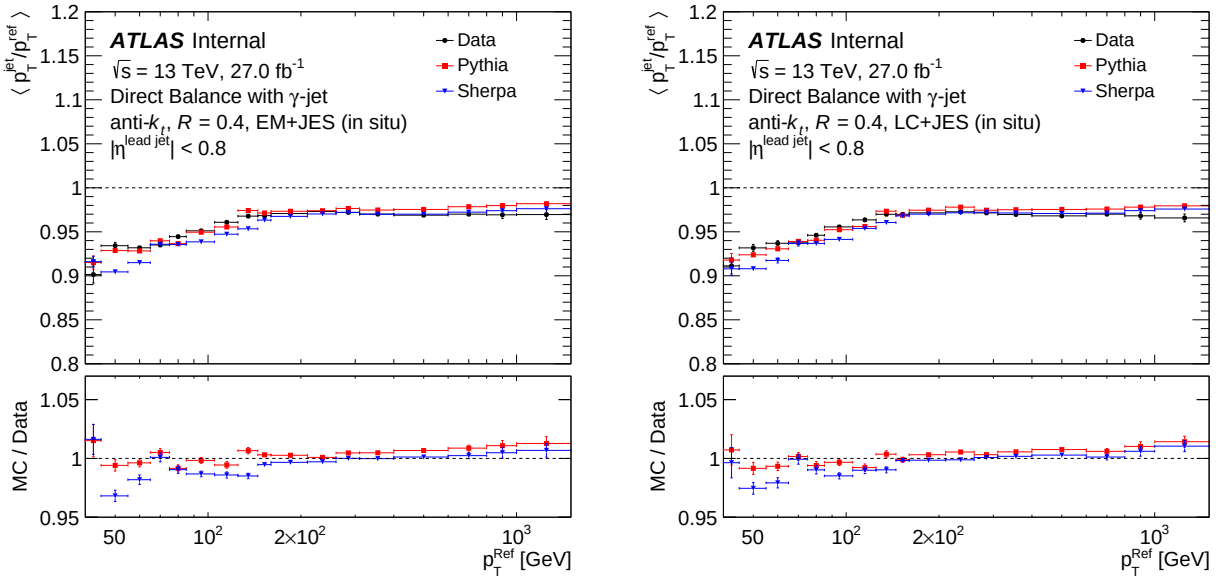

(a) *(b)*

Figure 4.26: Ratio $\left\langle p_T^{jet}/p_T^{ref} \right\rangle$ for jets fully calibrated at EM+JES scheme (a) and LC+JES scheme (b), with 2015 data using the γ+jet Direct Balance technique, as a function of p_T^{ref} for both data and MC simulation. Jets are selected in the central region of the hadronic calorimeter $|\eta^{leadjet}| < 0.8$. Error bars indicate the statistical uncertainties.

4.10 Conclusion

This chapter presents the in-situ calibration using the γ+jet Direct Balance method. The method is used for the 2015 and 2016 jets calibration with a p_T range respectively between 36 GeV and 950 GeV, and between 37 GeV and 1280 GeV. The corrections are at the level of 2-3% for EM, LC, and EMPFlow jets, and a flat distribution at the level of 1% is seen as a function of η. The second part of the chapter describes the sources of the JES uncertainty and how they are estimated. A total uncertainty at the level of ∼1.5-2.5% below 55 GeV, and ∼1% above is obtained with the γ+jet Direct Balance method for EM, LC, and EMPFlow jets.

Chapter 5

Jet energy resolution

"Insanity is doing the same thing over and over again and expecting different results. "

Albert Einstein

Contents

5.1 Definition

The precise knowledge of the Jet energy resolution (JER) is essential for physics analysis including jets in the final states. JER can be parametrised with three parameters:

$$\frac{\sigma(p_T)}{p_T} = \frac{N}{p_T} \oplus \frac{S}{\sqrt{p_T}} \oplus C, \tag{5.1}$$

where N is the effective noise, S is the stochastic term and C is the constant term. N includes electronic, detector noise and pile-up contributions. It is expected to be significant at low p_T. S parametrizes the stochastic fluctuation and is scaled as $1/\sqrt{p_T}$. In the intermediate region, it is expected that the S term becomes the limiting factor in the resolution. The C term includes contributions such as the signal losses in passive material (cryostat and solenoid coil). It is expected to dominate at high p_T.

5.2 Strategy

The in-situ techniques (Z/γ+jet and multijet) described in section 3.8 can be used to measure the jet energy resolution of the detector from the data. From 20 GeV to $\sim$ 1 TeV, the Z/γ+jet methods are used to extract the JER, while the balance between dijet events is used to extend these measurements to higher $|\eta|$ and p_T. The method is used in ATLAS for 7 TeV [143] and 8 TeV [123] data. The three parameters N, S and C can be extracted from a fit applied on the resolution estimated with the in-situ techniques. Since the fit depends on a large number of parameters from the in-situ techniques, and due to the large uncertainty at low p_T, an alternative method to determine N was developed in Run 1. The fit is therefore performed with a fixed value of N. The following section describes the estimation of the JER using the γ+jet Direct Balance technique.

5.3 Jet energy resolution with Run 1 data

The JER estimated in Run 1 with the three in-situ methods is shown in Figure 5.1 with EM (a) and LC (b) jets. Events with Z+jet [144] can be used to estimate the JER from $\sim$20 GeV to 250 GeV, with γ+jet from $\sim$35 GeV to 800 GeV, and with dijet from $\sim$ 45 GeV to 1.5 TeV. The methods are combined to perform the fit. With EM jets (a), a resolution of 14% is observed at 40 GeV and 2% at 1 TeV.

By fixing the N parameter in the fit, N, S, C are estimated to be:

$$(N, S, C) = (3.33^{+0.63}_{-0.63}, 0.71^{+0.030}_{-0.038}, 0.003^{+0.001}_{-0.001}), \text{(EM jets)}, \tag{5.2}$$

$$(N, S, C) = (4.12^{+0.74}_{-0.74}, 0.74^{+0.039}_{-0.048}, 0.023^{+0.002}_{-0.002}), \text{(LC jets)}, \tag{5.3}$$

5.4 Direct balance method with γ+jet

5.4.1 Description

The method used to extract the JER with the γ+jet Direct Balance method is an extension of the method used to compute the JES. The same event selection is applied and is described in section 6.4. Since the photon is measured very precisely by the detector, it is used as a reference for the measurement of the jet resolution. The method uses the width of the distribution instead of the central value in the case of JES. In the γ+jet direct balance method, the balance is defined as:

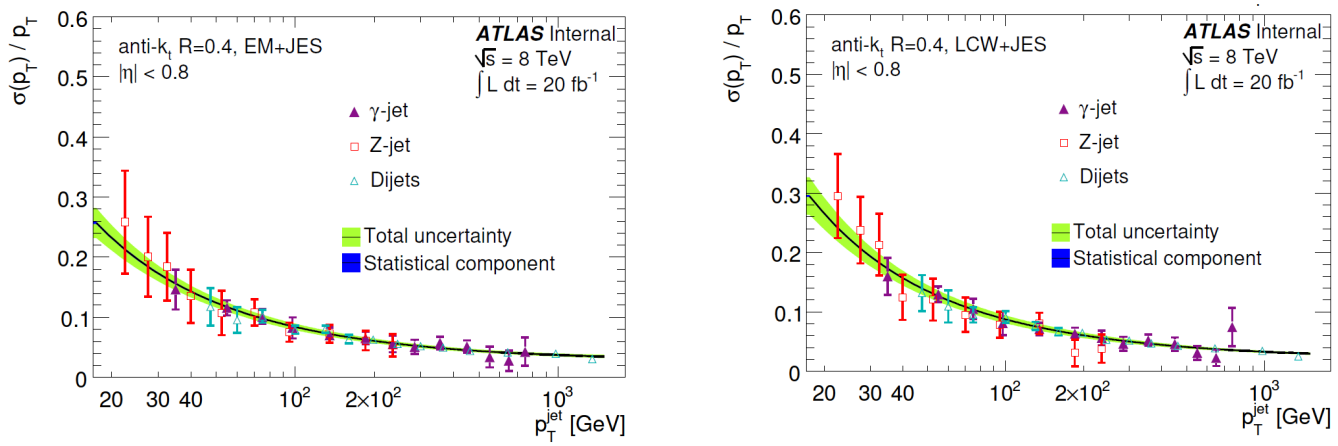

(a) *(b)*

Figure 5.1: Jet energy resolution with EM (a) and LC (b) jets as a function of p_T^{jet} using 8 TeV data. The resolution is based on the combination of Z+jet (red squares), γ+jet (purple triangles), and dijets (blue triangles) methods. Blue area shows the statistical uncertainties of the combination while the green area shows the total uncertainty.

$$\mathcal{B} = \frac{p_T^{jet}}{p_T^{ref}}, \tag{5.4}$$

where p_T^{jet} is the transverse momentum of the reconstructed jet (in data or Monte Carlo), and p_T^{ref} is the transverse momentum of the photon projected to the jet direction (Equation (3.10)). The jet energy resolution can be extracted using the standard deviation of the distribution of the balance. The width of the distribution of p_T^{jet}/p_T^{ref} can be expressed as the convolution sum of two terms:

$$\sigma\left(\frac{p_T^{jet}}{p_T^{ref}}\right) = \sigma\left(\frac{p_T^{jet}}{p_T^{truth}}\right) \oplus \sigma\left(\frac{p_T^{truth}}{p_T^{ref}}\right), \tag{5.5}$$

where p_T^{truth} corresponds to the jet transverse momentum at the particle-level. The term $\sigma(\frac{p_T^{jet}}{p_T^{truth}})$ corresponds to the jet resolution, which is the parameter of interest. The second term $\sigma(\frac{p_T^{truth}}{p_T^{ref}})$ corresponds to the standard deviation of $\frac{p_T^{truth}}{p_T^{ref}}$. This term includes physics effects that modify the balance. The resolution of the photon is negligible with respect to the jet resolution. The JER noted $\sigma_{in-situ}$ can be extracted from Equation (5.5) as:

$$\sigma_{in-situ} = \sqrt{\sigma\left(\frac{p_T^{jet}}{p_T^{ref}}\right)^2_{data} - \sigma\left(\frac{p_T^{truth}}{p_T^{ref}}\right)^2_{MC}}. \tag{5.6}$$

The first term of $\sigma_{in-situ}$ corresponds to the width of the balance distribution. This term can be extracted from data or Monte Carlo using jets at the reconstruction-level. The width of the distribution of $\left(p_T^{jet}/p_T^{ref}\right)$ depends on contributions arising from the detector measurements, and from the particle-level. Contributions at particle-level can be estimated using the simulation, and corresponds to the second term of $\sigma_{in-situ}$. This term is removed from the first term in order to estimate the detector effects only. Resolution at particle-level depends in particular on QCD radiations, hadronization,

pile-up, and underlying events. The difference between the resolution $\sigma^{MC}_{in-situ}$ computed with simulation only (Equation (5.7)), and the resolution σ_{MC} defined in Equation (5.8) corresponds to the non-closure uncertainty (section 5.4.3.1).

$$\sigma^{MC}_{in-situ} = \sqrt{\sigma\left(\frac{p_T^{jet}}{p_T^{ref}}\right)^2_{MC} - \sigma\left(\frac{p_T^{truth}}{p_T^{ref}}\right)^2_{MC}} \tag{5.7}$$

$$\sigma_{MC} = \sigma\left(\frac{p_T^{jet}}{p_T^{truth}}\right). \tag{5.8}$$

5.4.2 Results with γ+jet

The comparison between the JER extracted from simulation as a function of p_T^{ref} using EM (a), LC (b), and EMPFlow (c) is shown in Figure 5.2. The resolution improves as a function of p_T^{ref} from ∼14-15% at 40 GeV to ∼3-3.5% at 1 TeV for all jet schemes. This improvement is due to the fact that at higher energy, a larger fraction of particles is emitted in the jet cone, decreasing the energy fluctuations. A better resolution is expected with LC jets compared to EM jets due to the weights applied on electromagnetic and hadronic clusters, but a similar resolution is obtained at low p_T. This is due to pile-up effects and to errors in the identification of cluster nature. The resolution is slightly better at low p_T for jets at particle flow (EMPFlow jets), with a resolution below 14%. This improvement is due to a better pile-up rejection using tracks information. At high energy, a similar resolution is obtained between the three jets schemes. The ratio between the two generators is shown in bottom part. An agreement within 5% is seen between Pythia8 and Sherpa2.2.

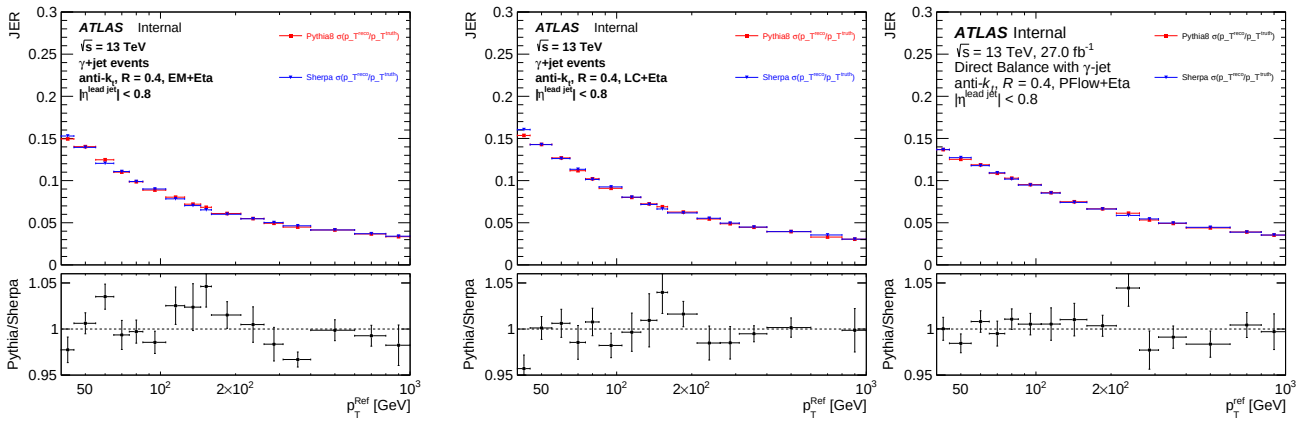

(a) *(b)* *(c)*

Figure 5.2: Width of the distribution p_T^{jet}/p_T^{truth} with EM (a), LC (b) and EMPFlow (c) jets calibrated up to the η-intercalibration as a function of p_T^{ref}. The width is estimated with a Gaussian fit, applied on both Monte Carlo simulations Pythia8 (red) and Sherpa2.2 (blue). The bottom graphs show the ratio of the resolution Pythia8/Sherpa2.2. Error bars show the statistical uncertainties.

The two terms used to extract the JER from data are shown in Figure 5.3. In black, the resolution of (p_T^{jet}/p_T^{ref}) using data, and the resolution of (p_T^{truth}/p_T^{ref}) simulated with Pythia8 and Sherpa2.2. The bottom part shows the ratio of the two resolutions. The width of the distributions with jets at particle level, is very similar between EM, LC and EMPFlow jets since the distribution depends only on the

event selection. At reconstruction level, a similar resolution is observed between EM and LC jets, and the improvements observed with particle flow at low p_T in Figure 5.2 is confirmed.

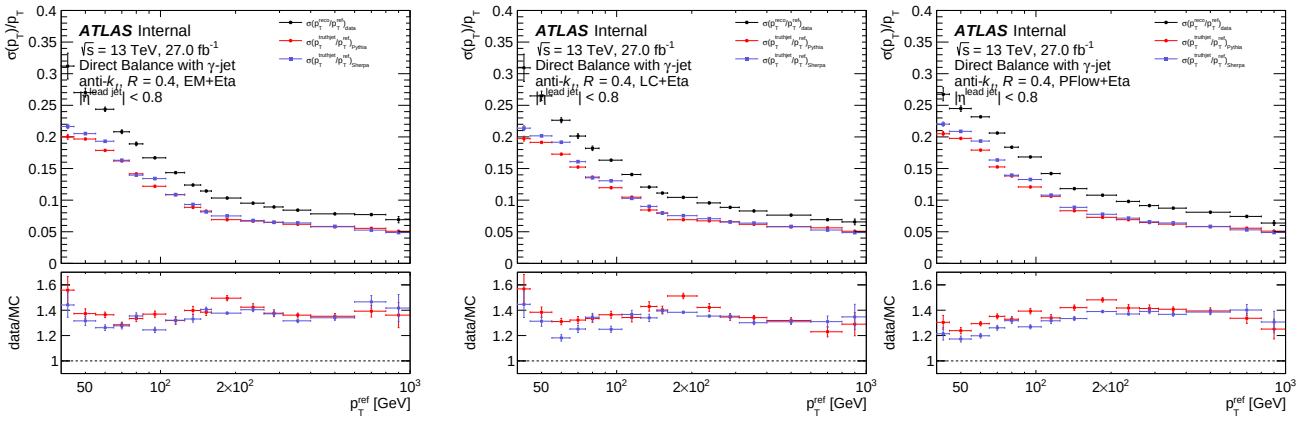

(a) *(b)* *(c)*

Figure 5.3: Width of the distribution p_T^{jet}/p_T^{ref} (black) using 2016 data, and $p_T^{truthjet}/p_T^{ref}$ using the Monte Carlo simulations Pythia8 (red) and Sherpa2.2 (blue) with EM (a), LC (b) and EMPFlow (c) jets calibrated up to η-intercalibration as a function of p_T^{ref}. Bottom graph shows the data-to-Monte Carlo ratio. The widths are estimated with a Gaussian fit. Error bars correspond to statistical uncertainties on the fit.

To compute the in-situ jet energy resolution, the quantity $\sigma(p_T^{truth}/p_T^{ref})$ is quadratically subtracted from $\sigma(\frac{p_T^{jet}}{p_T^{ref}})$ as described in Equation (6.16). Figure 5.4 shows the JER using EM (a), LC (b) and EMPFlow (c). The nominal JER is computed with Pythia8, and a comparison with Sherpa is also shown. The JER fully estimated with Pythia8 is used to compute the non-closure uncertainty. The bottom graph shows the ratio between $\sigma_{in-situ}$ and $\sigma_{in-situ}^{MC}$ for both Pythia8 and Sherpa. Large differences are seen at low p_T between $\sigma_{in-situ}$ and $\sigma_{in-situ}^{Pythia8}$ that are attributed to the pile-up activity. Differences are smaller using the particle flow. The comparison between the three resolutions is illustrated in Figure 5.5. An improvement of 7% and 4% in the JER is observed at 40 GeV and 45 GeV using the particle flow.

The JER as a function of η is shown in Figure 5.6. The bottom graphs show the differences between σ_{insitu} and σ_{insitu}^{MC} for both Pythia8 and Sherpa2.2. Jets with particle flow are better reproduced by the simulation, and a reasonable flat distribution is observed. Higher uncertainties are observed in large $|\eta|$ where the statistics of the γ+jet method is smaller and the performance of the calorimeter is weaker than in the central region.

5.4.3 Systematics uncertainties

The uncertainties on the jet energy resolution include uncertainty on non-closure, photon energy resolution, Monte Carlo, photon energy scale, sub-leading jet veto, Jet Vertex Tagging, $\Delta\Phi$ cut, and statistical uncertainty. The OOC is not included in the uncertainties and an additional non-closure effect is included compared to JES uncertainties. In the current version, the purity uncertainty is not added.

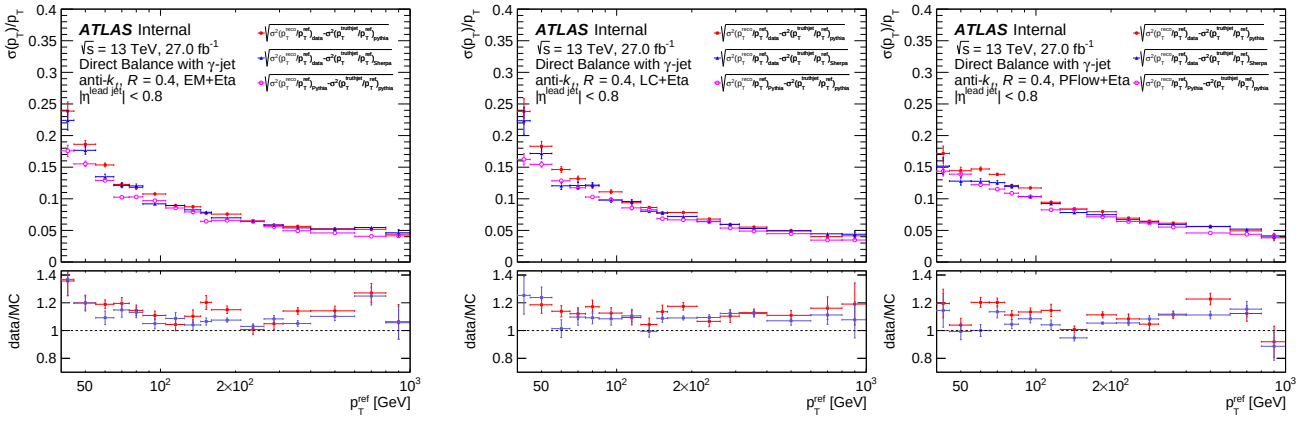

(a) *(b)* *(c)*

Figure 5.4: Jet energy resolution as a function of p_T^{ref} with EM (a), LC (b) and EMPFlow (c) jets calibrated up to the η-intercalibration, using 2016 data and Pythia8 (red points), 2016 data and Sherpa2.2 (up triangles), and Pythia8 only (pink circles). The width of the distributions are estimated with a Gaussian fit. The bottom graph shows the ratio between the JER extracted from data and MC, and the JER extracted from MC only, for both Pythia8 and Sherpa2.2. Error bars show the statistical uncertainties of the fit.

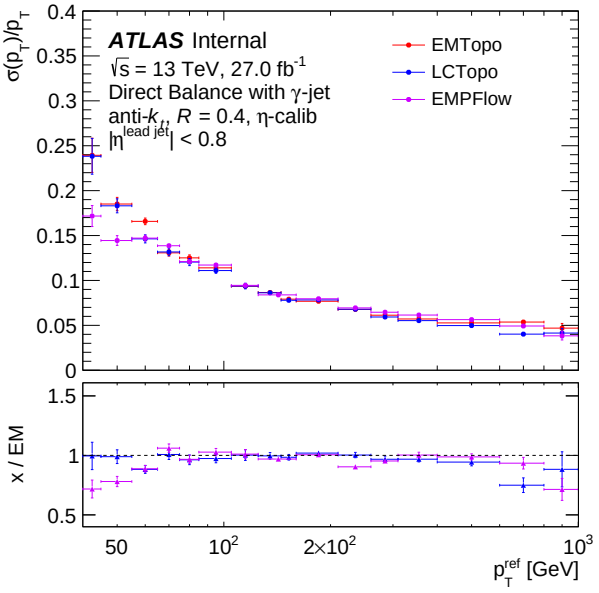

Figure 5.5: Comparison of the jet energy resolution between EM (a), LC (b) and EMPFlow (c) jets calibrated up to the η-intercalibration as a function of p_T^{ref} using 2016 data. The bottom graphs show the ratio between resolution of LC and EM jets (blue), and between EMPFlow and EM jets (pink). Error bars show the statistical uncertainties.

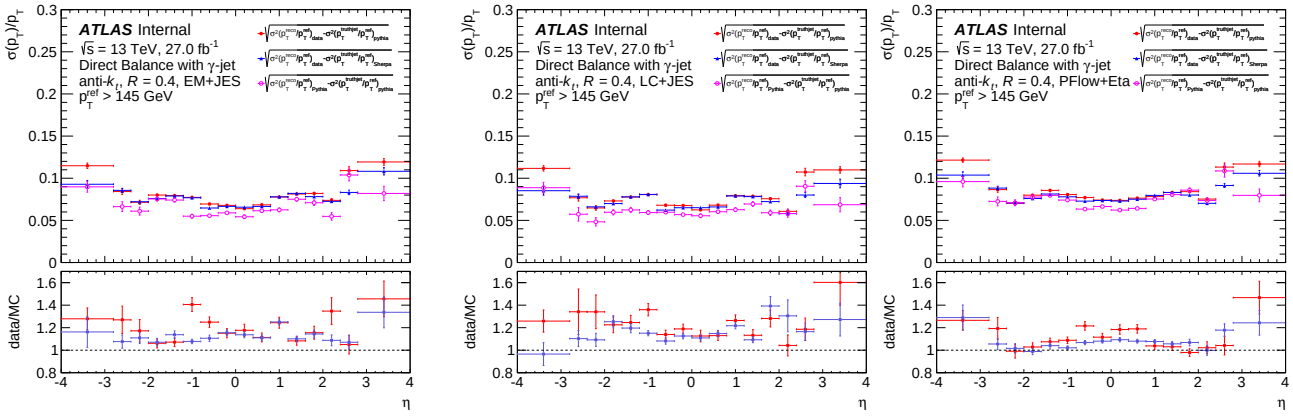

(a) *(b)* *(c)*

Figure 5.6: Jet energy resolution (JER) as a function of η with EM (a), LC (b) and EMPFlow (c) jets calibrated up to the η-intercalibration. The JER is extracted from the in-situ method using 2016 data and Pythia8 (red points), 2016 data and Sherpa2.2 (up triangles), and Pythia8 only (pink circles). The width of each distribution is computed with a Gaussian fit. The bottom graph shows the ratio between the JER extracted from data and Monte Carlo, and the JER extracted from Monte Carlo only, for both Pythia8 and Sherpa2.2. Error bars indicate the statistical uncertainties of the fit.

5.4.3.1 Non-closure uncertainty

The non-closure uncertainty corresponds to the dominant uncertainties of the JER. This uncertainty is defined in Equation (5.9) and the terms used to compute the non-closure uncertainty are shown in Figure 5.7. The ratio $\sigma_{in-situ}/\sigma_{MC}$ is shown in bottom part. The non-closure uncertainty tends to be smaller at low p_T.

$$\Delta_{closure} = \frac{\sigma_{in-situ}^{Pythia8} - \sigma_{Pythia8}}{\sigma_{in-situ}}. \tag{5.9}$$

5.4.3.2 JER uncertainty

The uncertainty up (a) and down (b) on EM jets calibrated with the full in-situ calibration is shown in Figure 5.8. The total uncertainty is estimated to 15% (a) and 18% (b) below 55 GeV, and is dominated by the non-closure effect. The uncertainty at low p_T is slightly higher with the loose selection on the sub-leading jet veto (b) than with the tight selection (a). The uncertainty decreases to ∼10-11% between 55 GeV and 400 GeV, increases to ∼18% below 800 GeV, and to 36-38% above 800 GeV due to statistics. The uncertainty is globally dominated by the non-closure component. From 500 GeV, the uncertainty down on the sub-leading jet cut (veto) is increased due to a tighter selection on the second jet, and less statistics.

A similar uncertainty is estimated with LC jets (Figure 5.9). The uncertainty down (a) is reasonably constant at the level of ∼10% between 40 GeV and 400 GeV. It is dominated by the Monte Carlo uncertainty below 65 GeV and by the non-closure effect between 85 GeV an 400 GeV. A small increase due to the non-closure component is observed between 200 and 400 GeV. Above 400 GeV, the uncertainty on the sub-leading jet veto is increased due to less statistics. The uncertainty up (b) is slightly higher at low p_T due to the sub-leading jet veto.

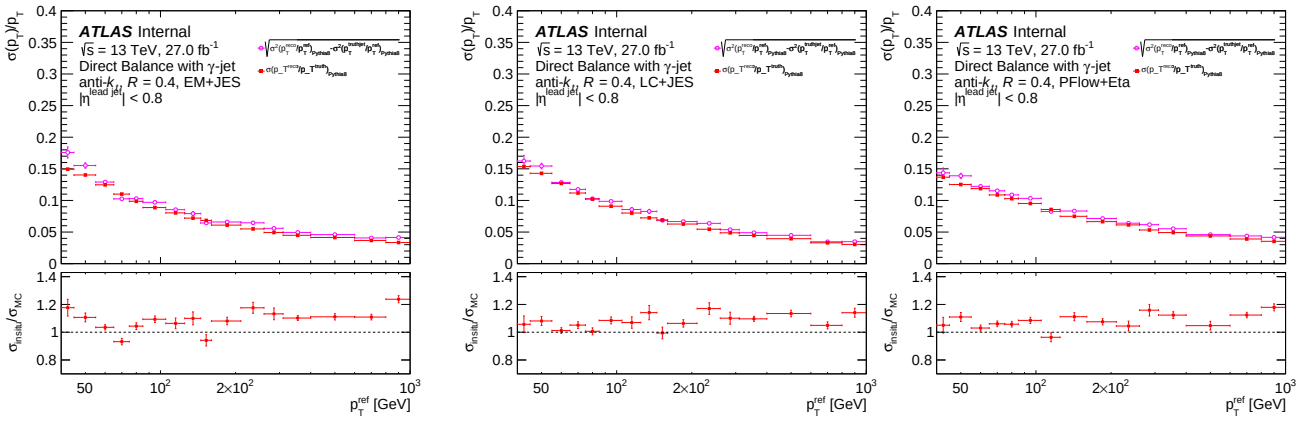

(a) (b) (c)

Figure 5.7: Estimation of the jet energy resolution (JER) as a function of p_T^{ref} with the Monte Carlo simulation Pythia8, using EM (a), LC (b) and EMPFlow (c) jets. In red (square) the JER is extracted from the in-situ Direct Balance method, in pink (circle) the JER is estimated from the Gaussian distribution of p_T^{jet}/p_T^{truth}. The bottom graph shows the ratio between the JER extracted from the in-situ method, and the JER extracted from the Gaussian distribution of p_T^{jet}/p_T^{truth}. Error bars show the statistical uncertainties of the fit.

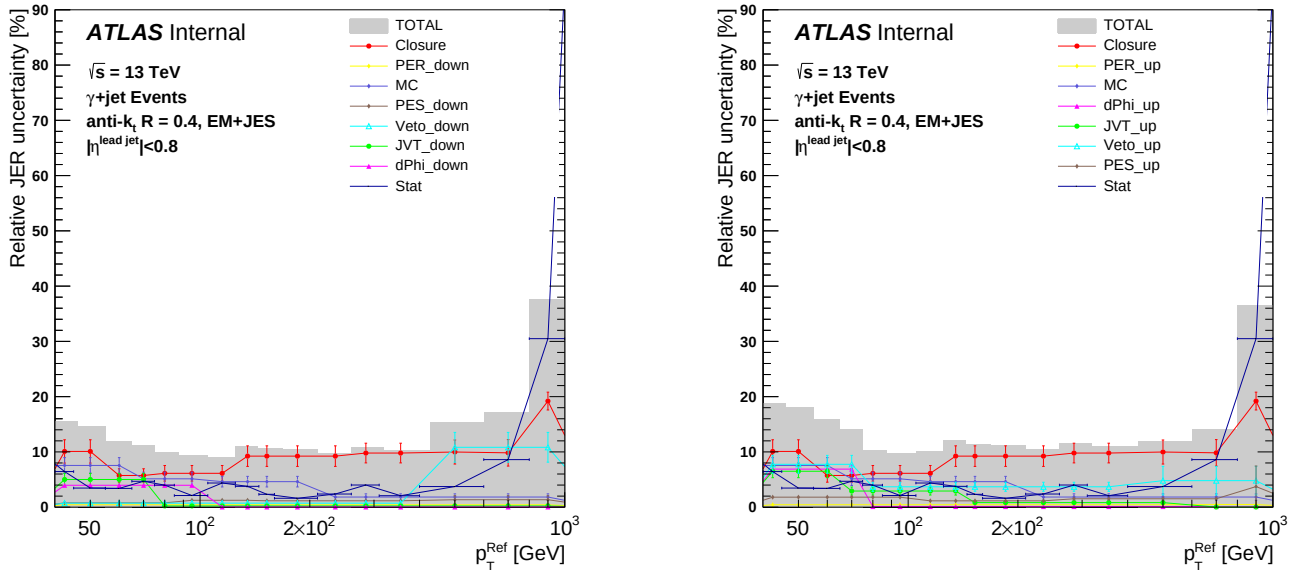

(a) (b)

Figure 5.8: Systematic uncertainties on the jet energy resolution (JER) as a function of p_T^{ref} with EM jets calibrated with the full in-situ calibration. Uncertainties with down variations (a) and up variations (b) are shown using 2016 data. The total uncertainty is illustrated in grey area and is computed with the quadratic sum of each uncertainty, including uncertainties on non-closure, photon energy resolution, Monte Carlo, photon energy scale, sub-leading jet veto, JVT, $\Delta\Phi$ cut, and statistical uncertainty. Error bar are estimated using a bootstrap method. A rebinning algorithm has been used to merge non-significant statistical variations.

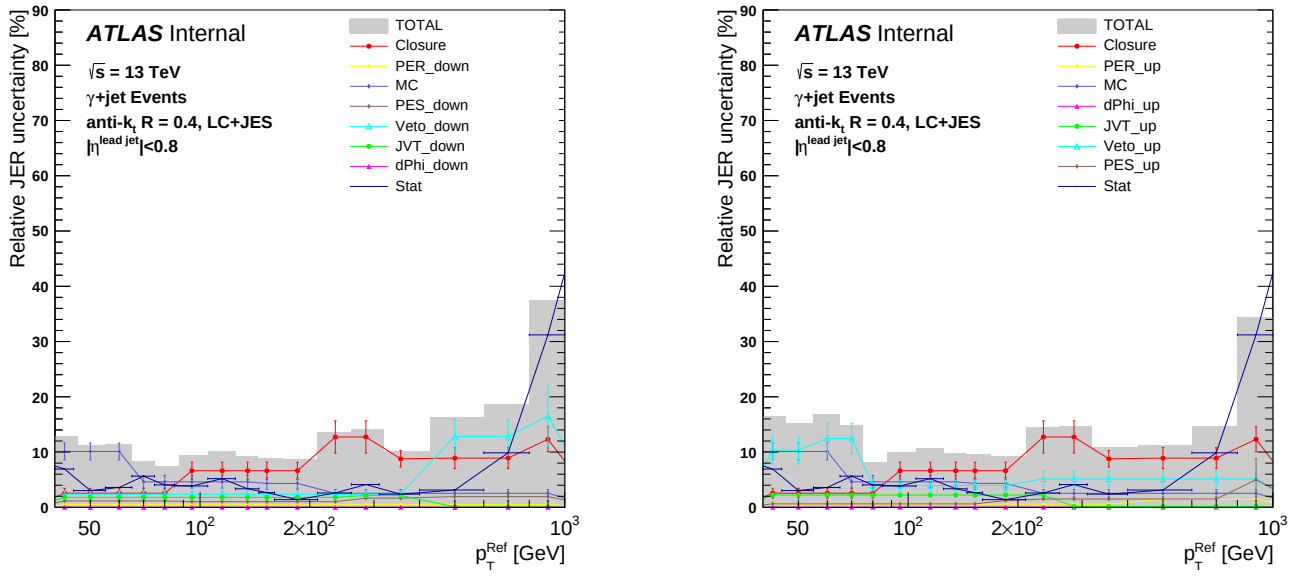

(a) *(b)*

Figure 5.9: Systematic uncertainties on the jet energy resolution (JER) as a function of p_T^{ref} with LC jets calibrated with the full in-situ calibration. Uncertainties with down variations (a) and up variations (b) are shown using 2016 data. The total uncertainty is illustrated in grey area and is computed with the quadratic sum of each uncertainty, including uncertainties on non-closure, photon energy resolution, Monte Carlo, photon energy scale, sub-leading jet veto, JVT, $\Delta\Phi$ cut, and statistical uncertainty. Error bar are estimated using a bootstrap method. A rebinning algorithm has been used to merge non-significant statistical variations.

Uncertainties with EMPFlow jets are shown in Figure 5.10. Below 65 GeV, the uncertainty is estimated at the level of 18-22% and is dominated by the uncertainty on the MC and sub-leading jet selections. The uncertainty between 65 GeV and 600 GeV is flat at the level of 10% and is dominated by the non-closure effect. The uncertainty sharply increases at 800 GeV to 34% due to the statistical component.

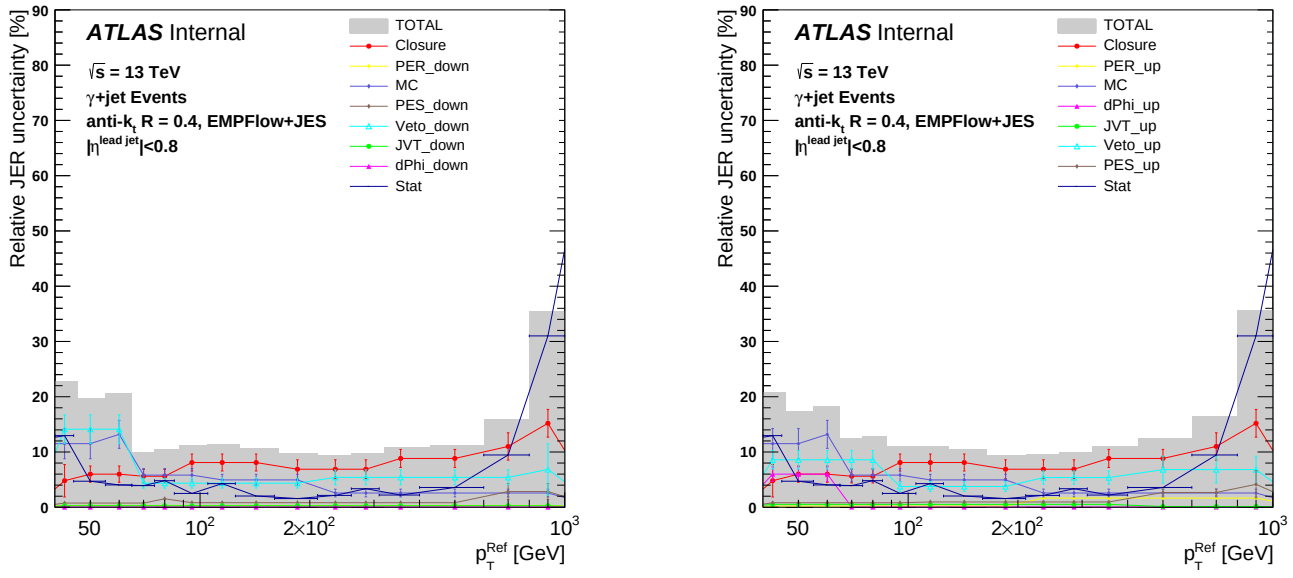

(a) *(b)*

Figure 5.10: Systematic uncertainties on the jet energy resolution (JER) as a function of p_T^{ref} with EMPFlow jets calibrated up to the η inter-calibration. Uncertainties with down variations (a) and up variations (b) are shown using 2016 data. The total uncertainty is illustrated in grey area and is computed with the quadratic sum of each uncertainty, including uncertainties on non-closure, photon energy resolution, Monte Carlo, photon energy scale, sub-leading jet veto, JVT, $\Delta\Phi$ cut, and statistical uncertainty. Error bar are estimated using a bootstrap method. A rebinning algorithm has been used to merge non-significant statistical variations.

5.5 Conclusion

This chapter presents the measurement of the jet energy resolution (JER) with the γ+jet Direct Balance method. The JER is extracted using the 2016 data with EM, LC, and EMPFlow jets. A resolution of $\sim$24% is obtained with EM and LC jets, and 17% with EMPflow at 40 GeV. The particle flow provides great improvements in the jet resolution at low p_T. A resolution of 4-5% is obtained at 1 TeV for all the jet schemes. The JER uncertainty is mostly dominated by the non-closure effect, and is estimated to 10-20% below 55 GeV, 10-11% between 55 GeV and 400 GeV, and 35-38% at 800 GeV. The combination with the other in-situ methods should be done in the future.

Chapter 6

The 0-lepton analysis

"La liberté intérieure permet de savourer la simplicité limpide du moment présent, libre du passé et affranchi du futur. "

Matthieu Ricard

Contents

6.1 Introduction

Supersymmetry is an extension of the Standard Model that unifies bosons and fermions. The theory predicts the existence of a superpartner for each particle of the Standard Model. Such superpartners could be observed at the LHC if they are light enough. The search for squarks and gluinos using the 2015 and 2016 data (Run2), with $\sqrt{s} = 13$ TeV is presented and includes an integrated luminosity of L = 36.1 fb^{-1}. The increase of the center of mass energy for the Run 2 compared to Run 1 ($\sqrt{s} = 8$ TeV) [30, 49, 145–147] allows the increase of the production cross-section of squarks and gluinos [43, 44] and allows covering new regions of the Minimal Supersymmetric Standard Model (MSSM). In the 0-lepton analysis, R-parity is assumed to be conserved, and supersymmetric particles are created in pairs. Another consequence of R-parity conservation is the stability of the Lightest Supersymmetric Particle (LSP). In the analysis, assumption is made that LSP is the lightest neutralino $\tilde{\chi}_1^0$. Since $\tilde{\chi}_1^0$ only interacts by weak interaction, it can only be detected by measuring the reconstructed missing transverse energy E_T^{miss} [148] [**?**] [101]. The masses of sparticles are free parameters and the strategy of the analysis is to search for squarks ($\tilde{q}$) and gluinos ($\tilde{g}$) production assuming the two first generations of squarks are degenerated. The squarks and gluinos are unstable and decay into a cascade of particles until a $\tilde{\chi}_1^0$ is produced. In the 0-lepton analysis, the signal is defined by multiple jets + E_T^{miss} with no lepton in the final state. Various decay modes are studied, such as the direct decay of a $\tilde{q}$ or a $\tilde{g}$ into the LSP: $\tilde{q} \to q\tilde{\chi}_1^0$ or $\tilde{g} \to qq'\tilde{\chi}_1^0$, or one-step decays via an intermediate particle. One-step decays include the emission of an intermediate chargino $\tilde{\chi}^{\pm}$ or a heavy neutralino $\tilde{\chi}_2^0$, and the emission of a Z/W boson in the final state: $\tilde{q} \to q\tilde{\chi}_1^{\pm} \to qW\tilde{\chi}_1^0$, $\tilde{g} \to \tilde{\chi}_1^{\pm}qq' \to qq'W\tilde{\chi}_1^0$ or $\tilde{g} \to \tilde{\chi}_2^0 qq' \to qq'Z\tilde{\chi}_1^0$.

The strategy of the analysis for the search of squarks and gluinos is described in section 6.2. Background processes and event selections are described in sections 6.3 and 6.4. A large contribution to the analysis during my Ph.D was on the signal optimizations and is described in section 6.5. The methods for background estimation and systematics uncertainties are described in sections 6.6 and 6.7. Informations on the fits are described in section 6.8, and the section 6.9 shows the results of the analysis.

6.2 Analysis strategy

The analysis is based on various selections applied to the data using discriminating variables to optimize the signal significance. The choice of discriminating variables and selections defines the signal regions (SRs). The optimization procedure and definition of the signal regions are described in section 6.5.3 and 6.5.5. Methods have been set up to estimate the Standard Model background in each signal region. Specific control regions (CRs) based on data are defined for each signal region to improve the background estimation. To test the background estimations in the SRs, specific validation

regions (VRs) are defined. A likelihood fit was performed for each SR assuming a background-only hypothesis to test the compatibility of the observed events in the VRs with the corresponding SM background-only expectation. The description of CRs and VRs is detailed in section 6.6. To extract the final results, a likelihood fit is performed. The fit determines the compatibility of the observed event yield in each SR with the corresponding Standard Model background-only fit expectation. If no excess is observed, model-dependant fits are applied to set exclusion limits on specific SUSY models. Two independent approaches are performed using a different set of optimization variables: m_{eff} and RJigsaw. For each SUSY model, the approach with the best sensitivity is chosen for the final results. In the following, the m_{eff} analysis will be presented with a focus on the contributions of the Ph.D. The Recursive Jigsaw (RJR) is a second and complementary approach using another set of kinematic variables. This approach have shown an improvement in the sensitivity of the searches in the SUSY models with small mass splitting between the sparticles (compressed spectra). The method is detailed in reference [48]. The results between both analysis are compared in section 6.9.

6.3 Background processes

The signal is characterized by at least two jets and missing transverse momentum in the detector with no lepton in the final state. The background corresponds to the Standard Model processes reproducing the signal. The main backgrounds are the following: Z+jets, W+jets, diboson, top and QCD.

Z+jet background consists of four components: Z$\rightarrow e^+e^-$, Z$\rightarrow \mu^+\mu^-$, Z$\rightarrow \tau^+\tau^-$ and Z$\rightarrow \nu\nu$. The two first components can be suppressed by requiring no lepton in the final state. The τ final leptons have a high probability to decay hadronically and be reconstructed as jets. This contribution is negligible with the selection applied on E_T^{miss}. The main Z+jets background is due to the Z$\rightarrow \nu\nu$ events. This background is irreducible and needs to be estimated.

W+jets events are also one of the largest 0-lepton backgrounds. The W can decay into (eν), ($\mu\nu$), ($\tau\nu$). The two first processes are largely reduced by requiring no lepton in the final state. The third one is dominant since the τ has a high probability to decay hadronically (65%) and to be reconstructed as a jet.

Diboson production (WW, WZ, ZZ) has large possible contributions of final states with multiple jets and escaping neutrinos. This background is dominated by WZ productions, with W$\rightarrow$qq and Z$\rightarrow \nu\nu$.

Top background includes top pair production and single top production. The top mainly decays into t$\rightarrow$bW (BR=99.8%). As for the W+jets background, if the W decays into an e/$\mu + \nu$, the background is suppressed with the lepton veto. The W$\rightarrow \tau\nu$ events are harder to suppress due to τ hadronization and reconstruction. The contribution of top background increases for large jet multiplicity.

The **QCD background**, or **multijet** background is characterized by events with mis-measured jets with fake missing transverse energy, or heavy flavour jets with emission of a neutrino in the final state. For this background, the E_T^{miss} is aligned to the mis-reconstructed jet. This property is used to reject QCD background. This effect is difficult to simulate efficiently and a fully data driven technique is used to estimate this background.

Each of these backgrounds has a specific estimation procedure detailed in section 6.6.

6.4 Event selection

6.4.1 Triggers

A selection is promptly applied on 2015 and 2016 data using specific triggers. The triggers require reconstructed E_T^{miss} [102] in the detector. The threshold of the triggers increased from 2015 to 2016 due to a larger pile-up. An offline selection of 250 GeV on E_T^{miss} is added in the pre-selection to obtain a 100% trigger efficiency.

6.4.2 Event cleaning

A first selection is applied on the data quality. The selection is based on the run number and luminosity block number. The jet cleaning [137] is a set of selections to reject reconstructed jets from non-collision processes. The selection criteria are based on jets properties and are used to distinguish jets candidates which do not originate from the proton-proton hard scattering collisions. The non-collision processes include detector noise, cosmic muons and beam halo. A loose cleaning selection is applied on all jets and a tight [137] selection is applied on the two leading jets. To reject the non-collision background, a selection on the jet time is applied. Events with jets reconstructed in a non functioning Tile module are rejected if the transverse missing energy is aligned with the jet. Muons which do not originate from the primary vertex are rejected to remove fake muons and cosmic muons.

6.4.3 Pre-selection

At least one primary vertex must be reconstructed. A threshold of 250 GeV is applied on E_T^{miss}, the efficiency of the trigger at this level is then 100%. A selection on the p_T of the two first jets is applied: p_T^{jet1} > 200 GeV and p_T^{jet2} > 50 GeV. A threshold is applied on the angle $\Delta\phi$ between jets and E_T^{miss}, with $\Delta\phi(j_{1,2,(3)}, met)$>0.4 to reject QCD background. A selection of 800 GeV on m_{eff} is required, with $m_{eff} = \sum_{i=1}^{n} |p_T^i| + E_T^{miss}$. More informations on m_{eff} and discriminating variables are provided in section 6.5.1.

6.4.4 Objects reconstruction

The selections applied for the objects reconstruction are summarized in Table 6.1 and 6.2. Jets with p_T> 20 GeV and $|\eta|$ <2.8 are selected [137]. A selection on JVT is applied to reject pile-up (Table 6.1 (a)). Photons with $p_T > 25$ GeV, and $|\eta| < 2.37$ are selected [149] (Table 6.1 (b)). Electrons [93] candidates are required to satisfy $p_T > 7$ GeV and $|\eta| < 2.47$ (Tabel 6.2 (a)). Muons [114] candidate must have $p_T > 7$ GeV, $|\eta| < 2.7$ (Table 6.2 (b)).

6.5 Signal optimization

6.5.1 Discriminating variables

Discriminating variables are used for the optimization of the signal region. The choice of the selections on these variables defines the signal regions and is detailed in section 6.5.5. This section defines all of the discriminating variables used in the analysis: N_{jet}, E_T^{miss}, p_T^{jets}, $|\eta_{jets}|$, m_{eff}, H_T, $\Delta\phi(jet, E_T^{miss})$, $\frac{E_T^{miss}}{\sqrt{H_T}}$, $\frac{E_T^{miss}}{m_{eff}(N_j)}$ and aplanarity. All these variables are directly used to define the signal regions:

Table 6.1: Description of the jet (a) and photon (b) pre-selections.

Cut	Value/description
Baseline jet	
Algorithm	anti-k_t4Topo $R = 0.4$
Acceptance	$p_{\mathrm{T}} > 20$ GeV, $\lvert\eta\rvert < 2.8$
Pileup suppression	$p_{\mathrm{T}} > 60$ GeV $\lVert \lvert\eta\rvert > 2.4 \rVert$ JVT > 0.59
b-jet	
b-tagging algorithm	MV2c10 at 77% efficiency point
Acceptance	$p_{\mathrm{T}} > 50$ GeV , $\lvert\eta\rvert < 2.5$
Reclustered jet	
Algorithm	anti-k_t $R = 1.0$
Input	Baseline jets with $p_{\mathrm{T}} > 25$ GeV

(a)

Cut	Value/description
Baseline photon	
Acceptance	$p_{\mathrm{T}} > 25$ GeV, $\lvert\eta\rvert < 2.37$
Quality	Loose
Overlap	$\Delta R(\gamma, \mathrm{jet}) > 0.4$
Signal photon	
Quality	Tight
Isolation	FixedCutTight

(b)

Table 6.2: Description of the electron (a) and muon (b) pre-selections.

Cut	Value/description
Baseline electron	
Algorithm	AuthorElectron
Acceptance	$p_{\mathrm{T}} > 7$, GeV, $\lvert\eta^{\mathrm{clust}}\rvert < 2.47$
Quality	LooseLH
Overlap	$\Delta R(e, \mathrm{jet}) > 0.4$
Signal Electron	
Acceptance	$p_{\mathrm{T}} > 7GeV$
Quality	TightLL
Isolation	GradientLoose
Track	$\lvert z_0^{PV} \cdot \sin\theta\rvert < 0.5$ mm
	$\lvert d_0^{PV}\rvert/\sigma(d_0^{PV}) < 5$

(a)

Cut	Value/description
Baseline muon	
Acceptance	$p_{\mathrm{T}} > 7GeV, \lvert\eta\rvert < 2.7$
Quality	Medium
Overlap	$\Delta R(\mu, \mathrm{jet}) > 0.4$
Signal muon	
Acceptance	$p_{\mathrm{T}} > 7GeV$
Isolation	GradientLoose
Track	$\lvert z_0^{PV} \cdot \sin\theta\rvert < 0.5$ mm
	$\lvert d_0^{PV}\rvert/\sigma(d_0^{PV}) < 3$

(b)

- The jet multiplicity N_{jet} is the minimal number of jets required in the event after the pre-selection. A selection p_T > 50 GeV is applied on each jet. N_{jet} is related to the decay mode of squarks and gluinos. The selections applied on the jet multiplicity depends on the decay mode and are usually lower for direct decay modes and higher for one-step decay modes. The jet multiplicity selection varies between 2 and 6 jets. A specific analysis is dedicated to higher jet multiplicity selections [150];

- The variable E_T^{miss} is reconstructed as the opposite of the transverse momentum sum of the objects measured in the detector: $\overrightarrow{E}_T^{miss} = -\sum \overrightarrow{p_T}$. With a perfect measurement of the p_T of all the particles originating from the collision, this value would be very close to zero. A high value of E_T^{miss} can arise from the mis-measurement of the p_T of the particles in the detector (fake E_T^{miss}), from emission of Standard Model particles in the final state that do not interact in the detector (neutrinos) or neutralinos in the case of the MSSM. A threshold on E_T^{miss} is applied at the pre-selection. The selection on the E_T^{miss} is not directly used for optimisation but is usually combined with m_{eff} or H_T;

- The effective mass is defined as $m_{eff} = \sum_{i=1}^{n} |p_T^i| + E_T^{miss}$. The selection on this variable depends on the supersymmetric model and tends to be harder for SUSY models with higher $m_{\tilde{q}}$ or $m_{\tilde{g}}$, for a fixed m_{LSP}. The variants $m_{eff}(N_j)$ and $m_{eff}(Incl)$ are also used and are defined, respectively, as $m_{eff(N_j)} = \sum_{i=1}^{N_j} |p_T^i| + E_T^{miss}$ and $m_{eff}(Incl) = \sum_{\substack{i=1 \\ p_T>50GeV}}^{n} |p_T^i| + E_T^{miss}$;

- H_T is defined as $H_T = \sum_{i=1}^{n} |p_T^i|$ and is characteristic of the jet activity of the event. The variable H_T is not used directly but is combined with E_T^{miss} to compute the E_T^{miss} significance;

- $\Delta\phi(jet, E_T^{miss})$ is a measure of the alignment between the jets $\overrightarrow{p_T}$ and $\overrightarrow{E}_T^{miss}$ and is a powerful variable to reject fake missing transverse energy due to detector mis-measurement or neutrino emission in the jet hadronization. Two variables are defined: $\Delta\phi(jet_{1,2,(3)}, E_T^{miss})$, and $\Delta\phi(jet_{i>3}), E_T^{miss})$. These variables are among the main selections to reject the QCD background.

- $\frac{E_T^{miss}}{\sqrt{H_T}}$ is the E_T^{miss} significance. This variable is highly correlated to the E_T^{miss} and takes into account the jet activity of the event. This variable allows a more efficient background rejection than selecting on E_T^{miss} and jets p_T separately for squarks models with direct decays;

- $\frac{E_T^{miss}}{m_{eff}(N_j)}$ is also highly correlated with $\frac{E_T^{miss}}{\sqrt{H_T}}$, and only one of them is used in a signal region. For direct decays, the variable $\frac{E_T^{miss}}{m_{eff}(N_j)}$ usually gives better performances for $\tilde{g}\tilde{g}$ production while $\frac{E_T^{miss}}{\sqrt{H_T}}$ is more used for $\tilde{q}\tilde{q}$;

- Aplanarity: The aplanarity is defined from the sphericity tensor and characterize the distribution of the energy clusters [151]. The aplanarity is computed only for events with at least 4 jets.

6.5.2 Discriminating variable distributions

This section shows the distributions of each discriminating variables after a 2-jets events pre-selection using 2015+2016 data (black points) compared to the Standard Model background expectation from simulation. Each coloured area represents the estimation of a specific background: multijet

(dark blue), diboson (pink), Z+jet (orange), W+jets (blue) and top (green). The purple and blue lines represent respectively the $\tilde{q}\tilde{q}$ and $\tilde{g}\tilde{g}$ one-step decay signals with emission of intermediate charginos for the models ($m_{\tilde{q}}$,$m_{\tilde{\chi}_0^\pm}$,$m_{\tilde{\chi}_1^0}$) = (900,160,60) and ($m_{\tilde{g}}$,$m_{\tilde{\chi}_0^\pm}$,$m_{\tilde{\chi}_1^0}$) = (1700,160,60). The ratio between data and Standard Model background expectation is shown on the bottom of each plot.

Figure 6.1 (a) shows the jet multiplicity distribution. The number of events in data with 2 jets multiplicity is approximately 30000 and progressively decreases to less than 1500 events after 6-jets selection and to less than 25 events after a 9-jets selection. The selections applied on the jet multiplicity after the optimisation are respectively 5j and 6j for the $\tilde{q}\tilde{q}$ and $\tilde{g}\tilde{g}$ signals shown on the distribution. Figure (b) shows the E_T^{miss} distribution. A threshold of 250 GeV is applied for the events pre-selection. The number of events sharply decreases with only 100 events after a 1000 GeV selection on E_T^{miss}. Distributions of p_T^{jet1} and $|\eta^{jet}|$ are respectively shown in (c) and (d). The variable p_T^{jet1} is generally not directly used for the selections, except in the SRs designed for small mass difference. A selection on the pseudo-rapidity is generally applied and varies between 0.8 and 2.8.

Figure 6.2 shows the $\Delta\phi(jet_{1,2,(3)}, E_T^{miss})$ distribution (a), and $\Delta\phi(jet_{i>3}, E_T^{miss})$ (b). No selection on $\Delta\phi$ is applied for (a) to illustrate the QCD background at low $\Delta\phi$, and the selection $\Delta\phi(jet_{1,2,(3)}, E_T^{miss})$ > 0.4 is applied on (b). A cut $\Delta\phi$ > 0.4 is applied in the pre-selection to reject the QCD background. Figure (c) shows the aplanarity, which peaks at low value for the background. Figure (d) shows the $\frac{E_T^{miss}}{m_{eff}(Incl)}$ distribution. If $\frac{E_T^{miss}}{\sqrt{H_T}}$ is used for the optimization, a selection of $\frac{E_T^{miss}}{m_{eff}(2)}$> 0.15 is at least applied.

Figure 6.3 shows the $\frac{E_T^{miss}}{\sqrt{H_T}}$ (a) and m_{eff} (b) distributions. If $\frac{E_T^{miss}}{\sqrt{H_T}}$ (a) is used for the optimization, a selection of $\frac{E_T^{miss}}{\sqrt{H_T}}$> 14 is at least applied. The selection on m_{eff} (b) is one of the main selections and defines the name of the signal region with the jet multiplicity. Events are required to have m_{eff} > 800 GeV to pass the pre-selection. This cut tends to be tightened for SUSY models with high squark/gluino masses.

A good agreement between data and MC is seen after the pre-selection for all the variables.

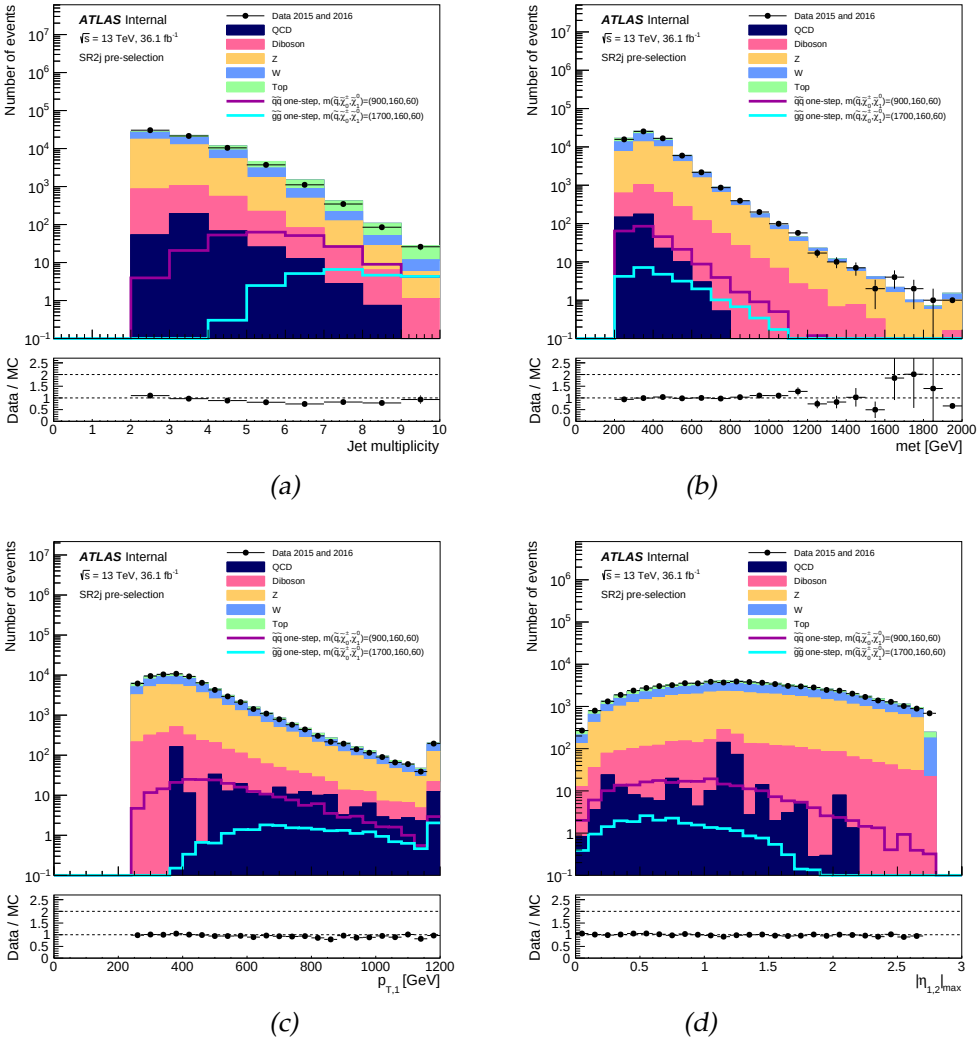

Figure 6.1: Distributions of jet multiplicity (a), E_T^{miss} (b), leading jet p_T (c), and $|\eta|$ after SR2j pre-selection using 2015 and 2016 data (black points). The Monte Carlo background expectation normalized to 36.1 fb^{-1} is illustrated in coloured area. The purple and blue lines respectively show the distribution of $\tilde{q}\tilde{q}$ and $\tilde{g}\tilde{g}$ one-step signals decaying with intermediate chargino. The error bars show the statistical uncertainties. The last bin contains the overflow.

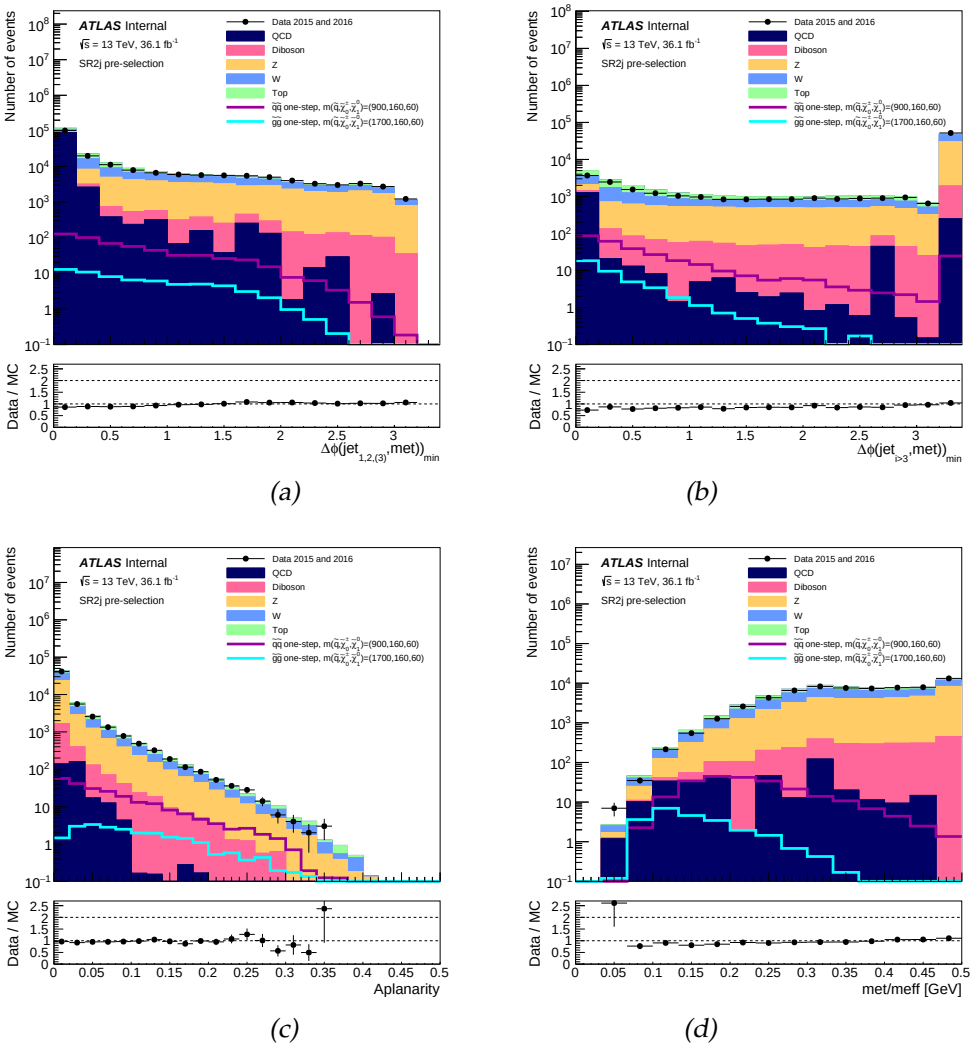

Figure 6.2: Distributions of $\Delta\Phi$ (a), $\Delta\Phi$R (b), aplanarity (c), and $\frac{E_T^{miss}}{m_{eff}(Incl)}$ (d). A SR2j events pre-selection is applied except on $\Delta\Phi$ on (a) and (b). No selections on $\Delta\Phi$ are applied for (a), and the selection $\Delta\phi(jet_{1,2,(3)}, E_T^{miss}) > 0.4$ is applied on (b). Black points represent 2015 and 2016 data. The Monte Carlo background expectation normalized to 36.1 fb^{-1} is illustrated in coloured area. The purple and blue lines respectively show the distribution of $\tilde{q}\tilde{q}$ and $\tilde{g}\tilde{g}$ one-step signals decaying with intermediate chargino. The error bars show the statistical uncertainties.

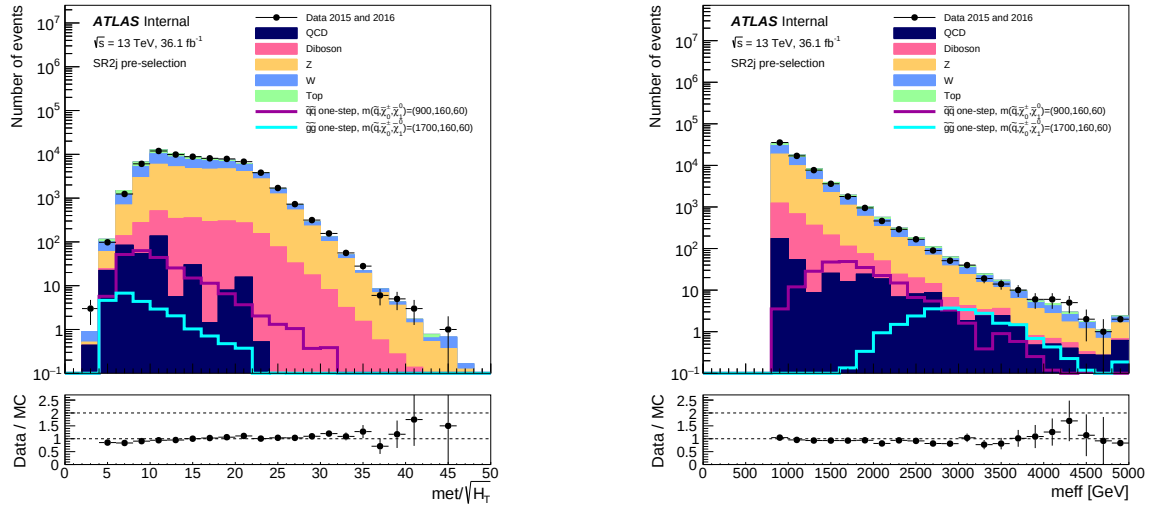

(a) *(b)*

Figure 6.3: Distribution of $\frac{E_T^{miss}}{\sqrt{H_T}}$ (a) and m_{eff}(Incl) (b) after SR2j pre-selection using 2015 and 2016 data (black points). The Monte Carlo background expectation normalized to 36.1 fb^{-1} is illustrated in coloured area. The purple and blue lines respectively show the distribution of $\tilde{q}\tilde{q}$ and $\tilde{g}\tilde{g}$ one-step signals decaying with intermediate chargino. The error bars show the statistical uncertainties. The last bin contains the overflow.

6.5.3 Optimization procedure

The optimization procedure is based on selections applied to the MC using unblinded CRs in order to have an accurate background prediction and systematics uncertainties evaluation. The value of the scale factors are obtained with the fit. Selections are optimized for expected exclusion limits on SUSY models. The main discriminating variables used for the optimization of the significance are N_{jets}, m_{eff}, E_T^{miss}, $\Delta\phi(j, E_T^{miss})$, $\frac{E_T^{miss}}{\sqrt{H_T}}$, or $\frac{E_T^{miss}}{m_{eff(N_j)}}$, p_T^{jets}, η and the Aplanarity. Most of these variables are differently sensitive to $\tilde{q}\tilde{q}/\tilde{g}\tilde{g}$ production and to the decay mode assumption, such as direct or one-step decay. A signal region is defined by a set of selections. Various signal regions have been optimized, each SR's name is defined by the jet multiplicity and the m_{eff} cut. The signal regions optimized for Moriond 2017 with $36.1 fb^{-1}$ are presented in section 6.5.5.

The first step of the optimization procedure is done using the signal and background distributions. On the distributions, signal and background are estimated with theoretical cross-sections normalized to the luminosity. The signal significance is computed with a cut and count method using the Z-value [152–154]. An uncertainty of 10% of the background estimation is included to compute the signal significances. This value corresponds to the average uncertainty of all the signal regions. Various selections are tested to maximize the signal significance. This method is fast, but the background estimation and the treatment of systematic uncertainties are less accurate. This step is used to identify the main discriminating variables and ranges for the cut values.

The second step for the signal region optimization uses the framework HistFitter [155]. The process of the method is the following: various signal regions and control regions are defined. For each signal region, the Standard Model background is estimated with a likelihood fit including CRs and all the systematic uncertainties. The expected exclusion regions are computed for each signal region and the most powerful discriminating signal regions are selected. In this method, the background estimation is data driven and a cross-check is performed on data with validation regions.

Section 6.5.4 describes the decay modes and grids studied in the 0-lepton analysis. These modes have been introduced in the first chapter in section 1.3.6.

6.5.4 One-step decay modes for squark and gluino pair production

Since the parameters of the MSSM [156] including the mass parameters are not fixed by the theory, various assumptions on the decay mode are studied. The 7 simplified models studied for the MSSM squarks and gluinos pair production are shown in Figures 1.10 and 1.11. During my Ph.D, I have optimized the signal regions for $\tilde{q}\tilde{q}$ and $\tilde{g}\tilde{g}$ productions with one-step decay modes. One-step decays include the emission of an intermediate particle before the emission of the lightest neutralino. Several grids are studied as a function of the nature of the intermediate particles and the mass of these sparticles.

The one-step decays of squarks/gluinos pair production with emission of two intermediate charginos are represented in Figures 1.10 (b) and 1.11 (b). In these topologies, the neutralinos and W bosons are produced in chargino decays. By definition, the 0-lepton analysis rejects events when W decays into leptons [157, 158]. Since the mass of the intermediate particle is a free parameter, two grids are used for each mode: one fixing $m_{\tilde{\chi}_1^0}$ = 60 GeV, and the other fixing x = 0.5 with:

$$x = |\frac{m_{\tilde{\chi}_1^\pm} - m_{\tilde{\chi}_1^0}}{m_{\tilde{q}/\tilde{g}} - m_{\tilde{\chi}_1^0}}|. \tag{6.1}$$

In this case, it means:

$$m_{\tilde{\chi}_1^\pm} = \frac{m_{\tilde{q}/\tilde{g}} + m_{\tilde{\chi}_1^0}}{2}. \tag{6.2}$$

The decay modes with one intermediate heavy neutralino and one chargino is represented in Figure 1.10 (c) and 1.11 (c). The decay modes including two intermediate heavy neutralinos is represented in Figure 1.11 (d). Some decay modes may not be allowed if $m_{\tilde{\chi}_2^0} > m_{\tilde{g}}$ for example (Figure 1.11 (d)). Several assumptions on the mass of the intermediate particle are studied and various signal regions have been optimized to test the models. The section 6.5.5 describes the signal regions used in the analysis.

6.5.5 Signal regions

The name of signal regions is defined by the jet multiplicity followed by the m_{eff} selection. Each signal region have been optimized to cover a specific grid region, but can also be used for other grids. The selections defining each signal region for $\tilde{q}$ and $\tilde{g}$ direct decay are described respectively in Table 6.3 and 6.4. The signal regions introduced during my Ph.D are summarized in Table 6.5 and have been optimized for one-step decays. In total, 24 signal regions have been set up including the two regions for boosted bosons (section 6.5.7). A typical signal region includes selections on E_T^{miss}, p_T^{jets}, η^{jets}, $\Delta\phi$, $\frac{E_T^{miss}}{\sqrt{H_T}}$ or $\frac{E_T^{miss}}{m_{eff}}$, m_{eff} and sometimes aplanarity. This set of selections is optimized for an exclusion hypothesis and the expected exclusion plots are represented in section 6.5.8.

Table 6.3: Optimized signal regions selections with $N_{jets} \geq 2$ and $N_{jets} \geq 3$.

Requirement	Signal Region							
	2j-1200	**2j-1600**	**2j-2000**	**2j-2400**	**2j-2800**	**2j-3600**	**2j-2100**	**3j-1300**
$E_{\mathrm{T}}^{\mathrm{miss}}$ [GeV] >	250							
$p_{\mathrm{T}}(j_1)$ [GeV] >	250	300	350				600	700
$p_{\mathrm{T}}(j_2)$ [GeV] >	250	300	350				50	50
$p_{\mathrm{T}}(j_3)$ [GeV] >	–							50
$\lvert\eta(j_{1,2})\rvert$ <	0.8	1.2					–	
$\Delta\phi(\mathrm{jet}_{1,2,(3)}, \vec{E}_{\mathrm{T}}^{\mathrm{miss}})_{\mathrm{min}}$ >	0.8						0.4	
$\Delta\phi(\mathrm{jet}_{i>3}, \vec{E}_{\mathrm{T}}^{\mathrm{miss}})_{\mathrm{min}}$ >	0.4						0.2	
$E_{\mathrm{T}}^{\mathrm{miss}}/\sqrt{H_{\mathrm{T}}}$ [GeV$^{1/2}$] >	14	18					26	16
m_{eff}(incl.) [GeV] >	1200	1600	2000	2400	2800	3600	2100	1300
Optimised for	SS direct with ΔM[GeV]=					SG pMSSM	Compressed	
	O(500)	O(700)	O(1000)	O(1200)	O(1500)	$m_{\tilde{q}}$ ~2500GeV	spectra	

6.5.6 Signal region optimization

This section is related to the optimization of the seven signal regions introduced for one-step decays, and describes the choices made to define each new signal region of the analysis. Each figure shows the distribution of the discriminating variables in one signal region, after the region was optimized with HistFitter. As described in section 6.5.3, the background for the optimization procedure is

Table 6.4: Optimized signal regions selections with $N_{jets} \geq 4$ and $N_{jets} \geq 5$.

Requirement	Signal Region						
	4j-1000	**4j-1400**	**4j-1800**	**4j-2200**	**4j-2600**	**4j-3000**	**5j-1700**
$E_{\mathrm{T}}^{\mathrm{miss}}$ [GeV] >	250						
$p_{\mathrm{T}}(j_1)$ [GeV] >	200						700
$p_{\mathrm{T}}(j_4)$ [GeV] >	100				150		50
$p_{\mathrm{T}}(j_5)$ [GeV] >	–						50
$\lvert\eta(j_{1,2,3,4})\rvert$ <	1.2	2.0					–
$\Delta\phi(\mathrm{jet}_{1,2,(3)}, \vec{E}_{\mathrm{T}}^{\mathrm{miss}})_{\mathrm{min}}$ >	0.4						
$\Delta\phi(\mathrm{jet}_{i>3}, \vec{E}_{\mathrm{T}}^{\mathrm{miss}})_{\mathrm{min}}$ >	0.4						0.2
Aplanarity >	0.04						–
$E_{\mathrm{T}}^{\mathrm{miss}}/m_{\mathrm{eff}}(N_{\mathrm{j}})$ >	0.3	0.25			0.2		0.3
m_{eff}(incl.) [GeV] >	1000	1400	1800	2200	2600	3000	1700
Optimised for	GG direct						
with ΔM[GeV]=	O(300)	O(500)	O(800)	O(1200)	O(1600)	O(2000)	O(200)

Table 6.5: Optimized signal regions selections with $N_{jets} \geq 5$ and $N_{jets} \geq 6$.

Requirement	Signal Region						
	5j-1600	**5j-2000**	**5j-2600**	**6j-1200**	**6j-1800**	**6j-2200**	**6j-2600**
$E_{\mathrm{T}}^{\mathrm{miss}}$ [GeV] >	250						
$p_{\mathrm{T}}(j_1)$ [GeV] >	200						
$p_{\mathrm{T}}(j_5)$ [GeV] >	50				100		
$p_{\mathrm{T}}(j_6)$ [GeV] >	–			50	100		
$\lvert\eta(j_{1,,,6})\rvert$ <	2.8			2.0	2.0	–	
$\Delta\phi(\mathrm{jet}_{1,2,(3)}, \vec{E}_{\mathrm{T}}^{\mathrm{miss}})_{\mathrm{min}}$ >	0.4		0.8	0.4			
$\Delta\phi(\mathrm{jet}_{i>3}, \vec{E}_{\mathrm{T}}^{\mathrm{miss}})_{\mathrm{min}}$ >	0.2	0.4		0.2			
Aplanarity >	0.08	–		0.04	–	0.08	
$E_{\mathrm{T}}^{\mathrm{miss}}/m_{\mathrm{eff}}(N_{\mathrm{j}})$ >	0.15	–		0.25	0.2		0.15
$E_{\mathrm{T}}^{\mathrm{miss}}/\sqrt{H_{\mathrm{T}}}$ [GeV$^{1/2}$] >	–	15	18	–			
m_{eff}(incl.) [GeV] >	1600	2000	2600	1200	1800	2200	2600

estimated with a fit on the CRs including each source of systematic uncertainty, while for the distributions the background is estimated with the theoretical cross-sections normalized to L = 36.1 fb^{-1}, with 10% of uncertainty. Each selection of the signal region is applied except the selection on the variable shown. The nominal selections are illustrated with red arrows. In the following, these distributions are called N-1 distributions.

The distributions of E_T^{miss} (met), p_T^{jet1}, $|\eta^{jet1,2,..}|$, $\Delta\phi$, aplanarity, $\frac{E_T^{miss}}{m_{eff(N_j)}}$, $\frac{E_T^{miss}}{\sqrt{H_T}}$, m_{eff} and N_{jet} are respectively shown for SR5j-1600 (fig. 6.4), SR5j-2000 (fig. 6.5), SR5j-2600 (fig. 6.6), SR6j-1200 (fig. 6.7), SR6j-1800 (fig. 6.8), SR6j-2200 (fig. 6.9), SR6j-2600 (fig. 6.10). Each figure includes the distributions of background (coloured area) and various signal points (coloured lines). The background includes estimation of diboson (pink), Z+jets (orange), W+jets (blue), top (green). The QCD background is negligible in the signal regions after the selections, and has not been included in the distributions. The last bin of each distribution corresponds to the overflow. The bottom of the distributions shows the significance as a function of the selection applied. The continuous lines show the significances for lower cut values, while dotted lines represent significances for upper cut values.

Various SUSY models are shown on each distribution. The name of the signal models is included in the legend (e.g SS_onestepCC_900_160_60 in Figure 6.4). The name contains the nature of sparticles pair production: SS ($\tilde{q}\tilde{q}$) or GG ($\tilde{g}\tilde{g}$); the decay mode (one-step); the nature of the intermediate sparticles: CC, N2, or N2C, respectively for two charginos, two heavy neutralinos, and one heavy neutralino plus one chargino; and the mass parameters of the sparticles. Each model is defined by 3 mass parameters including in the order: squarks/gluino mass ($m_{\tilde{q}/\tilde{g}}$), the intermediate sparticle mass ($m_{\tilde{\chi}_1^\pm/\tilde{\chi}_2^0}$), and the mass of LSP ($m_{\tilde{\chi}_1^0}$).

Figure 6.4 shows the N-1 variable distributions of the signal region 5j-1600. Four signals are included in the distributions and are illustrated with different coloured lines. The signal region 5j-1600 has been optimized using the signal SS_onestepCC_900_160_60 (blue line) which corresponds to $\tilde{q}$ pair production, with one-step decay, and m($\tilde{q}$,$\tilde{\chi}_0^\pm$,$\tilde{\chi}_1^0$) = (900,160,60) GeV. This signal was used for the optimization to define a signal region covering the intermediate region of SS_onestepCC_mlsp60 grid (Figure 6.17). The cut on $\Delta\phi$ is at 0.4 to reject the QCD background. The aplanarity cut is optimized at 0.08 using HistFitter. The selection on m_{eff} was optimized at 1600 GeV. The signal model SS_onestepCC_1100_460_60 (purple line) corresponds to the same decay topology using higher mass parameters for $m_{\tilde{q}}$ and $m_{\tilde{\chi}_0^\pm}$. In the SR5j-1600, the nominal significance for SS_onestepCC_900_160_60 and SS_onestepCC_1100_460_60 with the configuration described above are respectively 1.7 and 1.4. The three other points: SS_onestepCC_1100_460_60, SS_onestepCC_1125_575_25 (Figure 6.14), and SS_onestepN2C_1200_190_60 (Figure 6.20) have not been used for the optimization. The significance for these signals could probably by increased with a tighter selection on m_{eff}.

Figure 6.5 shows the N-1 distributions for the signal region 5j-2000. This signal region was optimized to cover the intermediate region (Δm($\tilde{q}, \tilde{\chi}_1^\pm$) $\sim$ 100 GeV) of $\tilde{q}\tilde{q}$ production with one-step decay including emission of two intermediate charginos (Figure 6.17). This region also covers high chargino mass region with one intermediate chargino and heavy neutralino (Figure 6.20). The region SR5j-2000 has been optimized with the signal SS_onestepCC_1000_900_60 (dark blue). This point is very closed to the boosted region (section 6.5.7) and was not covered by any signal region before SR5j-2000. The signal SS_onestepCC_1100_860_60 (purple line) is also shown on the Figure 6.5. The signal SS_onestepN2C_1200_1150_60 is included in N2C grid (Figure 6.20). The significance of this point can be improved by increasing the $\frac{met}{\sqrt{H_T}}$ cut.

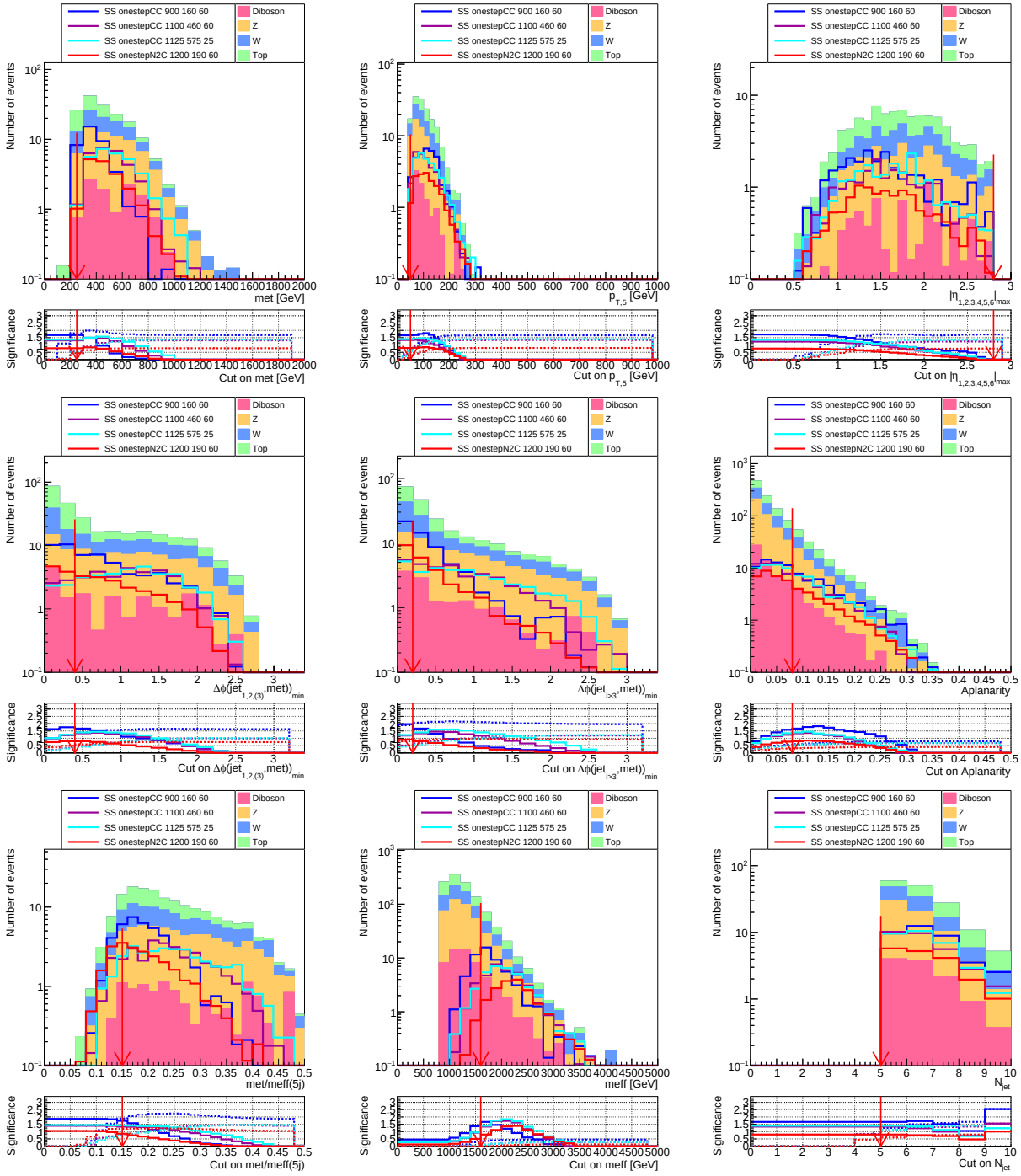

Figure 6.4: Distributions of discriminating variables in the signal region 5j-1600 using simulated events at $\sqrt{s}$ = 13 TeV. The Standard Model background expectation is illustrated in coloured areas and includes diboson, Z+jets, W+jets and top backgrounds. Various one-step decay signals with emission of two intermediate charginos (CC) or heavy neutralino and chargino (N2C) are shown with coloured lines. At the bottom of the distributions, the signal significance as a function of the cut value is shown. The red arrows show the nominal selection of each variable in the signal region. Luminosity is normalised to 36.5 fb^{-1}. Last bin contains the overflow.

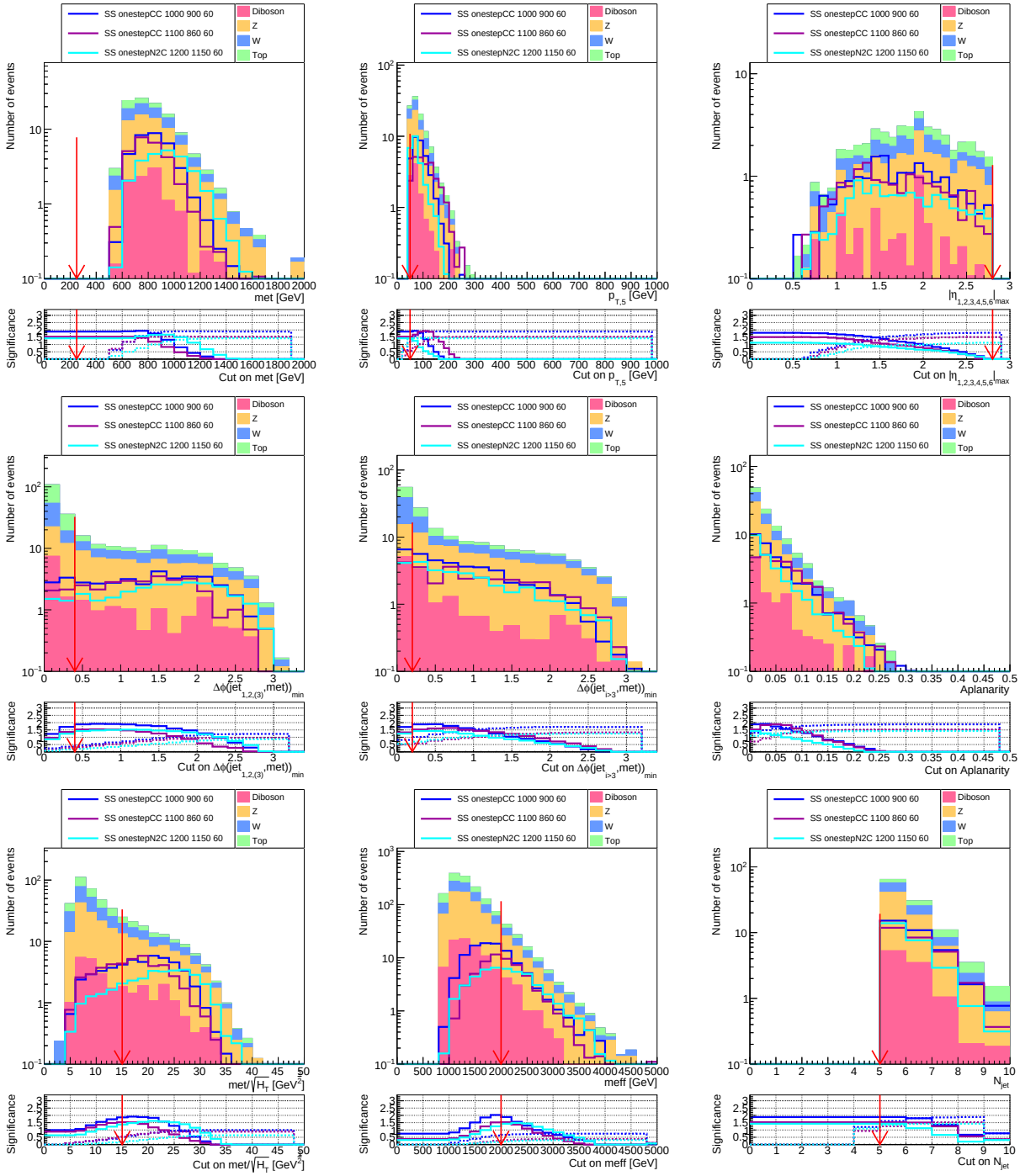

Figure 6.5: Distributions of discriminating variables in the signal region 5j-2000 using simulated events at $\sqrt{s}$ = 13 TeV. The Standard Model background expectation is illustrated in coloured areas and includes diboson, Z+jets, W+jets and top backgrounds. Various one-step decay signals with emission of two intermediate charginos (CC) or intermediate heavy neutralino and chargino (N2C) are shown with coloured lines. At the bottom of the distributions, the signal significance as a function of the cut value is shown. The red arrows show the nominal selection of each variable in the signal region. Luminosity is normalised to 36.5 fb^{-1}. Last bin contains the overflow.

Figure 6.6 shows the N-1 distributions for SR5j-2600. The signal region has been optimized to cover intermediate region of $\tilde{g}\tilde{g}$ production with two intermediate charginos and with m_{LSP} = 60 GeV (Figure 6.16). Various signals are compared, varying exclusively $m_{\tilde{g}}$ or $m_{\tilde{\chi}_0^\pm}$, with m_{LSP} fixed at 60 GeV. The signal was optimized on SS_onestepCC_1700_1500_60. The region with $m_{\tilde{g}} \sim m_{\tilde{\chi}_0^\pm}$ is the boosted region and needs a specific approach for optimization (section 6.5.7). The signal region also covers exclusive regions with intermediate heavy neutralinos (Figure 6.18).

Figure 6.7 shows the N-1 distributions in the signal region 6j-1200. The signal region has been optimized for the intermediate region of SS_onestepCC_x05 (Figure 6.14). The optimization was based on the point SS_onestepCC_525_425_325 which was not excluded without this signal region. The signal region 6j-1200 also covers the intermediate region of GG_onestepCC_x05 (Figure 6.15). The signal region 7j have not been tested in this analysis.

Figures 6.8 and 6.9 show the N-1 distributions for the signal region 6j-1800 and 6j-2200. These signal regions have been optimized to cover the region closed to the points GG_onestepCC_1665_1265_865 and GG_onestepCC_1785_1265_745.

Figure 6.10 shows the N-1 distributions for the signal region 6j-2600. This signal region was optimized to cover high gluino mass region for various decay modes (Figures 6.15, 6.16, 6.18 and 6.19). This signal region was optimized on the grid point GG_onestepCC_1700_160_60 which is represented in Figure 6.16. The statistical uncertainty is the main source of uncertainty in this region. The signal region also covers high gluino mass for the grid GG_onestepCC_x05, GG_onestepN2C_60 and SM_GG_N2 respectively in Figures 6.15, 6.18 and 6.19.

6.5.7 Boosted boson signal regions

The boosted region is the region of $\tilde{q}\tilde{q}$ or $\tilde{g}\tilde{g}$ one-step decay models, where the final state bosons W/Z are boosted. More specifically, it corresponds to models where the mass of primary supersymmetric particle is very close to the mass of the intermediate particle, and where the mass of the neutralino is very small compared to the mass of the intermediate particle. In this case we have:

$$\Delta m = |m_{\tilde{g}/\tilde{q}} - m_{\tilde{\chi}^\pm/\tilde{\chi}_2^0}| \simeq 0, \tag{6.3}$$

$$m_{\tilde{\chi}_1^0} << m_{\tilde{\chi}^\pm/\tilde{\chi}_2^0}. \tag{6.4}$$

In such a model, W/Z are boosted and the angle $\Delta R(q,q)$ between the decay products is small. In order to fully contain the decay product of W, jets with radius equal to 1.0 are used. These larger jets are reconstructed with the anti-k_T algorithm using as input the anti-k_T jets with R = 0.4. The re-clustered jet mass [159, 160] distribution is therefore centered on the mass of the final state boson. A selection on the mass of the re-clustered jet has been applied for the optimization.

The re-clustered jet mass distributions of leading jet (a) and sub-leading jet (b) with SR2jB-2400 selections are shown in Figure 6.11. The signal in red represents a $\tilde{g}\tilde{g}$ one-step decay with intermediate heavy neutralinos and with two Z bosons in the final state, while the signal in blue is a one-step decay with intermediate charginos and W boson in the final state. The distribution of the two signals are respectively centered on m_Z and m_W. The re-clustered jet mass selection consists of a selective range centered on the final boson mass. The first idea is to define two different signal regions for both W or Z in the final state. These signal regions called SR2jW and SR2jZ are studied. The selective ranges for re-clustered jet mass are respectively [60,100] and [70,110], and are centered on the W and Z masses.

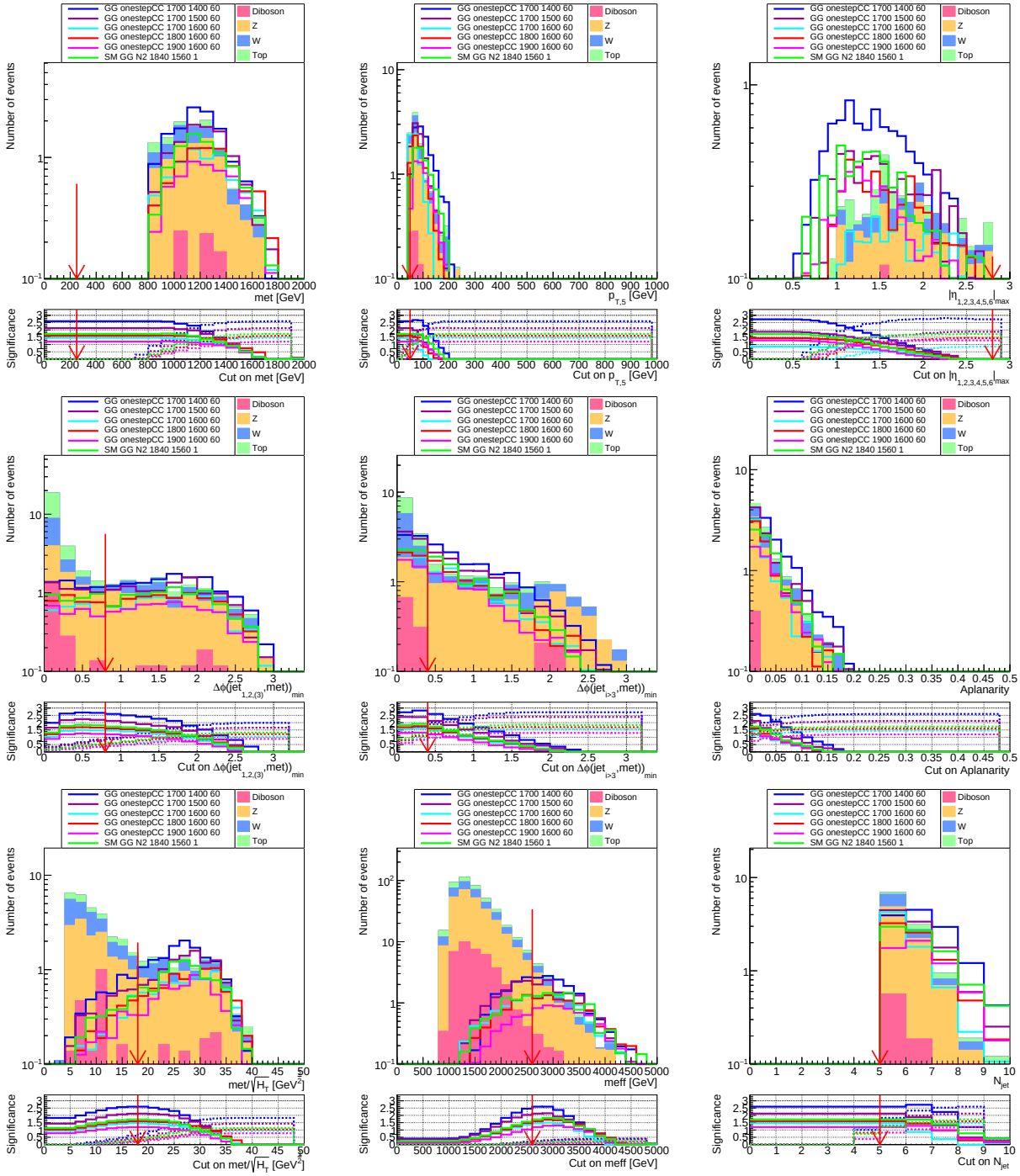

Figure 6.6: Distributions of discriminating variables in the signal region 5j-2600 using simulation. The Standard Model background expectation is illustrated in coloured areas and includes diboson, Z+jets, W+jets and top backgrounds. Various one-step decay signals with emission of two intermediate charginos (CC) or heavy neutralinos (N2) are shown with coloured lines. At the bottom of the distributions, the signal significance as a function of the cut value is shown. The red arrows show the nominal selection of each variable in the signal region. Luminosity is normalised to 36.5 fb^{-1}. Last bin contains the overflow.

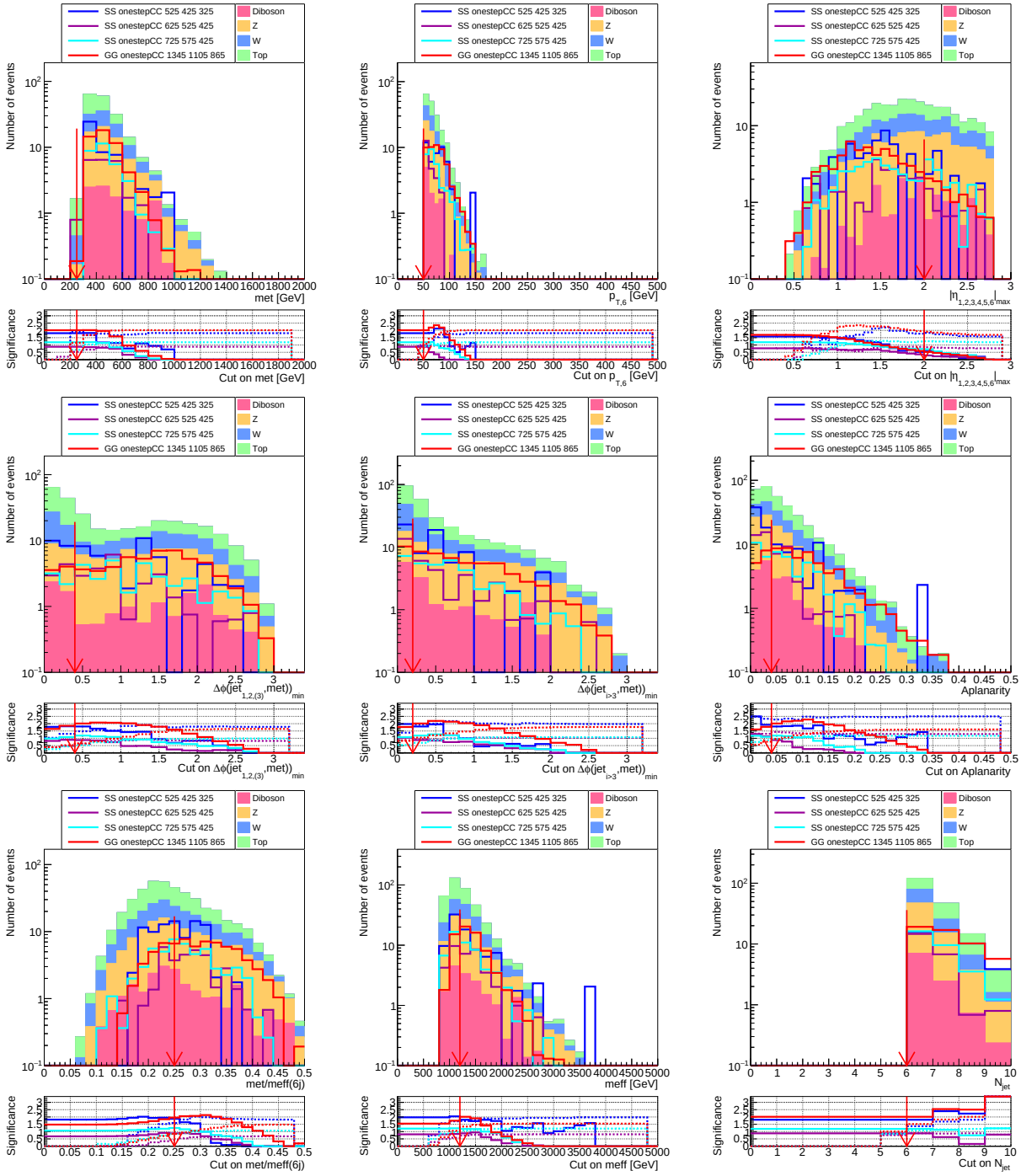

Figure 6.7: Distributions of discriminating variables in the signal region 6j-1200 using simulated events at $\sqrt{s}$ = 13 TeV. The Standard Model background expectation is illustrated in coloured areas and includes diboson, Z+jets, W+jets and top backgrounds. Various one-step decay signals with emission of two intermediate charginos (CC) are shown with coloured lines. At the bottom of the distributions, the signal significance as a function of the cut value is shown. The red arrows show the nominal selection of each variable in the signal region. Luminosity is normalised to 36.5 fb^{-1}. Last bin contains the overflow.

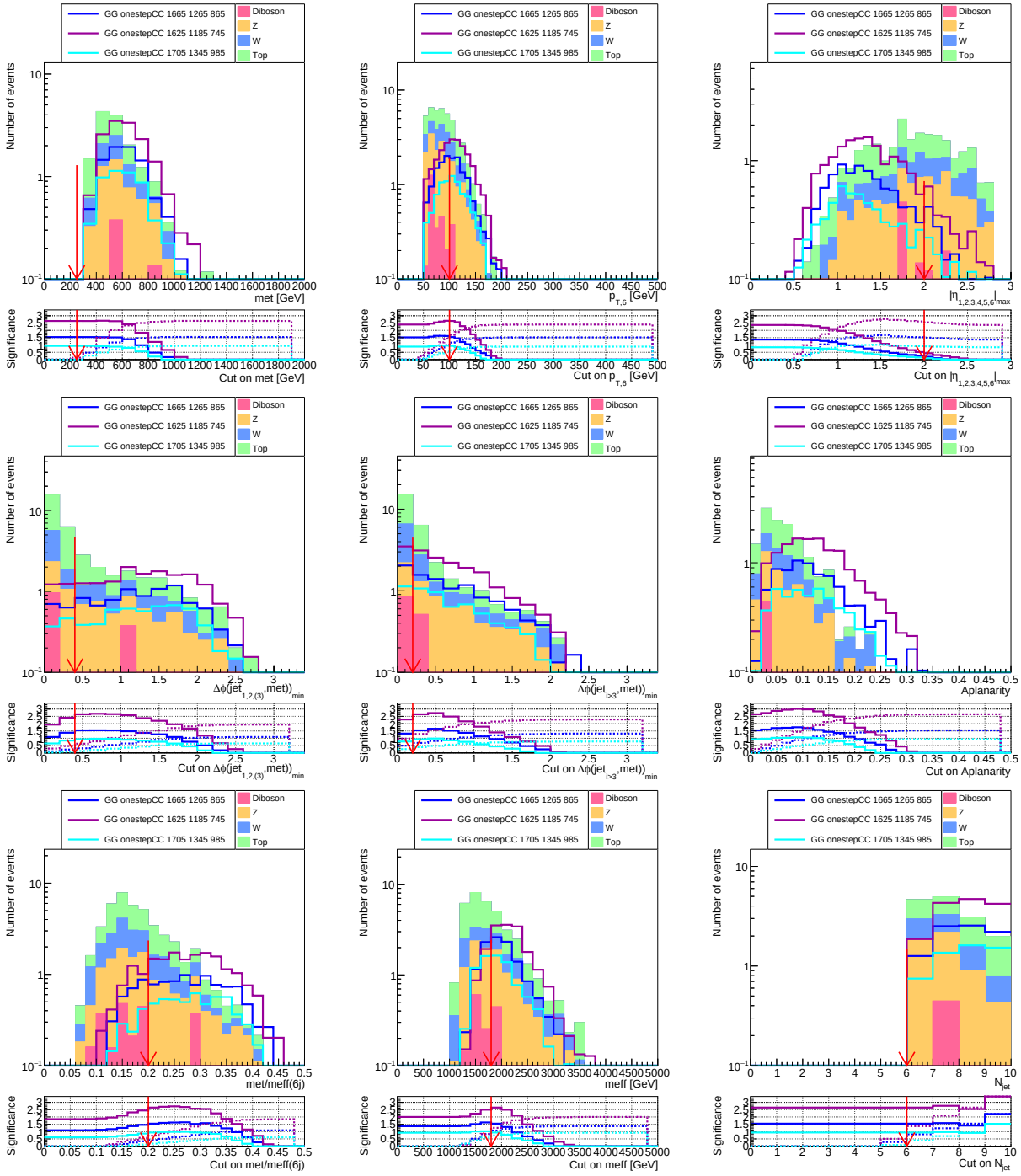

Figure 6.8: Distributions of discriminating variables in the signal region 6j-1800 using simulated events at $\sqrt{s}$ = 13 TeV. The Standard Model background expectation is illustrated in coloured areas and includes diboson, Z+jets, W+jets and top backgrounds. Various one-step decay signals with emission of two intermediate charginos (CC) are shown with coloured lines. At the bottom of the distributions, the signal significance as a function of the cut value is shown. The red arrows show the nominal selection of each variable in the signal region. Luminosity is normalised to 36.5 fb^{-1}. Last bin contains the overflow.

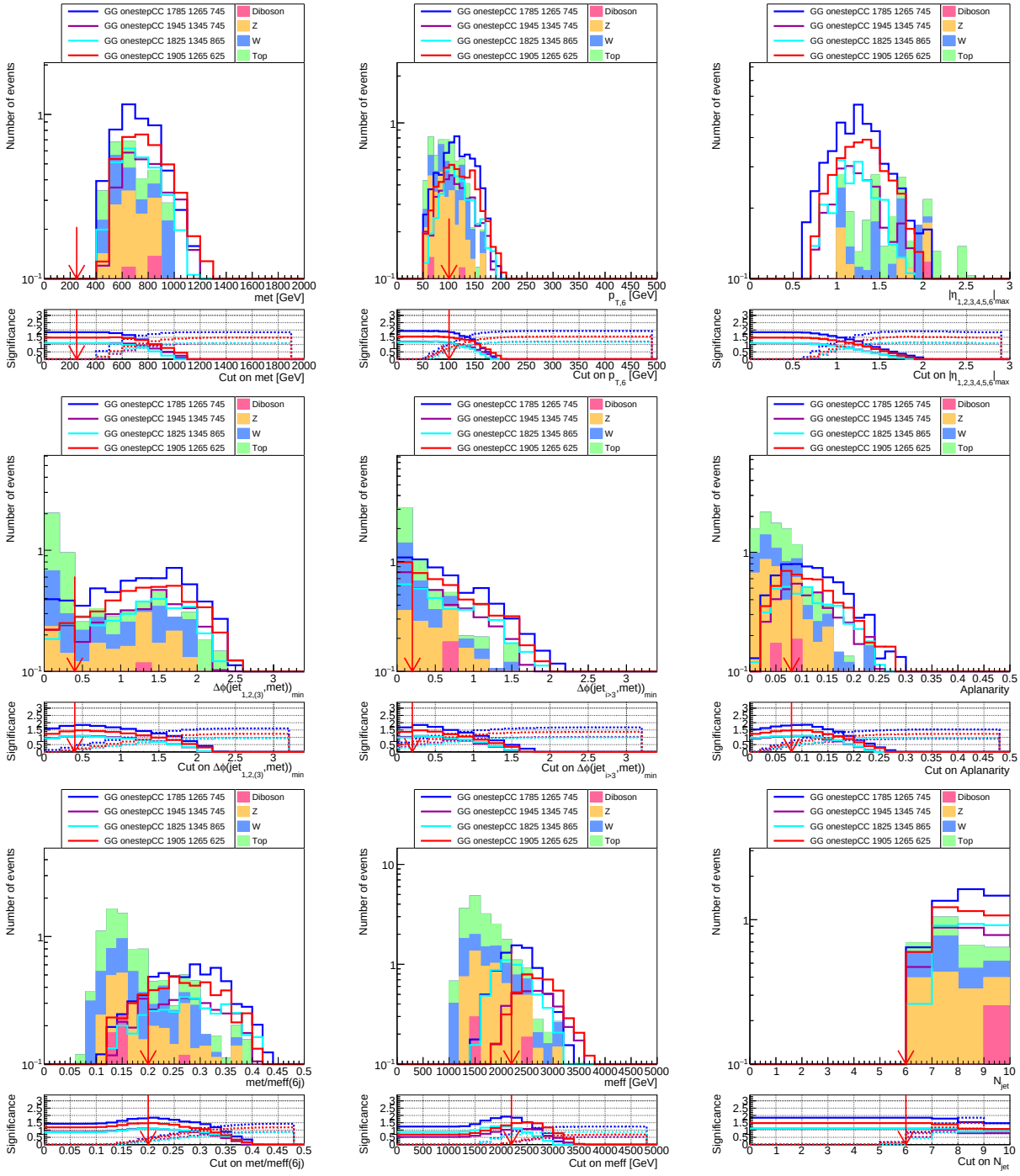

Figure 6.9: Distributions of discriminating variables in the signal region 6j-2200 using simulated events at $\sqrt{s}$ = 13 TeV. The Standard Model background expectation is illustrated in coloured areas and includes diboson, Z+jets, W+jets and top backgrounds. Various one-step decay signals with emission of two intermediate charginos (CC) are shown with coloured lines. At the bottom of the distributions, the signal significance as a function of the cut value is shown. The red arrows show the nominal selection of each variable in the signal region. Luminosity is normalised to 36.5 fb^{-1}.

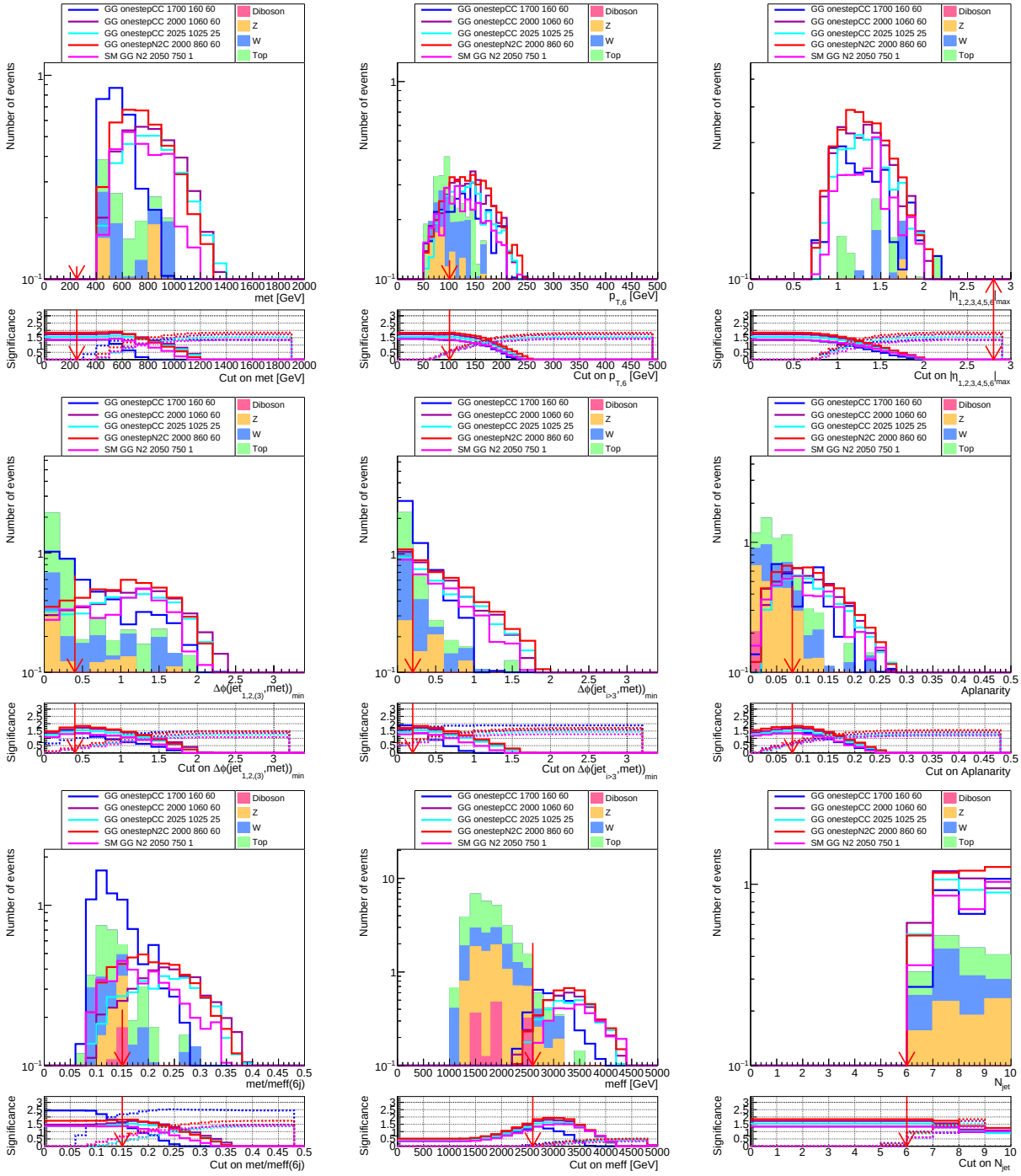

Figure 6.10: Distributions of discriminating variables in the signal region 6j-2600 using simulation. The Standard Model background expectation is illustrated in coloured areas and includes diboson, Z+jets, W+jets and top backgrounds. Various one-step decay signals with emission of two intermediate charginos (CC) or heavy neutralinos (N2) are shown with coloured lines. At the bottom of the distributions, the signal significance as a function of the cut value is shown. The red arrows show the nominal selection of each variable in the signal region. Luminosity is normalised to 36.5 fb^{-1}. Last bin contains the overflow.

To restrict the number of signal regions in the analysis, selection on a larger range including both W and Z mass ranges were proposed. This signal region has been defined as SR2jB with a range fixed to [60,110].

The impact of a larger range selection on the significance has been studied for several signal points and is summarized in Table 6.6 for two of them. Table 6.6 shows the signal significance for two signals regions SR2jW, SR2jZ and SR2jB. These 3 signal regions only differ by the choice of the re-clustered mass range. The signal GG_onestepCC_1800_1790_60 has a significance of 2.8, 2.6 and 2.7 respectively for SR2jW, SR2jZ and SR2jB. Since the boson in the final state is the W, the signal region with the best significance is the SR2jW. The signal SM_GG_N2_1735_1665_1 has a significance of 2.1, 2.7 and 2.3 for SR2jW, SR2jZ and SR2jB. Since the final boson of this signal is the Z boson, SR2jZ is more adapted for the signal isolation. After discussion with the team, the choice was made to include only SR2jB instead of SR2jW and SR2jZ. This allows the restriction of the number of signal regions, control regions and validation regions in the analysis.

Two different boosted bosons signal regions SR2jB were introduced for $\tilde{q}\tilde{q}$ and $\tilde{g}\tilde{g}$ productions. The selections defining SR2jB are summarized in Table 6.7. The signal region 2jB-2400 has been introduced for $\tilde{g}\tilde{g}$ production on the grid point ($m_{\tilde{g}}$, $m_{\tilde{\chi}^{\pm}}$, $m_{\tilde{\chi}^0_1}$) = (1800, 1790, 60) and, SR2jB-1600 has been introduced for $\tilde{q}\tilde{q}$ production on ($m_{\tilde{g}}$, $m_{\tilde{\chi}^{\pm}}$, $m_{\tilde{\chi}^0_1}$) = (1100, 1090, 60). The SR2jB-2400 is also used for the grid SM_GG_N2_mchi101 (Figure 1.11 (d)). The distributions of the other discriminating variables are shown in Figures 6.12 and 6.13.

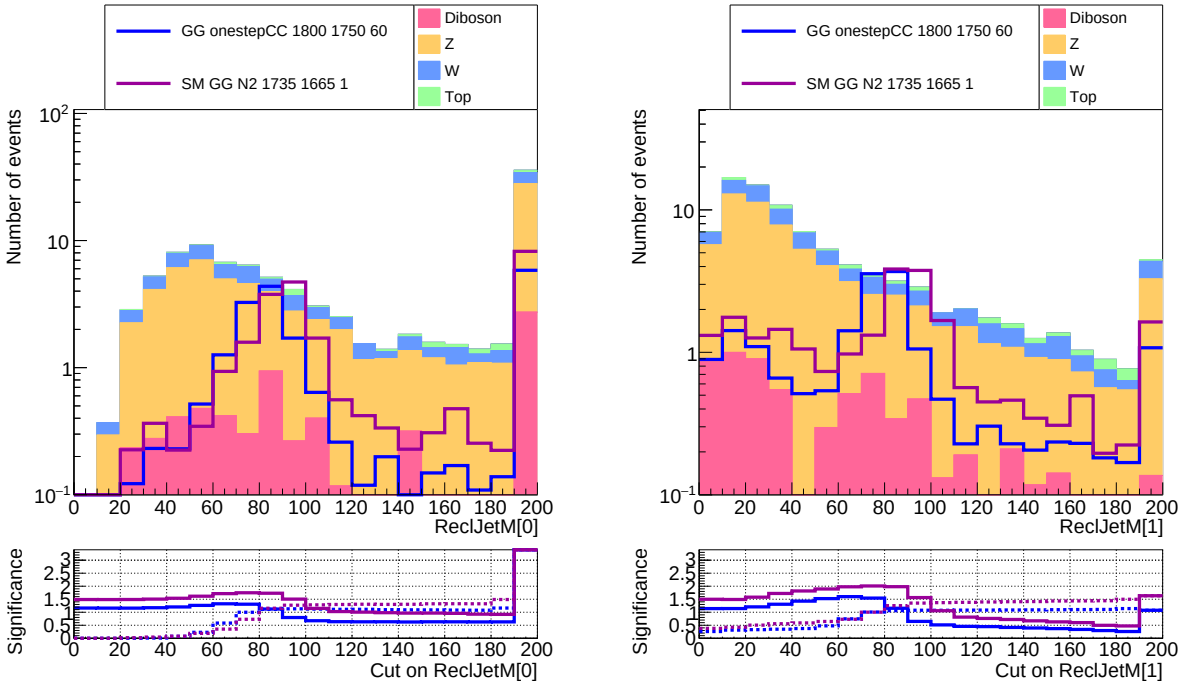

(a) *(b)*

Figure 6.11: Distribution of re-clustered jet mass for leading jet (a) and sub-leading jet (b) on background (colored areas) and signals in the signal region 2jB-2400. The purple line represents the $\tilde{g}\tilde{g}$ one-step signal decaying with intermediate heavy neutralino with Z boson in final state. The blue line represents the $\tilde{g}\tilde{g}$ one-step signal decaying with intermediate chargino with W boson in final state. The bottom of the plots shows the significance as a function of the re-clustered jet mass selection for selection on lower cut (continuous line) or upper cut (dotted line). The last bin contains the overflow.

Table 6.6: Comparison of the signal significance of two models, between three boosted region candidates.

Significance	SR2jW	SR2jZ	SR2jB
$GG\_onestepCC\_1800\_1790\_60$	2.8	2.6	2.7
$SM\_GG\_N2\_1735\_1665\_1$	2.1	2.7	2.3

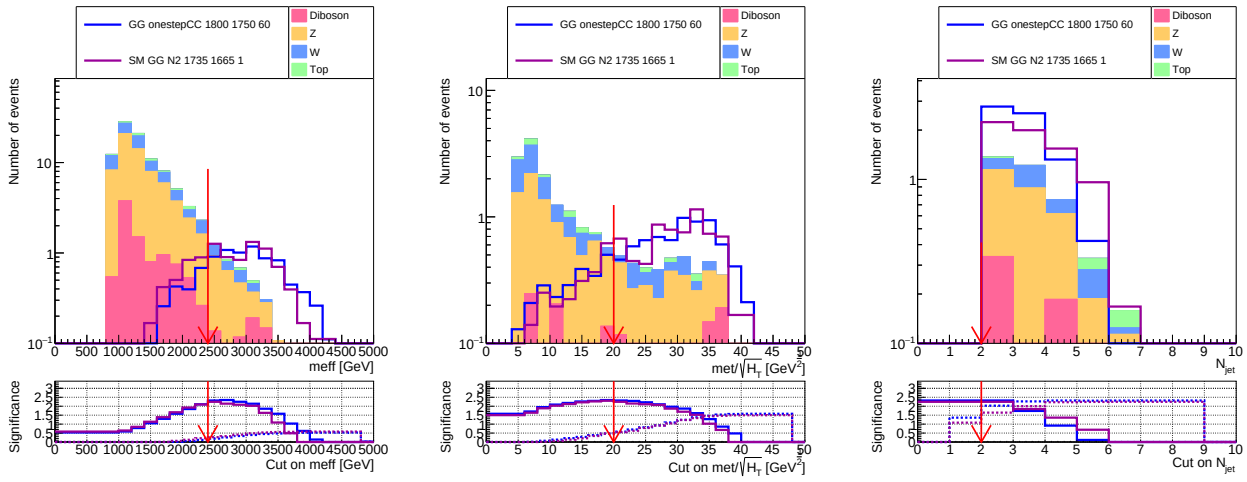

(a) *(b)* *(c)*

Figure 6.12: Distribution of m_{eff} (a), $\frac{E_T^{miss}}{H_T}$ (b), and N_{jets} (c) for Standard Model background expectation (coloured areas) and signals in the boosted region. Red arrows show the nominal selections on each variables.

Table 6.7: Selections applied in the boosted boson signal region.

Requirement	Signal Region	
	2jB-1600	**2jB-2400**
$E_{\mathrm{T}}^{\mathrm{miss}}$ [GeV] >	250	
$p_{\mathrm{T}}(\mathrm{RT}j_1)$ [GeV] >	200	
$p_{\mathrm{T}}(\mathrm{RT}j_2)$ [GeV] >	200	
$m(\mathrm{RT}j_1)$ [GeV]	[60,110]	
$m(\mathrm{RT}j_2)$ [GeV]	[60,110]	
$\Delta\phi(\mathrm{jet}_{1,2,(3)}, \vec{E}_{\mathrm{T}}^{\mathrm{miss}})_{\mathrm{min}}$ >	0.6	
$\Delta\phi(\mathrm{jet}_{i>3}, \vec{E}_{\mathrm{T}}^{\mathrm{miss}})_{\mathrm{min}}$ >	0.4	
$E_{\mathrm{T}}^{\mathrm{miss}}/\sqrt{H_{\mathrm{T}}}$ [GeV$^{1/2}$] >	20	
m_{eff}(incl.) [GeV] >	1600	2400
Optimised for	SS onestep	GG onestep

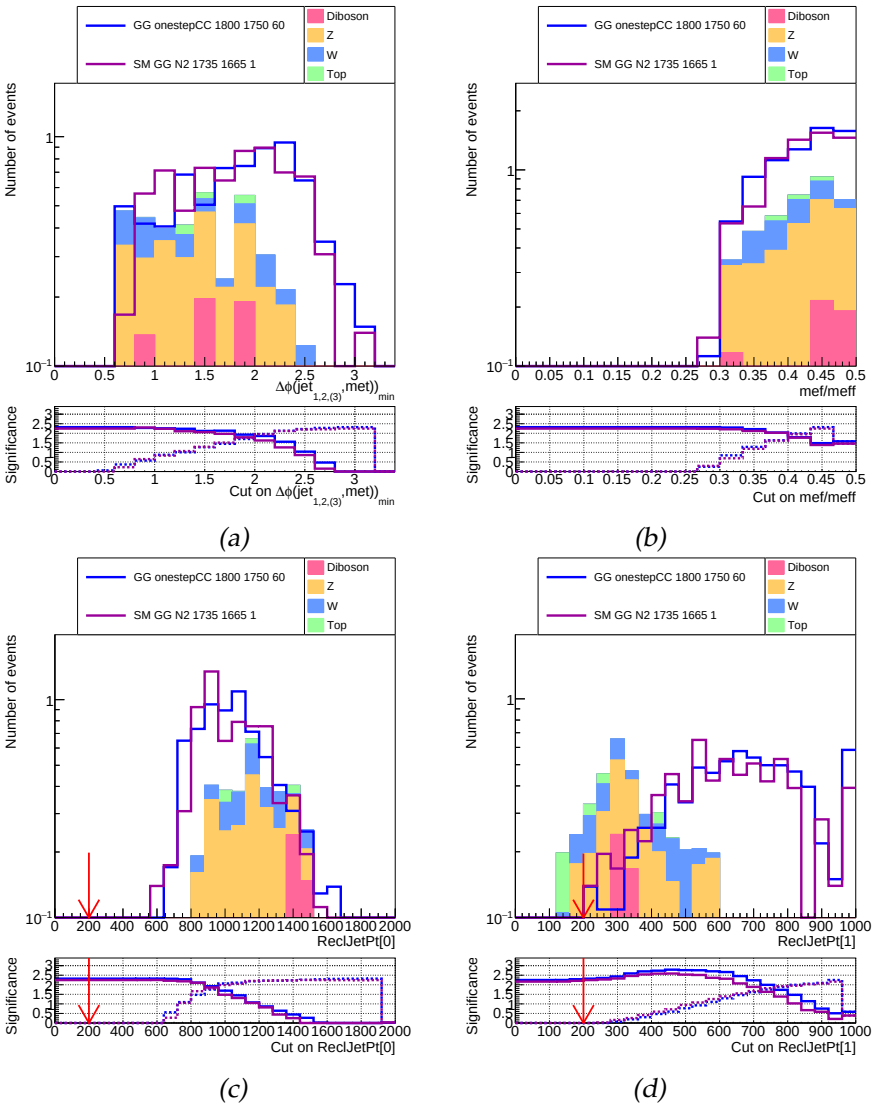

Figure 6.13: Distribution of $\Delta\Phi$ (a), $\frac{E_T^{miss}}{m_{eff}}$ (b), re-clustered leading jet p_T (c), and re-clustered sub-leading jet p_T (d) for Standard Model background expectation (coloured areas) and signals in the boosted region. Red arrows show the nominal selections on each variables.

6.5.8 Expected exclusion plots

This section presents the expected exclusion limits after the optimization. Each figure shows the limits on one grid (bottom), and the corresponding Feynman diagram for the decays of squarks/gluinos (top). Each grid is defined with two free parameters corresponding to $m_{\tilde{q}/\tilde{g}}$ and $m_{LSP/I.S}$, where $m_{I.S}$ corresponds to the mass of the intermediate sparticle. The expected limits obtained with a few SRs including the best SRs are shown in each figure (coloured lines). The name of the signal regions with the best sensitivity as a function of the mass parameters is indicated in the corresponding region.

The onestepCC_x05 models are defined by ($m_{\tilde{q}/\tilde{g}}$, $m_{\tilde{\chi}_1^0}$) with $m_{\tilde{\chi}^\pm} = \frac{1}{2}(m_{\tilde{q}/\tilde{g}} + m_{\tilde{\chi}_1^0})$. The expected exclusion limits of onestepCC_x05 for $\tilde{q}\tilde{q}$ and $\tilde{g}\tilde{g}$ productions are shown in Figures 6.14 and 6.15. In Figure 6.14, the signal regions giving the best expected exclusion limits are SR4j-1800 for high squark mass, SR4j-1400 in the region (∼1000,∼375), SR6j-1200 in the intermediate region, and SR3j-1300 in the compressed region. In Figure 6.15, the best signal regions are SR6j-2600 for low chargino mass and high gluino mass, SR6j-2200 and SR6j-1800 in the regions (∼1850,∼750) and (∼1650,∼825), SR6j-1200 in the intermediate region, and SR2j-2100/SR3j-1300 in the compressed region.

The onestepCC_mlsp60 models defined by ($m_{\tilde{q}/\tilde{g}}$, $m_{\tilde{\chi}^\pm}$) with $m_{\tilde{\chi}_1^0} = 60$ GeV. The expected exclusion limits of onestep_mlsp60 for $\tilde{q}\tilde{q}$ and $\tilde{g}\tilde{g}$ productions are shown in Figures 6.16 and 6.17. The best signal regions in Figure 6.16 are SR6j-2600 for high gluino mass, SR4j-2600 in the region (∼1900,∼1400), SR5j-2600 in the intermediate region, and SR2jB-2400 in the boosted region. For the $\tilde{q}\tilde{q}$ production (Figure 6.17), the signal region 5j-1600 is used for low chargino mass region, SR4j-1800 is used for high squarks mass, and SR2jB-1600 is used in the boosted region.

The SM_GG_N2 model is defined by ($\tilde{g}$, $m_{\tilde{\chi}_2^0}$). The expected exclusion limits of SM_GG_N2 with $m_{\tilde{\chi}_1^0} = 1$ GeV are shown in Figure 6.18. The choice of the signal regions is the same as in Figure 6.16, with SR6j-2600 for high gluinos mass, SR4j-2600 in the region (∼1950,∼1490), SR5j-2600 in the intermediate region, and SR2jB-2400 in the boosted region.

The models onestepCC_N2C are defined by ($m_{\tilde{q}/\tilde{g}}$, $m_{\tilde{\chi}^\pm}$). The expected exclusion limits of onestepCC_N2C with $m_{\tilde{\chi}_1^0} = 1$ GeV are shown in Figures 6.19 and 6.20. In Figure 6.19, the region SR6j-2600 is used for low charginos mass and high gluinos mass. The region 4j-2600 is used in the regions $m_{\tilde{\chi}^\pm} \sim 1400$ with high gluinos mass, and SR2j-2800 is used in the compressed region. In Figure 6.20, the region 5j-1600 is used for low charginos mass, 4j-2200 for high gluinos mass, and 5j-2000 for high charginos mass.

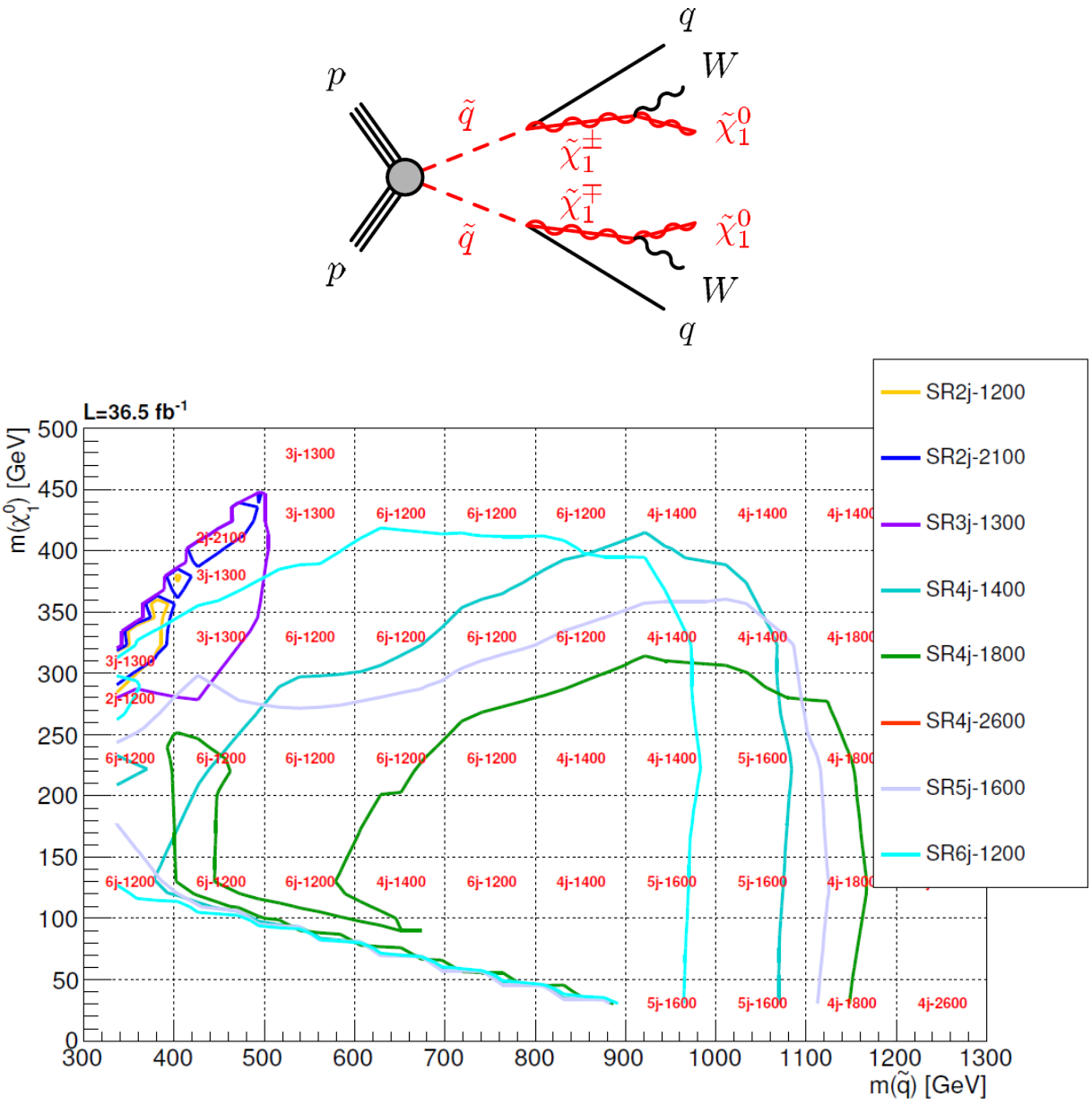

Figure 6.14: The expected 95% CL [161] exclusion limits for the squarks pair production with squark one-step decay, and W boson in the final state. The Monte Carlo is normalized to 36.5 fb^{-1}. Each point of the grid corresponds to a MSSM model defined by m($\tilde{q}$) (x-axis), m($\tilde{\chi}_1^0$) (y-axis) with m($\tilde{\chi}_1^{\pm}$) = $\frac{m(\tilde{q})+m(\tilde{\chi}_0^1)}{2}$. Only signal regions giving the lowest expected CLs for one of the points are shown on the grid. The one-step decay topology is shown on the top part.

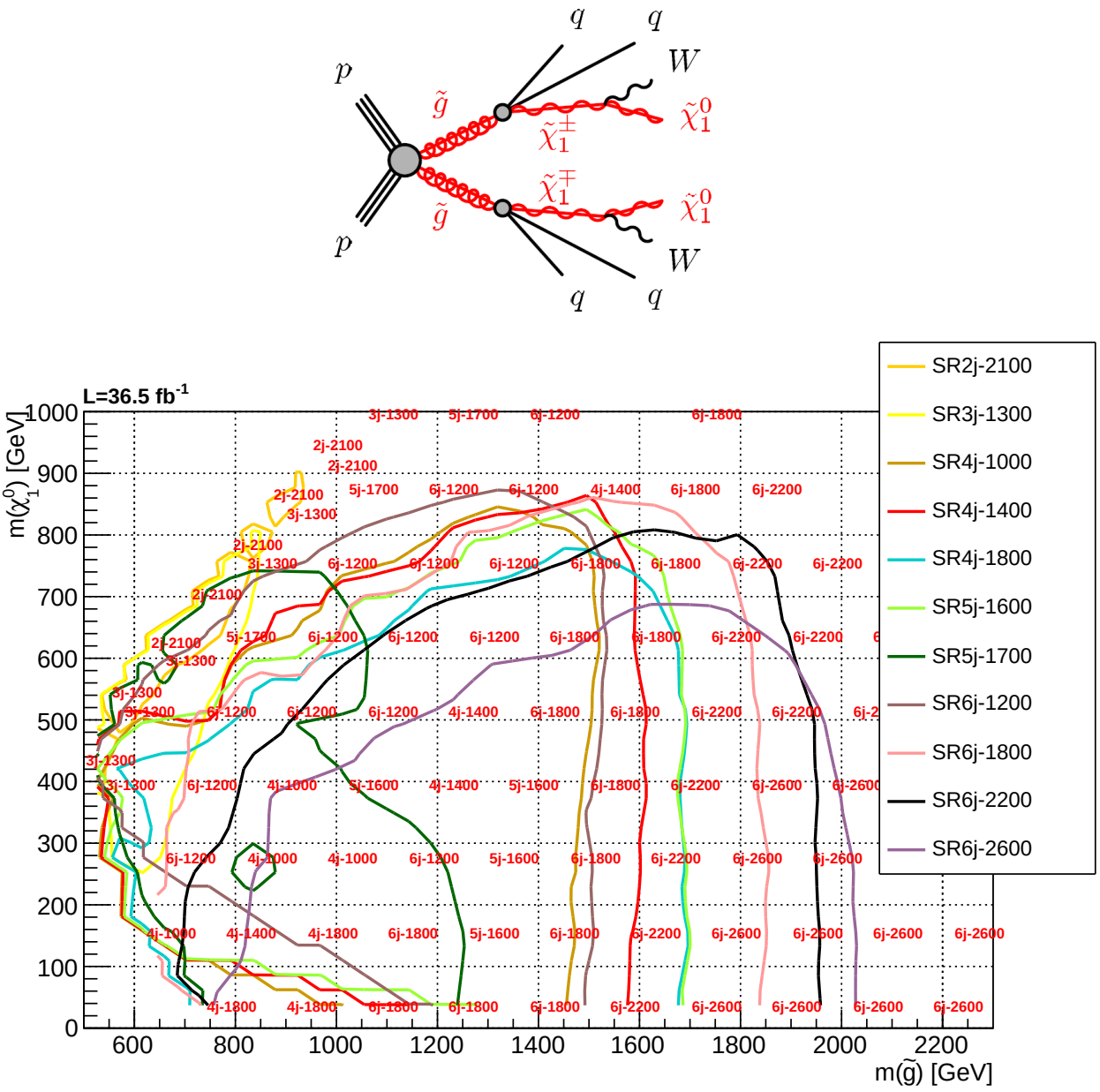

Figure 6.15: The expected 95% CL exclusion limits for the gluinos pair production with gluino one-step decay, and W boson in the final state. The Monte Carlo is normalized to 36.5 fb^{-1}. Each point of the grid corresponds to a MSSM model defined by m($\tilde{g}$) (x-axis), m($\tilde{\chi}_1^0$) (y-axis) with m($\tilde{\chi}_1^{\pm}$) = $\frac{m(\tilde{g})+m(\tilde{\chi}_0^1)}{2}$. Only signal regions giving the lowest expected CLs for one of the points are shown on the grid. The one-step decay topology is shown on the top part.

.

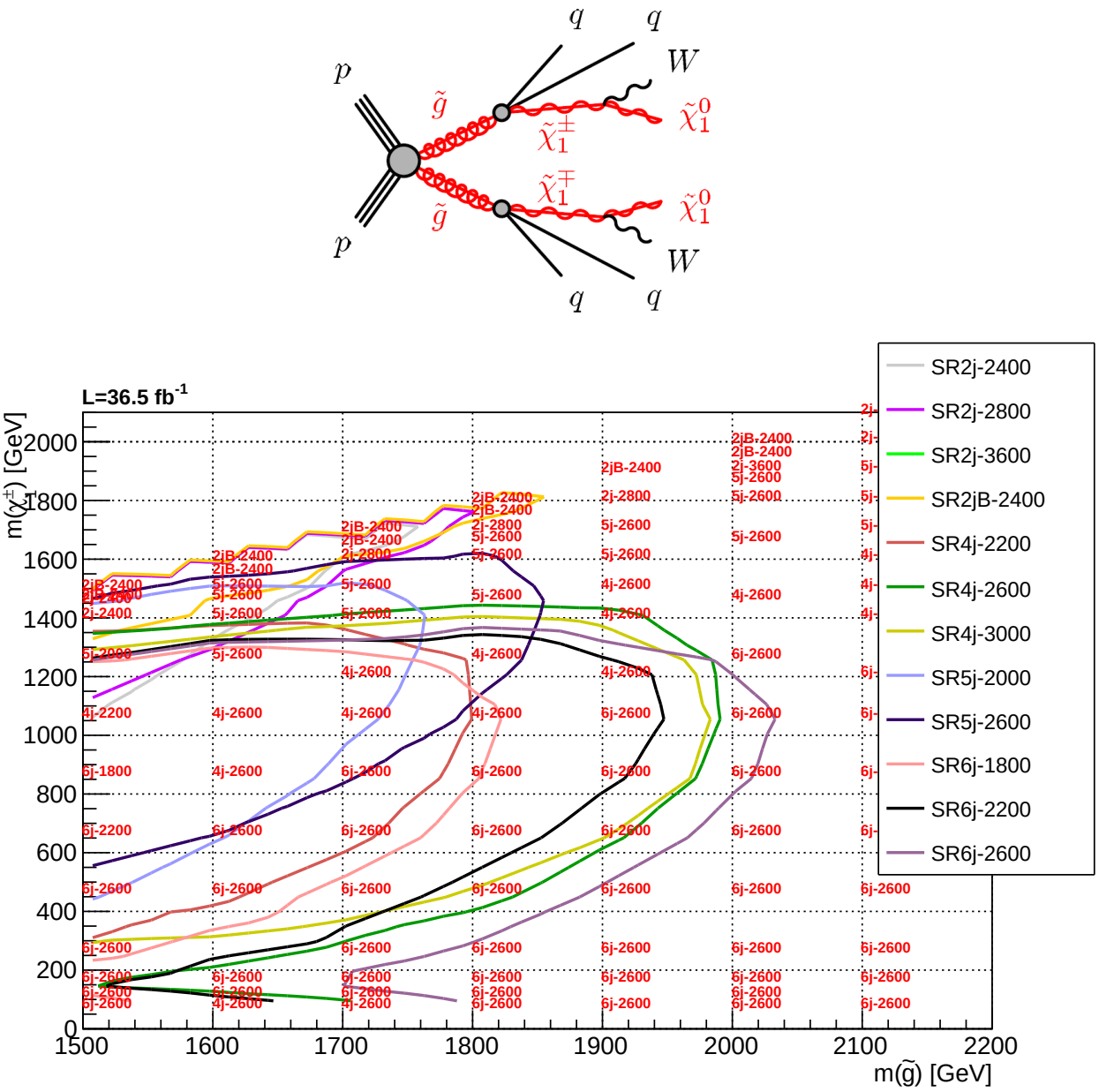

Figure 6.16: The expected 95% CL exclusion limits for the gluinos pair production with gluino one-step decay, and W boson in the final state. The Monte Carlo is normalized to 36.5 fb^{-1}. Each point of the grid corresponds to a MSSM model defined by m($\tilde{g}$) (x-axis), m($\tilde{\chi}_1^{\pm}$) (y-axis) with m($\tilde{\chi}_1^0$) = 60 GeV. Only signal regions giving the lowest expected CLs for one of the points are shown on the grid. The one-step decay topology is shown on the top part.

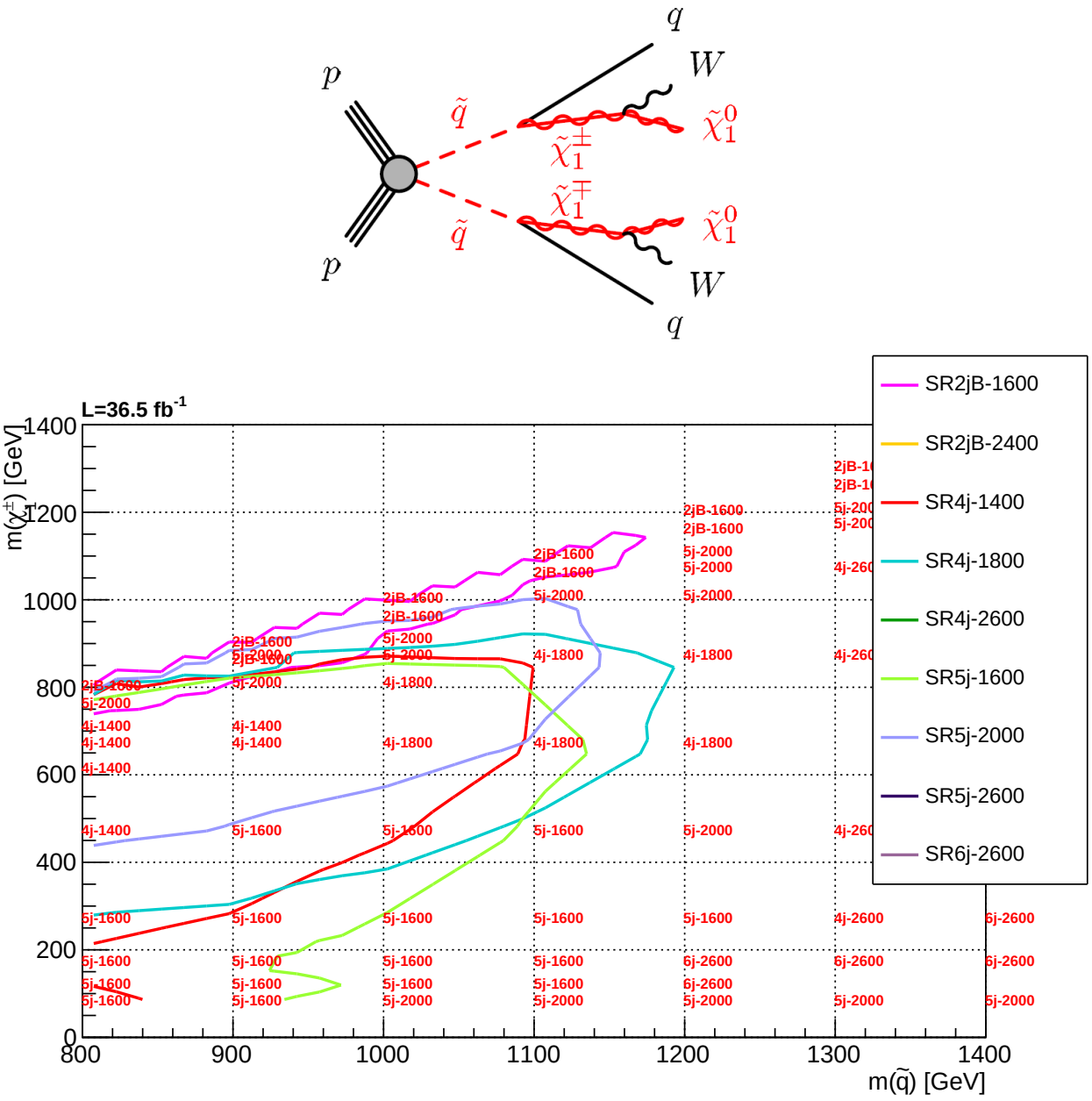

Figure 6.17: The expected 95% CL exclusion limits for the squarks pair production with squark one-step decay, and W boson in the final state. The Monte Carlo is normalized to 36.5 fb^{-1}. Each point of the grid corresponds to a MSSM model defined by m($\tilde{q}$) (x-axis), m($\tilde{\chi}_1^{\pm}$) (y-axis) with m($\tilde{\chi}_1^0$) = 60 GeV. Only signal regions giving the lowest expected CLs for one of the points are shown on the grid. The one-step decay topology is shown on the top part.

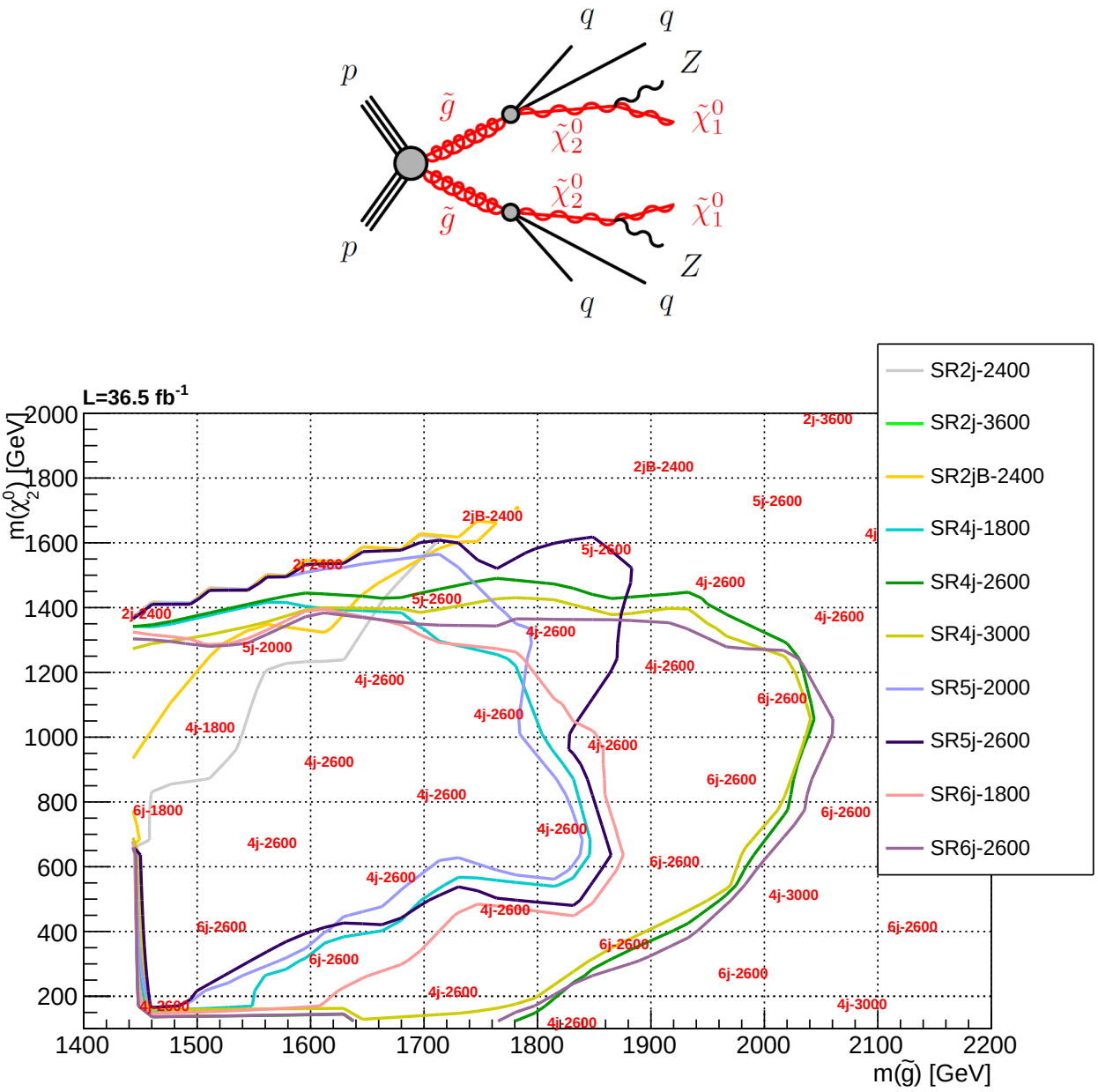

Figure 6.18: The expected 95% CL exclusion limits for the gluinos pair production with gluino one-step decay, and Z boson in the final state. The Monte Carlo is normalized to 36.5 fb^{-1}. Each point of the grid corresponds to a MSSM model defined by m($\tilde{g}$) (x-axis), m($\tilde{\chi}_2^0$) (y-axis) and m($\tilde{\chi}_1^0$) = 1 GeV. Only signal regions giving the lowest expected CLs for one of the points are shown on the grid. The one-step decay topology is shown on the top part.

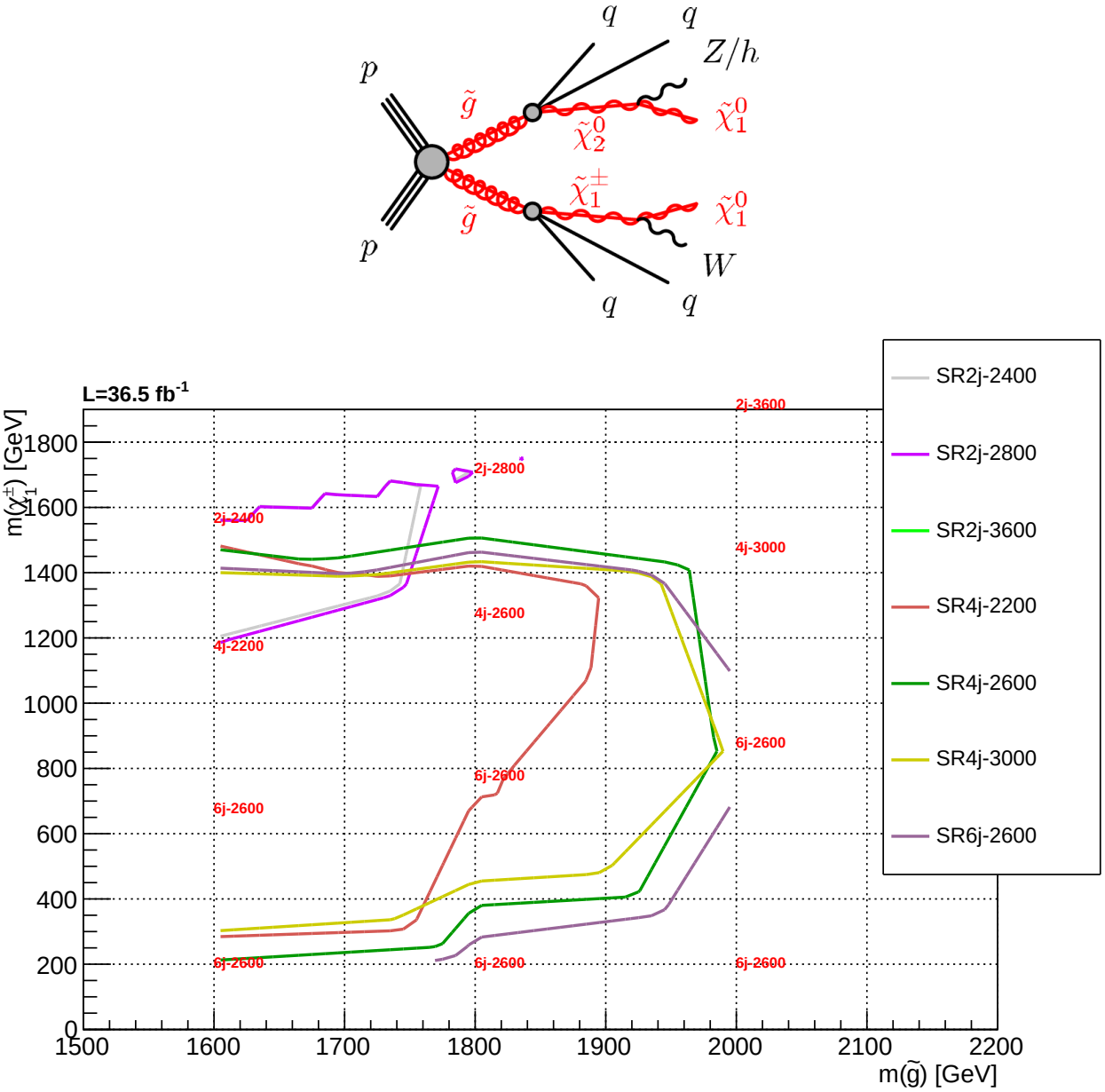

Figure 6.19: The expected 95% CL exclusion limits for the gluinos pair production with gluino one-step decay, and Z/h boson in the final state. The Monte Carlo is normalized to 36.5 fb^{-1}. Each point of the grid corresponds to a MSSM model defined by m($\tilde{g}$) (x-axis), m($\tilde{\chi}_1^{\pm}$) (y-axis) with m($\tilde{\chi}_1^0$) = 1 GeV. Only signal regions giving the lowest expected CLs for one of the points are shown on the grid. The one-step decay topology is shown on the top part.

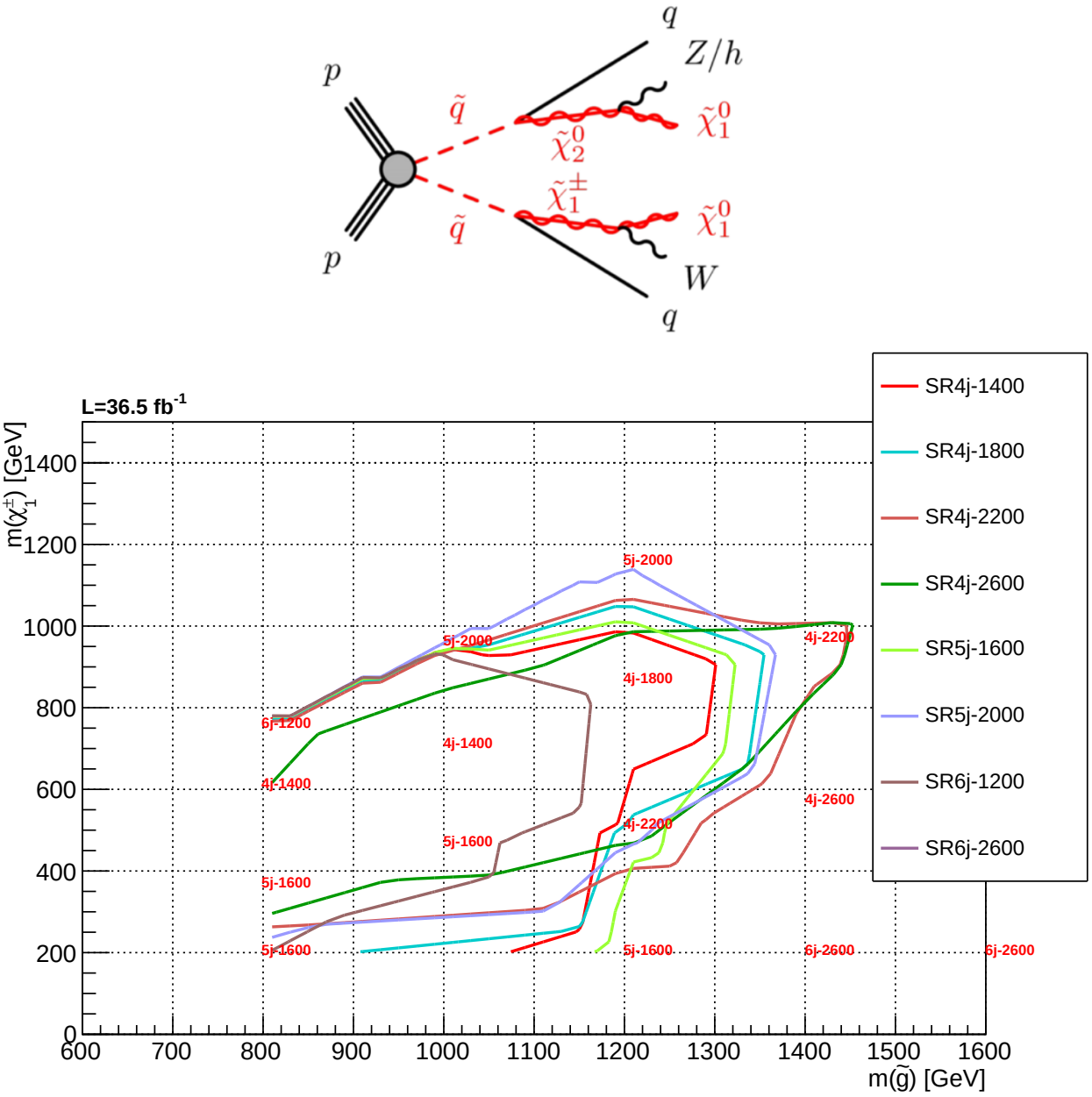

Figure 6.20: The expected 95% CL exclusion limits for the gluinos pair production with gluino one-step decay, and Z/h boson in the final state. The Monte Carlo is normalized to 36.5 fb^{-1}. Each point of the grid corresponds to a MSSM model defined by m($\tilde{q}$) (x-axis), m($\tilde{\chi}_1^{\pm}$) (y-axis) with m($\tilde{\chi}_1^0$) = 1 GeV. Only signal regions giving the lowest expected CLs for one of the points are shown on the grid. The one-step decay topology is shown on the top part.

6.6 Background estimation

This section describes the methods used to estimate the five main backgrounds of the analysis: W+jets, Z+jets, $t\bar{t}$, diboson and QCD background. The first four backgrounds are Standard Model electroweak processes with at least one neutrino in the final state. The QCD background is due to mis-measurements in the detector.

The diboson background is estimated with pure Monte Carlo simulation [162]. The other backgrounds are estimated with Monte Carlo, normalized to data from specific control regions. For each signal region, 4 control regions are defined: CRT, CRW, CRQ, CRY. The control regions CRW and CRT are used to normalize W+jets and top background processes as detailed in section 6.6.1. The Z+jets background is estimated from γ+jets events (CRY), using transfer factors. The method is described in section 6.6.2. The QCD background is estimated from the control region CRQ and is based on the jet smearing method. This method is fully data driven (section 6.6.3).

Table 6.8: Summary of control regions for Meff and RJR analysis. The table shows the targeted background process in each signal region, the process used in the control region for the estimation, and the selection applied in the control region for Meff and RJR analysis.

CR	SR background	CR process	CR selection (Meff-based)	CR selection (RJR-based)
Meff/RJR-CRγ	$Z(\rightarrow \nu\bar{\nu})$+jets	γ+jets	Isolated photon	Isolated photon
Meff/RJR-CRQ	Multi-jet	Multi-jet	SR with reversed requirements on (i) $\Delta\phi(\text{jet}, E_{\text{T}}^{\text{miss}})_{\text{min}}$ and (ii) $E_{\text{T}}^{\text{miss}}/m_{\text{eff}}(N_{\text{j}})$ or $E_{\text{T}}^{\text{miss}}/\sqrt{H_{\text{T}}}$	$\Delta_{\text{QCD}} < 0$ reversed requirement on $H_{1,1}^{\text{PP}}/H_{\text{N,1}}^{\text{PP}}$
Meff/RJR-CRW	$W(\rightarrow \ell\nu)$+jets	$W(\rightarrow \ell\nu)$+jets	30 GeV< $m_{\text{T}}(\ell, E_{\text{T}}^{\text{miss}})$ < 100 GeV, b-veto	
Meff/RJR-CRT	$t\bar{t}$(+EW) and single top	$t\bar{t} \rightarrow b\bar{b}qq'\ell\nu$	30 GeV< $m_{\text{T}}(\ell, E_{\text{T}}^{\text{miss}})$ < 100 GeV, b-tag	

6.6.1 W+jets, $t\bar{t}$ backgrounds

The W+jets and $t\bar{t}$ backgrounds are estimated with MC using data driven corrections estimated in CRW and CRT. The control region CRW is defined to select a pure sample of W$\rightarrow$lν+jets events. Events with exactly one isolated lepton (electron or muon) are selected, and the lepton is treated as a jet. A selection of 30 GeV < m_T(l,E_T^{miss}) < 100 GeV is applied, and b jets events are rejected. For CRT, a b-tagging [163, 164] is applied instead of b veto. Other selections are as close as possible to the SRs selections, with the constraint to get enough statistics. No selection on η, aplanarity, and $\Delta\phi$ are applied to increase the statistics, and selections on $\frac{E_T^{miss}}{m_{eff}}$ and $\frac{E_T^{miss}}{\sqrt{H_T}}$ are relaxed for tight SRs. Selections for each CR is described in tables 6.8 and 6.9. In the case of pure CR, the number of background events N_{SR}^{pred} predicted in the signal region for W+jets or $t\bar{t}$ is estimated as:

$$N_{SR}^{pred} = \frac{N_{CR}^{data} \times N_{SR}^{MC}}{N_{CR}^{MC}} = \mu \times N_{SR}^{MC} = N_{CR}^{data} \times TF, \tag{6.5}$$

Where μ are the normalization factors from the MC to the data, defined as $\mu = \frac{N_{CR}^{data}}{N_{CR}^{MC}}$, N_{CR}^{data} corresponds to the number of events in the control region, and N_{SR}^{MC} (N_{CR}^{MC}) correspond to the number of events predicted by the simulation in the SR (CR).

Table 6.9: Selections on the control regions. X represents the signal region cut value and varies from 2 to 10 for E_T^{miss} significance, and from 0.06 to 0.1 for $\frac{E_T^{miss}}{m_{eff}}$ depending on the signal region.

Cut	Control Region			
	CRY	CRW	CRT	CRQ
1	As for SR cut			
2	Single photon trigger	Single lepton triggers		As for SR cut 1
3-6	As for SR cuts 3-6			
7a	$\geq$ 1 signal photon No selected e/μ as for SR Cut 7	Exactly 1 selected electron or muon $p_T(e) > 27$ GeV or $p_T(\mu) > 27$ GeV		As for SR Cut 7
7b	–	No p_T >50 GeV sel. $\lvert\eta\rvert < 2.5$ jet with MV2c10 77% eff.	$\geq$ 1 p_T >50 GeV sel. $\lvert\eta\rvert < 2.5$ jet with MV2c10 77% eff.	–
7c	–	30 GeV < $m_T(\ell, E_T^{miss})$ < 100 GeV		–
Use below:	$E_T^{miss\prime} = \lvert E_T^{miss} + p_T^{\gamma}\rvert$	Treat lepton as a jet		–
$p_T(j_{1,2,\ldots,6})$	As for SR cuts			
$\lvert\eta(j_{1,2,..})\rvert$	As for SR cuts	No cut		As for SR cuts
Aplanarity	As for SR cut	No cut		As for SR cut
$\Delta\phi(j_i, E_T^{miss})$	As for SR cuts except in SR4j-3000, SR6j-2200 and SR6j-2600	No cut		$\Delta\phi(j_i, E_T^{miss}) < 0.2$,i={1,2,(3)} : [or $\Delta\phi(j_i, E_T^{miss}) < 0.1$,$p_T > 50$ GeV jets / (for 4j,5j,6j)]
$E_T^{miss}/m_{eff}(Nj)$ or $E_T^{miss}/\sqrt{H_T}$	As for SR cut except in SR4j-3000, SR6j-2200 and SR6j-2600	As for SR cut except in SR4j-3000, SR6j-2200 and SR6j-2600	As for SR cut except in SR4j-3000, SR6j-2200 and SR6j-2600 and all SR2j	$X - \Delta < E_T^{miss}/m_{eff}(Nj) < X$ $X - \Delta < E_T^{miss}/\sqrt{H_T} < X\sqrt{\text{GeV}}$ if $E_T^{miss}/m_{eff}(Nj) > X$ or $E_T^{miss}/\sqrt{H_T} > X$ in SR
m_{eff}(incl.)	As for SR cut			

6.6.2 Z+jets background

The Z+jets background is dominated by Z→$\nu\nu$ events due to the lepton veto in the final state. A method with γ+jets events in CRY is developed to estimate this background. This method uses the similitude in the p_T distribution of Z→ $\nu\nu$ and γ+jets events. A single photon trigger is applied in CRY, and events with lepton in the final state are rejected. The photon $\overrightarrow{p}_T$ is added to the $\overrightarrow{E}_T^{miss}$. For tight SRs, the selections on $\Delta\phi$, $\frac{E_T^{miss}}{m_{eff}}$ and $\frac{E_T^{miss}}{\sqrt{H_T}}$ are relaxed to get more statistics. The Z$\nu\nu$ background $N_{SR}^{Z\nu\nu,pred}$ in the signal region can then be predicted as follows:

$$N_{SR}^{Z\nu\nu,pred} = \frac{N_{CRY}^{data} \times N_{SR}^{MC}}{N_{CRY}^{MC}} = N_{CRY}^{data} \times TF(\gamma \longrightarrow Z(\rightarrow \nu\nu)), \tag{6.6}$$

where TF($\gamma \longrightarrow Z(\rightarrow \nu\nu)$ corresponds to the Transfer Factor from γ+jets to Z($\rightarrow \nu\nu$). To improve the predictions of γ+jets and TF, one could use the Z→ll+jets processes which are also similar to the Z→ $\nu\nu$ processes, but suffer from low statistics when tight cuts are applied. Specific regions CRZL and CRYL with loose cuts are defined, and are used to compute additional corrections (κ factors) for the Z+jets background estimation. The κ are defined as:

$$\kappa = \frac{N_{CRYL}^{\gamma+jets,data}}{N_{CRZL}^{Zll,data}} \frac{N_{CRZL}^{Zll,MC}}{N_{CRYL}^{\gamma+jets,MC}}, \tag{6.7}$$

Where $N_{CRYL}^{\gamma+jets,data}$ ($N_{CRZL}^{Zll,data}$) is the number of data events in CRYL (CRZL), and $N_{CRYL}^{\gamma+jets,MC}$ ($N_{CRZL}^{Zll,MC}$) is the number of γ+jets (Zll) events predicted by the MC in CRYL (CRZL). The κ are computed for each jet multiplicity using the loosest SRs and vary from 1.560±0.035 to 2.257±0.261. The combination of both Z→ll and γ+jets events improves the systematics uncertainty of the background estimation. The number of background events predicted in the SR is then:

$$N_{SR}^{Z\nu\nu,pred} = N_{SR}^{Z\nu\nu,MC} \frac{N_{CRY}^{\gamma+jets,data}}{N_{CRY}^{\gamma+jets,MC}} .\kappa. \tag{6.8}$$

The multijet background in the control region CRY can be estimated using the ABCD method. This method is already introduced for the estimation of the purity uncertainty with the γ+jet method in section 4.6.6. The motivation of this study is to estimate the background in CRY and to apply corrections on the Z+jets estimation which is one of the dominant background of the analysis. The purity is estimated using the ABCD method, including leakages and correlation corrections. The regions A,B,C,D are defined with Tight, Loose Not Tight (LNT), Isolated and non isolated criteria. The correlation factor between photon identification and isolation is estimated to be 1.36. The estimation of the purity in CRY is shown in Figure 6.21 as a function of the signal regions. The comparison of the purity estimation applying or not the leakage and correlation corrections is shown. With correlation and leakage corrections, the purity in CRY is estimated to be ~99% in average. The QCD background estimated with the ABCD method in CRY is found to be negligible. Therefore, it is not necessary to include the QCD background contribution in CRY for the fit.

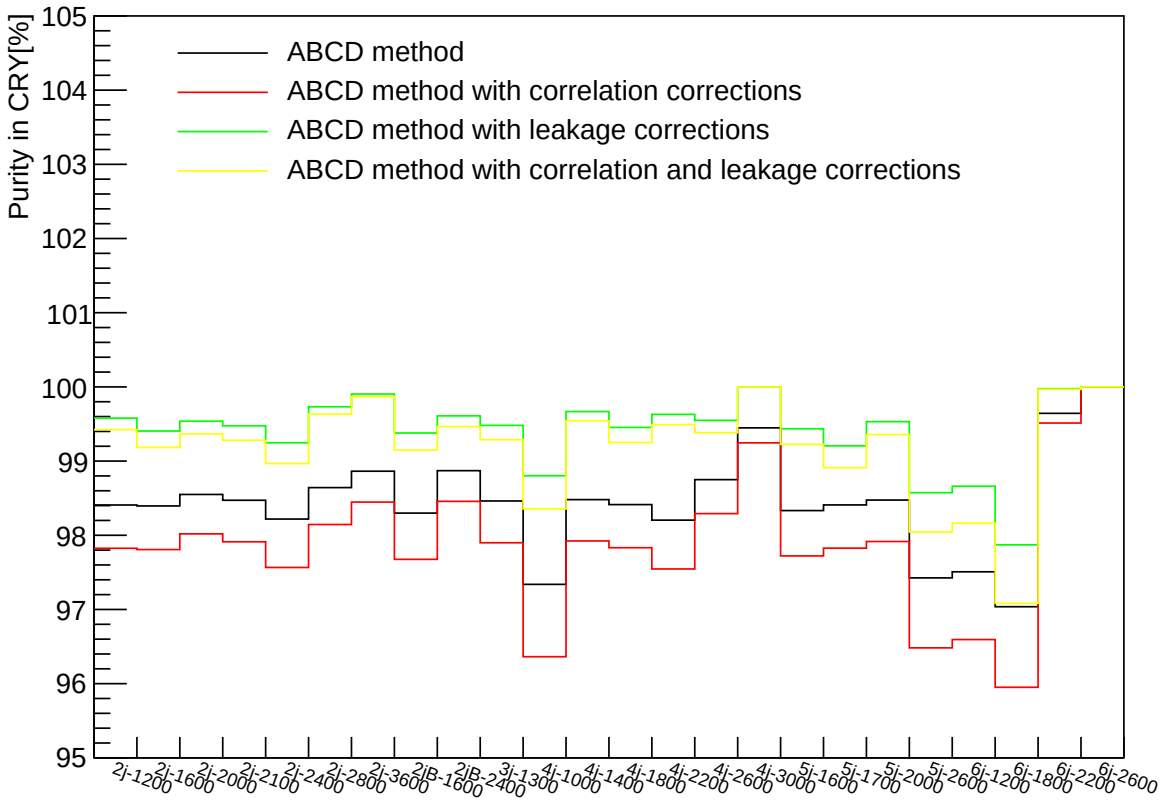

Figure 6.21: Purity estimation of CRY using ABCD method in the signal regions. In black the purity estimation without corrections, in red applying correlation corrections, in green applying leakage corrections, and in yellow applying correlation and leakage corrections.

6.6.3 QCD background

The multi-jet background is estimated using a data-driven technique [147], which applies a resolution function to well-measured multijet events in order to estimate the impact of jet energy mismeasurement and heavy-flavour semi-leptonic decays on E_T^{miss}. The method for the estimation is called the jet smearing method. First, the jet response defined as $R = \frac{p_T^{reco}}{p_T^{truth}}$ is measured. The Monte Carlo jet response is constructed from a matching between isolated truth and reconstructed jets. Events with low E_T^{miss} are multiplied by a random correction factor drawn from the jet response distribution. This process is repeated between 3000 and 10000 times to produced a sample of multijet pseudo-data. This pseudo data is then used to estimate the multijet distributions in the analysis, including the distribution in the control region. The distributions are used to determine the transfer factors from CRQ to signal regions. Events in CRQ are selected with low E_T^{miss} by reversing $\Delta\phi(j, E_T^{miss})$, $\frac{E_T^{miss}}{m_{eff}}$ and $\frac{E_T^{miss}}{\sqrt{H_T}}$ cuts (Table 6.9). A threshold is added to $\frac{E_T^{miss}}{m_{eff}}$ or $\frac{E_T^{miss}}{\sqrt{H_T}}$ cuts.

6.6.4 Control regions for boosted bosons

The distributions of re-clustered jet mass for leading and sub-leading jets in the boosted control regions 2jB-1600 and 2jB-2400 are shown in Figure 6.22 and 6.23. The top contribution tends to be overestimated by the Monte Carlo. Due to the tight selections in 2jB-2400, only a few events pass the selections, especially in CRW. Therefore, an intermediate control region is introduced, where at least one re-clustered jet instead of both must pass the mass selection. The m_{eff} distributions in CRs with respectively: no cut on re-clustered jets mass, selection on both re-clustered jets mass, and selection on one re-clustered jet mass only are shown in Figures 6.24, 6.25 and 6.26. The double arrows show the selections on m_{eff} in the regions 2jB-1600 and 2jB-2400. The choice of the selection on one of the two jets mass (Figure 6.26) is a good compromise taking into account the statistical constraints.

6.6.5 Definition of the validation regions

For each control region, a set of validation regions are defined to test the background predictions. The validation regions are defined with the same selections as for the CRs but adding missing cuts. In the following, VRX refers to VRY, VRW and VRT:

- VRXm is defined for $\frac{E_T^{miss}}{m_{eff}}$ or $\frac{E_T^{miss}}{\sqrt{H_T}}$ cuts,
- VRXdPhi is defined for the $\Delta\phi$ cut,
- VRXAp is defined for aplanarity cut,
- VRXeta is defined for the η cut,
- VRXB is defined for the re-clustered jet mass.

Another set of validation regions are defined as:

- VRXf, the full set of cuts in the control region are applied, with additional cuts on $\frac{E_T^{miss}}{m_{eff}}$ or $\frac{E_T^{miss}}{\sqrt{H_T}}$, $\Delta\phi$, ap, η.
- VRWM/VRTM, in these VRs, the lepton is treated as a missing particle instead of a jet as done in the CR.

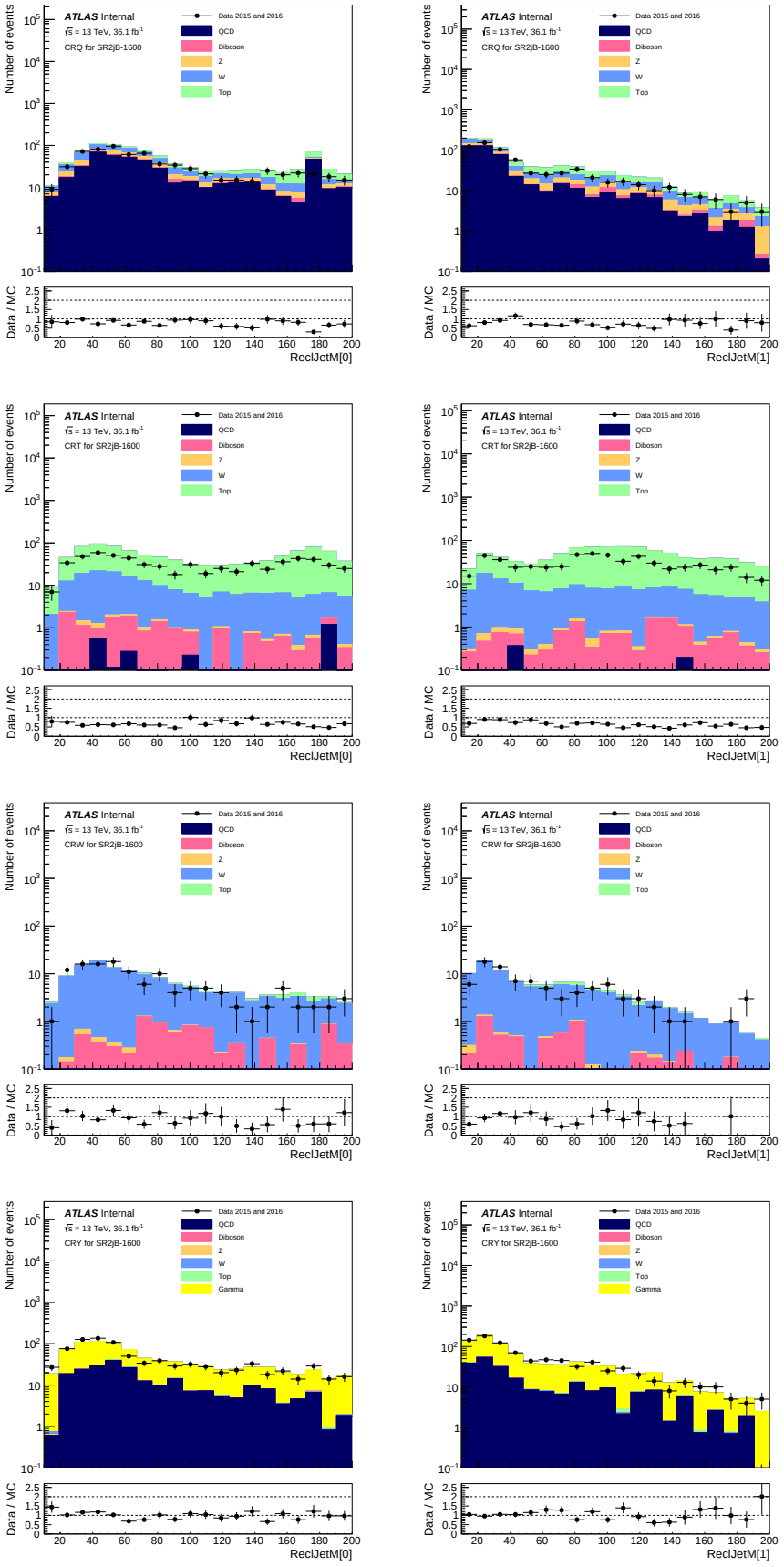

Figure 6.22: Distribution of mass for re-clustered leading jet (left) and sub-leading jet (right) in the boosted control regions 2jB-1600 for data and simulation. The Monte Carlo simulation is normalized to the theoretical cross-section. No event selection is applied on re-clustered jet mass.

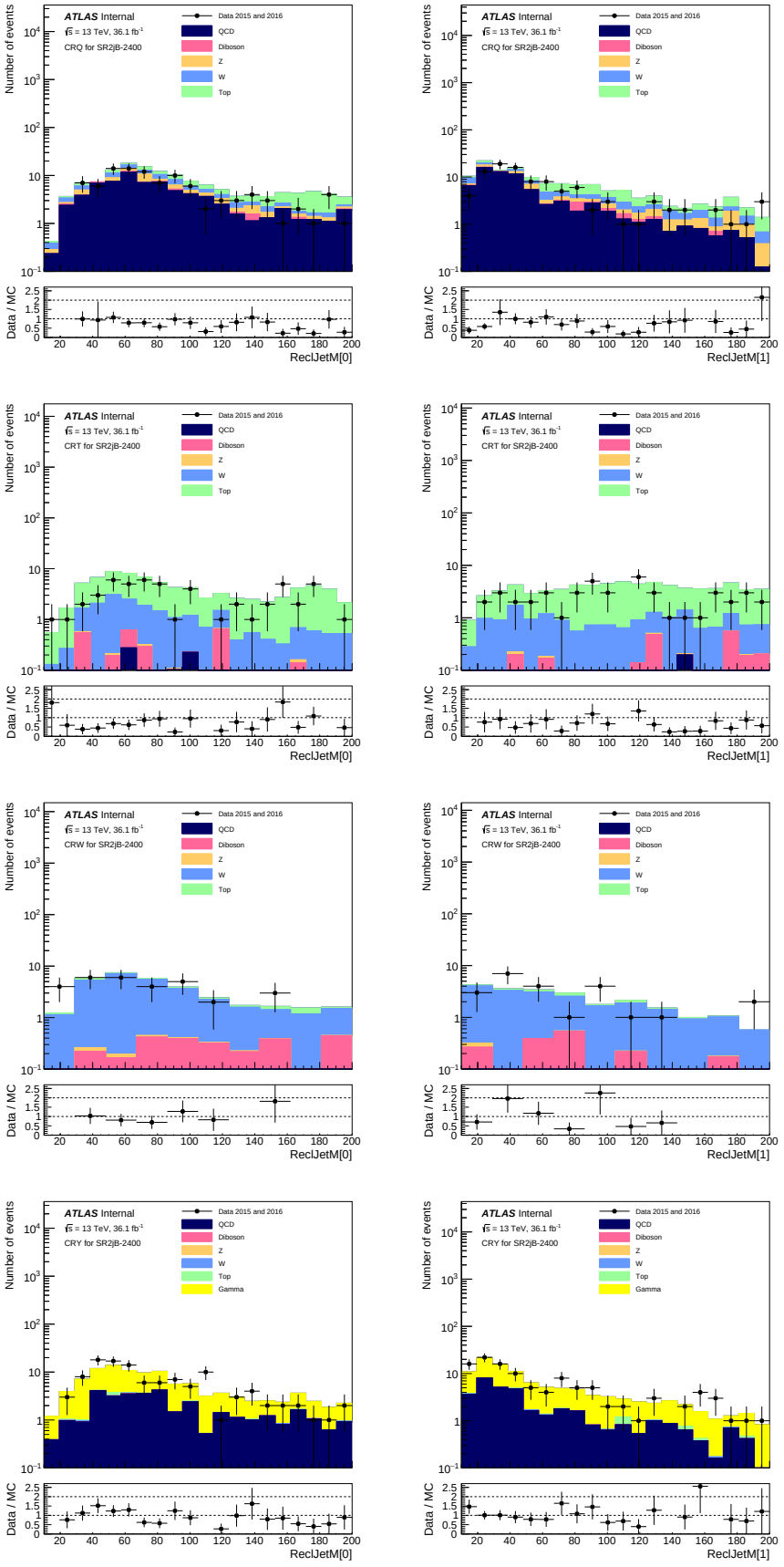

Figure 6.23: Distribution of mass for re-clustered leading jet (left) and sub-leading jet (right) in the boosted control regions 2jB-2400 for data and simulation. The Monte Carlo simulation is normalized to the theoretical cross-section. No event selection is applied on re-clustered jet mass.

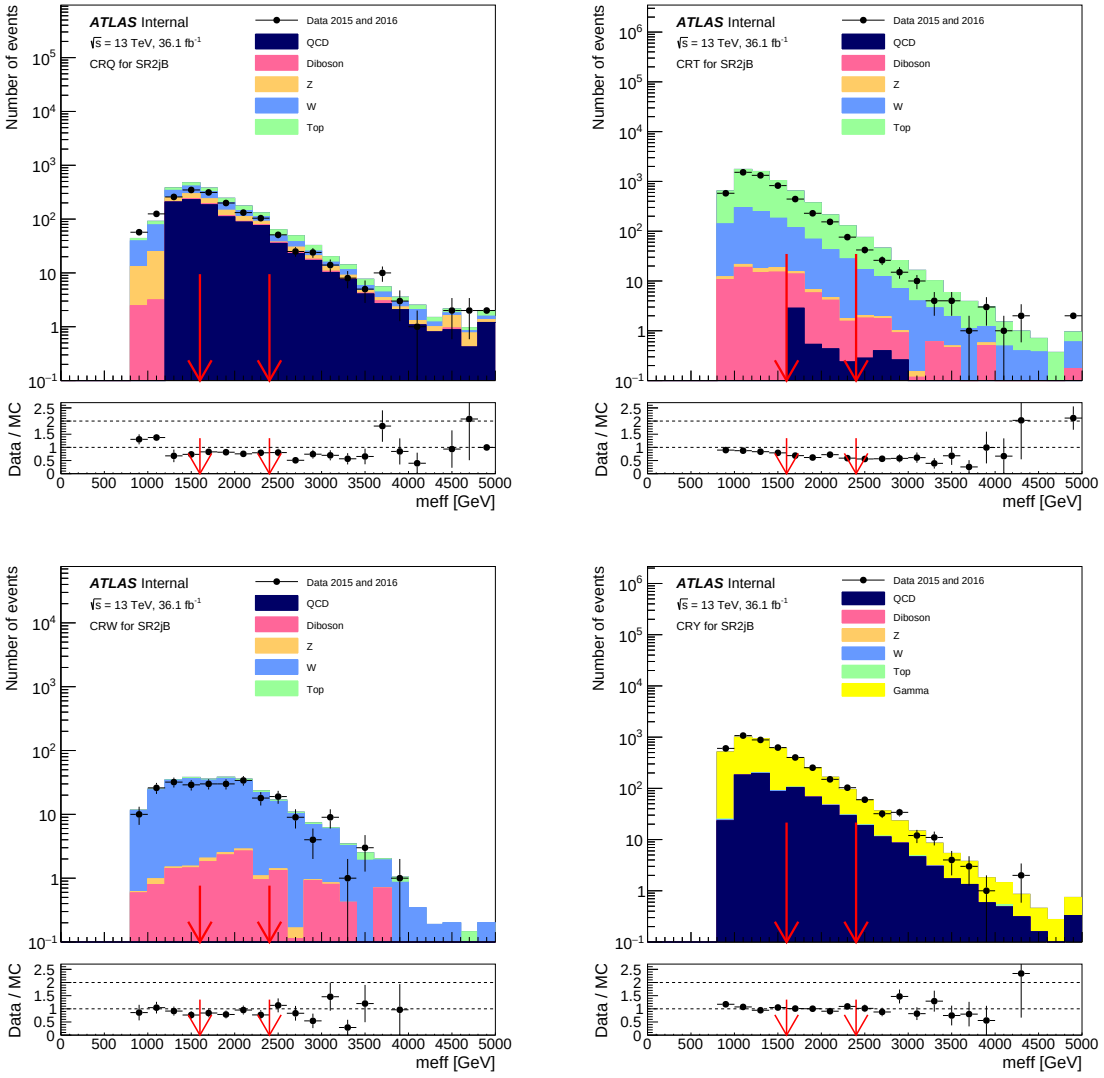

Figure 6.24: Distribution of m_{eff} in the boosted control regions, with no selection applied on re-clustered jet mass. The bottom part shows the data-to-MC simulation. Red arrows indicate the selections on m_{eff} for signal region 2j-1600 and 2j-2400. Monte Carlo simulation is normalized to the theoretical cross-section.

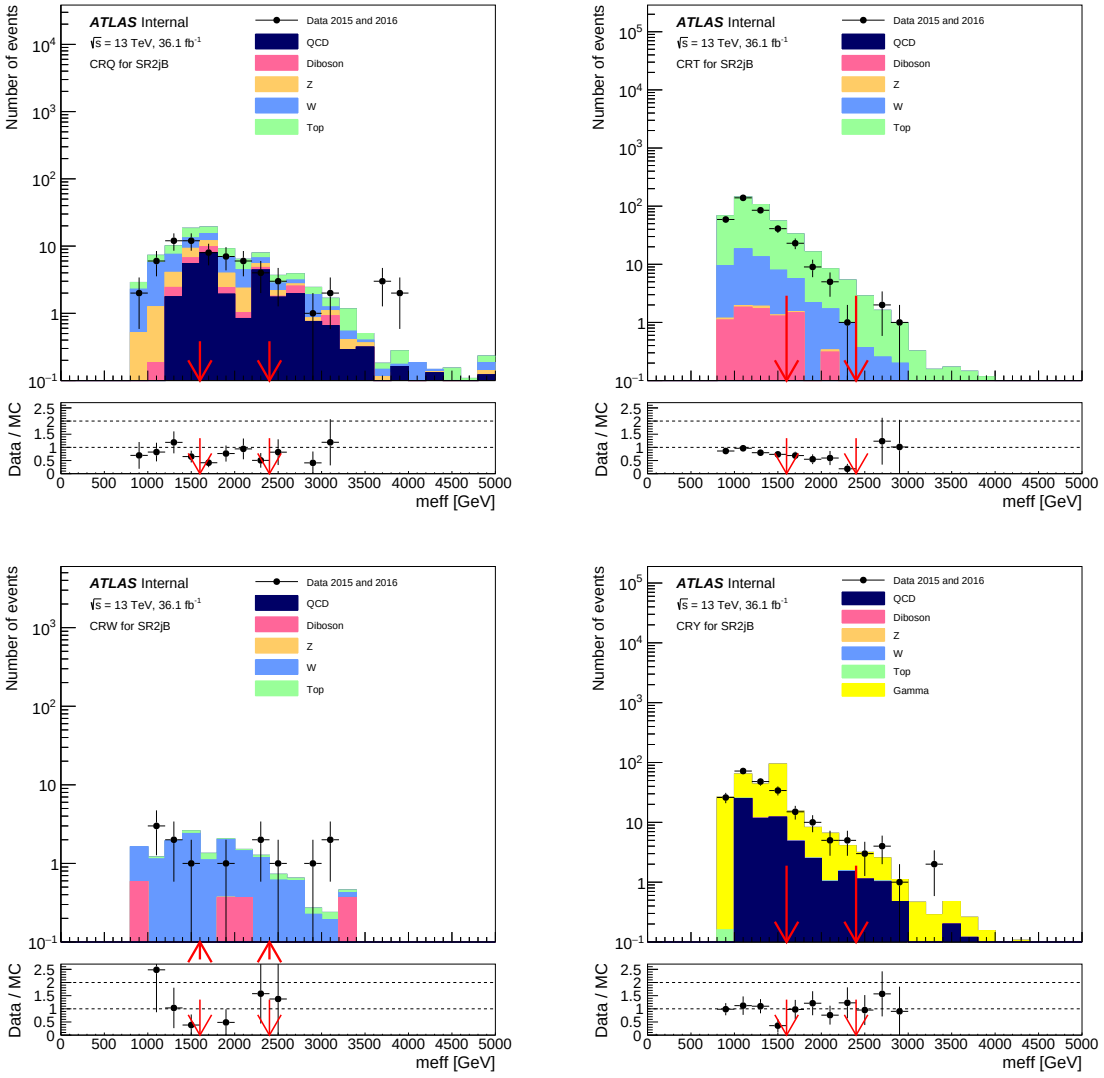

Figure 6.25: Distribution of m_{eff} in the boosted control regions, with selection applied on both re-clustered jets mass. The bottom part shows the data-to-MC simulation. Red arrows indicate the selections on m_{eff} for signal region 2j-1600 and 2j-2400. Monte Carlo simulation is normalized to the theoretical cross-section.

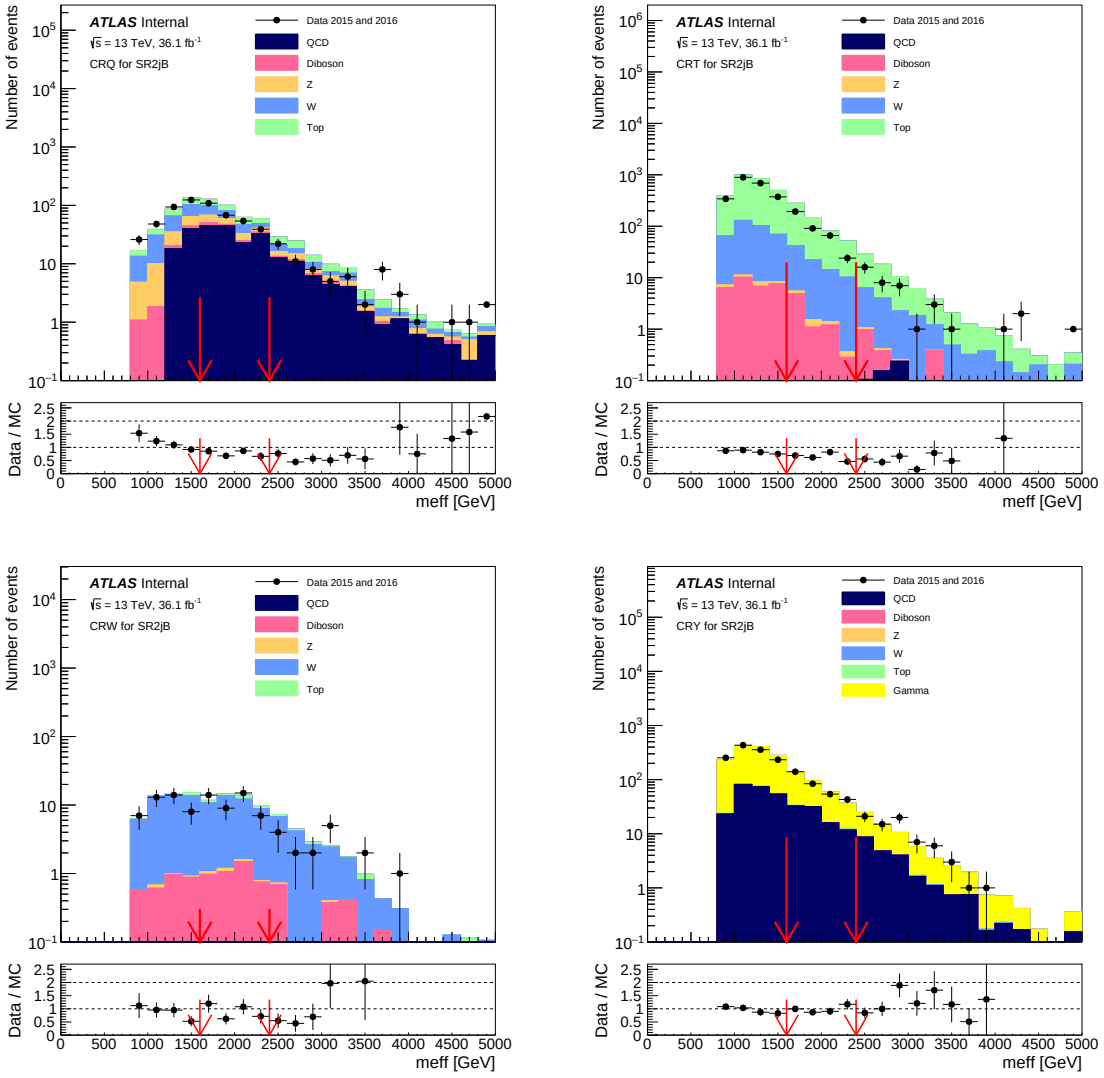

Figure 6.26: Distribution of m_{eff} in the boosted control regions. At least one of the two jets must pass the re-clustered jet mass selection. The bottom part shows the data-to-MC simulation. Red arrows indicate the selections on m_{eff} for signal region 2j-1600 and 2j-2400. Monte Carlo simulation is normalized to the theoretical cross-section.

6.7 Systematic uncertainties

The sources of uncertainties on the background estimation are the following:

- background scale factors from CRs (μ),
- W/Z theoretical uncertainties,
- top background uncertainties,
- diboson background estimation,
- QCD background estimation from jet smearing,
- uncertainties on κ,
- JES/JER + E_T^{miss} uncertainties.

The Z and W theoretical uncertainties are estimated by propagating the Z/W scale variations to the error on the transfer factor from CR to SR. The following variations are applied:

- renormalization scale variation (renorm),
- factorization scale variation (fac),
- resummation scale variation (qsf),
- CKKW matching scale variation (ckkw).

The impact of the scale variations on Z/W transfer factors in the signal regions is shown in Figure 6.27. The total uncertainty is computed as the quadratic sum of the scale variations, using truth samples. Due to the limited statistics of scale variations samples, the statistical uncertainties become large in the tight CRs/SRs (SR6j-1800 and SR6j-2600). I contributed to the evaluation of Z and W theoretical uncertainties. This part includes writing the code for the propagation of scale variations to the transfer factors, and the computation of the final uncertainties on Z/W including Figure 6.27.

Uncertainties on the top background are estimated with a comparison between the nominal and a reference Monte Carlo. The Matrix Element uncertainty is estimated by comparing Powheg and aMC@NLO, the parton shower is estimated comparing Herwig++ and Pythia8 and the radiation is estimated with a lower and higher value. The diboson uncertainty is estimated with Sherpa 2.2.1 and includes uncertainties on the total cross section, the renormalization and factorization scale variations, the PDF and α_s.

The QCD background uncertainties are estimated with a conservative flat uncertainty of 100%. The uncertainties on κ correspond to the statistical uncertainties on CRY and VRZ.

The uncertainties on JES/JER are estimated with the method described in section 3 and the E_T^{miss} uncertainty is provided by the JetEtMiss group [102]. The Jet Mass Scale (JMS) uncertainty is estimated in the boosted regions only, where selection on re-clustered jet mass is applied. The reclustering algorithm uses small jets with R = 0.4 as inputs. The uncertainty is obtained directly by propagating the small jet mass uncertainty to the larger jet. The JMS uncertainty is computed in CRs for two points in 2jB-1600 and 2jB-2400 and is shown in Table 6.10. The uncertainty on the Jet Mass Resolution (JMR) is estimated with the JetEtMiss recommendations to be 7% in both SR2jB.

Systematic uncertainties with limited impact, for example those which are much smaller than the luminosity uncertainty are neglected:

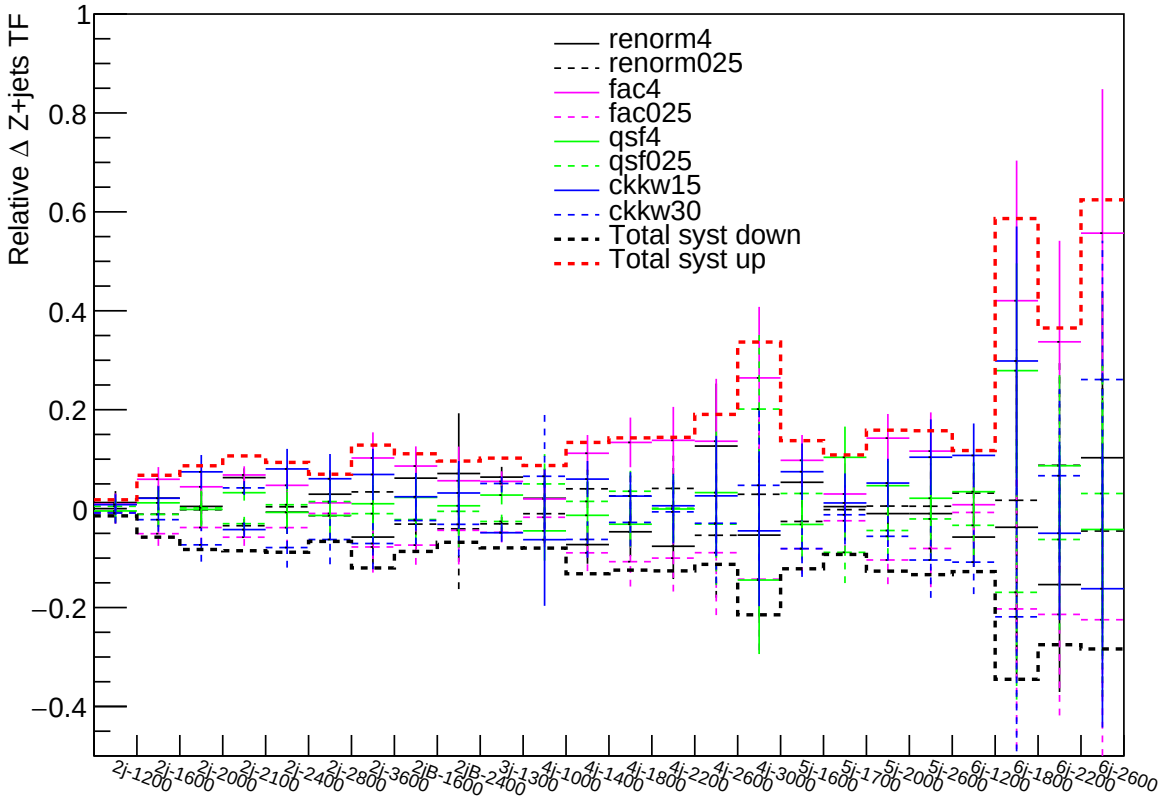

(a) Z scale variations

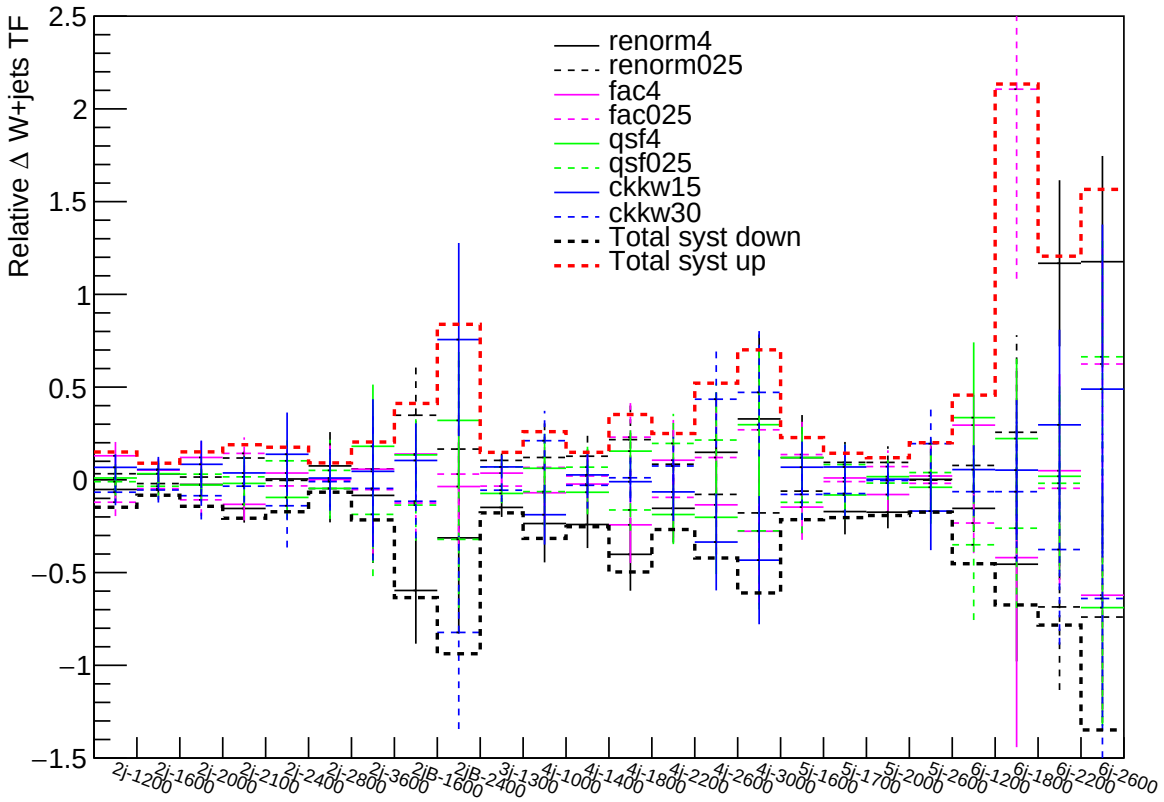

(b) W scale variations

Figure 6.27: Relative uncertainties on the transfer factors between control regions and signal regions for Z+jets (a) and W+jets (b) scale variations. The red and black dotted lines correspond to the quadratic sum of up and down uncertainties.

Table 6.10: Relative JMS uncertainty on the transfer factors for CRW,CRY, CRT, and on the diboson normalization in SR2jB-1600 and SR2jB-2400.

	2jB-1600	**2jB-2400**
W+jets	1.95 %	4.72%
Z+jets	1.73 %	4.50 %
Top	6.98%	5.09%
Diboson	2.85 %	7.96 %

- ElectronID, reconstrucion, isolation, trigger efficiency,
- Electron/photon energy scale, energy resolution,
- Muon ID, reconstruction, isolation, trigger efficiency,
- Muon momentum scale, momentum resoultion,
- Photon ID, reconstruction, isolation efficiency.

Table 6.11 (a) and 6.11 (b) show the impact of the main sources of uncertainties on the fit in the signal regions 6j-1200 and 6j-2600. The signal regions with tight m_{eff} cut are dominated by the statistical uncertainties (Table 6.11 (b)), while for loose m_{eff} cut, the uncertainties are dominated by the background uncertainty. In all regions, the modelling of the background is an important source of uncertainty. The experimental systematics on JES/JER or E_T^{miss} are almost negligible. The uncertainties in the boosted regions are shown in Table 6.12. Both are dominated by statistical uncertainties, and the uncertainties on JMS and JMR are estimated to be 1.8% and and 2.7% in SR2jB-1600 and 4.1% and 3.0% in SR2jB-2400.

Figure 6.28 shows the total uncertainties in the signal regions, with the contributions of the experimental, theoretical and statistical uncertainties on the control regions and the Monte Carlo. The statistical uncertainty in the control regions is dominant in most of signal regions. The region SR6j-2600 is dominated by the theoretical uncertainties due to low statistics in the Monte Carlo samples to compute the W/Z scale variations.

6.8 Search for squarks and gluinos procedure

A profile likelihood ratio is used to perform the estimation of the background, the discovery test and the exclusion tests. The profile likelihood ratio is obtained from a fit to the measurements in the signal regions and control regions. The fit is defined using the ZeroLeptonFitter and HistFitter softwares. Three fits can be performed:

1. The background fit normalizes all the background processes in the control regions. This fit is not constrained by the number of events in the signal regions.
2. The discovery fit includes the constraint of the number of events in the signal regions and adds a generic non-Standard Model signal process.

Table 6.11: Dominant systematic uncertainties on background estimation in SR6j-1200 (a) and SR6j-2600 (b). The percentages show the relative size on the total expected background uncertainty.

Uncertainty of channel	SR_cuts
Total background expectation	249.00
Total statistical ($\sqrt{N_{exp}}$)	±15.78
Total background systematic	±30.18 [12.12%]
alpha_TheoW	±18.73 [7.5%]
alpha_Pythia8Top	±12.57 [5.1%]
mu_Top	±10.62 [4.3%]
alpha_radiationTop	±10.34 [4.2%]
mu_Wjets	±7.22 [2.9%]
alpha_Kappa	±6.39 [2.6%]
alpha_TheoZ	±6.03 [2.4%]
alpha_HerwigppTop	±5.51 [2.2%]
mu_Zjets	±5.08 [2.0%]
alpha_generatorTop	±4.92 [2.0%]
gamma_stat_SR_cuts_bin_0	±4.00 [1.6%]
alpha_pileUp	±3.85 [1.5%]
alpha_JET_GroupedNP_3	±3.48 [1.4%]
alpha_FlatDiboson	±3.21 [1.3%]
alpha_JER	±2.96 [1.2%]
alpha_JET_GroupedNP_2	±2.40 [0.96%]
alpha_JET_GroupedNP_1	±2.13 [0.85%]
alpha_MET_SoftTrk_ResoPara	±0.92 [0.37%]
alpha_QCDError	±0.72 [0.29%]
alpha_MET_SoftTrk_ResoPerp	±0.62 [0.25%]
mu_Multijets	±0.09 [0.04%]
alpha_MET_SoftTrk_Scale	±0.06 [0.02%]

(a)

Uncertainty of channel	SR_cuts
Total background expectation	0.85
Total statistical ($\sqrt{N_{exp}}$)	±0.92
Total background systematic	±0.57 [66.68%]
alpha_generatorTop	±0.35 [40.8%]
alpha_TheoW	±0.23 [27.3%]
alpha_TheoZ	±0.17 [20.6%]
mu_Wjets	±0.14 [16.1%]
alpha_pileUp	±0.13 [15.3%]
alpha_HerwigppTop	±0.12 [14.3%]
mu_Zjets	±0.12 [14.0%]
alpha_JER	±0.10 [12.3%]
gamma_stat_SR_cuts_bin_0	±0.10 [11.7%]
alpha_Pythia8Top	±0.09 [10.1%]
mu_Top	±0.08 [9.3%]
alpha_Kappa	±0.04 [4.6%]
alpha_JET_GroupedNP_1	±0.03 [3.0%]
alpha_JET_GroupedNP_3	±0.02 [2.3%]
alpha_FlatDiboson	±0.02 [1.8%]
alpha_JET_GroupedNP_2	±0.01 [1.6%]
alpha_MET_SoftTrk_Scale	±0.01 [1.5%]
alpha_MET_SoftTrk_ResoPara	±0.01 [0.65%]
alpha_radiationTop	±0.00 [0.49%]
alpha_MET_SoftTrk_ResoPerp	±0.00 [0.17%]

(b)

Table 6.12: Dominant systematic uncertainties on background estimation in SR2jB-1600 (a) and SR2jB-2400 (b). The percentages show the relative size on the total expected background uncertainty.

Uncertainty of channel	SR_cuts
Total background expectation	20.60
Total statistical ($\sqrt{N_{exp}}$)	±4.54
Total background systematic	±3.62 [17.57%]
alpha_TheoW	±2.50 [12.2%]
alpha_JER	±1.09 [5.3%]
alpha_JET_GroupedNP_1	±1.05 [5.1%]
gamma_stat_SR_cuts_bin_0	±1.00 [4.9%]
mu_Wjets	±0.97 [4.7%]
alpha_TheoZ	±0.83 [4.0%]
mu_Zjets	±0.70 [3.4%]
alpha_FlatDiboson	±0.63 [3.1%]
alpha_pileUp	±0.58 [2.8%]
alpha_JMR	±0.55 [2.7%]
alpha_Pythia8Top	±0.38 [1.9%]
alpha_JMS	±0.37 [1.8%]
alpha_Kappa	±0.28 [1.3%]
alpha_generatorTop	±0.24 [1.2%]
alpha_HerwigppTop	±0.18 [0.88%]
alpha_JET_GroupedNP_2	±0.10 [0.48%]
alpha_JET_GroupedNP_3	±0.09 [0.45%]
alpha_MET_SoftTrk_ResoPerp	±0.07 [0.36%]
mu_Top	±0.05 [0.26%]
alpha_MET_SoftTrk_Scale	±0.04 [0.20%]
alpha_radiationTop	±0.03 [0.16%]
alpha_MET_SoftTrk_ResoPara	±0.03 [0.14%]

(a)

Uncertainty of channel	SR_cuts
Total background expectation	3.89
Total statistical ($\sqrt{N_{exp}}$)	±1.97
Total background systematic	±0.98 [25.21%]
alpha_Pythia8Top	±0.57 [14.7%]
alpha_TheoW	±0.50 [12.9%]
gamma_stat_SR_cuts_bin_0	±0.35 [8.9%]
mu_Zjets	±0.34 [8.7%]
mu_Wjets	±0.19 [5.0%]
alpha_TheoZ	±0.16 [4.1%]
alpha_JMS	±0.16 [4.1%]
alpha_JET_GroupedNP_1	±0.13 [3.3%]
alpha_JMR	±0.12 [3.0%]
alpha_pileUp	±0.07 [1.8%]
alpha_FlatDiboson	±0.06 [1.6%]
alpha_Kappa	±0.06 [1.6%]
alpha_JET_GroupedNP_3	±0.05 [1.3%]
alpha_MET_SoftTrk_Scale	±0.03 [0.69%]
alpha_HerwigppTop	±0.02 [0.57%]
alpha_generatorTop	±0.02 [0.56%]
alpha_JER	±0.02 [0.44%]
alpha_radiationTop	±0.02 [0.43%]
mu_Top	±0.02 [0.40%]
alpha_MET_SoftTrk_ResoPerp	±0.00 [0.06%]
alpha_JET_GroupedNP_2	±0.00 [0.05%]
alpha_MET_SoftTrk_ResoPara	±0.00 [0.04%]

(b)

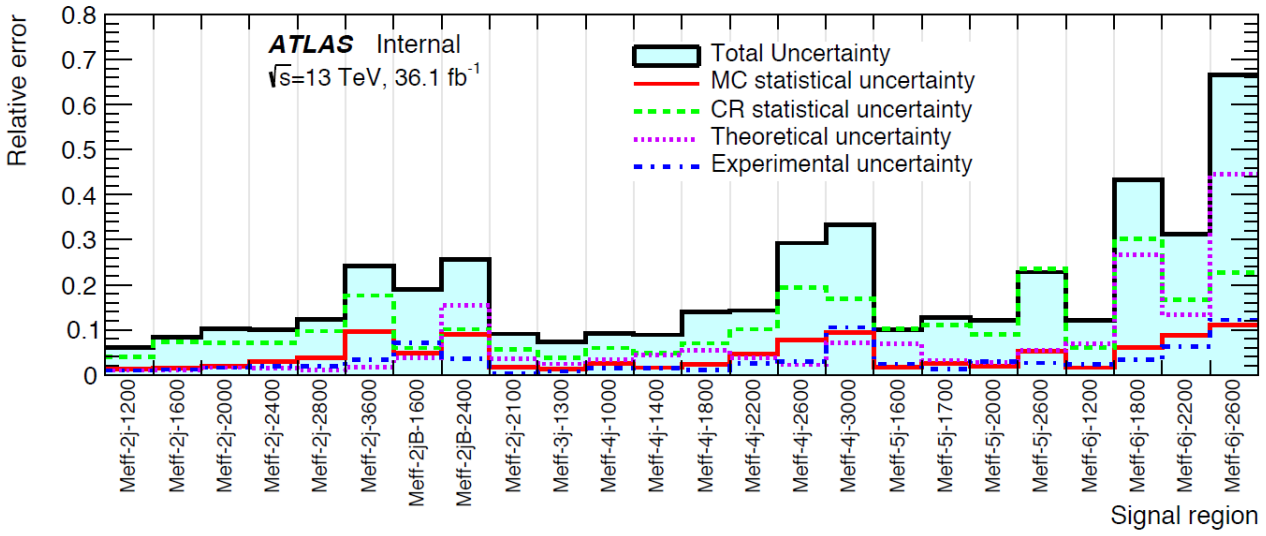

Figure 6.28: Estimation of the total uncertainty in each signal region. The total uncertainty includes experimental uncertainty, theoretical uncertainty, and statistical uncertainties on control regions and Monte Carlo.

3. The exclusion fit replaces the generic non-Standard Model signal process by the signal prediction of a specific SUSY model in the signal regions and control regions.

6.8.1 Likelihood function

The likelihood function for each of the channels is the product of the Poisson distributions of the signal region P_{SR} and control regions P_{CRW}, P_{CRT}, P_{CRY} and P_{CRQ}. Each Poisson distribution includes the observed number of events n_i and and the expected number of events λ_i. The systematic uncertainties are included by multiplying by the probability density function C_{syst}:

$$L(n|\mu, s, b, \theta) = P_{SR} \times P_{CRW} \times P_{CRT} \times P_{CRY} \times P_{CRQ} \times C_{Syst}, \tag{6.9}$$

Where n is the observed number of events in the signal region, μ are the free normalization factors for the signal or background. The background has no associated free parameter. The expected number of signal events s, for the specific model under consideration is estimated with Monte Carlo simulation. For the discovery fit, the signal strength μ_s is fixed at 0, otherwise μ_s is initially set to 1. b is the expected number of background events for each source of background, also estimated from MC. The θ are the nuisance parameters and parametrize the systematic uncertainties:

$$\lambda_i(\mu, s_i, b, \theta) = s_i(\theta).\mu_s + b_{i,j}(\theta).\mu_j + \sum_{j}^{W,Z,t\bar{t},QCD} b_i^{VV}(\theta), \tag{6.10}$$

Where j runs over background processes.

6.8.2 Treatment of systematic uncertainties

The systematic uncertainties are included in the log likelihood ratio using the probability density function $C_{Syst}(\theta^0, \theta)$, where θ^0 are the nominal values around which θ can be varied, for example

when maximazing the likelihood. For independent nuisance parameters, C_{Syst} is simply a product of their probability distribution, typically Gaussian function G:

$$C_{Syst}(\theta^0, \theta) = \prod_{j \in SU} G(\theta_j^0, \theta_j), \tag{6.11}$$

Where SU corresponds to the set of systematic uncertainties considered. The nuisance parameters can be treated as:

- Fully correlated across the different regions and physics processes (luminosity, jets, E_T^{miss}..).
- Fully correlated across the different regions but independant per process (theoretical uncertainties).
- Fully uncorrelated variables (like Monte Carlo statistical errors).

Table 6.13 summarizes all the uncertainties of the analysis, the physical process and source of this uncertainty and its specific treatment in the fit.

Table 6.13: Summary of systematic uncertainties included in the likelihood fit.

Name	Name in Fitter	Process	L Treatment	Comment
Luminosity				±4.1%
Pileup reweighting	pileUp	All	Fully correlated	See Section 3.4
MC statistics	stat		Uncorrelated	
κ factor	Kappa	Z/γ	Uncorrelated	
CR statistics	mu_X	W/Z/γ+jets/top	Uncorrelated	
Object modelling				
Jet energy scale (JES)	JET_GroupedNP_(1-3)			Strongly reduced uncertainties
Jet energy resolution (JER)	JER			Simple mode
Jet mass scale (JMS)	JMS			Only in boosted boson SR
Jet mass resolution (JMR)	JMR	All	Fully correlated	Only in boosted boson SR
JVT efficiency				**TO BE ADDED**
$E_{\mathrm{T}}^{\mathrm{miss}}$ soft term scale	MET_SoftTrk_Scale			
$E_{\mathrm{T}}^{\mathrm{miss}}$ soft term resolution	MET_SoftTrk_ResoPerp/Para			
b-tagging efficiency (b/c/light)	EFF_X			Only in CRW and CRT
Physics process modelling				
Cross-section and acceptance	FlatDiboson	Diboson	Uncorrelated	±50%[8](**TO BE UPDATED**)
Scale variation	GeneratorW/Z	W/Z/γ+jets	Correlated per process	SHERPA scale variation samples
Generator comparison	GeneratorTop	$t\bar{t}$		POWHEG-BOX vs aMC@NLO
Radiation	radiationTop	$t\bar{t}$	Correlated per process	High vs Low
Parton shower tunes	Pythia8/HerwigppTop	$t\bar{t}$		Pythia6 P2011 vs Pythia8 A14, Herwig++
Multi-jets method	QCDError	Multijet	Uncorrelated	±100%

6.8.3 Signal uncertainty

The uncertainties on the signal are less than a few percent and have a small impact on the final results. To test the theory uncertainties on the signal acceptance, different sources of theoretical uncertainties are checked such as:

- renormalization and factorization scale,
- ISR radiation with varying α_s,
- the matching between the matrix element and the parton shower,
- extra jet production.

6.9 Results, interpretation and limits

6.9.1 Background fit

Figure 6.29 shows the data and MC distributions of m_{eff}(incl) for the control regions associated to the signal region 4j-1000. For each control region, a scale factor μ is computed to extrapolate the background from the CR to the SR. The scale factors are represented in Figure 6.30. Top background contribution is systematically underestimated by the MC. Contributions from W/Z+jets are underestimated for high jet multiplicity, while QCD background is slightly underestimated for low jets multiplicity.

To test and validate the Standard Model background estimation, specific validation regions are defined (section 6.6.5). The validation procedure consists of comparing the Standard Model background prediction of the fit to the data in the validation regions. The summary of the pulls for all signal regions and validation regions are shown in Figure 6.31 and pulls equal to zero by construction are removed. Most of the pulls are close to zero. Some pulls are greater than 2 σ. Investigations done in these regions point to statistical uncertainties.

6.9.2 Results

The number of events observed in data and the background estimated with the background-only fits are presented in Figure 6.34. No significant excess is observed in the signal regions. The most significant excess is observed in SR2j-2100 with a standard deviation of 1.95σ. High statistical uncertainties are seen in high jet multiplicity and tight m_{eff} cut. The bottom of the figure shows the ratio between observed events in data and Standard Model predictions. The m_{eff} distributions in the signal regions 4j, 5j, 6j, and 2jB are shown in Figures 6.32 and 6.33.

Table 6.14 describe the background expectation normalized to the theoretical cross-section (top of each table), after the fit on control region (center), and the observed number of events in each signal region. The p-values and its corresponding standard deviation are shown in bottom part.

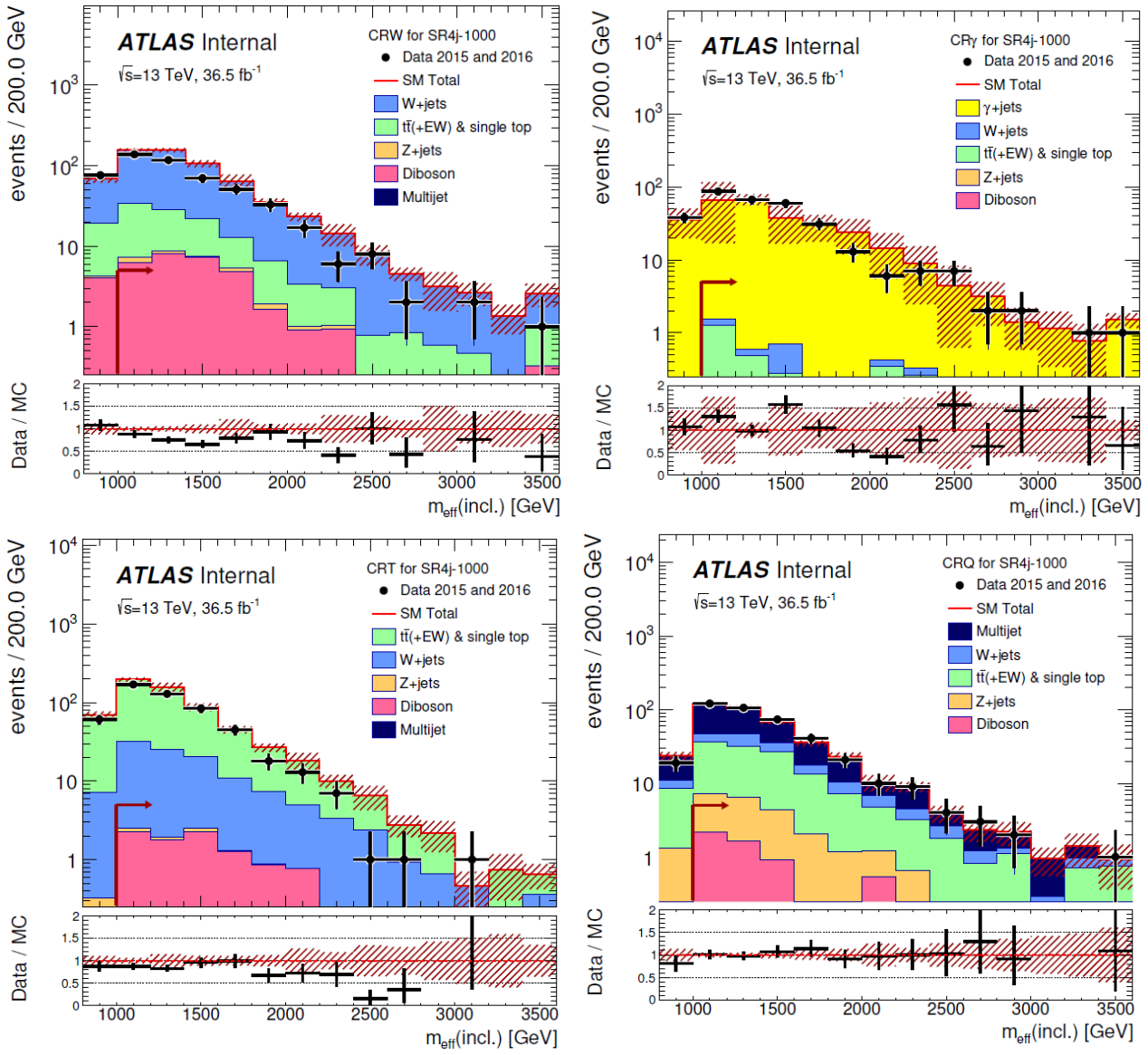

Figure 6.29: Distributions of m_{eff}(incl) in the control regions CRW, CRY, CRT, CRQ for SR4j-1000. The distributions show the Standard Model background expectation normalized to 36.5 fb^{-1}. The hatched error bands describe the combined experimental and Monte Carlo statistical uncertainties.

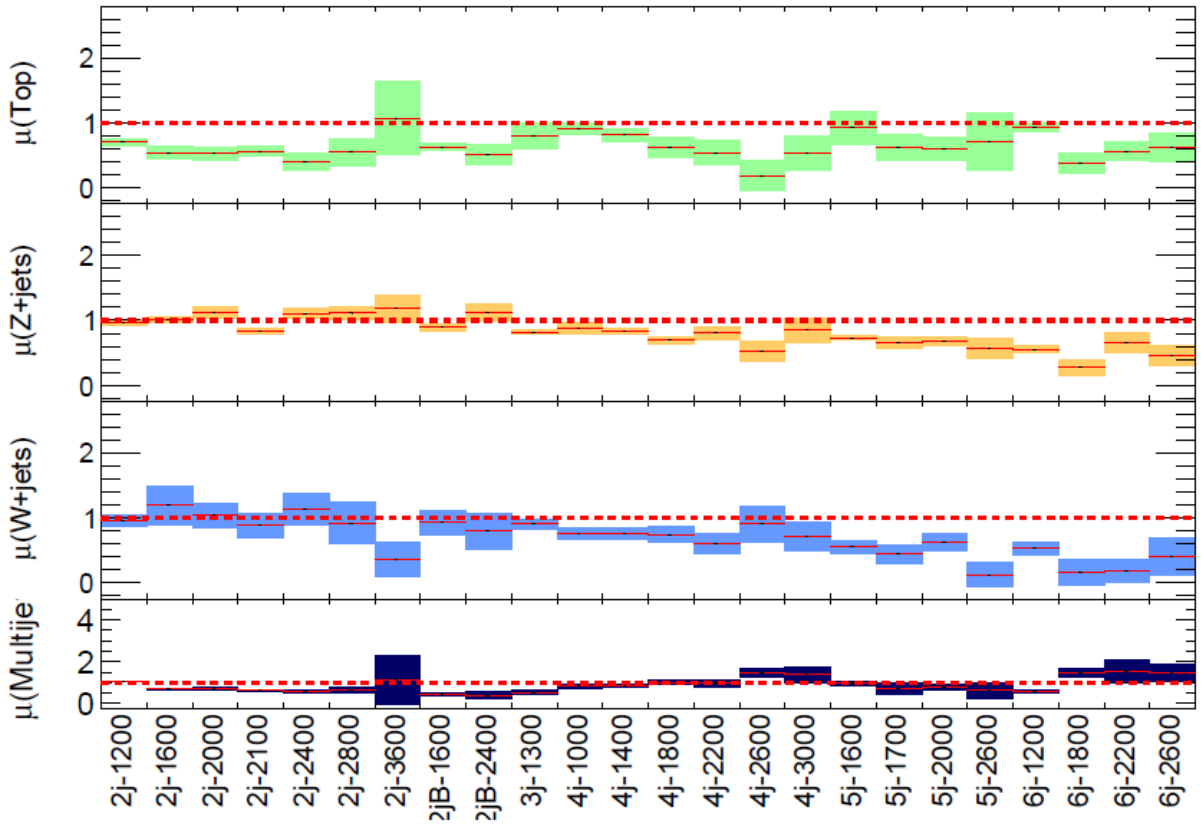

Figure 6.30: Fitted μ parameters for each background process as a function of the signal regions. The red dotted horizontal lines would correspond to pure Monte Carlo estimation.

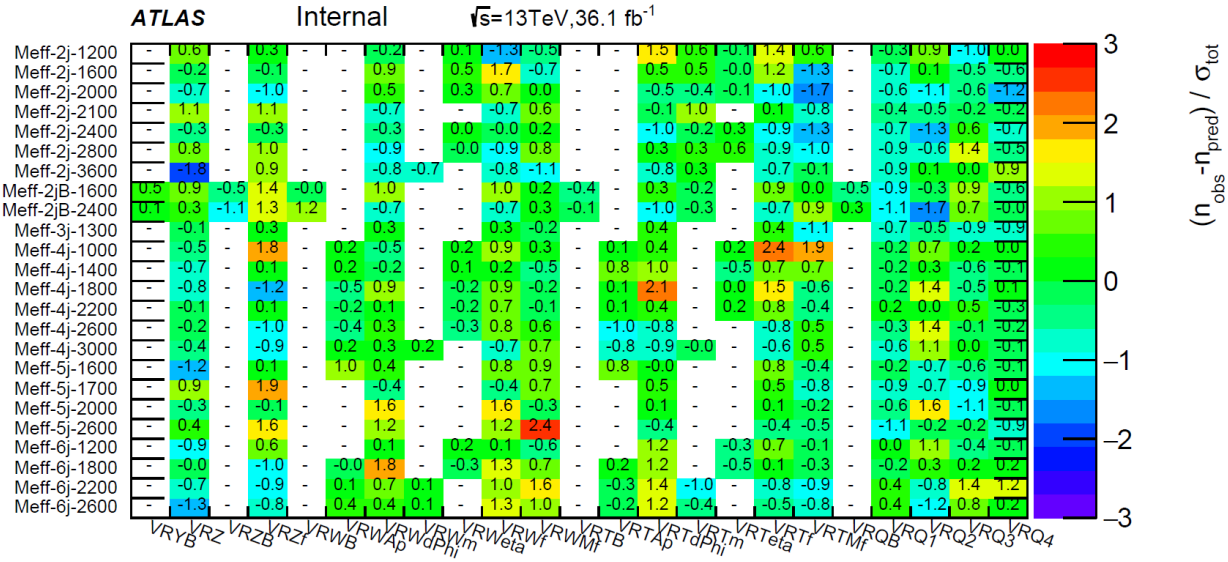

Figure 6.31: Summary of pull values in validation regions.

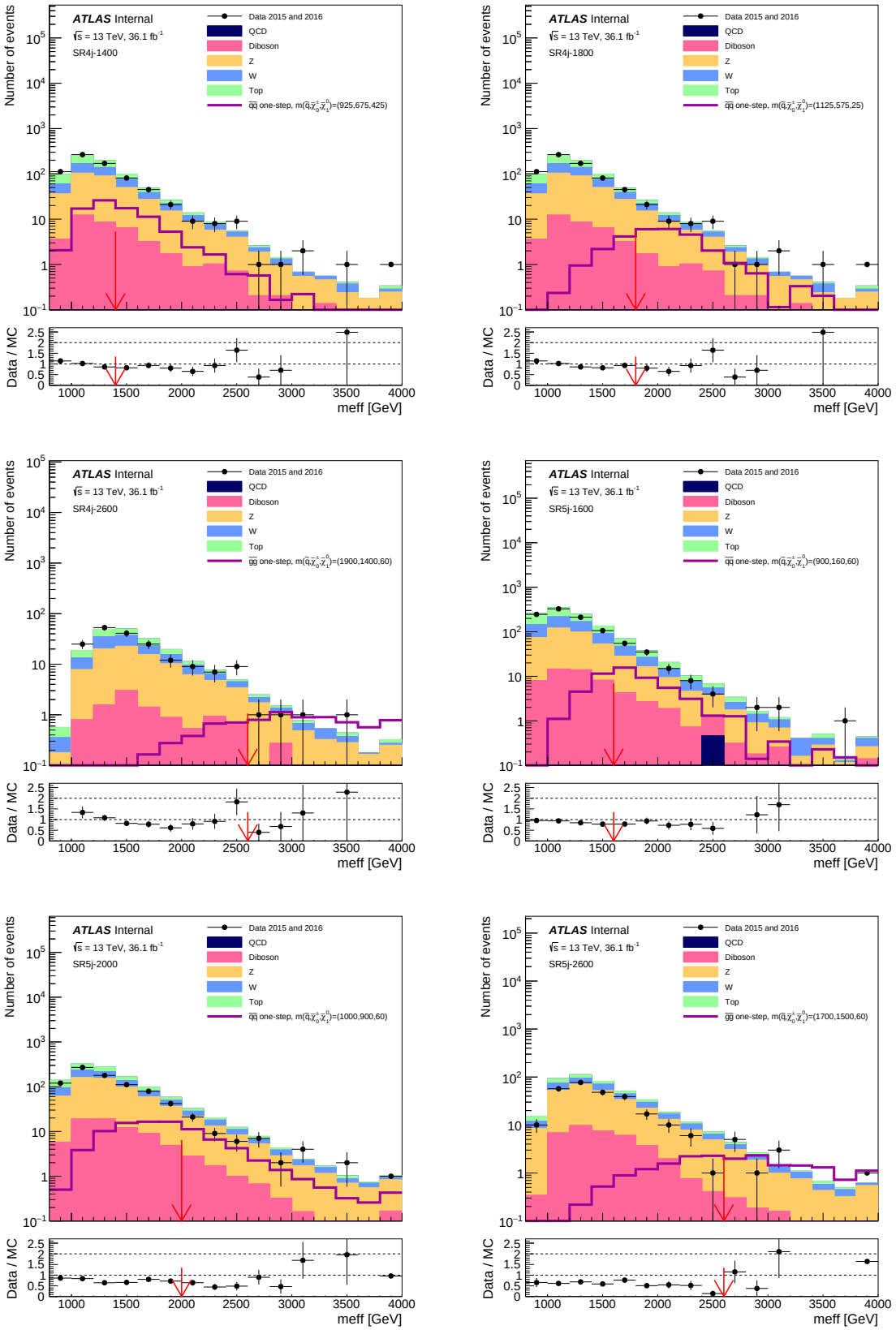

Figure 6.32: Observed m_{eff}(incl) distributions for 4j and 5j signal regions. The background (colored area) is estimated from Monte Carlo simulation before the fit on the control regions, and is normalized to theoretical cross-section and luminosity. The last bin includes the overflow. The red arrows indicate the nominal selection on m_{eff}(incl) in the signal region.

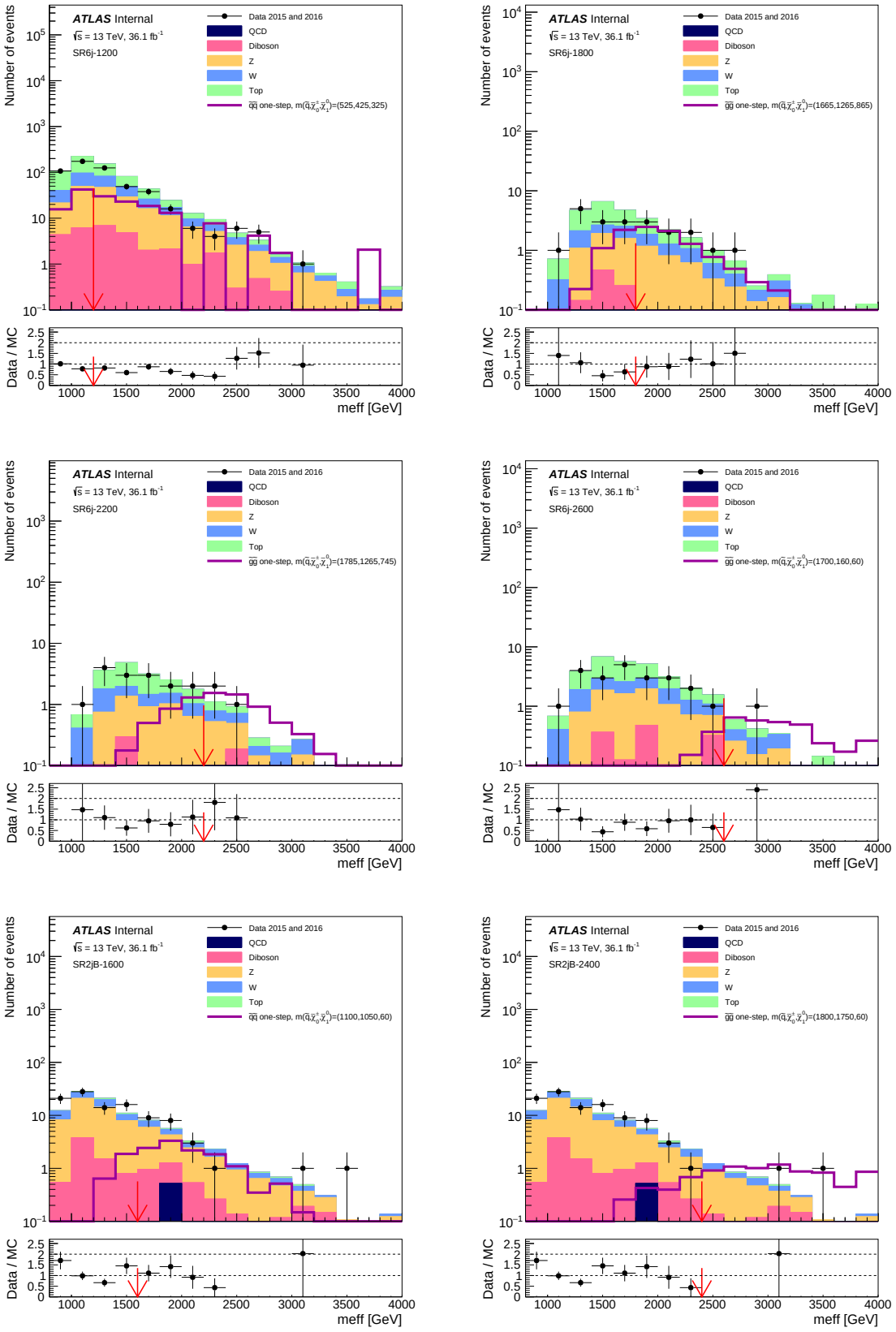

Figure 6.33: Observed m_{eff}(incl) distributions for 5j and 2jB signal regions. The background (colored area) is estimated from Monte Carlo simulation before the fit on the control regions, and is normalized to theoretical cross-section and luminosity. The last bin includes the overflow. The red arrows indicate the nominal selection on m_{eff}(incl) in the signal region.

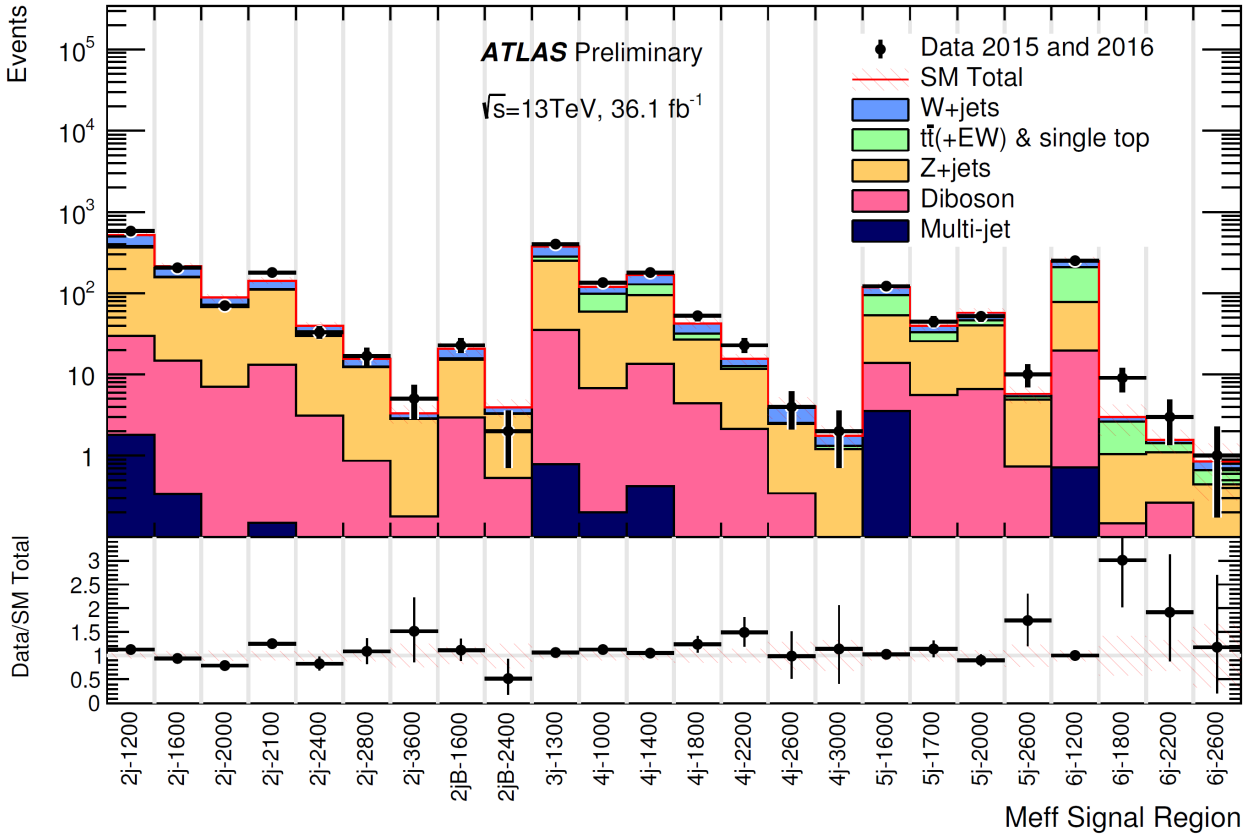

Figure 6.34: Comparison between observed data and background predictions as a function of signal region. The background expectations are estimated with the background-only fits. The bottom of the figure shows the ratio between data and Standard Model predictions.

Table 6.14: Number of events observed in each signal region compared with background estimations. The p-values (p_0) give the probabilities of the observations being consistent with the estimated backgrounds. The p-value is fixed at 0.5 for observed number of events lower than expected. The Gaussian standard deviations (Z) are also given.

Signal Region	**Meff-2j-1200**	**Meff-2j-1600**	**Meff-2j-2000**	**Meff-2j-2400**	**Meff-2j-2800**	**Meff-2j-3600**	**Meff-2j-B1600**	**Meff-2j-B2400**
MC expected events								
Diboson	28.17	14.37	7.02	3.09	0.86	0.18	2.94	0.53
Z/γ^*+jets	346.37	140.61	54.13	24.23	10.22	2.28	13.84	2.45
W+jets	142.39	47.49	18.33	8.23	3.37	1.11	5.16	0.71
$t\bar{t}$(+EW) + single top	21.40	5.84	2.54	1.13	0.32	0.04	0.86	0.10
Multi-jet	1.70	0.49	0.00	0.00	0.00	0.00	0.00	0.00
Fitted background events								
Diboson	28 ± 4	14.4 ± 2.3	7.0 ± 1.1	3.1 ± 0.5	0.86 ± 0.17	0.18 ± 0.07	2.9 ± 0.7	0.53 ± 0.1
Z/γ^*+jets	337 ± 19	141 ± 10	61 ± 8	26.8 ± 3.1	11.4 ± 1.4	2.7 ± 0.7	12.3 ± 1.8	2.7 ± 0.5
W+jets	136 ± 24	57 ± 16	19 ± 5	9.4 ± 2.6	3.1 ± 1.1	0.4 ± 0.31	4.8 ± 2.8	0.6 ± 0.6
$t\bar{t}$(+EW) + single top	15 ± 4	3.1 ± 1.7	1.34 ± 1.0	0.4 ± 0.4	0.18 ± 0.15	$0.04^{+0.04}_{-0.04}$	0.5 ± 0.5	$0.05^{+0.57}_{-0.05}$
Multi-jet	1.8 ± 1.8	0.34 ± 0.34	–	–	–	–	–	–
Total MC	540.04	208.80	82.02	36.68	14.78	3.60	22.80	3.79
Total bkg	517 ± 31	216 ± 18	88 ± 9	40 ± 4	15.5 ± 1.9	3.3 ± 0.8	21 ± 4	3.89 ± 1.0
Observed	582	204	70	33	17	5	23	2
$\langle\epsilon\sigma\rangle^{95}_{\rm obs}$ [fb]	3.8	1.02	0.51	0.34	0.34	0.21	0.43	0.11
$S^{95}_{\rm obs}$	135	37	18	12	12	7.6	16	4.0
$S^{95}_{\rm exp}$	85^{+30}_{-25}	53^{+19}_{-15}	27^{+8}_{-8}	17^{+6}_{-5}	10^{+4}_{-3}	$5.2^{+2.0}_{-1.0}$	14^{4}_{-3}	$5.2^{+2.2}_{-1.3}$
p_0 (Z)	0.06 (1.53)	0.50 (0.00)	0.50 (0.00)	0.50 (0.00)	0.25 (0.68)	0.11 (1.23)	0.36 (0.37)	0.50 (0.00)

Signal Region	**Meff-2j-2100**	**Meff-3j-1300**	**Meff-4j-1000**	**Meff-4j-1400**	**Meff-4j-1800**	**Meff-4j-2200**	**Meff-4j-2600**	**Meff-4j-3000**
MC expected events								
Diboson	12.87	34.43	6.56	13.18	4.40	2.14	0.35	0.06
Z/γ^*+jets	115.70	265.30	59.58	99.18	32.76	11.95	4.05	1.34
W+jets	33.90	105.92	28.91	51.75	14.57	4.49	1.66	0.61
$t\bar{t}$(+EW) + single top	4.96	36.08	42.86	41.67	7.64	1.71	0.63	0.21
Multi-jet	0.24	1.46	0.24	0.49	0.00	0.00	0.00	0.00
Fitted background events								
Diboson	13 ± 5	34 ± 6	6.6 ± 1.2	13.2 ± 2.2	4.4 ± 0.9	2.1 ± 0.5	0.35 ± 0.08	0.06 ± 0.03
Z/γ^*+jets	97 ± 8	218 ± 20	52 ± 7	82 ± 9	23 ± 4	9.6 ± 1.9	2.1 ± 0.7	1.2 ± 0.5
W+jets	30 ± 9	96 ± 18	22 ± 7	39 ± 9	11 ± 5	2.74 ± 1.0	1.5 ± 0.9	0.43 ± 0.33
$t\bar{t}$(+EW) + single top	2.8 ± 1.6	28 ± 10	39 ± 7	33 ± 10	4.7 ± 3.2	0.9 ± 0.5	$0.12^{+0.15}_{-0.12}$	0.11 ± 0.1
Multi-jet	0.15 ± 0.15	$0.79^{+0.80}_{-0.79}$	$0.20^{+0.20}_{-0.20}$	0.4 ± 0.4	–	–	–	–
Total MC	167.66	443.20	138.15	206.27	59.37	20.29	6.69	2.22
Total bkg	143 ± 13	378 ± 28	120 ± 11	169 ± 15	43 ± 6	15.4 ± 2.2	4.1 ± 1.2	1.8 ± 0.6
Observed	180	405	135	179	53	23	4	2
$\langle\epsilon\sigma\rangle^{95}_{\rm obs}$ [fb]	2.0	2.9	1.3	1.7	0.80	0.48	0.17	0.12
$S^{95}_{\rm obs}$	72	103	48	63	28.8	17	6.0	4.5
$S^{95}_{\rm exp}$	40^{+15}_{-10}	83^{+29}_{-23}	36^{+12}_{-9}	46^{+16}_{-14}	20^{+8}_{-6}	11^{+4}_{-3}	$6.0^{+2.1}_{-1.7}$	$4.3^{+1.8}_{-1.1}$
p_0 (Z)	0.03 (1.95)	0.22 (0.76)	0.13 (1.15)	0.12 (1.20)	0.15 (1.05)	0.06 (1.52)	0.50 (0.00)	0.44 (0.14)

Signal Region	**Meff-5j-1600**	**Meff-5j-1700**	**Meff-5j-2000**	**Meff-5j-2600**	**Meff-6j-1200**	**Meff-6j-1800**	**Meff-6j-2200**	**Meff-6j-2600**
MC expected events								
Diboson	10.29	5.61	6.59	0.73	19.00	0.15	0.26	0.09
Z/γ^*+jets	55.12	30.42	49.38	7.32	103.92	3.29	1.26	0.76
W+jets	41.39	15.21	18.42	2.60	78.02	2.15	0.70	0.47
$t\bar{t}$(+EW) + single top	44.63	11.71	9.77	0.75	139.99	4.31	0.61	0.36
Multi-jet	3.64	0.00	0.00	0.00	1.21	0.00	0.00	0.00
Fitted background events								
Diboson	10.3 ± 1.8	5.61 ± 1.0	6.6 ± 1.2	0.73 ± 0.13	19.0 ± 3.2	0.15 ± 0.11	0.26 ± 0.07	$0.09^{+0.11}_{-0.09}$
Z/γ^*+jets	40 ± 5	20 ± 4	34 ± 6	4.2 ± 1.3	58 ± 10	0.9 ± 0.5	0.8 ± 0.4	0.35 ± 0.22
W+jets	23 ± 7	6.7 ± 2.4	11.6 ± 3.1	$0.32^{+0.41}_{-0.32}$	41 ± 20	$0.36^{+0.59}_{-0.36}$	$0.12^{+0.18}_{-0.12}$	$0.19^{+0.27}_{-0.19}$
$t\bar{t}$(+EW) + single top	42 ± 11	7.3 ± 2.5	5.9 ± 2.3	0.5 ± 0.5	130 ± 23	1.6 ± 1.2	0.35 ± 0.24	$0.22^{+0.39}_{-0.22}$
Multi-jet	4 ± 4	–	–	–	$0.72^{+0.72}_{-0.72}$	–	–	–
Total MC	155.06	62.94	84.16	11.40	342.14	9.90	2.84	1.67
Total bkg	119 ± 12	39 ± 5	58 ± 7	5.7 ± 1.3	249 ± 30	3.0 ± 1.3	1.6 ± 0.5	0.9 ± 0.6
Observed	122	45	52	10	250	9	3	1
$\langle\epsilon\sigma\rangle^{95}_{\rm obs}$ [fb]	1.12	0.63	0.58	0.30	2.2	0.35	0.15	0.11
$S^{95}_{\rm obs}$	40	23	20.6	10.8	81.0	12.6	5.6	4.1
$S^{95}_{\rm exp}$	38^{+13}_{-11}	18^{+6}_{-5}	23^{+7}_{-7}	$7.2^{+2.9}_{-2.2}$	66^{+21}_{-16}	$8.7^{+2.8}_{-1.9}$	$4.2^{+1.5}_{-0.6}$	$3.5^{+1.5}_{-0.2}$
p_0 (Z)	0.35 (0.38)	0.22 (0.79)	0.50 (0.00)	0.11 (1.21)	0.50 (0.00)	0.08 (1.42)	0.16 (1.01)	0.19 (0.89)

6.9.3 Model dependent limits

Since no significant excess is observed, exclusion limits on the contribution of various SUSY models to the signal regions are computed. The exclusion limits of the two analysis Meff and RJigsaw are compared, and the best exclusion limit is chosen for the final results.

Figures 6.35 shows the exclusion limits for simplified models considering direct decay of squark (a) and gluino (b) into quark and LSP. The continuous red line shows the observed exclusion limits using 2015 and 2016 data. The limit is estimated with combination of M_{eff} and RJigsaw using the best expected sensitivity for each point. Observed exclusion limits using 2015 data only is shown for comparison. In this simplified model, the limit for light-flavour squark is 1.58 TeV assuming massless $\tilde{\chi}_1^0$ obtained with signal region RJR-S4 (a). The limit for gluino mass is 2.03 TeV, assuming massless $\tilde{\chi}_1^0$ obtained with Meff-4j-3000.

In Figures 6.36, limits are shown for squarks decaying via an intermediate chargino. Two models are considered, one is fixed at $m_{\tilde{\chi}_1^\pm} = \frac{m_{\tilde{g}}+m_{\tilde{\chi}_1^0}}{2}$ (a) and the other is fixed at $m_{\tilde{\chi}_1^\pm}$ = 60 GeV (b). On Figure 6.36 (a), results using M_{eff} analysis are compared with RJigsaw analysis. The upper limit on $m_{\tilde{q}}$ is 1.15 TeV for massless neutralinos. The expected limits between RJigsaw and M_{eff} are sensibly the same for $m_{\tilde{q}}$ > 900 GeV. In the compressed region (a), the higher exclusion limit is obtained with RJigsaw analysis, while in the intermediate region ($m_{\tilde{q}}$ ∼650 GeV), it is obtained with M_{eff} analysis. In (b), significant improvement is seen in the boosted region with SR2jB-1600 compared to other signal regions ($m_{\tilde{q}} \sim$ 1.1 TeV).

Limits for gluino decaying via an intermediate chargino are shown in Figures 6.37, with $m_{\tilde{\chi}_1^\pm} = \frac{m_{\tilde{g}}+m_{\tilde{\chi}_1^0}}{2}$ (a) and $m_{\tilde{\chi}_1^\pm}$ = 60 GeV (b). In 6.37 (a), the exclusion limits obtained with RJigsaw and M_{eff} analysis are shown. The upper limit for $m_{\tilde{g}}$ is 2.01 TeV for massless neutralinos and is obtained with M_{eff} analysis in the signal region 6j-2600. As for $\tilde{q}\tilde{q}$ production, in the compressed region the best exclusion limits are obtained with RJigsaw analysis. In the other regions, the best exclusion limits are obtained with M_{eff} analysis mainly in 5j and 6j signal regions. In (b), the best exclusion limit is obtained in the signal region 2jB-2400 (1.9 TeV).

Limits on gluino pair production via intermediate $\tilde{\chi}_2^0$ are shown in Figure 6.38, with $m_{\tilde{\chi}_1^0}$ fixed at 1 GeV. In these models, the upper limit on $m_{\tilde{g}}$ is $\sim$ 2 TeV for $m_{\tilde{\chi}_2^0} \sim$ 1 TeV, and is obtained with signal region 6j-2600. The best exclusion limit in the boosted region is obtained with the signal region 2jB-2400.

Figure 6.39 shows limits on $\tilde{q}\tilde{q}$ (a) and $\tilde{g}\tilde{g}$ (b) production decaying via an intermediate $\tilde{\chi}_2^0$ and $\tilde{\chi}_1^\pm$. The upper limits for $m_{\tilde{q}}$ and $m_{\tilde{g}}$ are respectively 1.26 TeV and 2.05 TeV.

6.10 Conclusion

This chapter presents the results for the searches for squarks and gluinos with jets, transverse missing energy and no lepton in the final state. The search is performed using the data collected at $\sqrt{s}$ = 13 TeV in 2015 and 2016 by ATLAS and corresponding to 36.1fb^{-1}. The strategy of the analysis, the main backgrounds, and the event selections are firstly described. New signal regions are included in the analysis. Seven signal regions are added to improve the sensitivity in the searches for squarks/gluinos decaying via an intermediate particle. These signal regions are defined with at least 5-6 jet multiplicity in the final state. Two signal regions dedicated to the models with boosted bosons

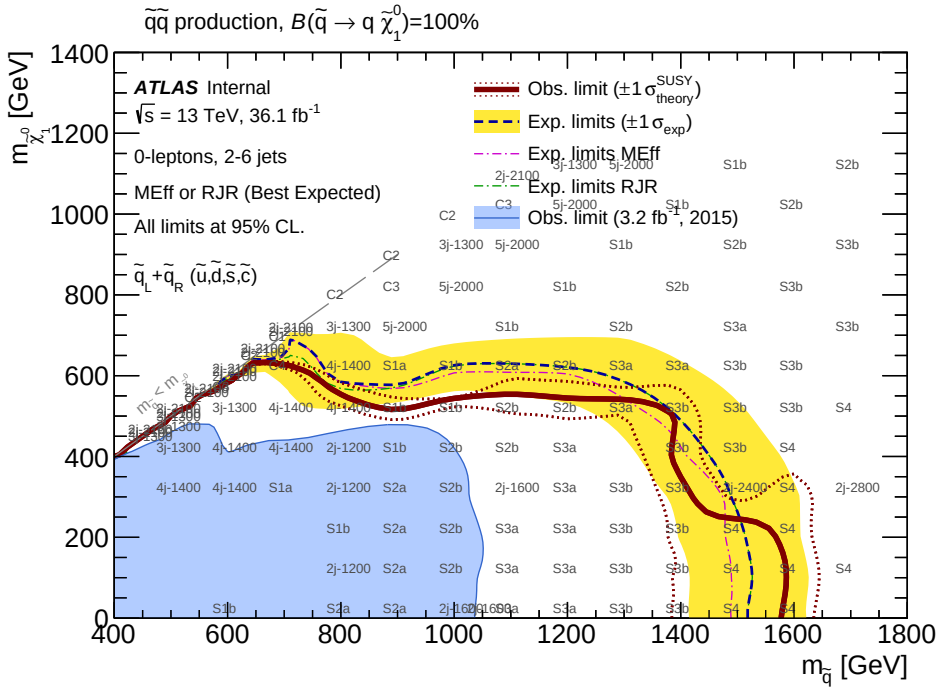

(a)

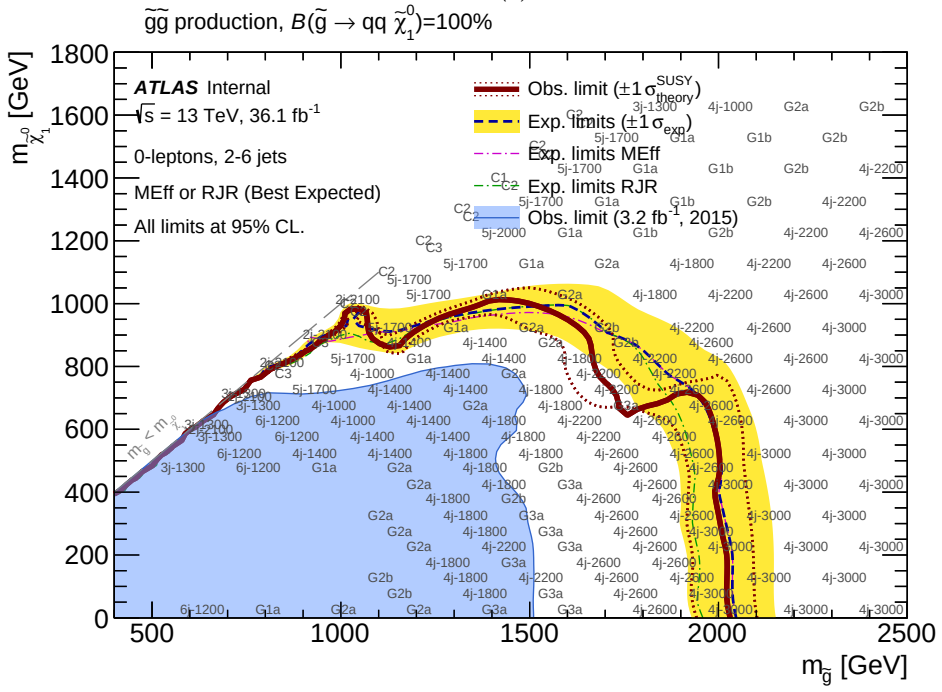

(b)

Figure 6.35: Exclusion limits of $\tilde{q}\tilde{q}$ (a) and $\tilde{g}\tilde{g}$ (b) production with direct decay of $\tilde{q}/\tilde{g}$ to quarks and $\tilde{\chi}_1^0$. Limits are shown in the plan ($m_{\tilde{\chi}_1^0}$, $m_{\tilde{q}/\tilde{g}}$) for simplified models with 95% of confidence level. The observed limits (red line), and best expected limits (blue dotted line) are shown. The red dotted lines include theoretical uncertainties on the cross-section. The yellow bands include experimental uncertainties and theoretical uncertainties on background. The expected limits (blue dotted line) are obtained using signal regions with the best sensitivity. Expected exclusion limits for RJigsaw and M_{eff} analysis are shown in green and pink dotted lines. For comparison, previous ATLAS results of the analysis using 2015 data are shown in blue area.

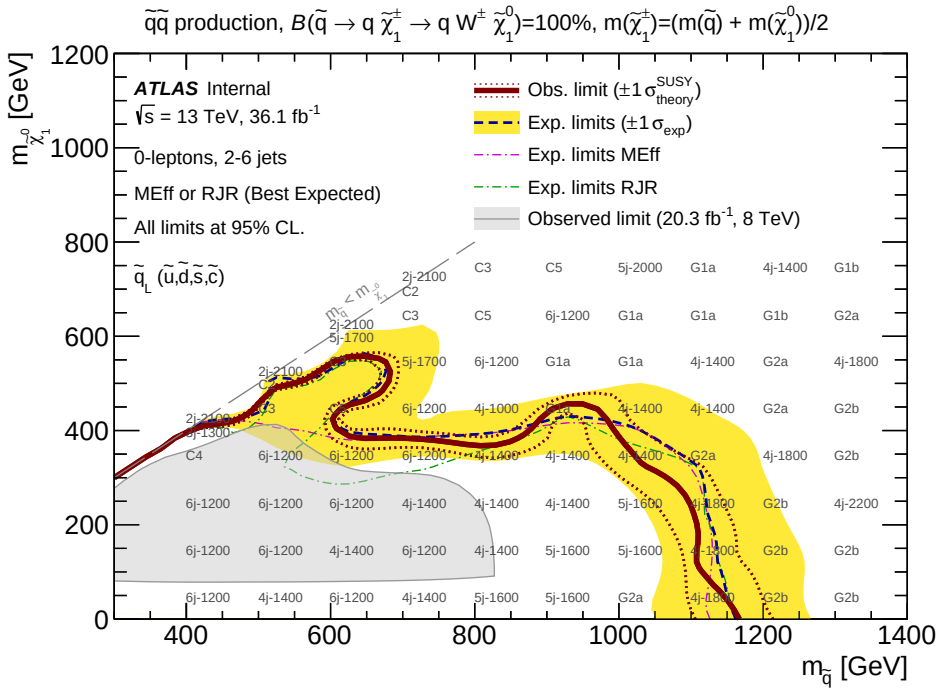

(a)

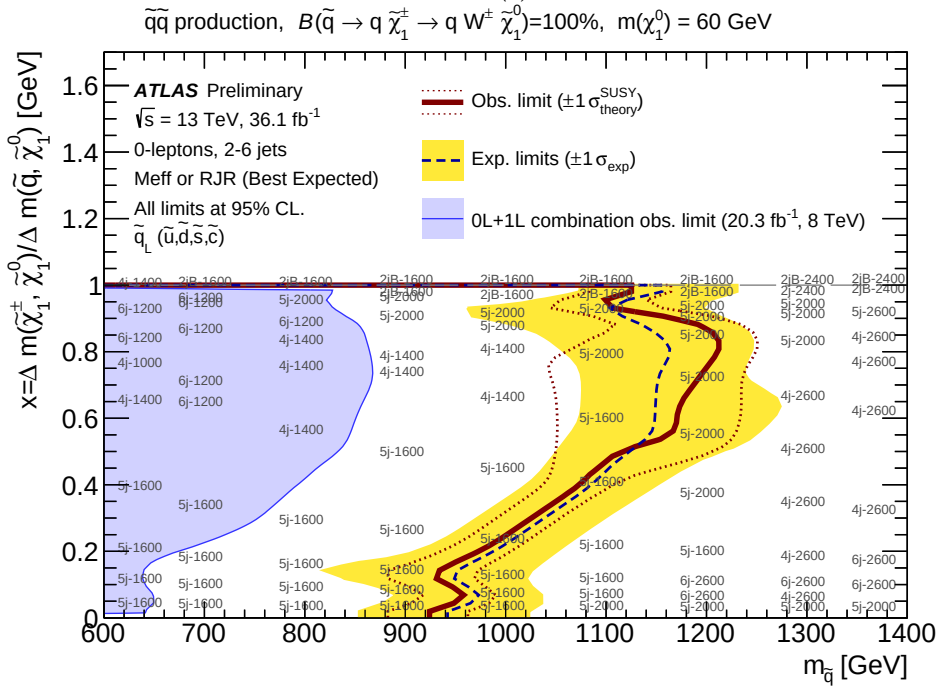

(b)

Figure 6.36: Exclusion limits of $\tilde{q}\tilde{q}$ production with one-step decay of $\tilde{q}$ via an intermediate $\tilde{\chi}_1^{\pm}$. Limits are shown for simplified models with 95% CL in the plan ($m_{\tilde{\chi}_1^0}$, $m_{\tilde{q}}$) (a) and (x, $m_{\tilde{q}}$) (b) corresponding respectively to $m_{\tilde{\chi}_1^{\pm}} = (m_{\tilde{\chi}_1^0} + m_{\tilde{q}})/2$ and $m_{\tilde{\chi}_1^0}$ = 60 GeV. The observed limits (red continuous line), and best expected limits (blue dotted line) are shown. The red dotted lines include theoretical uncertainties on the cross-section. The yellow bands include experimental uncertainties and theoretical uncertainties on background. In Figure (a), expected limits (blue dotted line) are obtained using signal regions with the best sensitivity between RJigsaw and M_{eff}, while Figure (b) shows results for M_{eff} analysis only. For comparison, previous ATLAS results combining 0-lepton and 1-lepton analysis in Run 1 [49], with $\sqrt{s}$ = 8 TeV are shown in blue areas.

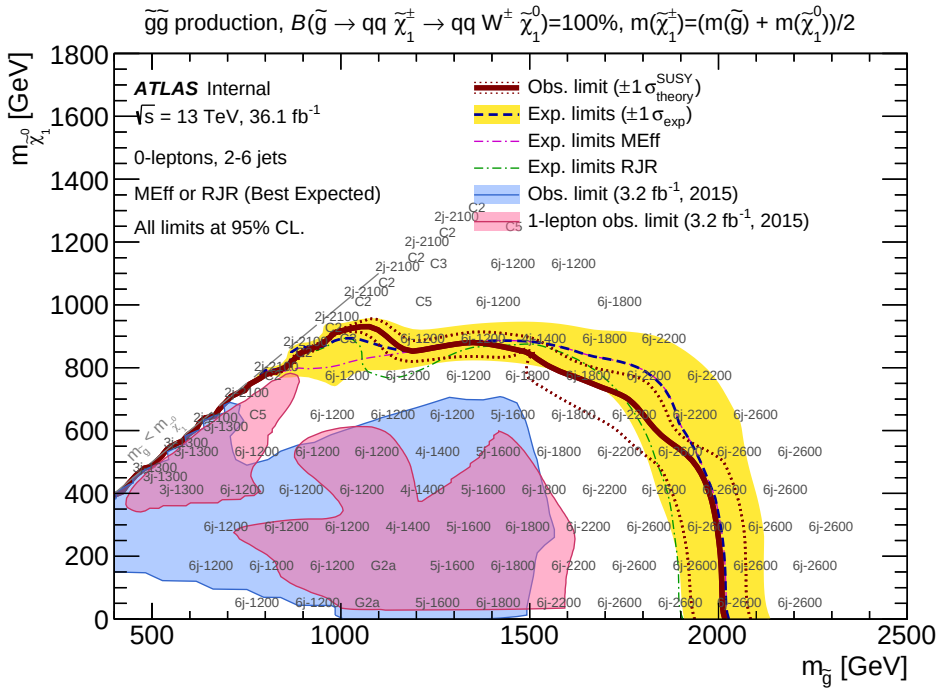

(a)

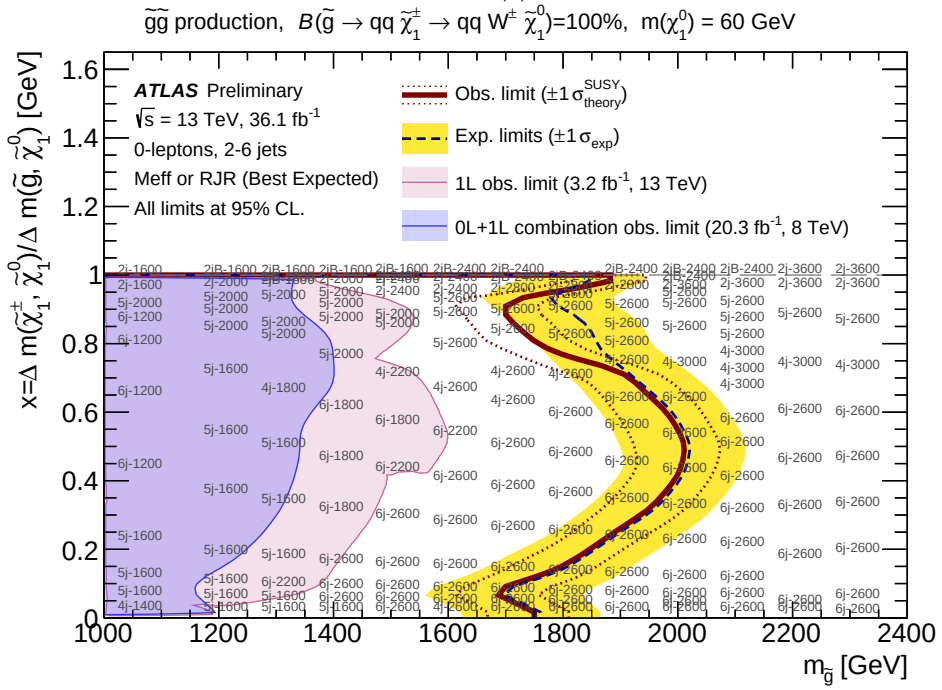

(b)

Figure 6.37: Exclusion limits of $\tilde{g}\tilde{g}$ production with one-step decay of $\tilde{g}$ via an intermediate $\tilde{\chi}_1^{\pm}$. Limits are shown for simplified models with 95% CL in the plan ($m_{\tilde{\chi}_1^0}$, $m_{\tilde{g}}$) (a) and (x, $m_{\tilde{g}}$) (b) corresponding respectively to $m_{\tilde{\chi}_1^{\pm}} = (m_{\tilde{\chi}_1^0} + m_{\tilde{g}})/2$ and $m_{\tilde{\chi}_1^0}$ = 60 GeV. The observed limits (red continuous line), and best expected limits (blue dotted line) are shown. The red dotted lines include theoretical uncertainties on the cross-section. The yellow bands include experimental uncertainties and theoretical uncertainties on background. In Figure (a), expected limits (blue dotted line) are obtained using signal regions with the best sensitivity between RJigsaw and M_{eff}, while Figure (b) shows results for M_{eff} analysis only. For comparison, previous ATLAS results using 2015 data (3.2 fb^{-1}) with 0-lepton and 1-lepton in the final state are shown respectively in blue and pink areas.

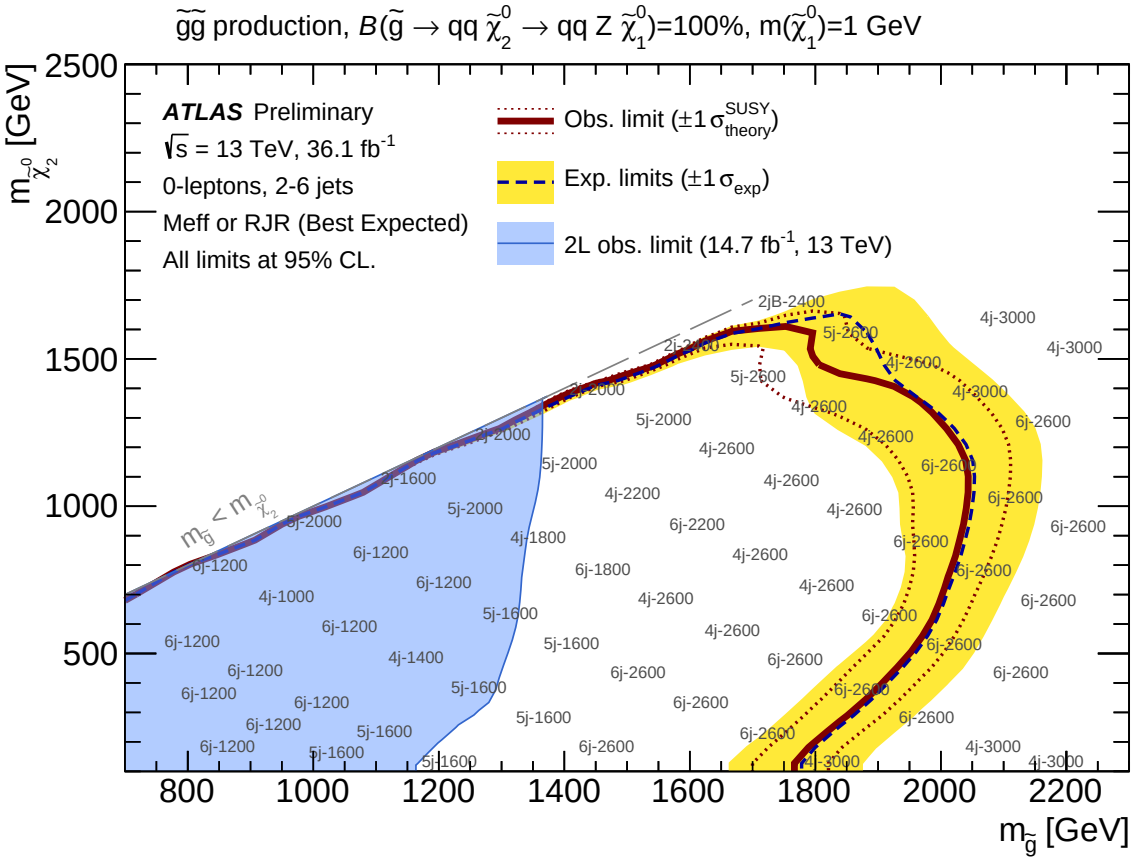

Figure 6.38: Exclusion limits of $\tilde{g}\tilde{g}$ production with one-step decay of $\tilde{g}$ via an intermediate $\tilde{\chi}_2^0$. Limits are shown for simplified models with 95% CL in the plan ($m_{\tilde{\chi}_2^0}$, $m_{\tilde{g}}$) with $m_{\tilde{\chi}_1^0}$ = 60 GeV. The observed limits (red continuous line), and best expected limits (blue dotted line) are shown. The red dotted lines include theoretical uncertainties on the cross-section. The yellow bands include experimental uncertainties and theoretical uncertainties on background. Expected limits (blue dotted line) are obtained using M_{eff} analysis. For comparison, previous ATLAS results using 14.7 fb^{-1}, and with 2-lepton in the final state are shown in blue area.

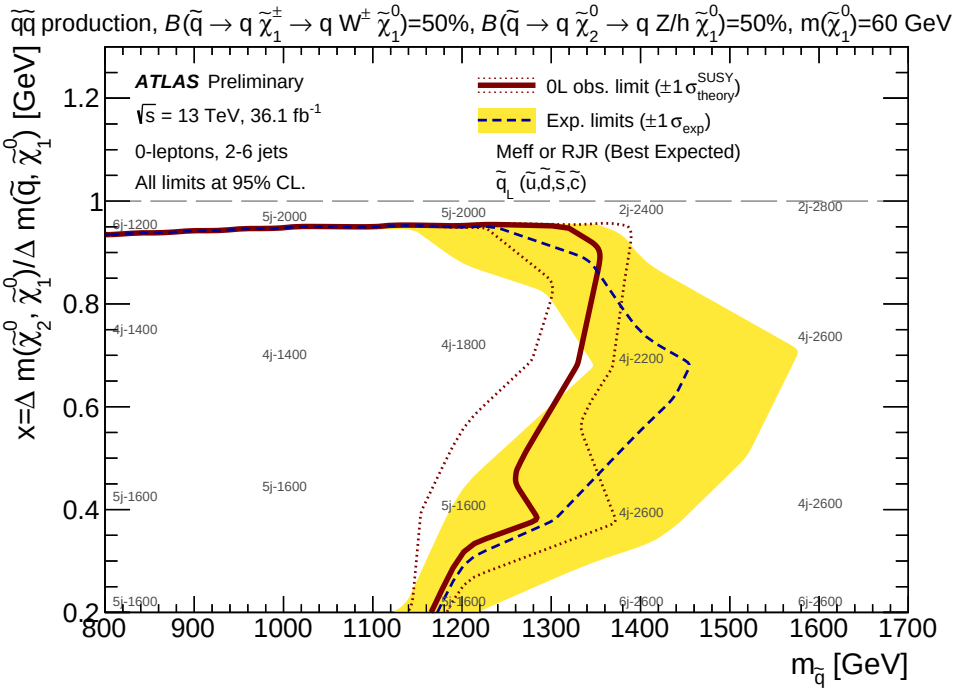

(a)

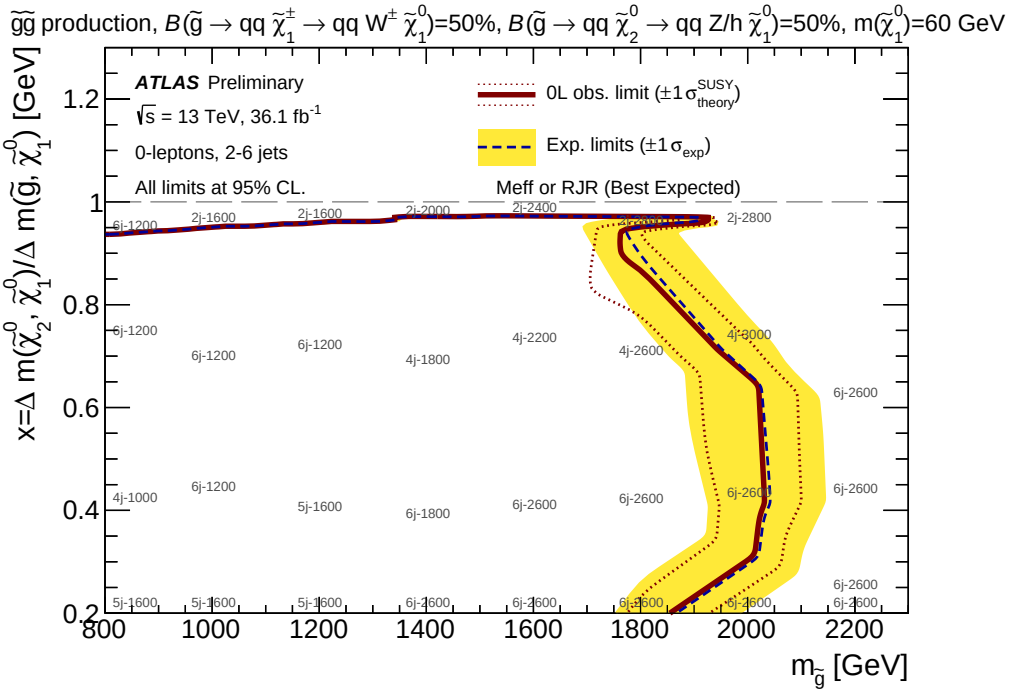

(b)

Figure 6.39: Exclusion limits of $\tilde{q}\tilde{q}$ (a) and $\tilde{g}\tilde{g}$ (b) production with one-step decay of $\tilde{q}\tilde{q}/\tilde{g}\tilde{g}$ via an intermediate $\tilde{\chi}_1^{\pm}$ and $\tilde{\chi}_2^0$. Limits are shown for simplified models with 95% CL in the plan (x, $m_{\tilde{q}}$) (a) and (x, $m_{\tilde{g}}$) (b) corresponding to $m_{\tilde{\chi}_1^0}$ = 60 GeV. The observed limits (red continuous line), and best expected limits (blue dotted line) are shown. The red dotted lines include theoretical uncertainties on the cross-section. The yellow bands include experimental uncertainties and theoretical uncertainties on background. Expected exclusion limits (blue dotted line) are obtained using M_{eff} analysis.

in the final state are also included. These regions are defined with at least 2 jets in the final state. The methods for the background estimation, the control regions, and the systematics uncertainties are described in the last part. No significant excess is observed in the signal regions. The last section shows the limits set on simplified models with a focus on the models with one-step decays. An exclusion at the order of 2 TeV is set on the mass of the gluinos, and 1.22 TeV on the mass of the squarks assuming the two first generations are mass-degenerated. These limits greatly improve the results set during the Run 1.

Conclusion

In this thesis, two different aspects are studied. The results are obtained using the 2015 and 2016 data collected with the ATLAS detector, and corresponding to a center of mass energy of $\sqrt{s}$ = 13 TeV.

The first part describes the method applied in ATLAS to calibrate the jets. The method is called Direct Balance (DB) and uses the precise measurement of the photon transverse momentum as a reference for the calibration. The method is applied to calibrate jets between 40 GeV and 1 TeV. Three different jet schemes are studied: jets at electromagnetic scale (EM), at local scale (LC), and with particle flow (EMPFlow). Corrections at the level of 2-3% on the transverse momentum are obtained for all the jet schemes. The sources of uncertainty and the method to estimate each contribution are detailed. The total uncertainty is evaluated to be around 1% in the major range of the calibration and is dominated by uncertainties on the photon energy scale and the simulation. These results are combined with the Z+jet and multijet methods to provide the final jet energy scale and jet uncertainty.

The γ+jet direct balance method is also used to extract the jet energy resolution of the detector. A similar resolution is found for jets at EM and LC scale, and a better resolution is observed at low p_T for jets with particle flow. This is a strong motivation for using the particle flow for jets reconstructed with higher luminosity. The uncertainty is evaluated to be at the order of 10% and is mostly dominated by the non-closure effect. At the moment this thesis is written, the combination with the other in-situ methods has not been done yet.

The second part describes the searches for squarks and gluinos with jets plus transverse missing energy, and no lepton in the final state. This channel corresponds to one of the most sensitive searches for physics beyond the Standard Model. Two complementary approaches have been developed in this analysis, and this work is based on the approach using the effective mass variable. This chapter is focused on the models with squarks and gluinos decaying into jets and missing transverse energy via an intermediate particle (one-step models). Seven new signal regions are included in the analysis, selecting at least 5 or 6 jets in the final state. Two other signal regions with at least 2 large jets are added to improve the sensitivity in the regions with boosted W/Z bosons in the final state. No significant excess is observed in the signal regions. The largest excess corresponding to 2.14 σ is found in the signal region Meff-2j-2100. The limits on simplified models of supersymmetry have been greatly improved since the Run 1. The best exclusion with 95% confidence level on the mass of the degenerate first and second generation of squarks with the one-step models is set to 1.22 TeV. This limit is obtained with squark decaying via an intermediate chargino with a mass of neutralino fixed at 60 GeV. A better sensitivity is obtained on the mass of the gluino. The mass of the gluino is excluded up to 2.05 TeV with several simplified models. In the future, improvements in the analysis can be done by using Boosted Decision Tree (BDT) or a multivariate analysis for the optimisation.

Appendices

.1 Distributions of the balance

In this appendix, the distributions for EM, LC, and EMPFlow jets are shown in the p_T^{ref} bins used for the in-situ calibration. Distributions are shown for 2016 data and Pythia8 with EM jets in figures 40 and 41, LC jets in figures 42 and 43, and EMPFlow jets in figures 44 and 45.

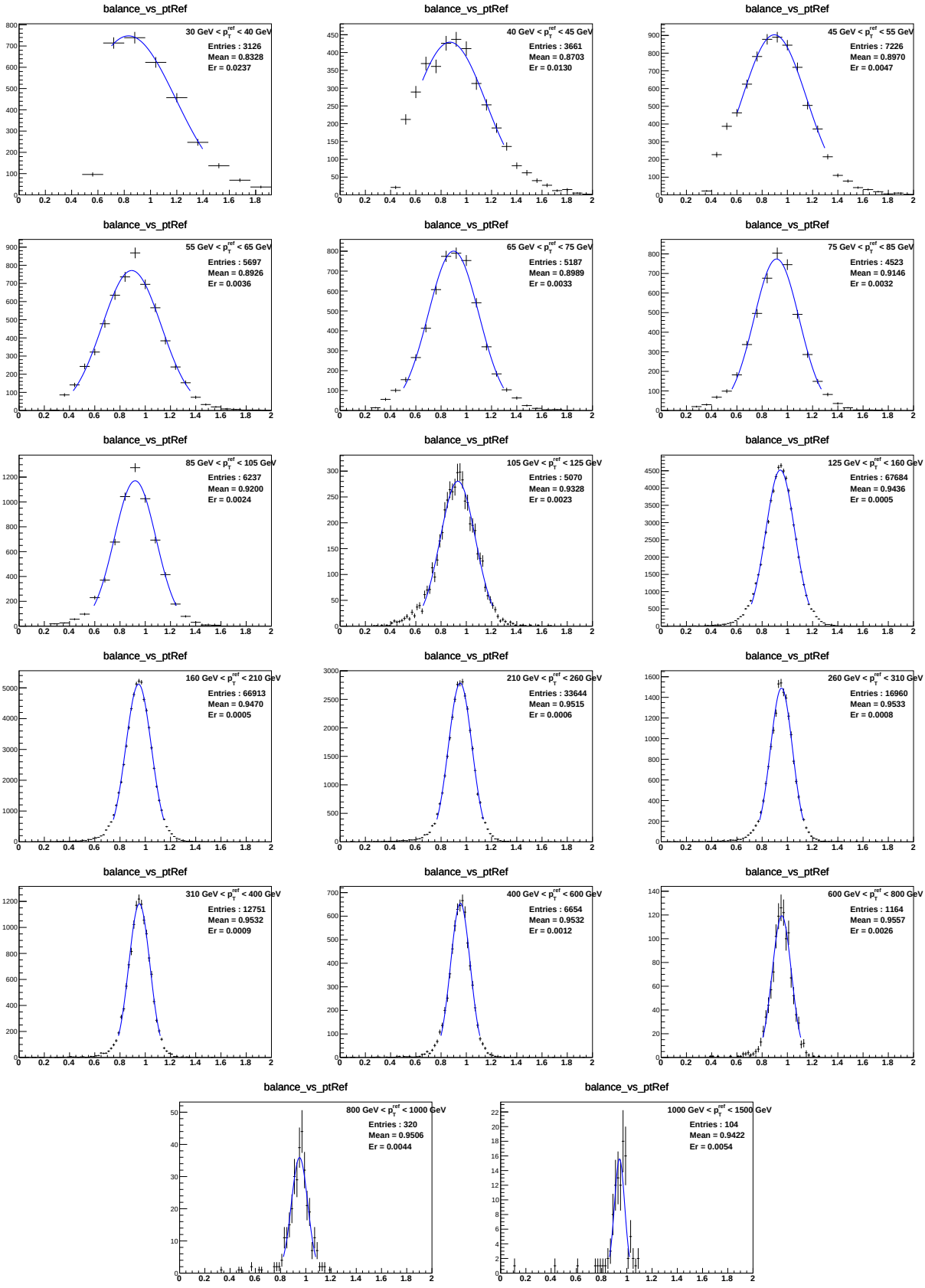

Figure 40: Distributions of p_T^{jet}/p_T^{ref} in different bins in p_T for EM jets calibrated up to η-intercalibration using 2016 data. Below 55 GeV, the Gaussian fit (blue line) has been performed using specific ranges due to bias in the left part of the distribution. The bin $30 < p_T < 40$ GeV is shown but is not used for the γ+jet calibration. Above 55 GeV, the fit range has been fixed to mean $\pm$ 2 σ for all bin.

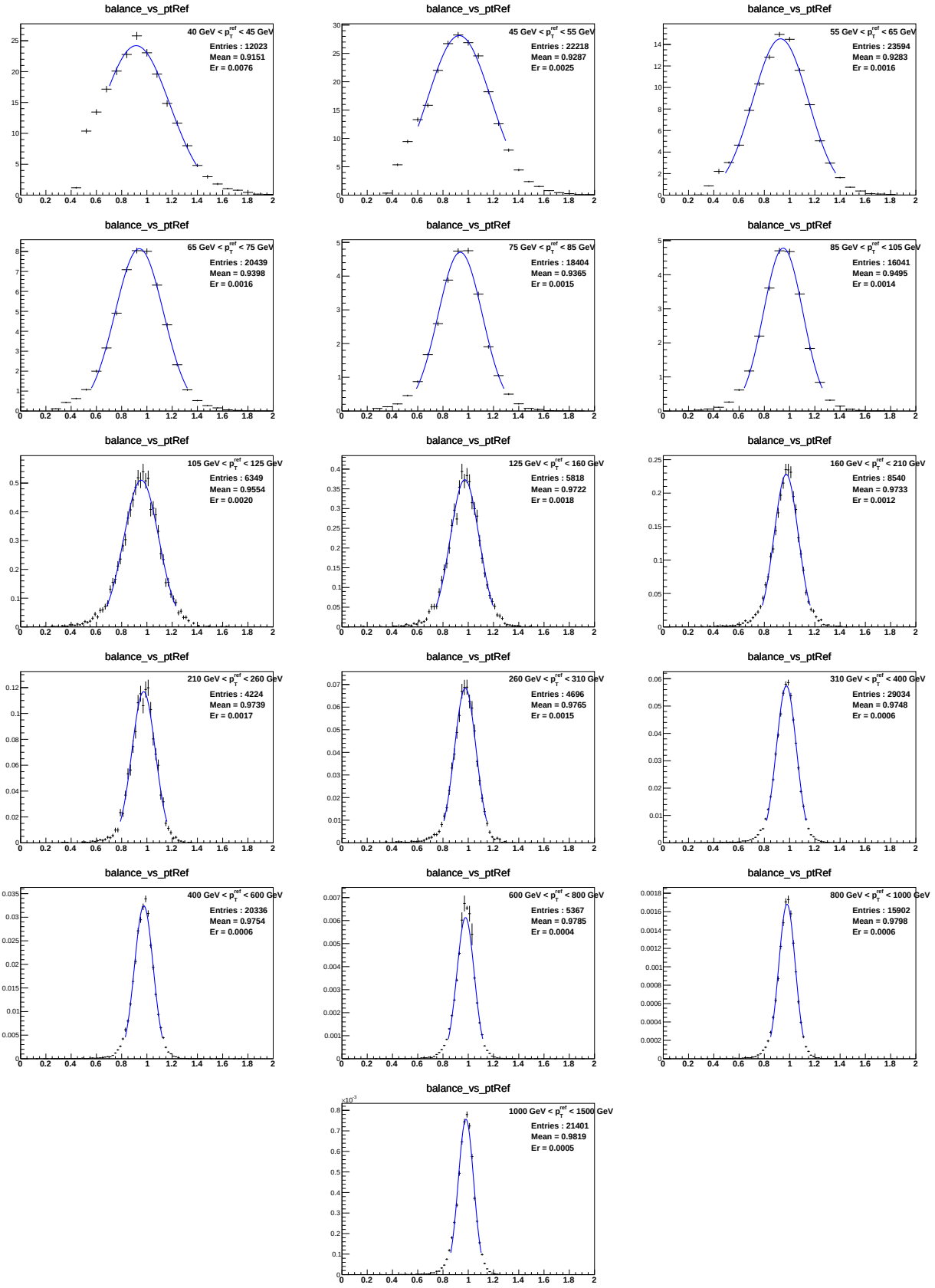

Figure 41: Distributions of p_T^{jet}/p_T^{ref} in different bins in p_T for EM jets calibrated up to η-intercalibration using the Monte Carlo simulation Pythia8. Below 55 GeV, the Gaussian fit (blue line) has been performed using specific ranges due to bias in the left part of the distribution. Above 55 GeV, the fit range has been fixed to mean $\pm$ 2 σ for all bin.

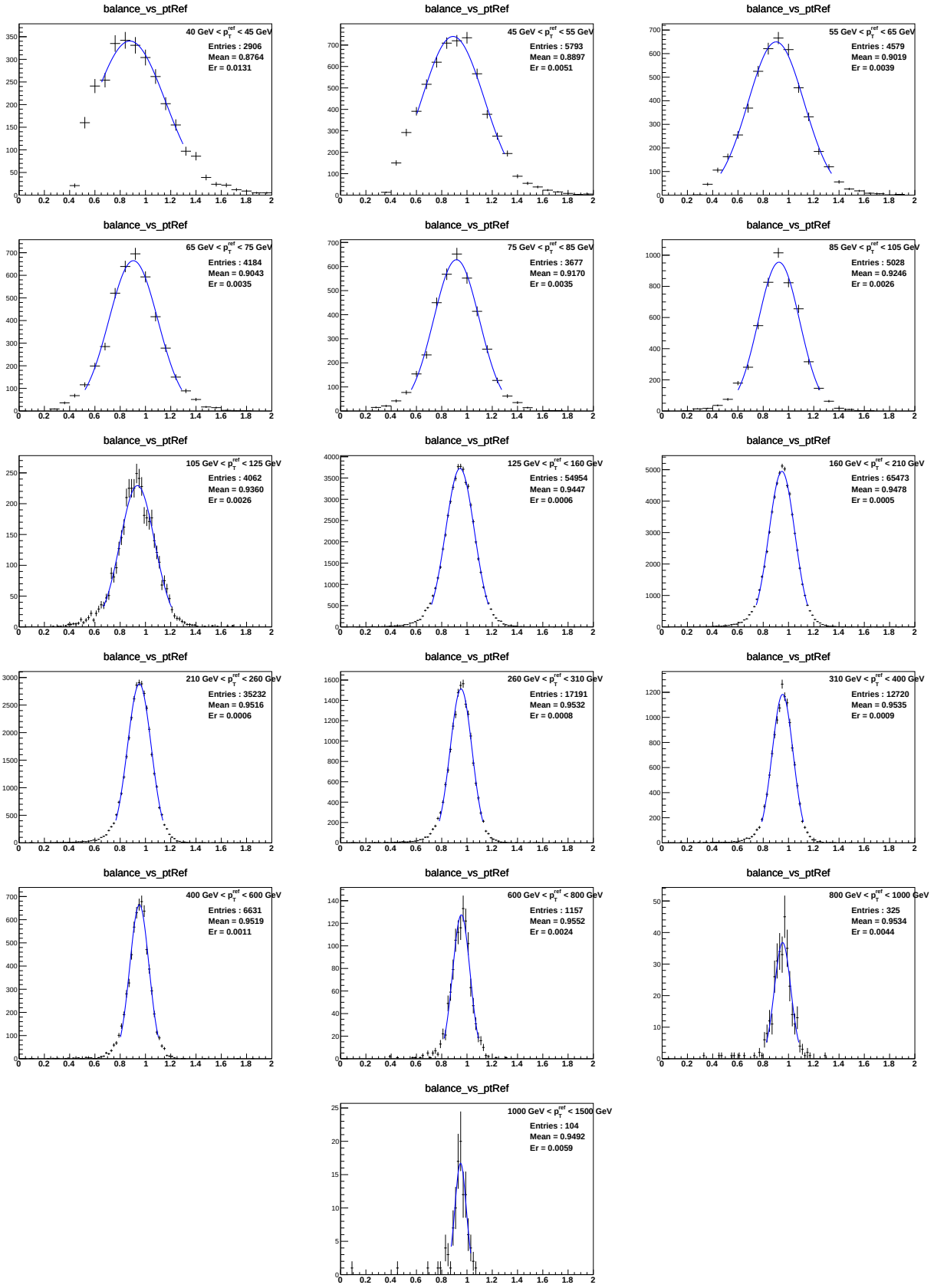

Figure 42: Distributions of p_T^{jet}/p_T^{ref} in different bins in p_T for LC jets calibrated up to η-intercalibration using 2016 data. Below 55 GeV, the Gaussian fit (blue line) has been performed using specific ranges due to bias in the left part of the distribution. Above 55 GeV, the fit range has been fixed to mean $\pm$ 2 σ for all bin.

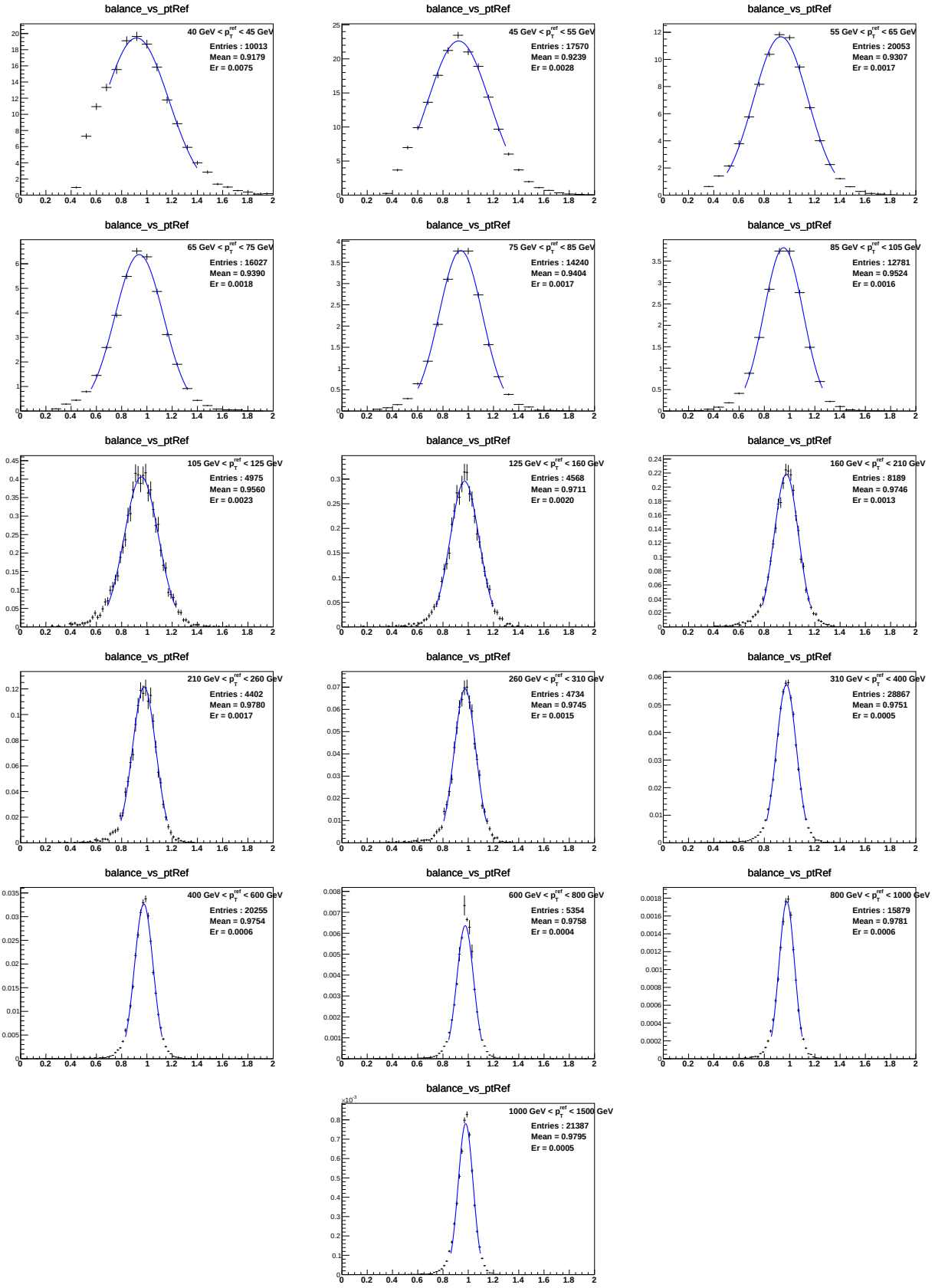

Figure 43: Distributions of p_T^{jet}/p_T^{ref} in different bins in p_T for LC jets calibrated up to η-intercalibration using the Monte Carlo simulation Pythia8. Below 55 GeV, the Gaussian fit (blue line) has been performed using specific ranges due to bias in the left part of the distribution. Above 55 GeV, the fit range has been fixed to mean $\pm$ 2 σ for all bin.

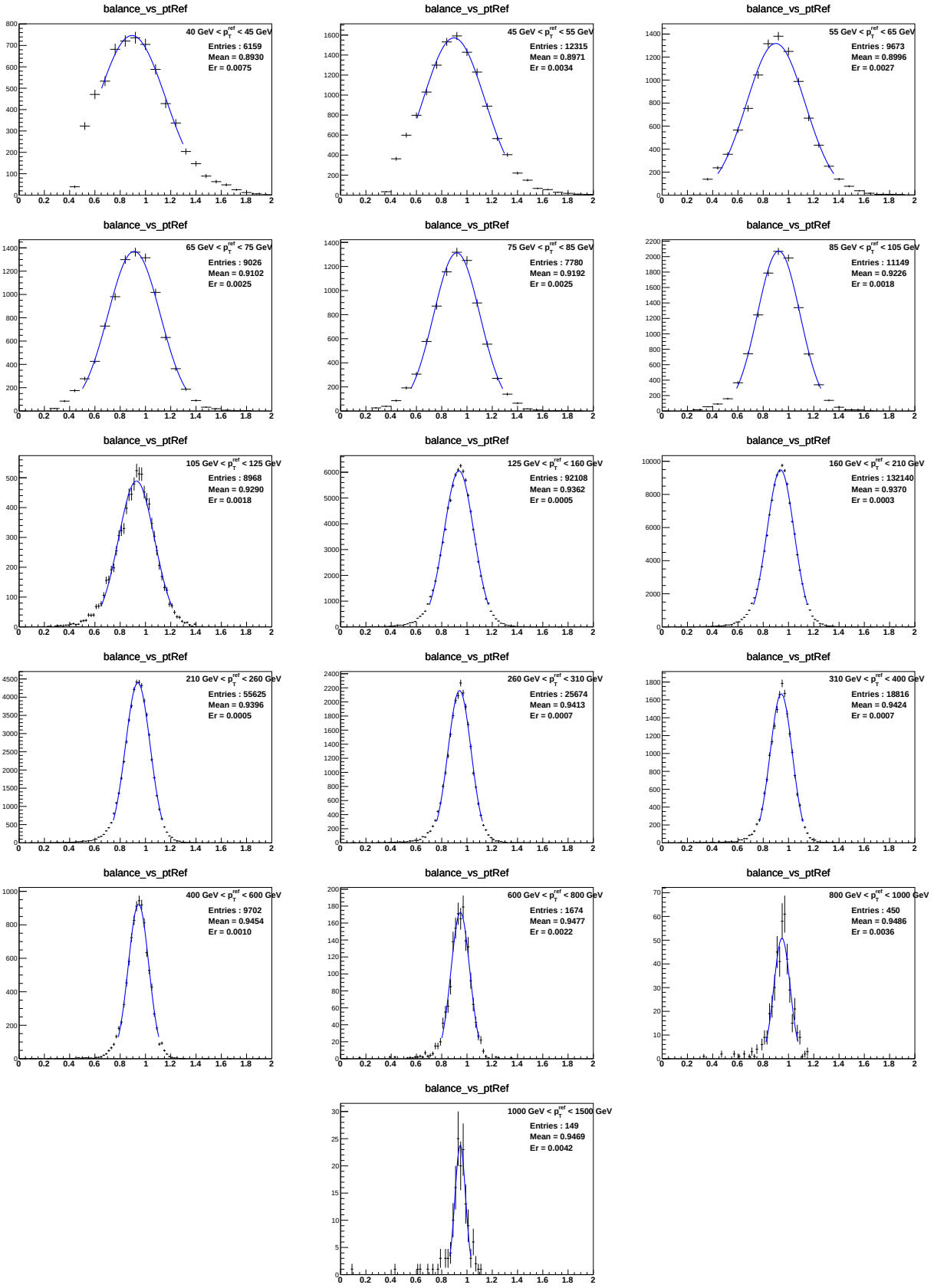

Figure 44: Distributions of p_T^{jet}/p_T^{ref} in different bins in p_T for LC jets calibrated up to η-intercalibration using data 2016. Below 55 GeV, the Gaussian fit (blue line) has been performed using specific ranges due to bias in the left part of the distribution. Above 55 GeV, the fit range has been fixed to mean $\pm$ 2 σ for all bin.

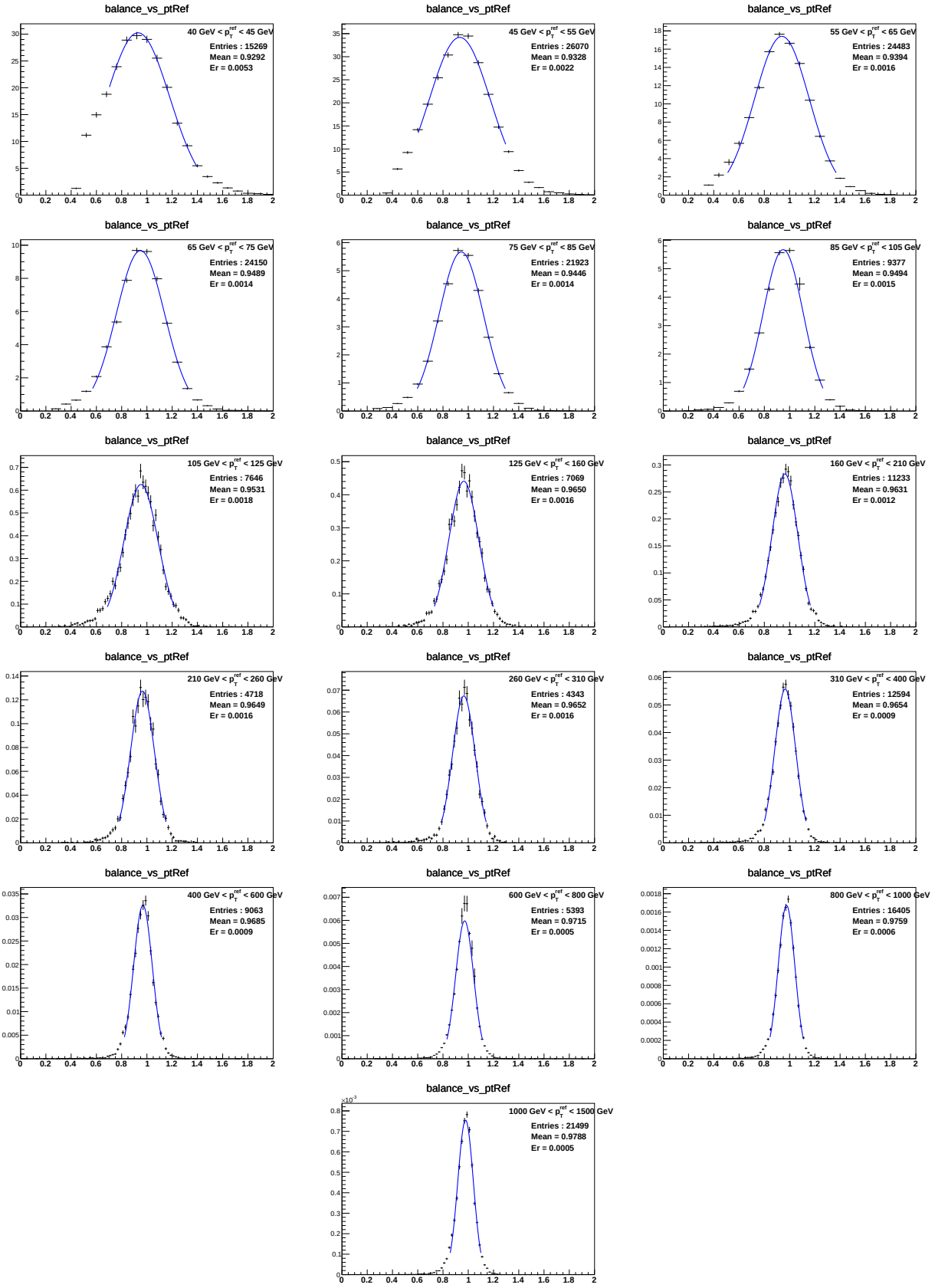

Figure 45: Distributions of p_T^{jet}/p_T^{ref} in different bins in p_T for LC jets calibrated up to η-intercalibration using the Monte Carlo simulation Pythia8. Below 55 GeV, the Gaussian fit (blue line) has been performed using specific ranges due to bias in the left part of the distribution. Above 55 GeV, the fit range has been fixed to mean $\pm$ 2 σ for all bin.

.2 Distribution of tracks energy density

In this appendix, the distributions of tracks energy density using 2016 data and Pythia8 are shown.

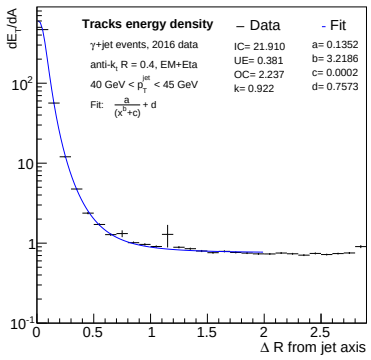
Tracks energy density
γ+jet events, 2016 data
anti-k$_t$ R = 0.4, EM+Eta
40 GeV < p_T^{jet} < 45 GeV
Fit: $\frac{a}{(x^b+c)}+d$
– Data
- Fit
IC= 21.910
UE= 0.381
OC= 2.237
k= 0.922
a= 0.1352
b= 3.2186
c= 0.0002
d= 0.7573
dE$_T$/dA
Δ R from jet axis

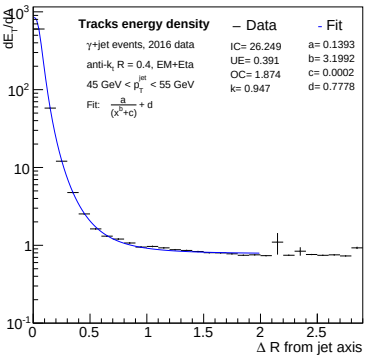
Tracks energy density
γ+jet events, 2016 data
anti-k$_t$ R = 0.4, EM+Eta
45 GeV < p_T^{jet} < 55 GeV
Fit: $\frac{a}{(x^b+c)}+d$
– Data
- Fit
IC= 26.249
UE= 0.391
OC= 1.874
k= 0.947
a= 0.1393
b= 3.1992
c= 0.0002
d= 0.7778
dE$_T$/dA
Δ R from jet axis

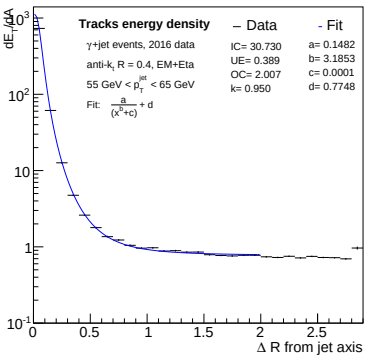
Tracks energy density
γ+jet events, 2016 data
anti-k$_t$ R = 0.4, EM+Eta
55 GeV < p_T^{jet} < 65 GeV
Fit: $\frac{a}{(x^b+c)}+d$
– Data
- Fit
IC= 30.730
UE= 0.389
OC= 2.007
k= 0.950
a= 0.1482
b= 3.1853
c= 0.0001
d= 0.7748
dE$_T$/dA
Δ R from jet axis

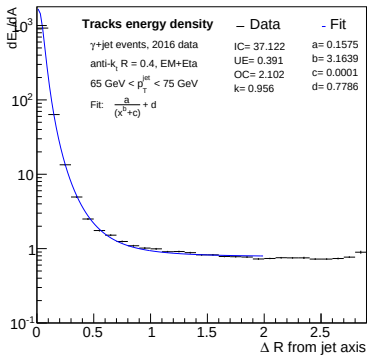
Tracks energy density
γ+jet events, 2016 data
anti-k$_t$ R = 0.4, EM+Eta
65 GeV < p_T^{jet} < 75 GeV
Fit: $\frac{a}{(x^b+c)}+d$
– Data
- Fit
IC= 37.122
UE= 0.391
OC= 2.102
k= 0.956
a= 0.1575
b= 3.1639
c= 0.0001
d= 0.7786
dE$_T$/dA
Δ R from jet axis

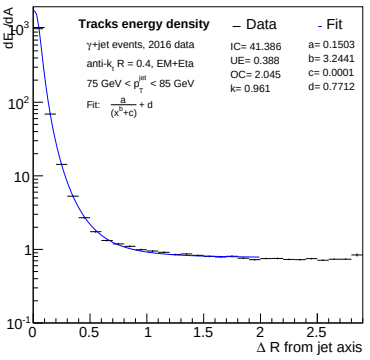
Tracks energy density
γ+jet events, 2016 data
anti-k$_t$ R = 0.4, EM+Eta
75 GeV < p_T^{jet} < 85 GeV
Fit: $\frac{a}{(x^b+c)}+d$
– Data
- Fit
IC= 41.386
UE= 0.388
OC= 2.045
k= 0.961
a= 0.1503
b= 3.2441
c= 0.0001
d= 0.7712
dE$_T$/dA
Δ R from jet axis

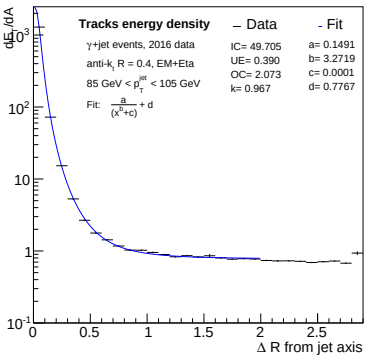
Tracks energy density
γ+jet events, 2016 data
anti-k$_t$ R = 0.4, EM+Eta
85 GeV < p_T^{jet} < 105 GeV
Fit: $\frac{a}{(x^b+c)}+d$
– Data
- Fit
IC= 49.705
UE= 0.390
OC= 2.073
k= 0.967
a= 0.1491
b= 3.2719
c= 0.0001
d= 0.7767
dE$_T$/dA
Δ R from jet axis

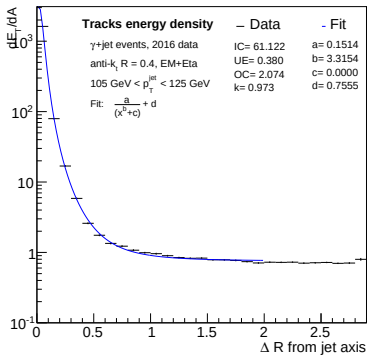
Tracks energy density
γ+jet events, 2016 data
anti-k$_t$ R = 0.4, EM+Eta
105 GeV < p_T^{jet} < 125 GeV
Fit: $\frac{a}{(x^b+c)}+d$
– Data
- Fit
IC= 61.122
UE= 0.380
OC= 2.074
k= 0.973
a= 0.1514
b= 3.3154
c= 0.0000
d= 0.7555
dE$_T$/dA
Δ R from jet axis

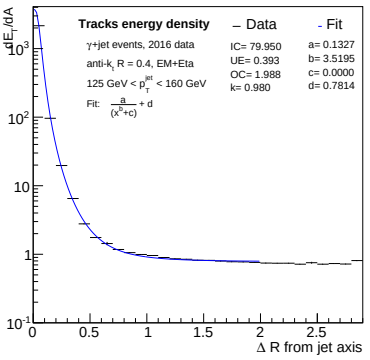
Tracks energy density
γ+jet events, 2016 data
anti-k$_t$ R = 0.4, EM+Eta
125 GeV < p_T^{jet} < 160 GeV
Fit: $\frac{a}{(x^b+c)}+d$
– Data
- Fit
IC= 79.950
UE= 0.393
OC= 1.988
k= 0.980
a= 0.1327
b= 3.5195
c= 0.0000
d= 0.7814
dE$_T$/dA
Δ R from jet axis

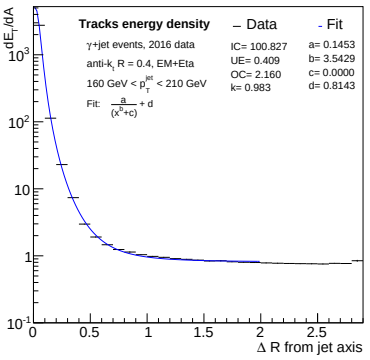
Tracks energy density
γ+jet events, 2016 data
anti-k$_t$ R = 0.4, EM+Eta
160 GeV < p_T^{jet} < 210 GeV
Fit: $\frac{a}{(x^b+c)}+d$
– Data
- Fit
IC= 100.827
UE= 0.409
OC= 2.160
k= 0.983
a= 0.1453
b= 3.5429
c= 0.0000
d= 0.8143
dE$_T$/dA
Δ R from jet axis

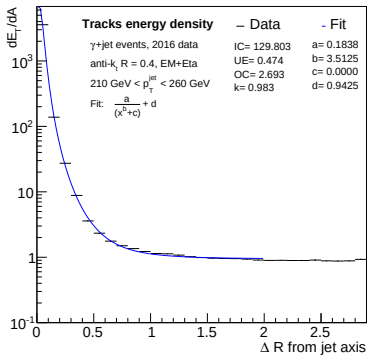
Tracks energy density
γ+jet events, 2016 data
anti-k$_t$ R = 0.4, EM+Eta
210 GeV < p_T^{jet} < 260 GeV
Fit: $\frac{a}{(x^b+c)}+d$
– Data
- Fit
IC= 129.803
UE= 0.474
OC= 2.693
k= 0.983
a= 0.1838
b= 3.5125
c= 0.0000
d= 0.9425
dE$_T$/dA
Δ R from jet axis

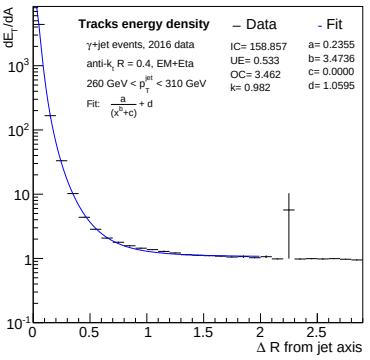
Tracks energy density
γ+jet events, 2016 data
anti-k$_t$ R = 0.4, EM+Eta
260 GeV < p_T^{jet} < 310 GeV
Fit: $\frac{a}{(x^b+c)}+d$
– Data
- Fit
IC= 158.857
UE= 0.533
OC= 3.462
k= 0.982
a= 0.2355
b= 3.4736
c= 0.0000
d= 1.0595
dE$_T$/dA
Δ R from jet axis

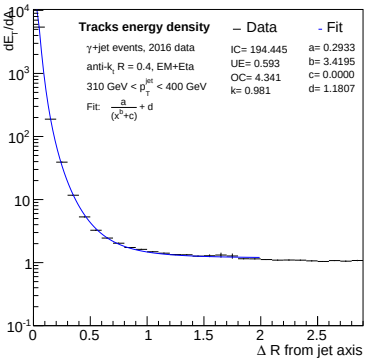
Tracks energy density
γ+jet events, 2016 data
anti-k$_t$ R = 0.4, EM+Eta
310 GeV < p_T^{jet} < 400 GeV
Fit: $\frac{a}{(x^b+c)}+d$
– Data
- Fit
IC= 194.445
UE= 0.593
OC= 4.341
k= 0.981
a= 0.2933
b= 3.4195
c= 0.0000
d= 1.1807
dE$_T$/dA
Δ R from jet axis

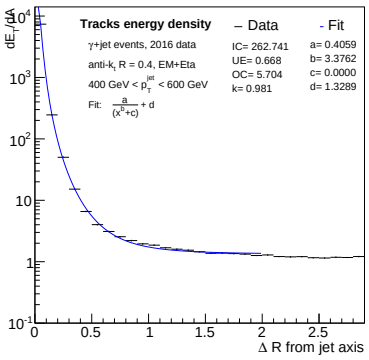
Tracks energy density
– Data
- Fit
γ+jet events, 2016 data
anti-k$_t$ R = 0.4, EM+Eta
400 GeV < p_T^{jet} < 600 GeV
Fit: $\frac{a}{(x^b+c)}+d$
IC= 262.741
UE= 0.668
OC= 5.704
k= 0.981
a= 0.4059
b= 3.3762
c= 0.0000
d= 1.3289
dE$_T$/dA
Δ R from jet axis

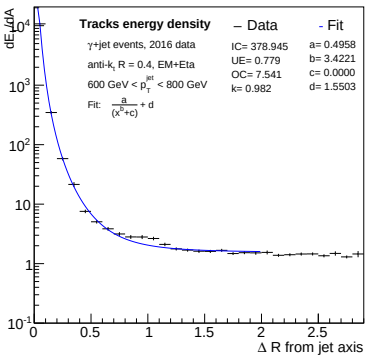
Tracks energy density
– Data
- Fit
γ+jet events, 2016 data
anti-k$_t$ R = 0.4, EM+Eta
600 GeV < p_T^{jet} < 800 GeV
Fit: $\frac{a}{(x^b+c)}+d$
IC= 378.945
UE= 0.779
OC= 7.541
k= 0.982
a= 0.4958
b= 3.4221
c= 0.0000
d= 1.5503
dE$_T$/dA
Δ R from jet axis

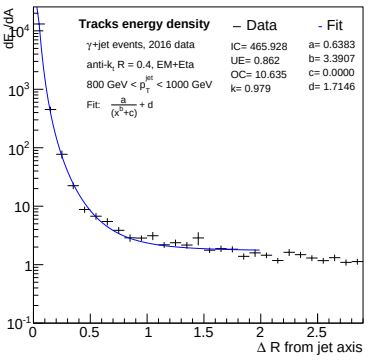
Tracks energy density
– Data
- Fit
γ+jet events, 2016 data
anti-k$_t$ R = 0.4, EM+Eta
800 GeV < p_T^{jet} < 1000 GeV
Fit: $\frac{a}{(x^b+c)}+d$
IC= 465.928
UE= 0.862
OC= 10.635
k= 0.979
a= 0.6383
b= 3.3907
c= 0.0000
d= 1.7146
dE$_T$/dA
Δ R from jet axis

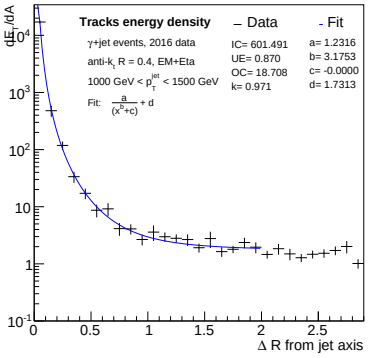
Tracks energy density
– Data
- Fit
γ+jet events, 2016 data
anti-k$_t$ R = 0.4, EM+Eta
1000 GeV < p_T^{jet} < 1500 GeV
Fit: $\frac{a}{(x^b+c)}+d$
IC= 601.491
UE= 0.870
OC= 18.708
k= 0.971
a= 1.2316
b= 3.1753
c= -0.0000
d= 1.7313
dE$_T$/dA
Δ R from jet axis

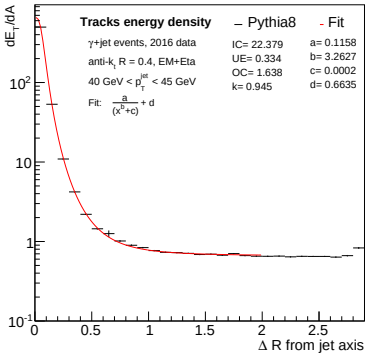
Tracks energy density
– Pythia8
- Fit
γ+jet events, 2016 data
anti-k$_t$ R = 0.4, EM+Eta
40 GeV < p_T^{jet} < 45 GeV
Fit: $\frac{a}{(x^b+c)}+d$
IC= 22.379
UE= 0.334
OC= 1.638
k= 0.945
a= 0.1158
b= 3.2627
c= 0.0002
d= 0.6635
dE$_T$/dA
Δ R from jet axis

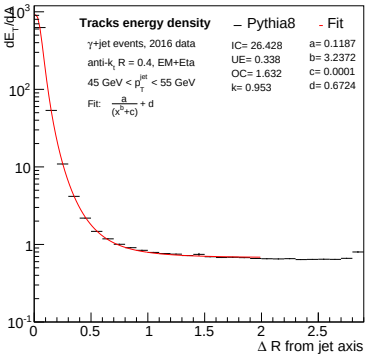
Tracks energy density
– Pythia8
- Fit
γ+jet events, 2016 data
anti-k$_t$ R = 0.4, EM+Eta
45 GeV < p_T^{jet} < 55 GeV
Fit: $\frac{a}{(x^b+c)}+d$
IC= 26.428
UE= 0.338
OC= 1.632
k= 0.953
a= 0.1187
b= 3.2372
c= 0.0001
d= 0.6724
dE$_T$/dA
Δ R from jet axis

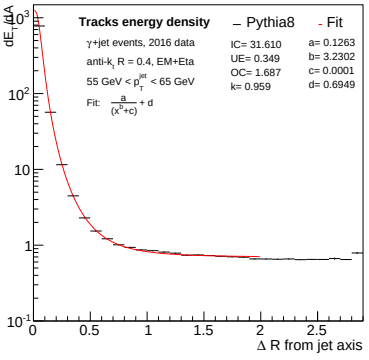
Tracks energy density
– Pythia8
- Fit
γ+jet events, 2016 data
anti-k$_t$ R = 0.4, EM+Eta
55 GeV < p_T^{jet} < 65 GeV
Fit: $\frac{a}{(x^b+c)}+d$
IC= 31.610
UE= 0.349
OC= 1.687
k= 0.959
a= 0.1263
b= 3.2302
c= 0.0001
d= 0.6949
dE$_T$/dA
Δ R from jet axis

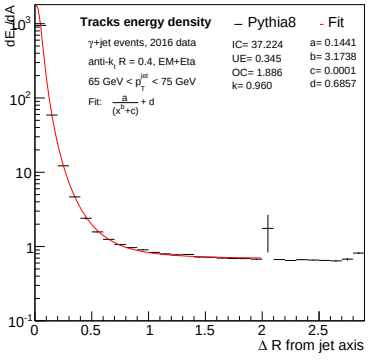
Tracks energy density
– Pythia8
- Fit
γ+jet events, 2016 data
anti-k$_t$ R = 0.4, EM+Eta
65 GeV < p_T^{jet} < 75 GeV
Fit: $\frac{a}{(x^b+c)}+d$
IC= 37.224
UE= 0.345
OC= 1.886
k= 0.960
a= 0.1441
b= 3.1738
c= 0.0001
d= 0.6857
dE$_T$/dA
Δ R from jet axis

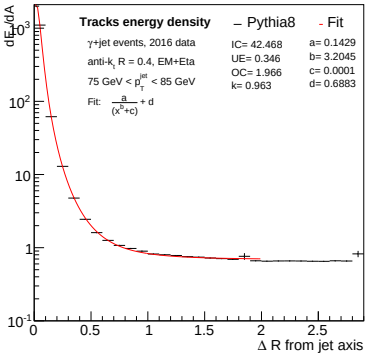
Tracks energy density
– Pythia8
- Fit
γ+jet events, 2016 data
anti-k$_t$ R = 0.4, EM+Eta
75 GeV < p_T^{jet} < 85 GeV
Fit: $\frac{a}{(x^b+c)}+d$
IC= 42.468
UE= 0.346
OC= 1.966
k= 0.963
a= 0.1429
b= 3.2045
c= 0.0001
d= 0.6883
dE$_T$/dA
Δ R from jet axis

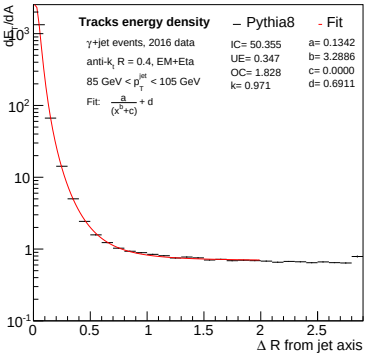
Tracks energy density
– Pythia8
- Fit
γ+jet events, 2016 data
anti-k$_t$ R = 0.4, EM+Eta
85 GeV < p_T^{jet} < 105 GeV
Fit: $\frac{a}{(x^b+c)}+d$
IC= 50.355
UE= 0.347
OC= 1.828
k= 0.971
a= 0.1342
b= 3.2886
c= 0.0000
d= 0.6911
dE$_T$/dA
Δ R from jet axis

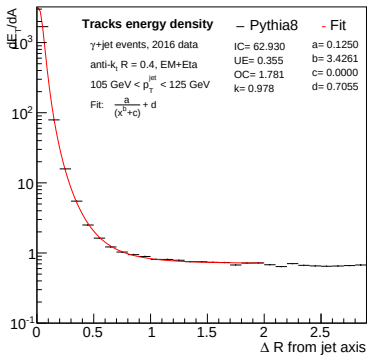
Tracks energy density
– Pythia8
- Fit
γ+jet events, 2016 data
anti-k$_t$ R = 0.4, EM+Eta
105 GeV < p$_T^{jet}$ < 125 GeV
Fit: $\frac{a}{(x^b+c)}+d$
IC= 62.930
UE= 0.355
OC= 1.781
k= 0.978
a= 0.1250
b= 3.4261
c= 0.0000
d= 0.7055
dE$_T$/dA
Δ R from jet axis

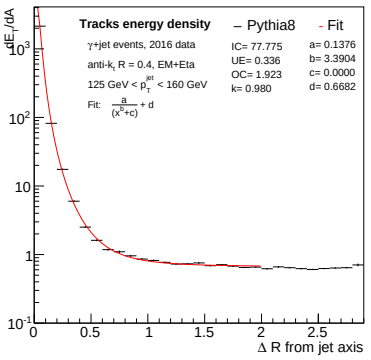
Tracks energy density
– Pythia8
- Fit
γ+jet events, 2016 data
anti-k$_t$ R = 0.4, EM+Eta
125 GeV < p$_T^{jet}$ < 160 GeV
Fit: $\frac{a}{(x^b+c)}+d$
IC= 77.775
UE= 0.336
OC= 1.923
k= 0.980
a= 0.1376
b= 3.3904
c= 0.0000
d= 0.6682
dE$_T$/dA
Δ R from jet axis

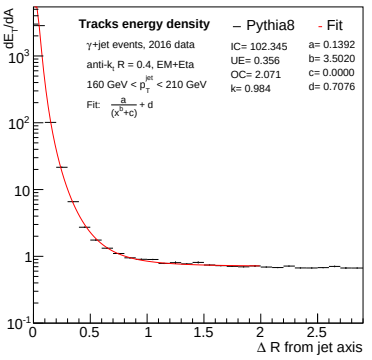
Tracks energy density
– Pythia8
- Fit
γ+jet events, 2016 data
anti-k$_t$ R = 0.4, EM+Eta
160 GeV < p$_T^{jet}$ < 210 GeV
Fit: $\frac{a}{(x^b+c)}+d$
IC= 102.345
UE= 0.356
OC= 2.071
k= 0.984
a= 0.1392
b= 3.5020
c= 0.0000
d= 0.7076
dE$_T$/dA
Δ R from jet axis

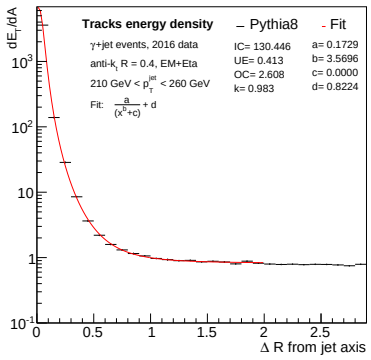
Tracks energy density
– Pythia8
- Fit
γ+jet events, 2016 data
anti-k$_t$ R = 0.4, EM+Eta
210 GeV < p$_T^{jet}$ < 260 GeV
Fit: $\frac{a}{(x^b+c)}+d$
IC= 130.446
UE= 0.413
OC= 2.608
k= 0.983
a= 0.1729
b= 3.5696
c= 0.0000
d= 0.8224
dE$_T$/dA
Δ R from jet axis

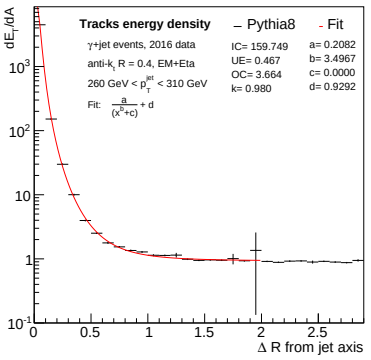
Tracks energy density
– Pythia8
- Fit
γ+jet events, 2016 data
anti-k$_t$ R = 0.4, EM+Eta
260 GeV < p$_T^{jet}$ < 310 GeV
Fit: $\frac{a}{(x^b+c)}+d$
IC= 159.749
UE= 0.467
OC= 3.664
k= 0.980
a= 0.2082
b= 3.4967
c= 0.0000
d= 0.9292
dE$_T$/dA
Δ R from jet axis

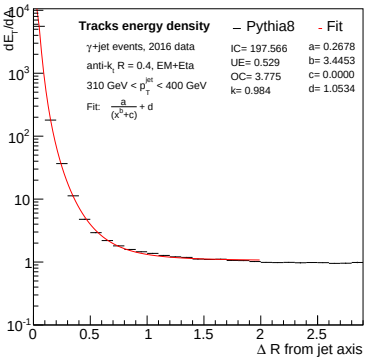
Tracks energy density
– Pythia8
- Fit
γ+jet events, 2016 data
anti-k$_t$ R = 0.4, EM+Eta
310 GeV < p$_T^{jet}$ < 400 GeV
Fit: $\frac{a}{(x^b+c)}+d$
IC= 197.566
UE= 0.529
OC= 3.775
k= 0.984
a= 0.2678
b= 3.4453
c= 0.0000
d= 1.0534
dE$_T$/dA
Δ R from jet axis

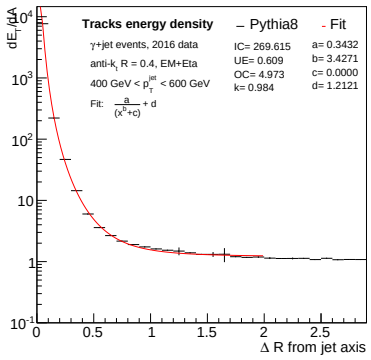
Tracks energy density
– Pythia8
- Fit
γ+jet events, 2016 data
anti-k$_t$ R = 0.4, EM+Eta
400 GeV < p$_T^{jet}$ < 600 GeV
Fit: $\frac{a}{(x^b+c)}+d$
IC= 269.615
UE= 0.609
OC= 4.973
k= 0.984
a= 0.3432
b= 3.4271
c= 0.0000
d= 1.2121
dE$_T$/dA
Δ R from jet axis

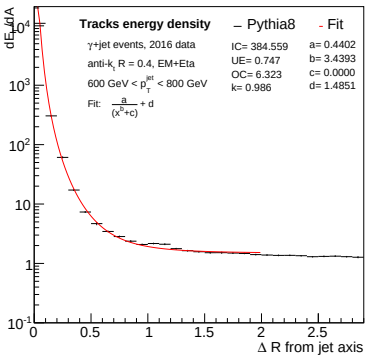
Tracks energy density
– Pythia8
- Fit
γ+jet events, 2016 data
anti-k$_t$ R = 0.4, EM+Eta
600 GeV < p$_T^{jet}$ < 800 GeV
Fit: $\frac{a}{(x^b+c)}+d$
IC= 384.559
UE= 0.747
OC= 6.323
k= 0.986
a= 0.4402
b= 3.4393
c= 0.0000
d= 1.4851
dE$_T$/dA
Δ R from jet axis

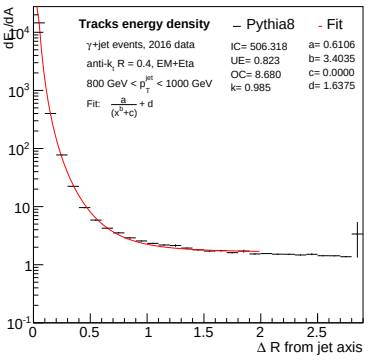
Tracks energy density
– Pythia8
- Fit
γ+jet events, 2016 data
anti-k$_t$ R = 0.4, EM+Eta
800 GeV < p$_T^{jet}$ < 1000 GeV
Fit: $\frac{a}{(x^b+c)}+d$
IC= 506.318
UE= 0.823
OC= 8.680
k= 0.985
a= 0.6106
b= 3.4035
c= 0.0000
d= 1.6375
dE$_T$/dA
Δ R from jet axis

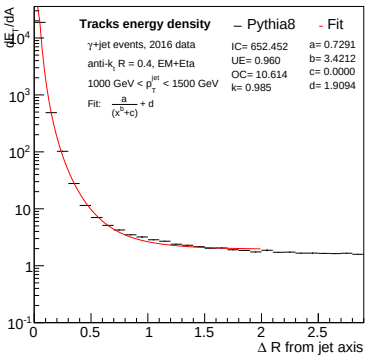
Tracks energy density
– Pythia8
- Fit
γ+jet events, 2016 data
anti-k$_t$ R = 0.4, EM+Eta
1000 GeV < p$_T^{jet}$ < 1500 GeV
Fit: $\frac{a}{(x^b+c)}+d$
IC= 652.452
UE= 0.960
OC= 10.614
k= 0.985
a= 0.7291
b= 3.4212
c= 0.0000
d= 1.9094
dE$_T$/dA
Δ R from jet axis

Résumé

Contexte théorique et supersymétrie

Le Modèle Standard de la physique des particules a été développé au cours du XXème siècle et permet aujourd'hui de décrire les particules élémentaires et leurs interactions avec une très grande précision. Il inclue trois des quatre forces fondamentales: l'électromagnétisme, la force nucléaire faible et la force nucléaire forte. Il s'agit d'une théorie quantique des champs relativiste basée sur les groupes de symétrie $SU(3)_C \times SU(2)_L \times U(1)_Y$. Les particules de matière peuvent être classées en deux familles: les quarks et les leptons. Elles correspondent à des fermions de spin 1/2. Les quarks sont composés de 6 particules: up, down, charm, strange, bottom, top. Les quarks up et down sont les quarks les plus stables. Dans la nature, les quarks ne peuvent pas être observés séparément. De la même façon les leptons sont composés de six particules: l'électron, le muon, le tau, de charge électrique -1, ainsi qu'un neutrino associé à chacun de charge électrique nulle. Les neutrinos ont la particularité de n'interagir que par force nucléaire faible et ne peuvent donc être détectés directement avec le détecteur ATLAS. Pour chaque fermion décrit, il existe une antiparticule de même masse et de charge électrique opposée. Chaque force décrite par le Modèle Standard est véhiculée par une ou plusieurs particules de spin 1 (boson). La force électromagnétique est véhiculée par le photon, la force nucléaire faible est véhiculée par les bosons Z et $W^{\pm}$, et la force nucléaire forte est véhiculée par 8 types de gluons. La particule hypothétique vecteur de la gravitation s'appelle le graviton mais n'a pas encore été découverte. La dernière particule du Modèle Standard est le boson de Higgs, et correspond a une particule de spin 0. Cette particule permet notamment d'expliquer la masse des bosons Z et $W^{\pm}$.

Le Modèle Standard décrit la physique des particules avec une grande précision mais certains problèmes restent sans solution. Ainsi, la matière et l'antimatière auraient dû être produites en quantité égale lors du Big Bang. Aujourd'hui, on observe que l'univers est presque entièrement composé de matière. Cette asymétrie n'est pas encore comprise. Le Modèle Standard n'explique pas l'oscillation et la masse de neutrinos. Il ne fournit pas de candidat pour la matière noire, matière hypothétique introduite afin d'expliquer la différence entre certaines observations cosmologiques sur la rotation des galaxies et les prédictions. Il n'inclue pas la gravitation dans son modèle. L'unification des quatre forces fondamentales correspond à un des plus grands challenges du XXème et XXIème siècle. Enfin, le Modèle Standard ne résout pas le problème de naturalité. Ce problème concerne le calcul théorique de la masse du boson de Higgs. Le calcul nécessite de prendre en compte l'échelle de nouvelle physique (à priori échelle de Planck, ou échelle de Grande Unification), et ces échelles sont à des ordres de grandeur très supérieurs à celle de la masse observée en 2012 (125 GeV). La supersymétrie est une extension du Modèle Standard. Elle unifie la famille des fermions avec la famille des bosons. Elle prédit que pour chaque fermion existant, il existe un boson associé ayant un spin différent de 1/2, et vice-versa. Chaque pair de fermion-boson est unifiée dans un objet appelé supermultiplet, et chaque composant au sein d'un supermultiplet correspond à un superpartner de l'autre composant. L'existence de ces nouvelles particules peut ainsi régler le problème de hiérarchie. En ajoutant des nouvelles particules dans le modèle, on ajoute également des nouvelles corrections radiatives pour le calcul de la masse du boson de Higgs. Si les nouvelles particules ont la même masse

que les particules du Modèle Standard et avec un spin différant de 1/2, alors ces corrections ont en plus la particularité de s'annuler exactement. La supersymétrie permet aussi d'unifier les constantes de couplage des groupes de gauge des trois forces du Modèle Standard. De nombreux modèles de supersymétrie fournissent également un bon candidat pour la matière noire.

Si la supersymétrie est exacte, alors pour chaque particule du Modèle Standard on peut associer une particule supersymétrique dont le spin diffère de 1/2. En particulier, il existerait une particule associée à l'électron de même masse et de spin 0. Cette particule n'a pas été découverte. Si la supersymétrie existe, il s'agit donc nécessairement d'une symétrie brisée. Le mécanisme de brisure de symétrie a déjà été appliqué avec succès puisqu'il a prédit l'existence du boson de Higgs. Un mécanisme similaire peut être appliqué pour la supersymétrie, avec la contrainte de conserver les propriétés du Modèle Standard.

Le MSSM (Modèle Minimal de Supersymétrie) est le modèle qui prédit le nombre minimal de nouvelles particules tout en respectant la supersymétrie. Les particules du Modèle Standard sont représentées sur la partie gauche de la Figure 6.46, et les particules du MSSM sont représentées sur la partie droite. Les particules recherchées au cours de la thèse sont les squarks et les gluinos et correspondent aux superpartenairs des quarks et des gluons. Les squarks et les gluons ont l'avantage de pouvoir être produites par interaction nucléaire forte entre deux gluons ou entre gluon-quark/antiquark. Cet avantage très important dans le cas d'un accélérateur de particules lourdes comme c'est le cas avec le LHC. Le MSSM comprend au total 124 paramètres libres, dont 19 paramètres liés au Modèle Standard.

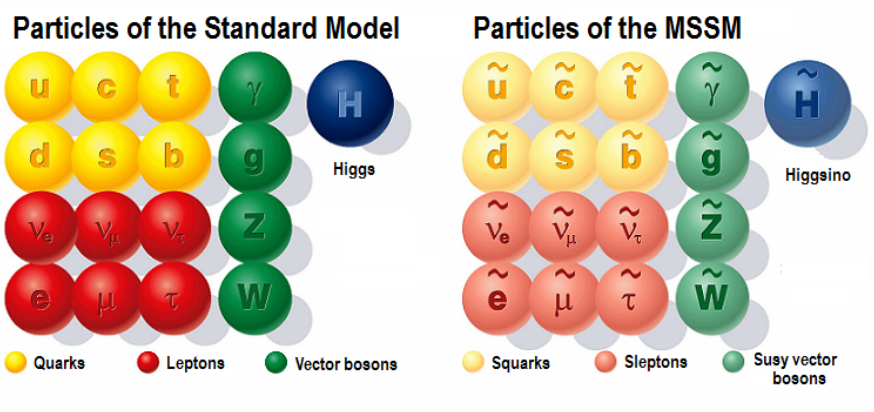

Figure 6.46: Particules du Modèle Standard (gauche) et leurs particules associées dans le cas du MSSM (droite). En jaune les quarks (gauche) et les quarks scalaires (droite), en rouge les leptons (gauche) et les leptons scalaires (droite), en vert les bosons de gauge (gauche) et les gauginos (droite), et en bleu le boson de Higgs (gauche) et le Higgsino associé (droite).

Afin de conserver la stabilité du proton, un nouveau nombre quantique appelé R-parité est introduit. Il dépend du nombre baryonique B, leptonique L, du spin S de la particule et il est défini par: $R = (-1)^{3(B-L)+2S}$. Il est ainsi négatif pour les particules supersymétriques, et positif pour les particules du Modèle Standard. Plusieurs modèles de supersymétrie sont étudiés dans ATLAS en fonction du mécanisme de brisure de symétrie et des hypothèses effectuées. Les modèles étudiés au cours de ma thèse correspondent à des modèles simplifiés de production et désintégration de pairs de squarks et gluinos. Ces modèles incluent un nombre restreint de particules, ce qui diminue drastiquement le nombre de paramètres libres. Les rapports d'embranchement sont fixés à 100% pour chaque modèle et les paramètres restant correspondent à la masse des particules supersymétriques.

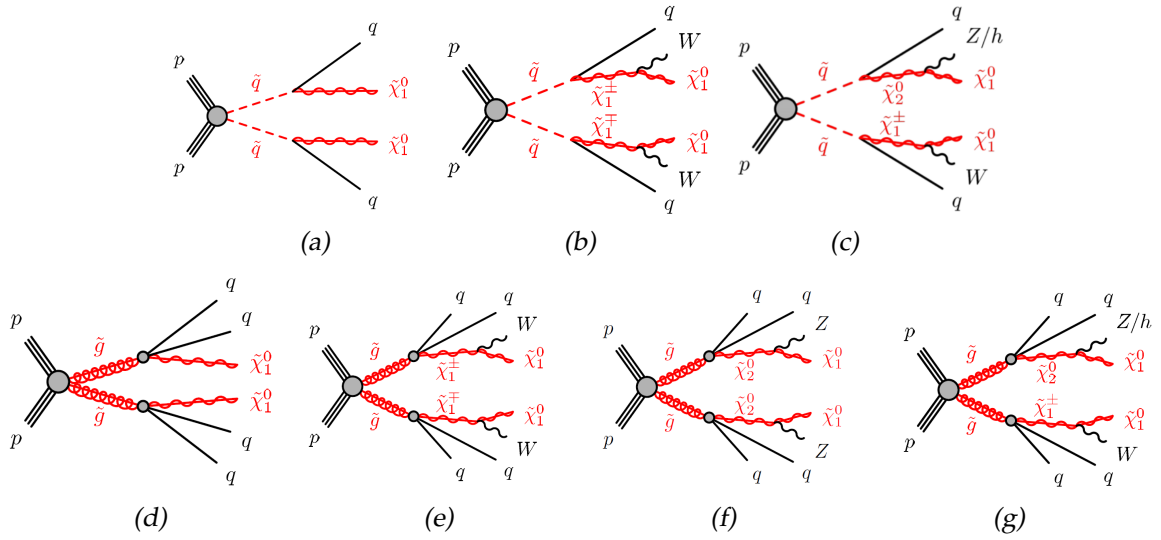

Figure 6.47: Decay topology of the MSSM squarks (a-c) and gluinos (b-d) pair production with direct and one-step decays [48].

L'expérience ATLAS du LHC

Le Grand Collisionneur de Hadrons (LHC) est le plus grand accélérateur de particules jamais construit. Il s'agit d'un accélérateur circulaire de 26.7 km de circonférence conçu pour produire des collisions proton-proton à une énergie nominale de 14 TeV. Des collisions d'ions lourds peuvent également être étudiées. L'accélérateur est construit au CERN (Genève) à 100 mètres de profondeur. A l'intérieur de l'anneau, la température est maintenue constante à une température de 1.9K grâce à un système de cryogénie à hélium liquide.

Les protons sont produits par paquets successifs qui forment des faisceaux de protons. Ils sont créés à partir d'un gaz ionisé d'hydrogène et progressivement accélérés à une vitesse proche de celle de la lumière via une succession d'accélérateurs. La fréquence de croisement des faisceaux est de 25ns. Le nombre d'interactions moyen en 2016 par croisement de faisceaux est alors de 24.9. Le nombre élevé est susceptible de perturber la performance des détecteurs. Au cours d'une interaction entre deux protons, on appelle pile-up les effets dus aux dépôts d'énergie additionnels provenant d'autres interactions. Les dépôts additionnels peuvent provenir d'une autre interaction au sein d'un même croisement, ou d'un croisement précédent.

La collaboration ATLAS comprend environ 3000 physiciens répartis dans plus de 38 pays et 180 institutions. Il s'agit de la plus grande collaboration en physique. Le détecteur de symétrie cylindrique, a une longueur de 46 m, une largeur de 25 m et pèse environ 7000 tonnes (Figure 6.48). Les collisions ont lieu au centre du détecteur. Il est composé de quatre sous détecteurs: le détecteur de traces, le calorimètre électromagnétique, le calorimètre hadronique, et le spectromètre à muon.

Le détecteur de traces est le plus proche du point de collision, il permet de reconstruire la trace des particules électriquement chargées, ainsi que les vertex primaires et secondaires. Il est lui-même composé de trois sous parties différentes qui sont combinées pour reconstruire les traces.

Le calorimètre électromagnétique est conçu afin de mesurer l'énergie des particules électromagnétiques comme l'électron, le positron et le photon. Il a une forme très caractéristique en forme d'accordéon afin de fournir des mesures symétriques en ϕ et est constitué d'une substance active (l'argon liquide), et d'une substance passive (le plomb). Il est formé d'un baril et de deux bouchons, ce qui lui permet de couvrir la région $|\eta| < 3.2$. Le calorimètre hadronique est conçu pour arrêter et mesurer l'énergie des particules lourdes. Il est constitué d'un calorimètre à tuiles scintillantes util-

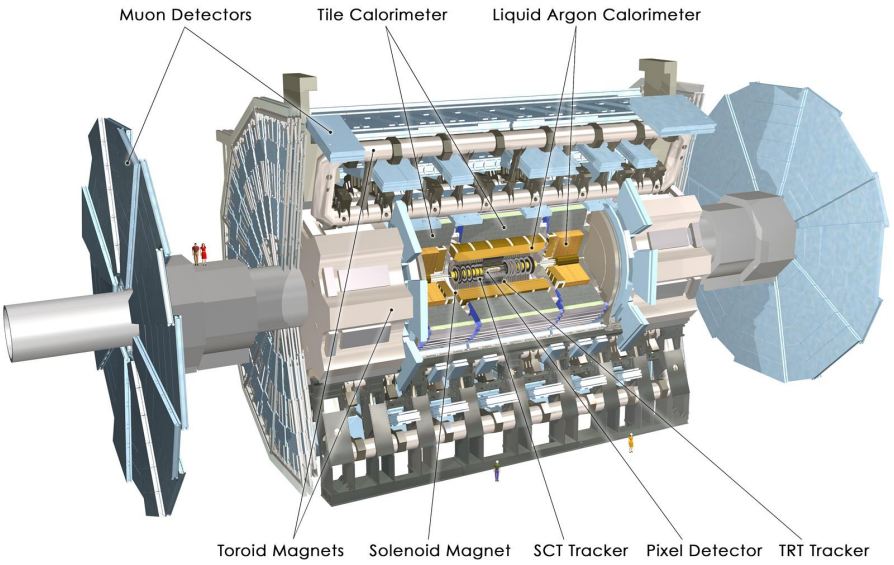

Figure 6.48: Le détecteur ATLAS.

isant l'acier comme absorbeur, de deux bouchons (HEC) ainsi que deux parties externes(FCAL) basés sur la technologie à Argon liquide. La taille du calorimètre d'ATLAS est conçue de manière à arrêter la majeur partie des gerbes électromagnétiques et hadroniques. Le spectromètre à muon mesure la déflexion des traces de muons dans un champ magnétique intense afin d'en déduire leur impulsion transverse.

Le système de déclenchement permet de décider très rapidement si l'événement est enregistré ou rejeté. Il est composé d'une partie hardware et d'une partie software. Il permet de diminuer successivement la fréquence d'enregistrement de 40 MHz à 100 kHz puis 1 kHz.

Reconstruction et calibration des jets

Un jet est un objet produit par l'hadronisation d'un quark ou d'un gluon. Les jets sont très importants dans la plupart des analyses de physique au LHC. Lorsqu'un quark ou un gluon est émis dans le détecteur suite à une collision, il s'hadronise avant d'interagir avec le détecteur. On appelle jet la collection d'objets émis dans un cône de rayon fixé. Les jets sont reconstruits par défaut à l'aide d'un algorithme appelé anti-k_t qui prend en entrée les dépôts d'énergie du calorimètre dans un rayon R = 0.4. Les jets reconstruits à partir d'autres entrées sont également étudiés au cours de la thèse. La reconstruction des jets est affectée par la non-compensation du calorimètre d'ATLAS (la réponse du détecteur pour une particule électromagnétique et hadronique n'est pas la même), les pertes d'énergie dans les matériaux défectueux, les fuites d'énergie en dehors des calorimètres, et les pertes induites par les algorithmes de clusterisation et de reconstruction. Plusieurs étapes sont nécessaires pour reconstruire et calibrer les jets. Ces corrections permettent de corriger la position de l'origine du jet, les effets de pile-up, la réponse du détecteur et la dépendance en énergie de la particule initiale (quark ou gluon). Une correction supplémentaire est appliquée sur les données. Cette correction appelée calibration in-situ est obtenue uniquement à partir des données collectées. Il s'agit de la contribution majeur de la thèse.

Par défaut, les jets sont reconstruits à partir des clusters topologiques du calorimètre. Un cluster correspond à un regroupement 3D de cellules adjacentes dans le calorimètre. Par défaut, les jets sont calibrés à l'échelle électromagnétique, on appelle ces jets les jets EMTopo. Une correction supplémentaire peut être appliquée sur l'énergie des clusters, en fonction de si le cluster provient d'une particule

électromagnétique ou hadronique. Cette correction permet de limiter les effets de non compensation du calorimètre d'ATLAS. Dans ce cas, on dit que le jet est calibré à l'échelle locale et les jets sont appelé LCTopo. Un troisième type de jet utilisant les informations obtenues avec le détecteur de traces a été étudié au cours de la thèse. Ce type de jet est principalement motivé par une meilleure résolution à basse énergie en utilisant le détecteur de trace qu'avec le calorimètre, ainsi que par la possibilité de rejeter le pile-up en associant les traces au vertex primaire. Ces jets sont nommés EMPFlow.

La dernière étape de la chaine de reconstruction et calibration s'appelle la calibration in-situ. Elle applique une correction résiduelle supplémentaire à l'impulsion transverse des jets. Cette correction s'applique dans les données uniquement. La première étape consiste à calibrer l'impulsion transverse des jets de manière relative en utilisant des événements dijet. La deuxième étape consiste à appliquer une calibration absolue sur l'impulsion des jets. On utilisera pour ça des événements Z+jets à basse énergie, γ+jet entre 40 GeV et environ 1.5 TeV, et multijets à plus grande énergie. Ces trois méthodes sont ensuite combinées pour la calibration finale.

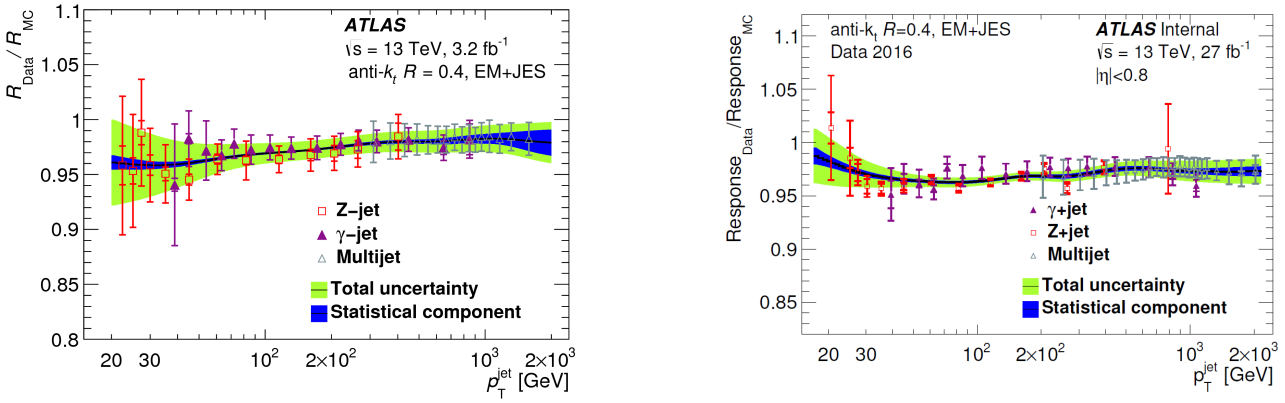

(a) *(b)*

Figure 6.49: Rapport des données sur le Monte Carlo en fonction de p_T pour les calibrations in-situ γ+jet, Z+jet et multijets. La correction finale (ligne noire), l'incertitude statistique (aire bleue) et l'incertitude totale (aire verte) sont également illustrées). La calibration utilisant les données 2015 comprend 3.2 fb^{-1} (a) et celle utilisant les données 2016 comprend 27.0 fb^{-1} (b) [133].

Calibration des jets avec la méthode in-situ γ+jet

La méthode γ+jet est utilisée pour corriger l'impulsion transverse des jets et est appliquée après la calibration relative. La méthode utilise la mesure très précise de l'impulsion du photon comme référence. Les événements avec un photon émis en opposition à un quark/gluon sont sélectionnés. Au premier ordre, si toutes les particules provenant de l'hadronisation du parton étaient incluses dans le cône, et si le photon était parfaitement mesuré, l'impulsion du photon et du jet serait identique. Cependant les mesures sur l'énergie du jet et du photon sont affectées par des erreurs systématiques, par les rayonnements QCD, et par les contributions du pile-up. Pour réduire les effets des radiations QCD, on utilisera plutôt l'impulsion du jet projetée sur la direction du photon:

$$p_T^{ref} = p_T^{\gamma} \times |\cos \Delta\phi(jet, \gamma)|, \tag{6.12}$$

avec $\Delta\phi$ l'angle entre le jet et le photon. On calcul alors la balance définie par:

$$\mathcal{B} = \frac{p_T^{leadingjet}}{p_T^{ref}}. \tag{6.13}$$

La balance est inférieure à 1 car les particules issues de l'hadronisation du parton en dehors du cône ne sont pas incluses dans le jet. La balance est calculée pour différents bins en énergie. Dans chaque bin, la balance est calculée en ajustant une fonction Gaussienne sur les distributions. La valeur centrale étant choisie comme étant la balance. Le rapport

$$\mathcal{R} = \frac{\langle B^{MC} \rangle}{\langle B^{data} \rangle}, \tag{6.14}$$

calculé dans chaque bin en énergie, est utilisé comme correction in-situ pour l'impulsion transverse des jets. Les systèmes de déclenchement utilisés dans l'analyse ont été programmés pour enregistrer les événements contenant un photon ayant une impulsion transverse suffisamment élevée. En dessous de 140 GeV (120 GeV en 2015), seule une partie des événements passant les coupures a été enregistrée pour limiter la quantité de données. Au total, onze systèmes de déclenchement différents (10 en 2015) ont été utilisés.

Les photons sélectionnés doivent passer les critères d'identification. Ces critères concernent la forme de la gerbe électromagnétique dans le calorimètre, ainsi que la répartition des dépôts d'énergie. Les photons de la partie centrale sont sélectionnés ($|\eta < 1.37|$) avec un seuil de 25 GeV sur leur impulsion transverse. Une coupure sur l'isolation est également appliquée de manière à rejeter le bruit de fond π^0, et à garder les photons convertis en pair e^+/e^-.

Les jets centraux sont sélectionnés ($\eta < 0.8$) et doivent satisfaire certains critères pour rejeter les faux jets. Une coupure de 20 GeV est appliquée sur l'impulsion transverse du jet. Les jets doivent également être correctement associés au vertex primaire pour supprimer les jets de pile-up.

Des sélections supplémentaires sont appliquées sur l'angle entre le jet et le photon ($\Delta\Phi > 2.8$) et sur l'impulsion du deuxième jet ($p_T^{jet2} < 15$ GeV) de manière à limiter l'impact des radiations QCD.

La balance est calculée dans chaque bin en p_T^{ref}. Elle suit une distribution Gaussienne sauf à bas p_T où la distribution est biaisée suite aux sélections appliquées. L'intervalle d'ajustement a donc été adapté pour les bins de plus basse énergie. La distribution de la balance dans les données 2016 pour deux bins différents est illustrée sur la Figure 6.50.

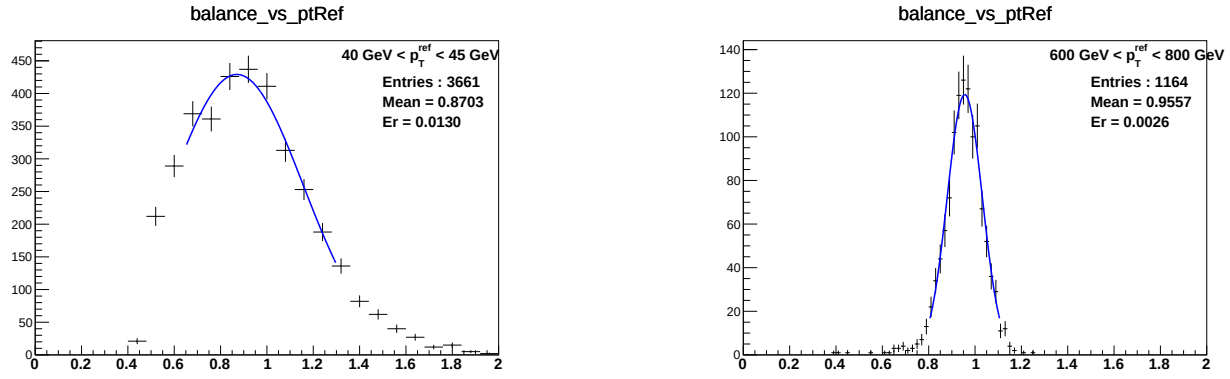

(a) *(b)*

Figure 6.50: Distribution de la balance en utilisant les données acquises en 2016 à $\sqrt{s}$ = 13 TeV. A gauche, le bin 40 GeV < p_T^{ref} < 45 GeV et à droite le bin 600 GeV < p_T^{ref} < 800 GeV.

La balance calculée en 2015 et 2016 avec les jets calibrés à l'échelle électromagnétique est représentée sur la Figure 6.51 (a). La balance est inférieure à 1 car les particules en dehors du cône de reconstruction ne sont pas prises en compte. La balance dans les données est également inférieure à celle dans les simulations. Le rapport des données sur la simulation est utilisé comme calibration. Une correction de l'ordre de 2-3% est ainsi appliquée. A basse énergie, la balance est plus faible qu'à grande énergie. Cette différence est due au fait qu'à grande énergie, les particules sont boostées à l'intérieur

du cône ce qui diminue les pertes d'énergie à l'extérieur du cône. Une différence de l'ordre de 1% est visible entre 2015 et 2016 dû à un changement dans le calorimètre Tile. La Figure 6.51 (b) montre une comparaison entre les trois types de jets en utilisant les données 2016. Un très bon accord de l'ordre de 1-2% est obtenu. La balance en fonction des angles η et ϕ est présenté dans la thèse.

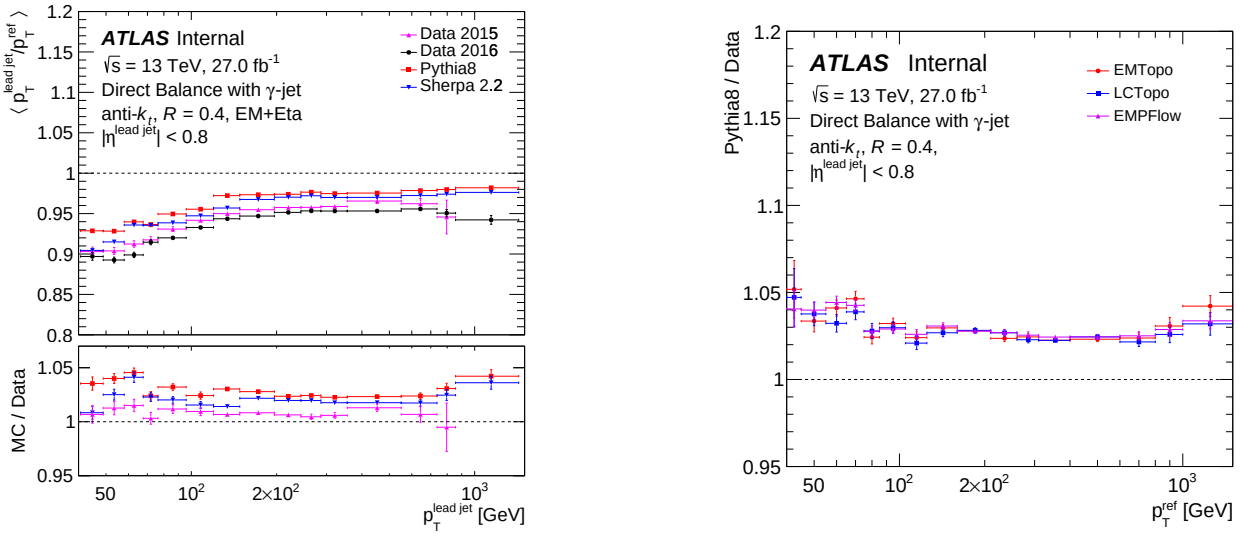

(a) *(b)*

Figure 6.51: A gauche la balance en fonction de p_T^{ref} en utilisant les données acquises en 2015 (rose), 2016 (noir), le générateur Monte Carlo nominal (rouge), et le générateur Monte Carlo de comparaison (bleu). Les jets sont calibrés à l'échelle électromagnétique. En bas de la figure de gauche, le rapport des données 2016 sur le Monte Carlo (rouge ou bleu), et le rapport des données 2015 sur les données 2016 (rose). A droite la balance en fonction de p_T^{ref} en utilisant les données 2016, et pour plusieurs types de jets. En rouge les jets calibrés à l'échelle électromagnétique, en bleu à l'échelle locale, en violet en utilisant l'information des traces des particules chargées.

Plusieurs facteurs peuvent perturber les résultats et ont été pris en compte lors de l'estimation des incertitudes. Une incertitude est liée au choix du simulateur Monte Carlo. Il s'agit de l'incertitude dominante. Cette incertitude est estimée en comparant les résultats obtenus avec le générateur nominal et le générateur de comparaison. Une incertitude est liée à l'énergie du photon est prise en compte. Il s'agit d'une incertitude dominante à grande énergie. L'incertitude sur la résolution du photon est négligeable. Une incertitude est liée au choix des coupures sur le p_T du deuxième jet, à l'angle entre le photon et le jet, à l'association entre le jet et le vertex primaire (JVT). Ces incertitudes sont estimées en faisant varier la coupure de sélection et en propageant les variations sur la correction finale. Une incertitude est liée à l'échantillon des données utilisées et concerne la pureté des événements photon+jet. Cette incertitude est calculée avec la méthode ABCD et elle est dominante à basse énergie. Enfin, la dernière incertitude concerne l'estimation des effets en dehors du cône du jet. Cette incertitude est estimée en utilisant les traces des particules chargées associées au jet et correspond à une des incertitudes dominantes à basse énergie avec la pureté. L'erreur sur les ajustements Gaussiens est utilisée comme erreur statistique. Afin de limiter les fluctuations statistiques lors de l'estimation des erreurs systématiques, une procédure appelée bootstrap a été utilisée pour l'estimation de chaque incertitude ainsi qu'un procédure de rebinning.

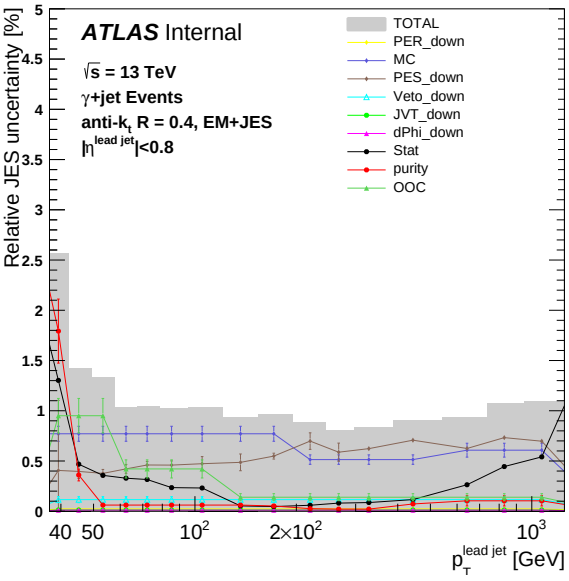

Figure 6.52: Incertitudes systématiques basses sur les jets calibrés à l'échelle électromagnétique, en utilisant la méthode γ+jet. L'incertitude totale (aire grise) est calculée par somme quadratique de tous les composants. L'incertitude totale comprend l'incertitude sur l'énergie et la résolution des photons (PES, PER), la simulation (MC), la coupure sur le deuxième jet (Veto), l'association du jet avec le vertex primaire (JVT), l'angle entre le photon et le jet (dPhi), l'incertitude statistique (Stat), la pureté et les effets en dehors du cône (OOC). Les bars verticales indiquent les erreurs statistiques sur les évaluations.

Mesure de la résolution des jets avec la méthode γ+jet

La méthode γ+jet direct balance peut également être utilisée pour mesurer la résolution en énergie des jets. Une bonne connaissance de la résolution des jets étant nécessaire pour de nombreuses analyses avec des jets dans l'état final. La résolution des jets peut être paramétrisée comme suit:

$$\frac{\sigma(p_T)}{p_T} = \frac{N}{p_T} \oplus \frac{S}{\sqrt{p_T}} \oplus C, \tag{6.15}$$

N étant le bruit de fond (électronique, détecteur, pile-up), S le terme stochastique, et C le terme constant. Ces trois paramètres peuvent être extraits avec la méthode γ+jet direct balance. Le principe de la méthode est le même que pour la calibration. La même sélection est appliquée aux événements, mais la largeur des distributions Gaussiennes est utilisée à la place de la valeur centrale dans le cas de la balance. La JER, appelée ici $\sigma_{in-situ}$ peut être exprimée comme suit:

$$\sigma_{in-situ} = \sqrt{\sigma\left(\frac{p_T^{jet}}{p_T^{ref}}\right)^2_{data} - \sigma\left(\frac{p_T^{truth}}{p_T^{ref}}\right)^2_{MC}}. \tag{6.16}$$

Le premier terme correspond à la largeur de la distribution de la balance dans les données. Il dépend en partie de la performance du détecteur, mais aussi de la largeur "naturelle" de la distribution. Cette largeur "naturelle" peut être estimée à partir des simulations. Elle correspond au deuxième terme de la formule et elle est soustraite quadratiquement à la distribution de la balance de manière à en déduire uniquement les effets du détecteur.

La résolution pour les trois types de jets est présentée sur la Figure 6.53. La résolution augmente avec le p_T car l'effet en dehors du cône est de plus en plus faible. On a ainsi une résolution de l'ordre de 4% à 1 TeV. A basse énergie on obtient une bien meilleure performance avec les jets EMPFlow. A 40 GeV, on a ainsi une résolution de 17% pour les jets EMPFlow, et 24% pour les jets EMTopo et LCTopo. Ces résultats s'éxpliquent par le fait que la résolution du détecteur de traces est meilleure que celle du calorimètre à basse énergie. De plus, l'utilisation des traces permet de rejeter une partie du pile-up ce qui améliore également la résolution.

Les incertitudes sont représentées sur la Figure 6.54. Une incertitude totale de l'ordre de 10% est obtenue sur la majeure partie de la gamme de calibration. L'incertitude de fermeture est l'incertitude dominante. Il s'agit d'une incertitude liée au choix de la méthode. L'incertitude sur les effets en dehors du cône n'est pas incluse car elle est comprise dans l'incertitude de fermeture.

La supersymétrie

La supersymétrie prédit l'existence de nouvelles particules. Ces particules pourraient être produites et détectées au LHC. Cette partie résume la recherche de squarks ($\tilde{q}$) et de gluinos ($\tilde{g}$) en utilisant les données acquises à $\sqrt{s}$ = 13 TeV en 2015 et 2016 par le détecteur ATLAS. L'augmentation de l'énergie de collision à 13 TeV permet d'augmenter la section efficace de production des particules et d'améliorer les recherches effectuées au cours du Run 1. De nouvelles régions du MSSM peuvent ainsi être atteintes. Dans l'analyse 0-lepton, la R-parité est considérée comme étant conservée au cours des interactions. Une conséquence de cette hypothèse est que les particules supersymétriques doivent être produites par paires. D'autres analyses se focalisent sur la recherche de modèles sans conservation de la R-parité. Le neutralino χ_1^0 est considéré comme étant la particule supersymétrique la plus légère. C'est ainsi la seule particule supersymétrique stable. Toutes les autres particules supersymétriques vont se désintégrer en une cascade de particules jusqu'à produire un neutralino. Le neutralino n'interagissant que par force nucléaire faible, il ne sera pas détecté par mesure directe et on va rechercher de l'énergie transverse manquante dans le détecteur. Dans l'analyse hadronique (0-lepton), le signal est défini par des jets et de l'énergie transverse manquante E_T^{miss} dans le détecteur.

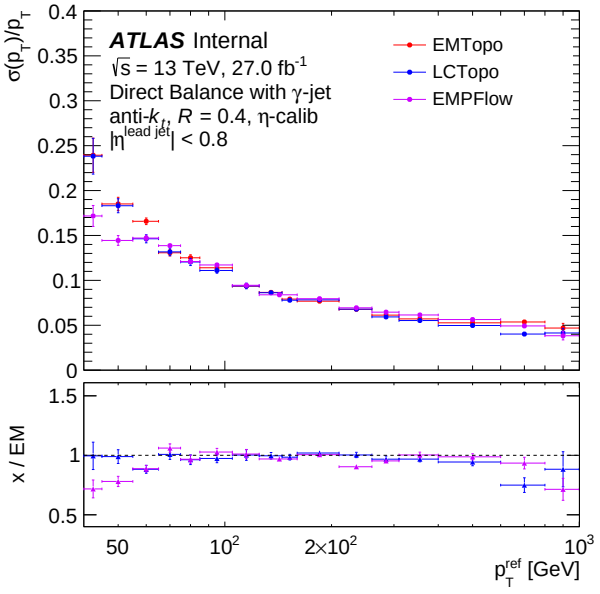

Figure 6.53: Comparaison de la résolution entre les trois types de jets: calibrés à l'échelle électromagnétique (rouge), à l'échelle locale (bleu), en utilisant la trace des particules chargées (violet). Les résultats sont obtenus en utilisant les données acquises en 2016 à $\sqrt{s}$ = 13 TeV. La partie du bas de la Figure montre le rapport EMPFlow sur EMTopo (violet) et LCTopo sur EMTopo (blue). Les barres d'erreur indiquent les erreurs statistiques.

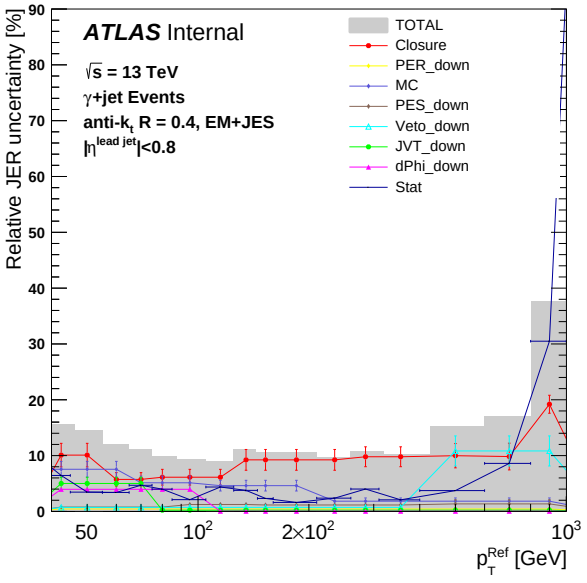

Figure 6.54: Incertitude sur la mesure de la résolution des jets calibrés à l'échelle électromagnétique, en utilisant les données acquises en 2016 à $\sqrt{s}$ = 13 TeV. L'incertitude totale (gris) comprend l'incertitude de fermeture, sur la résolution et l'énergie des photons, sur les simulations, sur la coupure du deuxième jet, sur l'association du jet avec le vertex primaire, sur l'angle entre le photon et le jet, et l'erreur statistique.

Plusieurs modèles sont étudiés. Mon travail de thèse a porté sur les modèles avec désintégration des squarks et des gluinos en jets + E_T^{miss} via une particule intermédiaire comme le neutralino lourd χ_2^0 ou les charginos $\chi_1^\pm$ (modèles one-step). Ces modèles sont illustrés sur la Figure 6.47. Les masses des particules supersymétriques sont des paramètres libres du modèle. En première approche et pour limiter le nombre de paramètres, les deux premières générations des squarks sont considérés comme étant dégénérés en masse.

Des nombreuses sélections sont appliquées aux données afin d'isoler le signal du bruit de fond. L'optimisation se fait à l'aide de variables discriminantes particulièrement bien adaptées au signal recherché, ou adaptées pour rejeter un certain type de bruit de fond. La stratégie de recherche est la suivante: 24 régions de signal (SRs) sont définies. Une région de signal correspond à des valeurs de coupures spécifiques, qui ont été optimisées sur un ou plusieurs modèles. Pour chaque région de signal, des régions de control (CRs) sont définies à partir des données de manière à améliorer l'estimation des bruits de fond. Afin de tester les estimations du bruit de fond, des régions de validation (VRs) sont également définies. Ces 3 types de régions sont orthogonaux afin d'éviter le recouvrement dans les données. Si le bruit de fond est validé, un ajustement de vraisemblance est appliqué dans chaque région de signal afin de tester l'hypothèse "bruit de fond seulement". L'ajustement teste la compatibilité entre les observations (données) et le Modèle Standard. Si aucun excès n'est observé, un ajustement est effectué de manière à exclure les modèles étudiés avec 95% CLs.

Les bruits de fond sont les événements du Modèle Standard qui reproduisent le signal recherché (2-6 jets + E_T^{miss}). On distingue 5 types de bruits de fond: Z+jet, W+jet, diboson, Top, QCD. Le dernier bruit de fond (QCD) correspond à des événements multijets dans le cas où un des jets est mal mesuré. On a alors de l'énergie transverse manquante due à une mauvaise mesure du détecteur. Une première présélection est appliquée dans les données de manière à sélectionner des événements avec des jets et de l'énergie transverse manquante. Plusieurs variables discriminantes sont ensuite utilisées pour l'optimisation: le nombre de jets N_{jet}, l'énergie transverse manquante E_T^{miss}, l'impulsion transverse des jets p_T^{jets}, leur angle d'émission η^{jets}, la masse effective définie par $m_{eff} = \sum_{i=1}^{n} |p_T^i| + E_T^{miss}$, l'angle minimum entre les jets et l'énergie transverse manquante $\Delta\phi(jet, E_T^{miss})$, d'autre variables combinées comme: $\frac{E_T^{miss}}{\sqrt{\sum_{i=1}^{n} |p_T^i|}}$, $\frac{E_T^{miss}}{m_{eff}(N_j)}$ ou des variables plus compliquées comme l'aplanarité qui prend en compte le plan d'émission des jets.

L'optimisation se fait en deux étapes. La première est une optimisation rapide basée sur les distributions du signal et du bruit de fond. Le bruit de fond est estimé à partir des simulations, et normalisé à la section efficace théorique et à la bonne luminosité. Une incertitude de 10% est considérée sur le bruit de fond. Avec ces paramètres, les distributions sont tracées de manière à avoir une bonne idée des valeurs de coupures sur les variables discriminantes.

La seconde étape de l'optimisation est plus longue. Chaque bruit de fond est estimé avec la section efficace théorique, et normalisé en utilisant la région de control adaptée. Les erreurs systématiques sont calculées proprement. Les estimations du bruit de fond sont testées et validées grâce aux régions de validation. Un grand nombre de coupures est testé en se basant sur les résultats de la première optimisation.

Au total, 24 régions de signal sont utilisées dans l'analyse 0-lepton, dont 7 optimisées pendant la thèse sur les modèle one-step (désintgégration via une particule intermédiaire) et deux optimisées pour les régions boostées (bosons W/Z boostés dans l'état final). La valeur des coupures dans chaque région est décrite sur le Tableau 6.15

Pour la région boostée, une nouvelle variable de sélection a été introduite. Il s'agit de la masse et de l'impulsion transverse des jets de rayon R = 1.0 reconstruits à partir des jets R = 0.4 utilisés par défaut dans ATLAS. Dans le cas d'un événement recherché, ces "grands" jets ont ainsi une masse centrés sur la masse du W ou du Z.

Les principales sources d'incertitude sont dues à la normalisation des bruits de fond à partir des

Requirement	Signal Region						
	5j-1600	**5j-2000**	**5j-2600**	**6j-1200**	**6j-1800**	**6j-2200**	**6j-2600**
$E_{\mathrm{T}}^{\mathrm{miss}}$ [GeV] >	250						
$p_{\mathrm{T}}(j_1)$ [GeV] >	200						
$p_{\mathrm{T}}(j_5)$ [GeV] >	50			100			
$p_{\mathrm{T}}(j_6)$ [GeV] >	–			50	100		
$\lvert\eta(j_{1,..6})\rvert$ <	2.8			2.0	2.0	–	
$\Delta\phi(\mathrm{jet}_{1,2,(3)}, \vec{E}_{\mathrm{T}}^{\mathrm{miss}})_{\mathrm{min}}$ >	0.4		0.8	0.4			
$\Delta\phi(\mathrm{jet}_{i>3}, \vec{E}_{\mathrm{T}}^{\mathrm{miss}})_{\mathrm{min}}$ >	0.2	0.4		0.2			
Aplanarity >	0.08	–		0.04	–	0.08	
$E_{\mathrm{T}}^{\mathrm{miss}}/m_{\mathrm{eff}}(N_j)$ >	0.15	–		0.25	0.2		0.15
$E_{\mathrm{T}}^{\mathrm{miss}}/\sqrt{H_{\mathrm{T}}}$ [GeV$^{1/2}$] >	–	15	18	–			
m_{eff}(incl.) [GeV] >	1600	2000	2600	1200	1800	2200	2600

(a)

Requirement	Signal Region	
	2jB-1600	**2jB-2400**
$E_{\mathrm{T}}^{\mathrm{miss}}$ [GeV] >	250	
$p_{\mathrm{T}}(\mathrm{RT}j_1)$ [GeV] >	200	
$p_{\mathrm{T}}(\mathrm{RT}j_2)$ [GeV] >	200	
$m(\mathrm{RT}j_1)$ [GeV]	[60,110]	
$m(\mathrm{RT}j_2)$ [GeV]	[60,110]	
$\Delta\phi(\mathrm{jet}_{1,2,(3)}, \vec{E}_{\mathrm{T}}^{\mathrm{miss}})_{\mathrm{min}}$ >	0.6	
$\Delta\phi(\mathrm{jet}_{i>3}, \vec{E}_{\mathrm{T}}^{\mathrm{miss}})_{\mathrm{min}}$ >	0.4	
$E_{\mathrm{T}}^{\mathrm{miss}}/\sqrt{H_{\mathrm{T}}}$ [GeV$^{1/2}$] >	20	
m_{eff}(incl.) [GeV] >	1600	2400
Optimised for	SS onestep	GG onestep

(b)

Table 6.15: A gauche les régions de signal optimisées à partir des modèles one-step, et à droite les régions de signal optimisées pour la région boostée.

régions de control, et aux incertitudes théoriques. Les incertitudes expérimentales sur la modélisation, l'énergie, la résolution des jets et l'énergie transverse manquante sont négligeables.

Une illustration des différents bruits de fond et des données observées est visible sur la Figure 6.55 pour deux régions de signal différentes. Les résultats de l'analyse dans chaque région de signal sont représentés sur la Figure 6.56. Aucun excès significatif n'est observé dans les différentes régions. L'excès maximal est observée dans la région SR2j-2100 et correspond à une déviation standard de 2.14σ. Les erreurs statistiques sont plus importantes dans les régions avec une grande multiplicité de jets ou une large coupure sur m_{eff}.

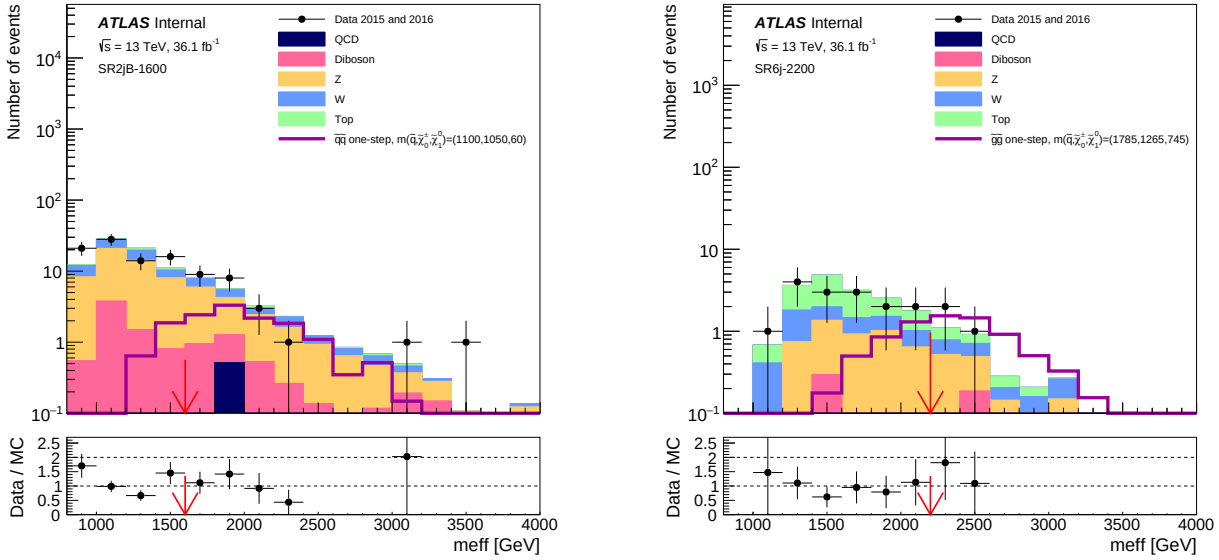

(a) *(b)*

Figure 6.55: La distributions des différents bruits de fond (aires colorées) et les données observées (points noirs). A gauche la région de signal boostée SR2jB-1600, et à droite la région de signal SR6j-2200. Les bruits de fond sont normalisés à la section efficace théorique.

Comme aucun excès n'a été observé, des limites ont été posées sur les modèles étudiés. Les limites sur deux modèles différents correspondant à la production d'une paire de gluinos sont représentées sur la Figure 6.57. La limite maximale posée sur la masse du gluino correspond à 2.01 TeV. Elle est

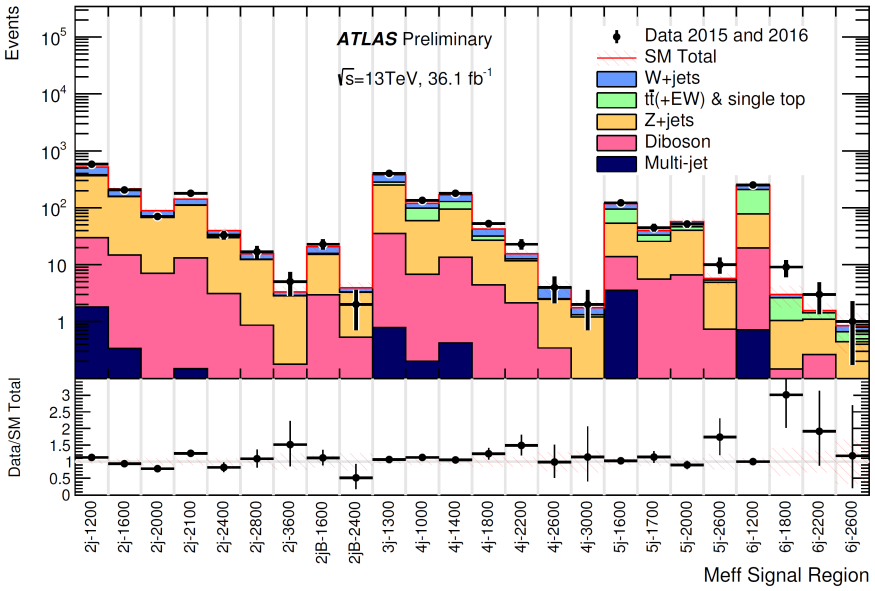

Figure 6.56: Comparaison entre les données et les estimations du bruit de fond en fonction des différentes régions de signal. Le bas de la figure montre le rapport entre les données et les prédictions. Les barres d'erreur indiquent les erreurs statistiques.

atteinte pour $x \simeq 0.5$ (a) et pour un neutralino de masse nulle (b). La limite est posée avec la région de signal SR6j2600. La région boostée correspond à $x \simeq 1$ et une limite de 1.9 TeV est posée pour cette région. Cette limite est atteinte dans la région SR2jB2400.

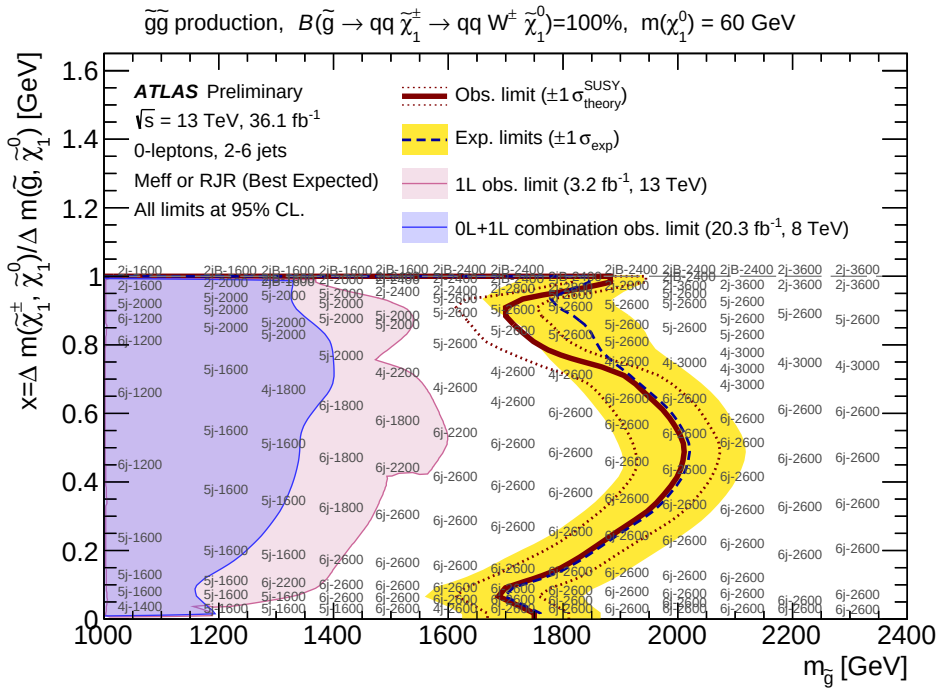

(a)

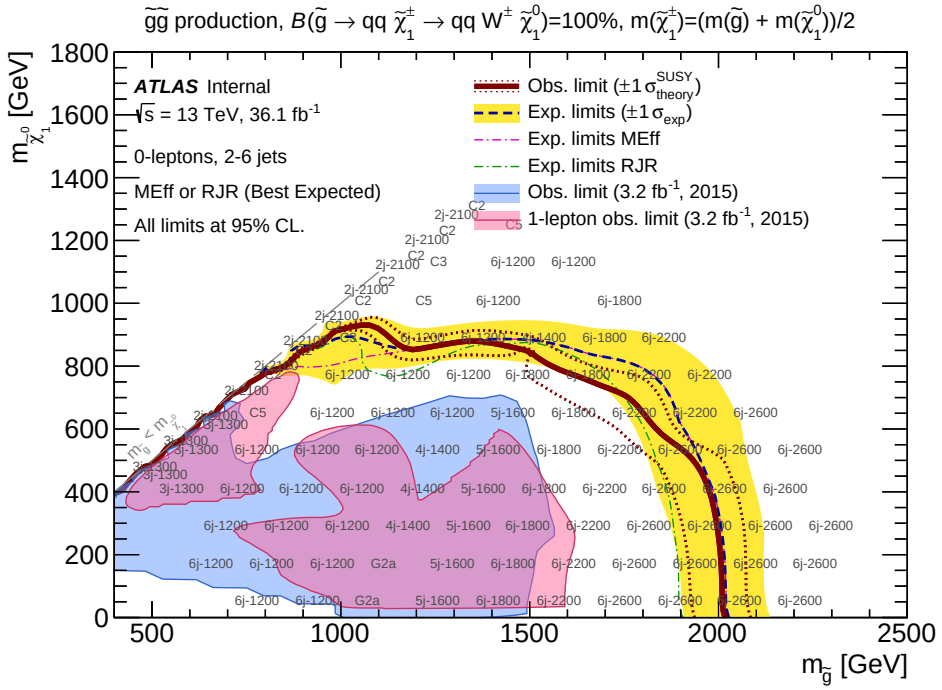

(b)

Figure 6.57: Limites d'exclusion pour deux modèles correspondant à la production d'une paire de gluinos se désintégrant en jets + neutralino via une particule intermédiaire. Les limites sont tracées avec un intervalle de confiance de 95% dans le plan (x, $m_{\tilde{g}}$) (a) et ($m_{\tilde{\chi}_1^0}$, $m_{\tilde{g}}$) (b) correspondant respectivement à $m_{\tilde{\chi}_1^0}$ = 60 GeV et $m_{\tilde{\chi}_1^{\pm}} = (m_{\tilde{\chi}_1^0} + m_{\tilde{g}})/2$. Les limites observées (lignes continues rouges) et les limites attendues (lignes discontinues bleues) sont montrées. Les lignes discontinues rouges correspondent aux limites calculées avec les incertitudes théoriques sur la section efficace. Les bandes jaunes sont calculées avec les incertitudes expérimentales et les incertitudes théoriques sur le bruit de fond. Sur la Figure (b), la meilleure région de signal entre l'analyse présentée et une analyse alternative appelée RJigsaw est choisie pour chaque point.

Conclusion

Deux sujets sont étudiés au cours de la thèse: la reconstruction et la calibration des jets, ainsi que la recherche de supersymétrie. Les recherches reposent sur les données acquises à $\sqrt{s}$ = 13 TeV en 2015 et 2016 avec le détecteur ATLAS du LHC (CERN). La méthode développée au cours de la thèse s'appelle la méthode γ+jet direct balance. Elle correspond à la dernière étape de la calibration et se base sur la mesure très précise des photons pour calibrer l'impulsion transverse des jets. Elle permet de calibrer les jets entre 40 GeV et 1.5 TeV. Trois types de jets sont étudiés: les jets calibrés à l'échelle électromagnétique, locale, et en utilisant l'information des traces des particules chargées. Une correction de l'ordre de 2-3% est obtenue pour tous les types de jets. Les sources d'incertitude sont détaillées. L'incertitude totale est de l'ordre de 1% dans la majeure partie de la gamme en énergie. Ces résultats sont combinés avec la méthode Z+jet et multijets pour la calibration finale et sont actuellement utilisés par la Collaboration ATLAS. La méthode γ+jet permet également de mesurer la résolution des jets. Une résolution de l'ordre de 4% est obtenue à 1 TeV. L'incertitude totale est dominée par l'incertitude de fermeture et est de l'ordre de 10%.

La seconde partie de la thèse décrit la recherche des squarks et gluinos dans le canal hadronique. Ce dernier est un des plus précis pour la recherche de physique au-delà du Modèle Standard. Mon travail s'est principalement porté sur l'optimisation des régions de signal pour les modèle one-step. Neuf nouvelles régions de signal ont été introduites dans l'analyse pour un total de 24 régions de signal. L'excès maximal est obtenu dans la région SR2j-2100 et correspond à 2.14 σ. Les limites sur les modèles étudiés ont été grandement améliorées depuis le Run 1. Une exclusion atteignant 2 TeV (95% CLs) est posée sur la masse du gluino. Cette limite est obtenue pour différents modèles. De même, une exclusion allant jusqu'à 1.22 TeV est posée sur la masse des squarks en considérant que les deux premières générations de squarks sont dégénérées. Les futures données à $\sqrt{s}$ = 13 TeV et $\sqrt{s}$ = 14 TeV vont permettre d'améliorer les recherches et d'atteindre des nouvelles régions de supersymétrie. L'utilisation des Boost Decision Tree (BDT) pourra également améliorer le travail lié à l'optimisation des régions de signal.

Bibliography

[1] S. L. Glashow. Partial Symmetries of Weak Interactions. *Nucl. Phys.*, 22:579–588, 1961. http://inspirehep.net/record/4328.

[2] S. Weinberg. A Model of Leptons. *Phys. Rev. Lett.*, 19:1264–1266, 1967. https://inspirehep.net/record/51188?ln=fr.

[3] A. Salam. 1968. "Weak and electromagnetic interactions", in Elementary particle theory: relativistic groups and analyticity, N. Svartholm, ed., p. 367. Almqvist & Wiksell, 1968. Proceedings of the eighth Nobel symposium.

[4] M. Veltman G. 't Hooft. 1968. "Regularization and Renormalization of Gauge Fields",http://www.sciencedirect.com/science/article/pii/0550321372902799?via%3Dihub.

[5] ATLAS Collaboration. Observation of a new particle in the search for the Standard Model Higgs boson with the ATLAS detector at the LHC. *Phys. Lett.*, B716:1–29, 2012. https://arxiv.org/abs/1207.7214.

[6] CMS Collaboration. Observation of a new boson at a mass of 125 GeV with the CMS experiment at the LHC. *Phys. Lett.*, B716:30–61, 2012. https://arxiv.org/abs/1207.7235.

[7] M. E. Peskin and D. V. Schroeder. *An Introduction to quantum field theory*. 1995.

[8] M. Herrero. The Standard model. *NATO Sci. Ser. C*, 534:1–59, 1999. https://arxiv.org/abs/hep-ph/9812242v1.

[9] F. Englert and R. Brout. Broken Symmetry and the Mass of Gauge Vector Mesons. *Phys. Rev. Lett.*, 13:321–323, Aug 1964. https://link.aps.org/doi/10.1103/PhysRevLett.13.321.

[10] P.W. Higgs. Broken symmetries, massless particles and gauge fields. *Physics Letters*, 12(2):132 – 133, 1964. http://www.sciencedirect.com/science/article/pii/0031916364911369.

[11] P. W. Higgs. Broken Symmetries and the Masses of Gauge Bosons. *Phys. Rev. Lett.*, 13:508–509, Oct 1964. https://link.aps.org/doi/10.1103/PhysRevLett.13.508.

[12] P. W. Higgs. Spontaneous Symmetry Breakdown without Massless Bosons. *Phys. Rev.*, 145:1156–1163, May 1966. https://link.aps.org/doi/10.1103/PhysRev.145.1156.

[13] T. W. B. Kibble. Symmetry Breaking in Non-Abelian Gauge Theories. *Phys. Rev.*, 155:1554–1561, Mar 1967. https://link.aps.org/doi/10.1103/PhysRev.155.1554.

[14] G. S. Guralnik, C. R. Hagen, and T. W. B. Kibble. Global Conservation Laws and Massless Particles. *Phys. Rev. Lett.*, 13:585–587, Nov 1964. https://link.aps.org/doi/10.1103/PhysRevLett.13.585.

[15] Lubej Matic. Standard Model. http://www.physik.uzh.ch/groups/serra/StandardModel.html.

[16] R. Barbier et al. R-parity violating supersymmetry. *Phys. Rept.*, 420:1–202, 2005. https://arxiv.org/abs/hep-ph/0406039.

[17] Morad Aaboud et al. Measurement of the W-boson mass in pp collisions at $\sqrt{s} = 7$ TeV with the ATLAS detector. 2017. https://arxiv.org/pdf/1701.07240.pdf.

[18] C. Patrignani et al. Review of Particle Physics. *Chin. Phys.*, C40(10):100001, 2016. http://cds.cern.ch/record/2241948.

[19] ATLAS and CMS Collaboration. Measurements of the Higgs boson production and decay rates and constraints on its couplings from a combined ATLAS and CMS analysis of the LHC pp collision data at $\sqrt{s} = 7$ and 8 TeV. *JHEP*, 08:045, 2016. https://arxiv.org/abs/1606.02266.

[20] A. Pomarol. "Beyond the Standard Model". *Universitat Autonoma de Barcelona, Bellaterra, Spain*, February 2012. ARXIV:1202.1391V1 [HEP-PH]. https://arxiv.org/abs/1202.1391.

[21] The matter-antimatter asymmetry problem. Jan 2014. http://cds.cern.ch/record/1998489.

[22] Y. Fukuda et al. Measurements of the solar neutrino flux from Super-Kamiokande's first 300 days. *Phys. Rev. Lett.*, 81:1158–1162, 1998. [Erratum: Phys. Rev. Lett.81,4279(1998)].

[23] T. Araki et al. Measurement of neutrino oscillation with KamLAND: Evidence of spectral distortion. *Phys. Rev. Lett.*, 94:081801, 2005. https://arxiv.org/abs/hep-ex/0406035.

[24] Stephen Patrick Martin. "A Supersymmetry Primer". September 2011. [ARXIV:HEP-PH/9709356V6]. https://arxiv.org/abs/hep-ph/9709356.

[25] D. I. Kazakov. Beyond the standard model: In search of supersymmetry. In *2000 European School of high-energy physics, Caramulo, Portugal, 20 Aug-2 Sep 2000: Proceedings*, pages 125–199, 2000. https://arxiv.org/abs/hep-ph/0012288.

[26] Ian J. R. Aitchison. Supersymmetry and the MSSM: An Elementary introduction. 2005. https://arxiv.org/abs/hep-ph/0505105.

[27] P. Fayet. "Spontaneously broken supersymmetric theories of weak, electromagnetic and strong interactions". *Physics Letters* B. http://www.sciencedirect.com/science/article/pii/0370269377908528?via%3Dihub#aep-bibliography-id3.

[28] P. Fayet. "Supersymmetry and weak, electromagnetic and strong interactions". *Physics Letters* B. http://www.sciencedirect.com/science/article/pii/0370269376903191?via%3Dihub.

[29] P. Fayet Glennys R. Farrar. "Phenomenology of the production, decay, and detection of new hadronic states associated with supersymmetry". *Physics Letters* B. http://www.sciencedirect.com/science/article/pii/0370269378908584?via%3Dihub.

[30] ATLAS Collaboration. Summary of the searches for squarks and gluinos using $\sqrt{s} = 8$ TeV pp collisions with the ATLAS experiment at the LHC. *JHEP*, 10:054, 2015. https://arxiv.org/abs/1507.05525.

[31] ATLAS Collaboration. Summary of the ATLAS experiment's sensitivity to supersymmetry after LHC Run 1 — interpreted in the phenomenological MSSM. *JHEP*, 10:134, 2015. https://arxiv.org/abs/1508.06608.

[32] A. Djouadi, J.L Kneur, and G. Moultaka. SuSpect: A Fortran code for the supersymmetric and Higgs particle spectrum in the MSSM. *Comput. Phys. Commun.*, 176:426–455, 2007. https://arxiv.org/abs/hep-ph/0211331.

[33] C. F. Berger, J. S. Gainer, J. L. Hewett, and T. G. Rizzo. Supersymmetry Without Prejudice. *JHEP*, 02:023, 2009. https://arxiv.org/abs/0812.0980.

[34] M. W. Cahill-Rowley, J. L. Hewett, S. Hoeche, A. Ismail, and T. G. Rizzo. The New Look pMSSM with Neutralino and Gravitino LSPs. *Eur. Phys. J.*, C72:2156, 2012. https://arxiv.org/abs/1206.4321.

[35] M. Marjanovic. *Search for strongly produced supersymmetric particles with the ATLAS detector and interpretation in the pMSSM*. Theses, Université Paris-Saclay, November 2015. https://tel.archives-ouvertes.fr/tel-01327222.

[36] A. H. Chamseddine, R. Arnowitt, and Pran Nath. Locally supersymmetric grand unification. *Phys. Rev. Lett.*, 49:970–974, Oct 1982. https://journals.aps.org/prl/abstract/10.1103/PhysRevLett.49.970.

[37] R. Barbieri, S. Ferrara, and C.A. Savoy. Gauge models with spontaneously broken local supersymmetry. *Physics Letters B*, 119(4):343 – 347, 1982.

[38] L. Ibáñez. Locally supersymmetric su(5) grand unification. *Physics Letters B*, 118(1):73 – 78, 1982.

[39] L. Hall, J. Lykken, and S. Weinberg. Supergravity as the messenger of supersymmetry breaking. *Phys. Rev. D*, 27:2359–2378, May 1983. https://link.aps.org/doi/10.1103/PhysRevD.27.2359.

[40] N. Ohta. Grand unified theories based on local supersymmetry. *Progress of Theoretical Physics*, 70(2):542, 1983. http://dx.doi.org/10.1143/PTP.70.542.

[41] D. Alves. Simplified Models for LHC New Physics Searches. *J. Phys.*, G39:105005, 2012. https://arxiv.org/abs/1105.2838.

[42] J. Alwall, P. Schuster, and N. Toro. Simplified Models for a First Characterization of New Physics at the LHC. *Phys. Rev.*, D79:075020, 2009. https://arxiv.org/abs/0810.3921.

[43] C. Borschensky, M. Krämer, A. Kulesza, M. Mangano, S. Padhi, T. Plehn, and X. Portell. Squark and gluino production cross sections in pp collisions at $\sqrt{s}$ = 13, 14, 33 and 100 TeV. *Eur. Phys. J.*, C74(12):3174, 2014. https://arxiv.org/abs/1407.5066.

[44] W. Beenakker, R. Hopker, M. Spira, and P. M. Zerwas. Squark and gluino production at hadron colliders. *Nucl. Phys.*, B492:51–103, 1997. https://arxiv.org/abs/hep-ph/9610490.

[45] Michael Spira. Higgs and SUSY particle production at hadron colliders. In *Supersymmetry and unification of fundamental interactions. Proceedings, 10th International Conference, SUSY'02, Hamburg, Germany, June 17-23, 2002*, pages 217–226, 2002. https://arxiv.org/abs/hep-ph/0211145.

[46] Tilman Plehn. Measuring the MSSM Lagrangean. *Czech. J. Phys.*, 55:B213–B220, 2005. https://arxiv.org/abs/hep-ph/0410063.

[47] Public Results - LHC SUSY Cross Section Working Group . https://twiki.cern.ch/twiki/bin/view/LHCPhysics/SUSYCrossSections.

[48] ATLAS Collaboration. "Search for squarks and gluinos in final states with jets and missing transverse momentum using 36 fb^{-1} of $\sqrt{s} = 13\mathrm{T}e\mathrm{V}$ pp collision data with the ATLAS detector". Technical Report ATLAS-COM-CONF-2017-020, CERN, Geneva, Mar 2017. https://cds.cern.ch/record/2256027.

[49] ATLAS Collaboration. "Search for squarks and gluinos with the ATLAS detector in final states with jets and missing transverse momentum using 20.3 fb^{-1} of $\sqrt{s} = 8\mathrm{T}e\mathrm{V}$ proton-proton collision data". *JHEP*, 25 April 2014. https://arxiv.org/abs/1405.7875.

[50] O. S. Brüning, P. Collier, P Lebrun, S. Myers, R. Ostojic, J. Poole, and P. Proudlock. *LHC Design Report*. CERN Yellow Reports: Monographs. CERN, Geneva, 2004. https://cds.cern.ch/record/782076.

[51] The ALICE Collaboration. The ALICE experiment at the CERN LHC. *Journal of Instrumentation*, 3(08):S08002, 2008. http://stacks.iop.org/1748-0221/3/i=08/a=S08002.

[52] The ATLAS Collaboration. The ATLAS Experiment at the CERN Large Hadron Collider. *Journal of Instrumentation*, 3(08):S08003, 2008. http://stacks.iop.org/1748-0221/3/i=08/a=S08003.

[53] The CMS Collaboration. The CMS experiment at the CERN LHC. *Journal of Instrumentation*, 3(08):S08004, 2008. http://stacks.iop.org/1748-0221/3/i=08/a=S08004.

[54] The LHCb Collaboration. The LHCb Detector at the LHC. *Journal of Instrumentation*, 3(08):S08005, 2008. http://stacks.iop.org/1748-0221/3/i=08/a=S08005.

[55] The TOTEM Collaboration. The TOTEM Experiment at the CERN Large Hadron Collider. *Journal of Instrumentation*, 3(08):S08007, 2008. http://stacks.iop.org/1748-0221/3/i=08/a=S08007.

[56] The LHCf Collaboration. The LHCf detector at the CERN Large Hadron Collider. *Journal of Instrumentation*, 3(08):S08006, 2008. http://stacks.iop.org/1748-0221/3/i=08/a=S08006.

[57] Measurement of the Rate of Collisions from Satellite Bunches for the April-May 2010 LHC Luminosity Calibration. Technical Report ATLAS-CONF-2010-102, CERN, Geneva, Dec 2010. http://cds.cern.ch/record/1317334.

[58] F. Marcastel. CERN's Accelerator Complex. La chaîne des accélérateurs du CERN. Oct 2013. https://cds.cern.ch/record/1621583.

[59] ATLAS Collaboration. Improved luminosity determination in pp collisions at $\sqrt{s}$ = 7 TeV using the ATLAS detector at the LHC. *Eur. Phys. J.*, C73(8):2518, 2013. https://arxiv.org/abs/1302.4393.

[60] Luminosity Determination in pp Collisions at $\sqrt{s}$ = 7 TeV using the ATLAS Detector in 2011. Technical Report ATLAS-CONF-2011-116, CERN, Geneva, Aug 2011. http://cds.cern.ch/record/1376384.

[61] Updated Luminosity Determination in pp Collisions at root(s)=7 TeV using the ATLAS Detector. Technical Report ATLAS-CONF-2011-011, CERN, Geneva, Mar 2011. http://cds.cern.ch/record/1334563.

[62] ATLAS Collaboration. Luminosity Determination in pp Collisions at $\sqrt{s} = 7$ TeV Using the ATLAS Detector at the LHC. *Eur. Phys. J.*, C71:1630, 2011. https://arxiv.org/abs/1101.2185.

[63] ATLAS Experiment, Public Results, Luminosity Run 1. https://twiki.cern.ch/twiki/bin/view/AtlasPublic/LuminosityPublicResults.

[64] ATLAS Collaboration. Luminosity determination in pp collisions at $\sqrt{s}$ = 8 TeV using the ATLAS detector at the LHC. *Eur. Phys. J.*, C76(12):653, 2016. https://arxiv.org/abs/1608.03953.

[65] ATLAS Experiment, Public Results, Luminosity Run 2. https://twiki.cern.ch/twiki/bin/view/AtlasPublic/LuminosityPublicResultsRun2.

[66] ATLAS Collaboration. Performance of the ATLAS Inner Detector Track and Vertex Reconstruction in the High Pile-Up LHC Environment. 2012. https://inspirehep.net/record/1204277.

[67] LHC Commissioning with beam. http://lhc-commissioning.web.cern.ch/lhc-commissioning/.

[68] LHC commissioning - schedule-update. http://lhc-commissioning.web.cern.ch/lhc-commissioning/schedule/LHC-schedule-update.pdf.

[69] Futur of LHC - Beate H. https://www.sns.ias.edu/ckfinder/userfiles/files/Heinemann-PiTP-II.pdf.

[70] LHC: Status, Prospects and Future Challenges - Elias Métral - LHCP2016, 2016. https://pos.sissa.it/archive/conferences/276/002/LHCP2016_002.pdf.

[71] LHC Performance Workshop (Chamonix 2016) , 2016. https://indico.cern.ch/event/486336/contributions/2006462/attachments/1238124/1824002/Fk_Bordry_Chamonix_2016_Conclusions_final.pdf.

[72] ATLAS Collaboration. Letter of Intent for the Phase-I Upgrade of the ATLAS Experiment. Technical Report CERN-LHCC-2011-012. LHCC-I-020, CERN, Geneva, Nov 2011. https://cds.cern.ch/record/1402470.

[73] G Apollinari, I Béjar A., O Brüning, M Lamont, and L Rossi. *High-Luminosity Large Hadron Collider (HL-LHC): Preliminary Design Report*. CERN Yellow Reports: Monographs. CERN, Geneva, 2015. http://cds.cern.ch/record/2116337.

[74] ATLAS Collaboration. Performance assumptions based on full simulation for an upgraded ATLAS detector at a High-Luminosity LHC. Technical Report ATL-PHYS-PUB-2013-009, CERN, Geneva, Sep 2013. https://cds.cern.ch/record/1604420.

[75] The ATLAS Collaboration. *ATLAS detector and physics performance: Technical Design Report, 1*. Technical Design Report ATLAS. CERN, Geneva, 1999. https://cds.cern.ch/record/391176.

[76] ATLAS Collaboration. Expected Performance of the ATLAS Experiment - Detector, Trigger and Physics. 2009. https://arxiv.org/abs/0901.0512.

[77] ATLAS Collaboration. *ATLAS inner detector: Technical Design Report, 1*. Technical Design Report ATLAS. CERN, Geneva, 1997. https://cds.cern.ch/record/331063.

[78] ATLAS Collaboration. Charged-particle distributions in $\sqrt{s}$=13 TeV p p interactions measured with the ATLAS detector at the LHC. Technical Report ATLAS-CONF-2015-028, CERN, Geneva, Jul 2015. http://cds.cern.ch/record/2037701.

[79] M. S. Alam et al. ATLAS pixel detector: Technical design report. 1998. https://inspirehep.net/record/487239?ln=fr.

[80] ATLAS Collaboration. The ATLAS Pixel Detector. 2004. https://arxiv.org/abs/physics/0412138.

[81] M Capeans, G Darbo, K Einsweiller, M Elsing, T Flick, M Garcia-Sciveres, C Gemme, H Pernegger, O Rohne, and R Vuillermet. ATLAS Insertable B-Layer Technical Design Report. Technical Report CERN-LHCC-2010-013. ATLAS-TDR-19, Sep 2010. https://cds.cern.ch/record/1291633.

[82] S. Pires. Impact of the Insertable B-Layer on b-tagging performance for ATLAS Run-II. *Acta Physica Polonica B*, 45(7):1567–1574, 2014. on behalf of the ATLAS Collaboration.

[83] V. A. Mitsou. The ATLAS transition radiation tracker. In *Astroparticle, particle and space physics, detectors and medical physics applications. Proceedings, 8th Conference, ICATPP 2003, Como, Italy, October 6-10, 2003*, pages 497–501, 2003. http://cds.cern.ch/record/686973?ln=fr.

[84] ATLAS Collaboration. Particle Identification Performance of the ATLAS Transition Radiation Tracker. Technical Report ATLAS-CONF-2011-128, CERN, Geneva, Sep 2011. https://cds.cern.ch/record/1383793.

[85] ATLAS Collaboration. The Run-2 ATLAS Trigger System. Technical Report ATL-DAQ-PROC-2016-003, CERN, Geneva, Feb 2016. https://cds.cern.ch/record/2133909.

[86] ATLAS Collaboration. Performance of the ATLAS Trigger System in 2015. *Eur. Phys. J.*, C77(5):317, 2017. https://arxiv.org/abs/1611.09661.

[87] ATLAS Collaboration. Track Reconstruction Performance of the ATLAS Inner Detector at $\sqrt{s} =$ 13 TeV. Technical Report ATL-PHYS-PUB-2015-018, CERN, Geneva, Jul 2015. https://cds.cern.ch/record/2037683.

[88] ATLAS Collaboration. Performance of the ATLAS Track Reconstruction Algorithms in Dense Environments in LHC run 2. 2017. https://arxiv.org/abs/1704.07983.

[89] ATLAS Collaboration. Vertex Reconstruction Performance of the ATLAS Detector at $\sqrt{s}$=13 TeV. Technical Report ATL-PHYS-PUB-2015-026, CERN, Geneva, Jul 2015. http://cds.cern.ch/record/2037717.

[90] V Lacuesta. Track and vertex reconstruction in the atlas experiment. *Journal of Instrumentation*, 8(02):C02035, 2013. http://stacks.iop.org/1748-0221/8/i=02/a=C02035.

[91] The ATLAS Collaboration. Public Results - Approved Plots of the Tracking Combined Performance Group. https://atlas.web.cern.ch/Atlas/GROUPS/PHYSICS/PLOTS/IDTR-2016-013/.

[92] ATLAS Collaboration. Topological cell clustering in the ATLAS calorimeters and its performance in LHC Run 1. 2016. https://arxiv.org/abs/1603.02934.

[93] Electron efficiency measurements with the ATLAS detector using the 2015 LHC proton-proton collision data. Technical Report ATLAS-CONF-2016-024, CERN, Geneva, Jun 2016. http://cds.cern.ch/record/2157687.

[94] Photon identification in 2015 ATLAS data. Technical Report ATL-PHYS-PUB-2016-014, CERN, Geneva, Aug 2016. http://cds.cern.ch/record/2203125.

[95] ATLAS Collaboration. Electron and photon energy calibration with the ATLAS detector using data collected in 2015 at $\sqrt{s} = 13$ TeV. Technical Report ATL-PHYS-PUB-2016-015, CERN, Geneva, Aug 2016. https://cds.cern.ch/record/2203514.

[96] ATLAS Collaboration. Electron and photon energy calibration with the ATLAS detector using LHC Run 1 data. *Eur. Phys. J.*, C74(10):3071, 2014. https://arxiv.org/abs/1407.5063.

[97] Public Results - Central electrons energy scale factors and resolution constant term using Z to ee events from 2015 and 2016 data. https://atlas.web.cern.ch/Atlas/GROUPS/PHYSICS/PLOTS/EGAM-2017-002/index.html.

[98] ATLAS Collaboration. Muon reconstruction performance of the ATLAS detector in proton–proton collision data at $\sqrt{s}$=13 TeV. *Eur. Phys. J. C*, 76(arXiv:1603.05598. CERN-EP-2016-033):292. 45 p, Mar 2016. Comments: Comments: 27 pages inlcuding cover page plus author list (45 pages total), 12 figures, 3 tables, submitted to Eur. Phys. J. C. All figures including auxiliary figures are available at https://atlas.web.cern.ch/Atlas/GROUPS/PHYSICS/PAPERS/PERF-2015-10/, https://cds.cern.ch/record/2139897.

[99] Matteo Cacciari, Gavin P. Salam, and Gregory Soyez. The anti-k_t jet clustering algorithm. *JHEP*, 04:063, 2008. https://arxiv.org/abs/0802.1189.

[100] ATLAS Collaboration. Properties of Jets and Inputs to Jet Reconstruction and Calibration with the ATLAS Detector Using Proton-Proton Collisions at $\sqrt{s} = 13$ TeV. Technical Report ATL-PHYS-PUB-2015-036, CERN, Geneva, Aug 2015. https://cds.cern.ch/record/2044564.

[101] ATLAS Collaboration. Performance of missing transverse momentum reconstruction for the ATLAS detector in the first proton-proton collisions at at $\sqrt{s}$= 13 TeV. Technical Report ATL-PHYS-PUB-2015-027, CERN, Geneva, Jul 2015. https://cds.cern.ch/record/2037904.

[102] ATLAS Collaboration. Performance of algorithms that reconstruct missing transverse momentum in $\sqrt{s} = 8$ TeV proton-proton collisions in the ATLAS detector. *Eur. Phys. J.*, C77(4):241, 2017. https://arxiv.org/abs/1609.09324.

[103] ATLAS Collaboration. Public plots: Missing transverse energy performance and systematic uncertainties using the full 2015 dataset. http://atlas.web.cern.ch/Atlas/GROUPS/PHYSICS/PLOTS/JETM-2016-003/.

[104] ATLAS Collaboration. Jet energy measurement with the ATLAS detector in proton-proton collisions at $\sqrt{s} = 7$ TeV. *Eur. Phys. J.*, C73(3):2304, 2013. https://arxiv.org/abs/1112.6426.

[105] ATLAS Collaboration. Jet energy scale measurements and their systematic uncertainties in proton-proton collisions at $\sqrt{s}$ = 13 TeV with the ATLAS detector . 2017. https://atlas.web.cern.ch/Atlas/GROUPS/PHYSICS/PAPERS/PERF-2016-04/.

[106] ATLAS Collaboration. Jet energy measurement and its systematic uncertainty in proton-proton collisions at $\sqrt{s} = 7$ TeV with the ATLAS detector. *Eur. Phys. J.*, C75:17, 2015. https://arxiv.org/abs/1406.0076.

[107] Jet Calibration and Systematic Uncertainties for Jets Reconstructed in the ATLAS Detector at $\sqrt{s} = 13$ TeV. Technical Report ATL-PHYS-PUB-2015-015, CERN, Geneva, Jul 2015. https://cds.cern.ch/record/2037613.

[108] ATLAS Collaboration. Jet energy scale and its systematic uncertainty in proton–proton collisions at $\sqrt{s} = 7$ TeV with ATLAS 2010 data. ATLAS-CONF-2011-032, 2011.

[109] Matteo Cacciari, Gavin P. Salam, and Gregory Soyez. FastJet User Manual. *Eur. Phys. J.*, C72:1896, 2012. https://arxiv.org/abs/1111.6097.

[110] S. Agostinelli et al. GEANT4: A simulation toolkit. *Nucl. Instrum. Meth. A*, 506:250, 2003. http://inspirehep.net/record/856179.

[111] A. Ribon et al. Status of geant4 hadronic physics for the simulation of lhc experiments at the start of the lhc physics program. 2010. https://lcgapp.cern.ch/project/docs/noteStatusHadronic2010.pdf.

[112] ATLAS Collaboration. Performance of primary vertex reconstruction in proton–proton collisions at $\sqrt{s} = 7$ TeV in the ATLAS experiment. ATLAS-CONF-2010-069, 2010. https://cds.cern.ch/record/1281344.

[113] ATLAS Collaboration. Performance of pile-up mitigation techniques for jets in pp collisions at $\sqrt{s} = 8$ TeV using the ATLAS detector. *Eur. Phys. J.*, C76(11):581, 2016. https://arxiv.org/abs/1510.03823.

[114] ATLAS Collaboration. Muon reconstruction performance of the ATLAS detector in proton–proton collision data at $\sqrt{s}$ =13 TeV. *Eur. Phys. J.*, C76(5):292, 2016. https://arxiv.org/abs/1603.05598.

[115] ATLAS Collaboration. Light-quark and gluon jet discrimination in pp collisions at $\sqrt{s} = 7$ TeV with the ATLAS detector. *Eur. Phys. J.*, C74(8):3023, 2014. https://inspirehep.net/record/1298030.

[116] T. Barillari et al. Local hadronic calibration. 2009. https://cds.cern.ch/record/1112035.

[117] ATLAS Collaboration. Jet reconstruction and performance using particle flow with the ATLAS Detector. 2017. https://arxiv.org/abs/1703.10485.

[118] Studies of the ATLAS Inner Detector material using $\sqrt{s}$ =13 TeV pp collision data. Technical Report ATL-PHYS-PUB-2015-050, CERN, Geneva, Nov 2015. https://cds.cern.ch/record/2109010.

[119] CMS Collaboration. Determination of jet energy calibration and transverse momentum resolution in CMS. *Journal of Instrumentation*, 6:11002, November 2011. http://adsabs.harvard.edu/abs/2011JInst...611002C.

[120] ATLAS Collaboration. Early Inner Detector Tracking Performance in the 2015 data at $\sqrt{s}$ = 13 TeV. Technical Report ATL-PHYS-PUB-2015-051, CERN, Geneva, Dec 2015. https://cds.cern.ch/record/2110140.

[121] ATLAS Collaboration. The Optimization of ATLAS Track Reconstruction in Dense Environments. Technical Report ATL-PHYS-PUB-2015-006, CERN, Geneva, Mar 2015. https://cds.cern.ch/record/2002609.

[122] G. Corcella, I. G. Knowles, G. Marchesini, S. Moretti, K. Odagiri, P. Richardson, M. H. Seymour, and B. R. Webber. HERWIG 6.5 release note. 2002. https://arxiv.org/abs/hep-ph/0210213.

[123] ATLAS collaboration. Determination of jet calibration and energy resolution in proton-proton collisions at $\sqrt{s}$ = 8 TeV using the ATLAS detector. Technical Report ATL-COM-PHYS-2017-164, CERN, Geneva, Feb 2017. https://cds.cern.ch/record/2253046.

[124] Matteo Cacciari and Gavin P. Salam. Pileup subtraction using jet areas. *Phys. Lett.*, B659:119–126, 2008. https://arxiv.org/abs/0707.1378.

[125] Jet global sequential corrections with the ATLAS detector in proton-proton collisions at $\sqrt{s}$ = 8 TeV. Technical Report ATLAS-CONF-2015-002, CERN, Geneva, Mar 2015. https://cds.cern.ch/record/2001682.

[126] ATLAS Collaboration. Track-based underlying event measurements in pp collisions at $\sqrt{s} = 900$ GeV and 7 TeV with the ATLAS Detector at the LHC. ATLAS-CONF-2010-081, 2010. https://cds.cern.ch/record/1298845.

[127] ATLAS Collaboration. Measurement of underlying event characteristics using charged particles in pp collisions at $\sqrt{s} = 900$ GeV and 7 TeV with the ATLAS detector in a limited phase space. ATLAS-CONF-2011-009, 2011. https://cds.cern.ch/record/1330721.

[128] ATLAS Collaboration. Summary of ATLAS Pythia 8 tunes. ATL-PHYS-PUB-2012-003, 2012. https://cds.cern.ch/record/1474107.

[129] Torbjorn Sjostrand, Stephen Mrenna, and Peter Z. Skands. A Brief Introduction to PYTHIA 8.1. *Comput. Phys. Commun.*, 178:852, 2008. https://arxiv.org/abs/0710.3820.

[130] T. Gleisberg, Stefan. Hoche, F. Krauss, M. Schonherr, S. Schumann, et al. Event generation with SHERPA 1.1. *JHEP*, 02:007, 2009. https://arxiv.org/abs/0811.4622.

[131] Jean-Baptiste Sauvan. *Z+jets at the LHC : jet energy calibration and cross section measurements with the ATLAS detector*. Theses, Université Paris Sud - Paris XI, Sep 2012. https://tel.archives-ouvertes.fr/tel-00747024.

[132] Guillaume Lefebvre. *Etalonnage des jets et mesure de la section efficace de production de paires de quarks top dans le canal hadronique à $\sqrt{s}$ = 8 TeV avec l'expérience ATLAS auprès du LHC*. Theses, Université Paris Diderot, Paris VII, Sep 2014. https://inspirehep.net/record/1382006/files/.

[133] ATLAS Collaboration. ATLAS 2016 jet calibration recommendation. https://twiki.cern.ch/twiki/bin/view/AtlasProtected/ApplyJetCalibration2016#Calibrating_jets_in_Release_21.

[134] ATLAS Collaboration. A measurement of the calorimeter response to single hadrons and determination of the jet energy scale uncertainty using LHC Run-1 pp-collision data with the ATLAS detector. *Eur. Phys. J.*, C77(1):26, 2017. https://arxiv.org/abs/1607.08842.

[135] ATLAS Collaboration. ATLAS 2015 jet calibration recommendation. https://twiki.cern.ch/twiki/bin/view/AtlasProtected/ApplyJetCalibration2015.

[136] Determination of the jet energy scale and resolution at ATLAS using Z/γ–jet events in data at $\sqrt{s} = 8$ TeV. Technical Report ATLAS-CONF-2015-057, CERN, Geneva, Oct 2015. https://cds.cern.ch/record/2059846.

[137] Selection of jets produced in 13TeV proton-proton collisions with the ATLAS detector. Technical Report ATLAS-CONF-2015-029, CERN, Geneva, Jul 2015. https://cds.cern.ch/record/2037702.

[138] Tagging and suppression of pileup jets with the ATLAS detector. Technical Report ATLAS-CONF-2014-018, CERN, Geneva, May 2014. https://cds.cern.ch/record/1700870.

[139] ATLAS Collaboration. Monte Carlo Generators for the Production of a W or Z/γ^* Boson in Association with Jets at ATLAS in Run 2. Technical Report ATL-PHYS-PUB-2016-003, CERN, Geneva, Jan 2016. https://cds.cern.ch/record/2120133.

[140] ATLAS Collaboration. Jet energy scale measurements and their systematic uncertainties in proton-proton collisions at $\sqrt{s}$ = 13 TeV with the ATLAS detector. Technical Report ATL-COM-PHYS-2016-213, CERN, Geneva, Mar 2016. https://arxiv.org/abs/1703.09665.

[141] ATLAS Collaboration. Measurement of the inclusive isolated prompt photon cross section in pp collisions at $\sqrt{s}$ = 7 TeV with the ATLAS detector. *Phys. Rev. D*, 83(arXiv:1012.4389. CERN-PH-EP-2010-068):052005. 33 p, Dec 2010. https://cds.cern.ch/record/1318459.

[142] Gerhard Bohm and Günter Zech. Introduction to statistics and data analysis for physicists. 2010. https://arxiv.org/abs/0707.1378.

[143] ATLAS collaboration. Jet energy resolution in proton-proton collisions at $\sqrt{s}$ = 7 TeV recorded in 2010 with the ATLAS detector. Technical Report ATL-COM-PHYS-2017-164, CERN, Geneva, Feb 2017. https://arxiv.org/abs/1210.6210.

[144] Guillaume Lefebvre. *Etalonage des jets et mesure de la section efficace de production de paires de quarks top dans le canal hadronique à $\sqrt{s}$ = 8 TeV avec l'expérience ATLAS auprès du LHC*. PhD thesis, 2014. http://www.theses.fr/2014PA077242.

[145] ATLAS Collaboration. Search for squarks and gluinos using final states with jets and missing transverse momentum with the ATLAS detector in $\sqrt{s} = 7$ TeV proton-proton collisions. *Phys. Lett.*, B701:186–203, 2011. https://arxiv.org/abs/1102.5290.

[146] ATLAS Collaboration. Search for squarks and gluinos using final states with jets and missing transverse momentum with the ATLAS detector in $\sqrt{s} = 7$ TeV proton-proton collisions. *Phys. Lett.*, B710:67–85, 2012. https://arxiv.org/abs/1109.6572.

[147] ATLAS Collaboration. Search for squarks and gluinos with the ATLAS detector in final states with jets and missing transverse momentum using 4.7 fb^{-1} of $\sqrt{s} = 7$ TeV proton-proton collision data. *Phys. Rev.*, D87(1):012008, 2013. https://arxiv.org/abs/1208.0949.

[148] ATLAS Collaboration. Performance of Missing Transverse Momentum Reconstruction in Proton-Proton Collisions at 7 TeV with ATLAS. *Eur. Phys. J.*, C72:1844, 2012. https://inspirehep.net/record/925553.

[149] ATLAS Collaboration. Measurement of the photon identification efficiencies with the ATLAS detector using LHC Run-1 data. *Eur. Phys. J.*, C76(12):666, 2016. https://arxiv.org/abs/1606.01813.

[150] ATLAS Collaboration. Search for new phenomena with large jet multiplicities and missing transverse momentum using large-radius jets and flavour-tagging at ATLAS in 13 TeV pp collisions. Technical Report ATLAS-CONF-2017-033, CERN, Geneva, May 2017. https://atlas.web.cern.ch/Atlas/GROUPS/PHYSICS/CONFNOTES/ATLAS-CONF-2017-033/.

[151] Chunhui Chen. New approach to identifying boosted hadronically-decaying particle using jet substructure in its center-of-mass frame. *Phys. Rev.*, D85:034007, 2012. https://arxiv.org/abs/1112.2567.

[152] D. Cousins Robert, T. Linnemann James, and Tucker Jordan. Evaluation of three methods for calculating statistical significance when incorporating a systematic uncertainty into a test of the background-only hypothesis for a Poisson process. 2007. https://arxiv.org/abs/physics/0702156.

[153] Cranmer Kyle. Statistical Challenges for Searches for New Physics at the LHC. 2005. https://arxiv.org/abs/physics/0511028.

[154] Linnemann J. T. Measures of Significance in HEP and Astrophysics. 2005. https://arxiv.org/abs/physics/0312059.

[155] M. Baak, G. J. Besjes, D. Côte, A. Koutsman, J. Lorenz, and D. Short. HistFitter software framework for statistical data analysis. *Eur. Phys. J.*, C75:153, 2015. https://arxiv.org/abs/1410.1280.

[156] A. Djouadi et al. The Minimal supersymmetric standard model: Group summary report. In *GDR (Groupement De Recherche) - Supersymetrie Montpellier, France, April 15-17, 1998*, 1998. https://arxiv.org/abs/hep-ph/9901246.

[157] Search for new phenomena in a lepton plus high jet multiplicity final state with the ATLAS experiment using $\sqrt{s}$ = 13 TeV proton–proton collision data. Technical Report ATLAS-CONF-2017-013, CERN, Geneva, Mar 2017. https://cds.cern.ch/record/2257717.

[158] ATLAS Collaboration. Search for gluinos in events with an isolated lepton, jets and missing transverse momentum at $\sqrt{s}$ = 13 TeV with the ATLAS detector. *Eur. Phys. J.*, C76(10):565, 2016. https://arxiv.org/abs/1605.04285.

[159] Benjamin Nachman, Pascal Nef, Ariel Schwartzman, Maximilian Swiatlowski, and Chaowaroj Wanotayaroj. Jets from Jets: Re-clustering as a tool for large radius jet reconstruction and grooming at the LHC. *JHEP*, 02:075, 2015. https://arxiv.org/abs/1407.2922.

[160] Jet mass reconstruction with the ATLAS Detector in early Run 2 data. Technical Report ATLAS-CONF-2016-035, CERN, Geneva, Jul 2016. https://cds.cern.ch/record/2200211.

[161] A L Read. Presentation of search results: the cl s technique. *Journal of Physics G: Nuclear and Particle Physics*, 28(10):2693, 2002. http://stacks.iop.org/0954-3899/28/i=10/a=313.

[162] Multi-Boson Simulation for 13 TeV ATLAS Analyses. Technical Report ATL-PHYS-PUB-2016-002, CERN, Geneva, Jan 2016. https://cds.cern.ch/record/2119986.

[163] ATLAS Collaboration. Performance of b-Jet Identification in the ATLAS Experiment. *JINST*, 11(04):P04008, 2016. https://arxiv.org/abs/1512.01094.

[164] Optimisation of the ATLAS b-tagging performance for the 2016 LHC Run. Technical Report ATL-PHYS-PUB-2016-012, CERN, Geneva, Jun 2016. https://cds.cern.ch/record/2160731.

Remerciements

La thèse est l'aboutissement d'un long travail de recherche qui n'aurait pas pu se faire sans l'aide de nombreuses personnes. Je tiens à remercier dans un premier temps Nikola Makovec pour son encadrement régulier, son implication et ses conseils judicieux tout au long de la thèse. Merci à Achille Stocchi de m'avoir accueilli au LAL où j'ai pu effectuer mes trois années de recherche et d'avoir présidé mon jury de thèse. Merci aux deux rapporteurs, Filip Moortgat et Pascal Pralavorio d'avoir lu attentivement mon manuscrit et d'avoir permis de l'améliorer. Merci également à Caroline Collard et Christophe Clement d'avoir accepté de faire partie de mon jury de thèse et d'évaluer mon travail.

Je tiens à remercier tous les membres du groupe ATLAS au LAL pour leur aide au cours des trois années. Merci particulièrement à Laurent Duflot pour son expertise technique, R.D pour les corrections d'anglais, Luc Poggioli pour son humour très développé, Dirk Zerwas pour sa bonne humeur, et Marc Escalier pour les discussions. Un grand merci à Dimitris Varouchas avec qui j'ai partagé mon bureau pendant la dernière année de thèse, et à Geneviève Gilbert pour son aide administrative pendant les trois années. Merci également aux personnes du service informatique et du service mission pour leur aide et leur disponibilité.

Un grand merci à tous les doctorants du laboratoire dont j'ai eu le plaisir d'être le représentant pendant mes deux premières années de thèse. Merci à Steven pour son humour fin et subtil, pour les parties de concept, le tennis, les films et les nombreuses discussions. Merci à Christophe avec d'avoir partagé le fameux bureau 140 pendant notre première année de thèse. Merci également à Charles et David pour les parties de civilisation, les concours de fléchettes et les discussions. Merci également à David pour la clarté de ses explications et sa pédagogie. Merci à Antinéa, Antoine et Corentin de prendre soin du comité des étudiants du labo. Je suis certain qu'il est entre de bonnes mains. Merci aussi aux anciens: Marija, Mohamad et Cyril pour leur aide technique et leurs conseils au début de thèse. Un merci particulier à Vagelis pour son aide et son soutien. Merci à Sylvain pour les virées nocturnes et les longues discussions. Merci à Pierre, Cheikh et Steven pour la semaine des doctoriales qui nous laisse plein de bons souvenirs. Merci à Themis pour ce fameux rendez-vous qu'on n'oubliera jamais. Merci également à Huijin pour les diners tard au laboratoire pendant la période de rédaction.

Un immense merci à Alvaro pour son soutien et ses très bons conseils depuis le Master 1. Merci pour sa patience et le temps passé ensemble à découvrir le monde. Un immense merci à Daniel, Pierre et Marie pour les soirées, les voyages, et tout ce que l'avenir nous réserve. Un immense merci aussi à Gaetan, Mattieu, Max, Pierre, Remi et Vincent pour leur soutien pendant la thèse et pour m'avoir supporté depuis si longtemps. Merci également à Gaetan pour m'avoir aidé pendant la rédaction, et à Hermine pour son soutien à la FBL et depuis la Suisse.

Je tiens à remercier ma famille pour son soutien, ses encouragements, pour avoir toujours été présente quand il fallait, et qui m'a aidé à tracer mon propre chemin.

Je remercie enfin les nombreuses personnes que je n'ai pu citer et qui m'ont aidé à aller de l'avant.